Mode Engineering of Single Photons from Cavity Spontaneous Parametric Down-Conversion Source and Quantum Dots

by

Uttam Paudel

A dissertation submitted in partial fulfillment
of the requirements for the degree of
Doctor of Philosophy
(Physics)
in The University of Michigan
2017

Doctoral Committee:

Professor Duncan G. Steel, Chair
Emeritus Professor Paul R. Berman
Associate Professor Hui Deng
Assistant Professor Parag B. Deotare
Professor Mackillo Kira

Uttam Paudel

upaudel@umich.edu

ORCID iD: 0000-0002-7833-6669

To numerous curious individuals who set the foundation for logic, mathematical and scientific inquiries

and to

Mina, Marta, and Pratima,

three strong women without whom I would not have gotten this far.

ACKNOWLEDGEMENTS

Growing up in a small village in Nepal that was devoid of basic necessities such as electricity, running water, and proper sanitation, I never imagined that one day I would get trained by some of the finest scientists in the world. Yet, a series of fortunate events and the generosity of many people that decided to give me a chance brought me to Berkeley for undergraduate and the University of Michigan for my graduate education. I would like to express my deep gratitude to the many teachers that shaped me and the wonderful system we have in this country that helped me to get this far in life. Similarly, my academic pursuit would not have been possible if my parents, Bishnu and Mina, had not decided to immigrate to the US, even if that meant them having to start from zero doing menial jobs. Thank you, Pratima didi for being the pillar of our family and Shekhar bhai for being there when our parents needed us.

To work with Duncan Steel was probably one of the best decisions I made while at graduate school. From the day I met him, I have been awed and inspired by Duncan and have been striving to acquire many of the great qualities that he possesses. I have never seen such a logical individual who strives for everything to be rigorous and leak-proof, yet is equally compassionate, caring and relatable. Duncan is truly a wonderful mentor, who is always working towards fostering the academic, intellectual and personal growth of his students. Thank you for giving me all the freedom that I could imagine and guiding me throughout my Ph.D. I hope I will walk out of graduate school as a competent scientist. I look forward to collaborating and learning from

you for many more years to come.

Paul Berman is another such inspirational person that I have been privileged to know personally and be trained by in quantum optics and spectroscopy. His yearlong classes, many email exchanges, and numerous office visits have educated me about many subtle ideas and phenomena in light-matter interactions that are often ignored by busy scientists. I apologize for bothering you with my silly, half-thought out questions, though I cannot promise that I will stop doing so in the near future. Special thanks to my undergraduate mentor Yury Kolomensy for introducing me to the world of research, Padam Sapkota for getting me interested in mathematics and Ted Stolze for helping me shape my worldview. I would also like to thank my committee members for reading my thesis and helping to improve it.

The acknowledgment section would be incomplete without thanking the lab members. When I first joined the lab, Cameron Nelson mentored me for a few months and soon afterward our relationship transited from mentor-mentee to besties. Cameron is one of the finest partners to work with that one could ask for. Thank you for always being there. I will truly miss spending long hours together in the dark lab, ranting about life, watching trashy comedy videos that I secretly enjoyed yet always denied. Much of the experimental techniques that I learned in Duncan's lab were from Alex Burgers. Thank you for mentoring me. I always admired you for your perfectionist attitude. I would like to thank Aaron Ross for lending your pressure tuned etalon, without which a lot of my measurements would not have been possible. I always enjoyed having all those interesting physics and political conversations with you. It was my privilege to work with John Schabiley, Colin Chow, Humza Khan, Adam Katcher, Midhat Farooq, Christine Drown, Lu Ma, Victoria Zhang, Alex Ying, and Rae Stearny.

A lot of the work presented in this thesis would not have been possible without the help of our collaborators. Many thanks to Dan Gammon and Allan Bracker

for growing the quantum dot samples. Also, thanks to JJ Wong, Paul Kwiat, Mike Goggin, and Jian Yang from UIUC for the collaboration on constructing the SPDC source. JJ helped me to get up to speed with the experiment and taught me the basics of SPDC that ultimately lead us to successfully building and understanding the source. I enjoyed the brief collaboration I had with Tanvi Gujarati on some of the theoretical calculations that we hope to publish soon.

Many thanks to Joe Sheldon, student service, and the machine shop folks for your help, and Finn Larsen for being there when I needed help trying to navigate through graduate school.

Nick and Joe have been some of my closest friends which whom I share every detail about my life and research. I always enjoyed talking with you guys. Thank you for being there and listening to my ramblings. Also, I would like to thank some of my good friends that I met while at graduate school: Arash Arabi, Rahul Datta, Deshpreet Bedi, Scott Stephenson, Meredith Henstridge, ATLAS friends, HET friends, the Nepali gang, and many more friends that I could not mention due to space limitation. I hope to have a long lasting friendship with you all.

At last, I would like to thank Marta Luengo, the most important person in my life who assisted me in every possible way one could ask for. Besides Duncan, Marta is probably the only person who read every single word of my thesis and was always there to help me get through my Ph.D. I often joke around with friends that Marta is the biggest achievement of my graduate school career. Without her, I would not have gotten this far. I truly am grateful for her continuous emotional and intellectual support, not to mention all the delicious meals she made for me for almost every day of the last 4.5 years.

TABLE OF CONTENTS

LIST OF FIGURES

LIST OF TABLES

LIST OF APPENDICES

LIST OF ABBREVIATIONS

SHG second harmonic generation

SFG sum frequency generation

DFG difference frequency generation

OPG optical parametric generation

SPDC spontaneous parametric down-conversion

IR infra-red

MBE molecular beam epitaxy

InAs indium arsenide

AlAs aluminum arsenide

DBR distributed Bragg reflector

HOM Hong-Ou-Mandel

CHAPTER I

Customized Single Photons for Quantum Networks

1.1 Brief Motivation for Quantum Information Technology

Over the past few decades there has been much interest in quantum information technologies, motivated by both basic science and engineering. In the basic science front, much interest come from information theory and testing quantum mechanics [1, 2, 3]. The interest for quantum engineering can be broadly categorized as quantum computing and quantum communication [4]. Proposals to exploit phenomena such as entanglement and the superposition principle that are unique to quantum mechanics for computation purposes trace back to Richard Feynman [5]. The idea behind a quantum computer is to use quantum bits (qubits) instead of classical bits for computing [6, 7], where the quantum degree of freedom such as spins of a single electron or polarization of single photons can be used as qubits. The pioneering work of Peter Shor formulating a quantum algorithm for integer factorization that can outperform classical algorithms gave much credibility to the idea of building a quantum computer [8, 4]. Since then, much progress has been made on that frontier. One of the primary goals of the quantum communication community is to build an attack-proof quantum key distribution with a large key distribution rate that allows secure transmission of information over a long distance [9, 10]. The single-particle nature of single photons and properties like non-local entanglement between two particles can be exploited to

generate such attack-proof secure quantum communication channels [11, 9].

A quantum network is a distributed system that allows quantum information to be stored in local clusters and transmitted over distance as needed, making it useful for both quantum computation and quantum communication applications. Such a quantum network would allow the realization of ambitious protocols such as a quantum internet [12], where one can process information locally with quantum nodes and distribute quantum software over a long distance. Even though the no-cloning theorem prohibits a quantum state to be replicated into multiple copies [13], a fragile quantum state can be transferred across distant nodes through teleportation and remote entanglement swapping [14, 15]. A quantum repeater is a small module of a large quantum network that can store information, perform logic operations, and purify quantum states with error correction codes and transmit them to the next module [16]. Such quantum repeaters form an intermediate link between nodes, ultimately leading to very long distance quantum connections between distant networks.

The basic building blocks of a quantum network can be broken into two parts: matter nodes confined in space for storing and manipulating information and photonic qubits capable of linking the distant nodes [17]. Quantum nodes can be linked several different ways. By bringing the two matter qubits in proximity, they can be entangled with each other through the local Coulomb interaction [18, 19]. Alternatively, by performing Bell state's analysis with Hong-Ou-Mandel (HOM) interference between the flying qubits that are entangled with the nodes of interest, one can interface distant nodes [20, 21]. Similarly, there exists a third class of protocols where the nodes separated by some distance can be connected with each other through the direct absorption of single photons [22, 23, 24, 25, 26], where two nodes of interest are linked by channeling photons from one node to another [27]. In this thesis, we will perform the second and third classes of measurements that will be crucial for building a scalable quantum network.

1.1.1 Quantum Dots and Parametric Down-Conversion: Candidates for Quantum Networks

There exists various candidates for building scalable quantum network, such as semiconductor quantum dots (QDs), gate-defined quantum dots, trapped ions, superconducting junctions, NV centers, etc., each with their own advantages [28, 29, 30, 31, 7]. Among them, InAs/GaAs QDs are a strong candidate that can be a source of both matter nodes and photonic qubits. Semiconductor QDs are formed by growing with molecular beam epitaxy (MBE) techniques. The mature industrial complex for semiconductors and knowledge acquired over the half century of research and developments could be utilized for building quantum networks and quantum computers with QDs. Also, as QDs can be grown in a laboratory, the optoelectronic properties of the system can be engineered and manipulated as desired, making it more flexible than other sources. Single QDs behave atom-like [32] and have a large dipole moment (ranging from $30 - 100$ Debye [33]), much larger than an atomic system. The direct bandgap of InAs/GaAs and the strong dipole moment makes them interact strongly with optical fields. In addition, QDs can be integrated with photonic crystal cavities and waveguides to further enhance the light-matter coupling and manipulate the directional emission from system. Such optoelectronic integration is important for scaling the system and for many photonics applications.

A negatively charged trion state in a QD gives rise to two Lambda-systems with the ground state occupied by a single electron that can be used as a spin qubit [34, 35, 36]. When prepared in a coherent superposition state, the coherence time (T_2^*) of the trion state in an InAs/GaAs QD at 4 K temperature is shown to be a few ns, with the intrinsic coherence time (T_2) exceeding a few μs [37, 36], forming a good candidate for single electron spin qubits. As the electrons are confined inside the semiconductor nanostructure, it removes the need of using a complicated trap setup that otherwise is required with ions. The strong light-matter interactions due to the

large dipole moment allow the spin qubit to be arbitrarily manipulated with ultra-fast laser pulses at picoseconds time scales [34, 35]. Such arbitrary manipulation of a spin qubit, along with fast optical initialization, allows more than 1000 gate operations to be performed within the coherence time. This satisfies some of the important DiVencenzo criteria for using trions as spin qubits for scalable quantum computer architectures [38, 39, 40, 41, 42]. In addition, it has been recently shown that a negatively charged trion state from an InAs QD can generate spin-photon entangled states [43, 44, 21], and teleportation and remote entanglement between two QDs have been recently demonstrated [45, 46]. These features makes QDs a compelling system to build a spin quantum network.

A realistic quantum network could be composed of several different systems, each with different electronic and optical properties. To envision such a hybrid network that could utilize the best features of each system, one needs to build a highly flexible flying qubit that can form links between two disparate systems [16, 47]. A type II spontaneous parametric down-conversion (SPDC) source could form a flexible link that can generate a pair of entangled photons [48]. With an appropriate crystal design, an SPDC system can be used as a source of photon pairs that are either degenerate or highly non-degenerate in wavelength, with the wavelength tunabled by several hundred nanometers [49]. Such tunable photon pairs can be used to link two systems at very different wavelengths. In addition, by placing the down-conversion crystal inside an optical cavity, it is shown that the emitted photons' temporal and spectral properties can be modified as desired while enhancing the count rates of the down-conversion photons [50]. Such large wavelength tunability, along with customizable spectrum, makes cavity-SPDC an excellent source to generate highly flexible entangled photon sources.

1.2 Photonics Qubits: Single Photons as Messengers in a Quantum Network

The generation of single photons and manipulation of the quantum state of it will be crucial for a quantum network. With single photons, quantum information can be encoded in their various degrees of freedom, such as the polarization, orbital angular momentum, spatial mode, and frequency spectrum. In addition to forming a quantum link for a quantum network, single photons are an excellent messenger for distributing cryptographic keys that allow faithful transfer of information between two remote parties [11]. Thus it is important to be able to engineer the properties of single photons for them to be used as photonic qubits.

1.2.1 Mode Engineered Single Photons

Polarization, spatial, spectral, and temporal are some of the modes, characterizations and manipulations of which will be importance when using single photons as links in quantum networks. Through the use of waveplates and polarizers, one can arbitrary change the polarization degree of freedom. Especially, with the advancement in photonic industries, there are multiple commercial companies that build waveplates and polarizers integrated with single mode fibers. Spatial mode matching can be achieved through the use of fibers. A single mode fiber has a sufficiently small core size (about a few μm) and can sustain only the TEM_{00} mode of the electric field propagating through it. It can be used as a spatial filter, such that the spatial mode of the photons used in the experiments are guaranteed to be nearly identical. Through the use of holograms and spatial light modulators one can shape the spatial modes of photons [51].

The spectral degree of freedom can be modified through the use of passive filtering, which is important for linking disparate system. For instance, the photons generated

through parametric processes come with a several nanometer bandwidth, whereas solid state systems such as QDs and defect centers have typical bandwidths of a few hundred MHz. To interface those two sources with each other, a sufficiently narrow-bandwidth filter that matches the property of the QD photons can be used to filter out the down-conversion field. However, such a passive filtering scheme removes the majority of the spectrum that doesn't match with the QD photons, lowering the usable photon counts. Alternatively, when the parametric crystal is placed inside an optical cavity, the modified density of states of the cavity (cavity modes) forces the down-conversion to happen only within the modes of the cavity. This allows full mode engineering of the down-converted field.

Similarly, an electro-optics phase modulator allows redistribution of the photon's spectral modes. Despite the widespread use of polarization qubits to transmit information, they are prone to decoherence when transmitted over a long distance through a fiber [52, 53, 54]. Frequency qubits [15], on the other hand, are known to be robust against any mechanically or environmentally-induced decoherence in a fiber [55, 56, 57]. Such frequency qubits can be generated through the modulation of a single photon by an electro-optic phase modulator [56, 58], where the information is encoded in the relative amplitude between the sidebands. Recently, Lukens and Lougovski have proposed a universal linear-optical quantum computing (LOQC) platform using frequency components generated from an electro-optics modulator [56]. Similarly, there have been proof-of-concept demonstrations of the BB84 protocol using phase modulated weak coherent sources [55, 59]. As single photons emitted by QDs have narrow natural linewidths (< 200 MHz), they can be used for phase-encoded BB84 protocol through the application of phase modulators.

In this thesis, we will perform spectral engineering of single photons using cavity-SPDC source and an electro-optic phase modulator. Such spectral engineering of single photons lays the foundation for using cavity-SPDC photons and QDs for various

quantum information applications.

1.2.2 Semantics of Single Photons

There has been much discussion about the semantics and the fundamental nature of single photons [60, 61]. Every time we use the word single photon or a single-mode field, we meant a radiation field localized in time or space with a finite momentum, frequency, and time spread. Such fields are by definition multi-mode in nature, and are not necessarily as simple as a single quanta with energy $\hbar\omega$, as it is sometimes commonly misbelieved to be. Due to the time-energy[1] and position-momentum uncertainty relationships, a true single-mode field with such sharp momentum and energy has an ill defined timing and position information, which means such a field would spread out everywhere in the Universe and in all past-present-future times. Such fields are close to be fictitious [60]. There have been numerous papers written inquiring about the nature of photons [60, 61], however by taking the pragmatic approach Roy Glauber took on describing a photon, "a photon is what a photodetector detects and is located where the photodetector detects it" [61], one can explain most of the quantum optics experiments that involve photons. A single photon can be defined as one unit of energy in the superposition of the field modes, where the positive component of the quantized transverse electric field operator in a free-space can be written as [63, 64],

$$E^{+}(r,t) = -\sum_{k,\mu} \sqrt{\frac{\hbar\omega_0}{2\epsilon_0}} f_{k,\mu}(r) a_{k,\mu}(t) \tag{1.1}$$

where $f_{k,\mu}(r)$ is the spatial mode distribution and the electric field is summed over all polarization (μ) and momentum states (k). When applied with a number operator $N \equiv a^{\dagger}a$, such state returns a single photon in the mode (k,μ).

To fully understand the property of the single photons, it is important to under-

[1] since time is not an operator, the uncertainity relationship is not same as for other canonical commutation relationships. See Mandelstam and Tamm's discussion on the subject matter for detail [62]

stand the origin of it. For instance, the radiation emitted by a two-level system such as a single QD can be calculated using the source-field formalism [65]. Remarkably enough, the emitted field can be fully described by simply employing the dipole and atomic operator of the two-level system. When the initial field is polarized along the z direction, the scattered radiation at angle θ can be expressed in terms of the atomic operator [65]

$$E^{+}(R,t) = -\left(\frac{\omega^2 \mu_{12} sin\theta}{4\pi\epsilon_0 c^2 R}\right)\sigma_{-}(t - R/c) \tag{1.2}$$

where σ_{-} is a lowering operator that lowers the atom from the excited state to the ground state and, similarly, $E^{-}(R,t)$ is proportional to the raising operator σ_{+}. It is important to note that the given radiation field is similar to a dipole oscillating in z-direction. Analogous to what one gets from a classical dipole oscillator, the field is emitted in 4π direction with radius ct, where t is the time the field has been emitted for. With a detector at a position R and time t, one can measure the intensity of the field by integrating over the detector's active area for a finite time. Despite the radiation field emitted by a two-level system having a similar form as a classical dipole radiation, there are several important distinctions to be made, one such feature is anti-bunching behavior of the emitted radiation field that is unique to single emitters [66]. For rest of the thesis we will denote such radiation field as a single photon state.

Even though we will frequently use the term single photons, we do not necessarily imply that we have a true Fock state $|n\rangle$ with $n = 1$. Such states are equally rare in real life. Despite the popular notion that a single emitter emits a true single photon Fock state, it is not an accurate statement, because the multi-photon emission probability might be negligible but is finite. Also, due to the finite collection efficiency, for the majority of the shots of an experiment, a detector does not see any photons, which makes the state being probabilistic. The state vector of the photons will be

dominated by a large vacuum mode

$$|\psi\rangle \sim |0\rangle + \eta \sum_{\vec{k},\epsilon} c_{k,\epsilon} e^{i\vec{k}\cdot\vec{r}-i\omega t} |1_{\vec{k},\hat{\epsilon}}\rangle + \eta^2 \sum_{\vec{k}_1,\epsilon_1} \sum_{\vec{k}_2,\epsilon_2} c1_{k_1,\epsilon} c2_{k_2,\epsilon_2} e^{i\vec{k_1}\cdot\vec{r}-i\omega_1 t} e^{i\vec{k_2}\cdot\vec{r}-i\omega_2 t} |1_{\vec{k_1},\hat{\epsilon}_2}\rangle \otimes |1_{\vec{k_2},\hat{\epsilon}_2}\rangle + ... \tag{1.3}$$

where η is the coupling constant and c's are mode-function. One can obtain a true single particle Fock state by projecting a component of the state vector. In theory, this could be achieved with photon sources, such as SPDC or bi-excitons in QDs where a true single Fock state is achieved through heralding processes by detecting an idler photon [67, 68, 69]. However, this requires one to have a number-resolving single-photon detector. Development of such detectors is still in infancy. Thus, despite the popular colloquial notion that the heralded photons are true single photons, the detectors in use are almost never number-resolving. Even with the detectors with near unity efficiency, with such heralding protocols, at best one gets rid of the vacuum modes, reducing the state of the heralded photon to be

$$|\psi_{heralded}\rangle \sim \eta \sum_{\vec{k},\epsilon} c_{k,\epsilon} e^{i\vec{k}\cdot\vec{r}-i\omega t} |1_{\vec{k},\hat{\epsilon}}\rangle + \eta^2 \sum_{\vec{k}_1,\epsilon_1} \sum_{\vec{k}_2,\epsilon_2} c1_{k_1,\epsilon} c2_{k_2,\epsilon_2} e^{i\vec{k_1}\cdot\vec{r}-i\omega_1 t} e^{i\vec{k_2}\cdot\vec{r}-i\omega_2 t} |1_{\vec{k_1},\hat{\epsilon}_2}\rangle \otimes |1_{\vec{k_2},\hat{\epsilon}_2}\rangle + ..., \tag{1.4}$$

which still has a finite probability for multi-pair emission [70]. Despite these shortcomings, single photons from quantum emitters and heralded SPDC are the closest source of true single photons that we currently have. Thus, for rest of the thesis, we will refer to such states as single photons.

1.3 Summary of The Thesis

The central theme of this thesis work is the generation of customized single photons using different sources. In the first half of the thesis, we will discuss the implementation of cavity-enhanced spontaneous parametric down-conversion (cavity-SPDC) source designed to mode match with the QD photons. We will show that the cavity-

SPDC source is capable of emitting an "on-demand" heralded single photon. We will report on the optical studies of single QDs, which are crucial for using them as a single photon source and spin qubits. We will give a detailed theoretical description of two-photon interference measurements and demonstrate such experiments using QD photons. We will show the coupling of the cavity-SPDC photons with a QD through direct absorption and two-photon interference measurements. Such two-photon interference measurements are at the heart of most quantum information protocols. As an alternative approach to modifying the spectral mode of single photons, we will employ phase modulation techniques with the single photons emitted by a cw-excited single QD to generate well-defined additional frequency components. Through two-photon interference measurements, we will show that the indistinguishability of such mode engineered photons remains well-preserved. These experimental results should lay the foundations towards building a scalable quantum network.

1.4 List of Publications

- Frequency-dressing a stream of single photons with preserved coherence, U. Paudel, *et al.*, arXiv:1706.07499(2017) (Under Review)

- Direct absorption of cavity-SPDC photons by a single quantum dot, U. Paudel, *et al.*,(In Preparation)

- Theory of two-photon interference with phase modulated photon packets, U. Paudel, *et al.*,(In Preparation)

- Resonant absorption spectrum of two laterally coupled quantum dots, U. Paudel, *et al.*,(In preparation)

1.5 Contribution Disclosure

The cavity-SPDC work is initially designed by Jian Yang from Paul Kwiat's Laboratory at UIUC and later implemented by JJ Wong and the author. The source was realigned and optimized at Michigan and the detail experimental and theoretical characterizations are done at Michigan by the author himself. Mike Goggin assisted on optimizing the source and Humza Khan assisted on writing some analysis code. All SPDC data are taken and analyzed at Michigan by the author.

The InAs/GaAs samples used in this thesis is grown by Dan Gammon and Allan Bracker from Naval Research Laboratory. Alex Burgers was involved in the initial characterization of the sample and generation of the frequency qubit using a phase modulator. Aaron Ross lent his scanning Fabry-Pérot for characterizing the source. All the data are taken and analyzed by the author under the supervision of Duncan Steel.

CHAPTER II

Classical Theory of Second-Order Nonlinear Polarizability in Crystal Optics

The second-order and third-order polarizability are two of the most widely studied nonlinear phenomena that give rise to much interesting physics. Third-order polarizability has been extensively used in our laboratory to study light-matter interaction and has been covered thoroughly in previous dissertation works [71, 72]. As this thesis work exploits second-order polarizability in crystal optics for second-harmonic generation and down-conversion, a thorough understanding of the subject matter is crucial. We will revisit the classical theory of the second-harmonic generation for the plane wave limit and derive the intensity profile and phase matching conditions. This chapter will work as a testbed for both theoretical and experimental understanding of nonlinear crystal optics that will be very relevant in designing the experimental setup for down-conversion.

2.1 Introduction

Since the discovery of second-harmonic generation (SHG) by Peter Franken et al. at the University of Michigan in 1961 [73], the field of nonlinear optics has grown into a mature field of study, drawing attention from both basic science and applied

communities. When electromagnetic radiation is applied to a medium, charges redistribute in the medium creating an internal electrical polarization. The potential due to such displacement can be written as,

$$V(r) = Ar^2 + Br^3 + ... \tag{2.1}$$

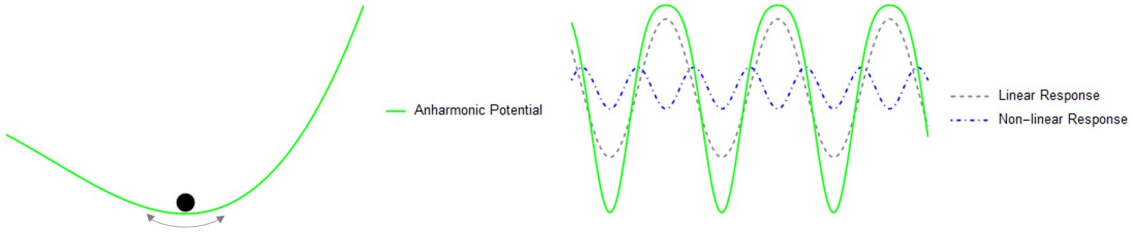

Figure 2.1: Cartoon of an anharmonic potential and it's frequency response to an applied field. The figure on the right shows the linear (gray dash) and nonlinear (blue dash) frequency responses of the oscillator. The periodic green plot is the sum of the linear and nonlinear response.

For a symmetric harmonic potential $V(-r) = V(r)$, the electric field causes the dipole of atoms to oscillates at frequency of the applied radiation field, making the polarization of the system linear in the applied electric field. However, virtually all atomic media have anharmonic potentials that result in higher order polarizability by an applied field. Most of the nonlinear phenomena in optics can be attributed to the higher order terms of such polarization.

The polarization (P) of a medium in the presence of an electric field (E) can be written as,

$$P^i = P_0 + \epsilon_0(\chi^{(1)}_{ij}E^j + \chi^{(2)}_{ijk}E^jE^k + \chi^{(3)}_{ijkl}E^jE^kE^l + ...) \tag{2.2}$$

where, $\chi^{(n)}_{ijk}$ is the electric susceptibility of the rank $n+1$ tensor and $i, j, k, l = \{x, y, z\}$

coordinates. The first-order χ is responsible for well-known phenomena like the index of refraction and dispersion, whereas the higher order terms give rise to a wide variety of phenomena, such as SHG, sum frequency generation (SFG), difference frequency generation (DFG), optical parametric generation (OPG), spontaneous parametric down-conversion (SPDC), four-wave mixing, and the optical Kerr effect, that were "unexplored"until the discovery of SHG.

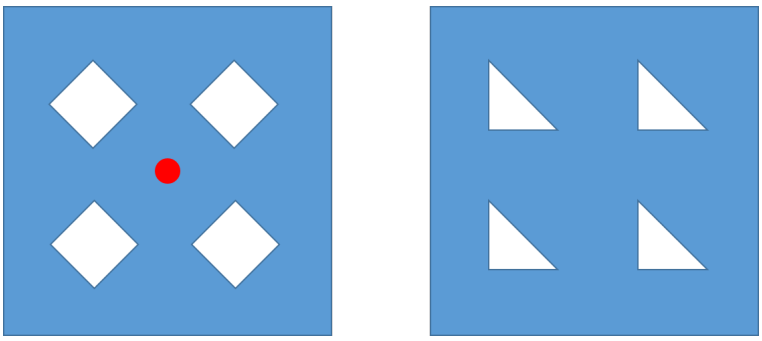

Figure 2.2: Cartoon of centrosymmetric(L) and non-centrosymmetric (R) lattice structures.

Symmetry arguments are a powerful tool commonly exploited in physics with which one can gain an insight about a system without having to solve complicated mathematical problems. For the sake of this thesis we will not go in detail on group theory of materials. If, in the unit cell of a crystal point (x, y, z) is indistinguishable from $(-x, -y, -z)$, such crystal has inversion symmetry. A material with a symmetric point in the crystal structure along which it has inversion symmetry is called a centrosymmetric material (see figure 2.2). In eq. (2.2) for $n = 1$ the polarization is odd under inversion symmetry ie.,

$$E(-r) = -E(r) \Rightarrow P(-r) = -P(r)$$

however for n = even, the symmetry is broken

$$E(-r) = -E(r) \Rightarrow P(-r) = P(r)$$

Non-centrosymmetric crystals with broken inversion symmetry have nonzero $\chi^{(2n)}$, where $n \in \mathbb{Z}_{>0}$.

In light of the phenomena of our interests, we will look into the mathematical structure of $\chi^{(2)}_{ijk}$ in detail, which is important for the SHG and OPG processes that are crucial to this thesis. The second-order polarization can be written as,

$$P^i(\omega_n + \omega_m) = \epsilon_0 \sum_{j,k} \sum_{n,m} (\chi^{(2)}_{ijk}(\omega_m + \omega_n, \omega_n, \omega_m) E^j(\omega_n) E^k(\omega_m)) \tag{2.3}$$

where, ω_n and ω_m are two input fields and the output field is $\omega_m + \omega_n$, where the sum of the energy of the input fields is equal to the output field. $\chi^{(2)}_{ijk}$ is a tensor with 27 elements. The number of independent elements of $\chi^{(2)}$ can be reduced to 18 by taking account of the following symmetry arguments [74, 75, 76]:

1. Intrinsic permutation symmetry
   $\chi^{(2)}_{ijk}(\omega_n + \omega_m, \omega_m, \omega_n) = \chi^{(2)}_{ikj}(\omega_n + \omega_m, \omega_n, \omega_m)$

2. Complex conjugate of polarizibility is equal to negative frequency
   $\chi^{(2)*}_{ijk}(-\omega_n - \omega_m, \omega_m, \omega_n) = \chi^{(2)}_{ikj}(\omega_n + \omega_m, -\omega_m, -\omega_n)$

3. Commutative symmetry
   $\chi^{(2)}_{ijk}(-\omega_n - \omega_m, \omega_m, \omega_n) = \chi^{(2)}_{jik}(\omega_m, -\omega_n - \omega_m, \omega_n) = \chi^{(2)}_{kji}(\omega_n, \omega_m, -\omega_n - \omega_m,)$

The remaining 18 parameters can be rewritten as a 2D matrix d_{il}, where the last two indices jk of $\chi^{(2)}$ are contracted to l. Under the new notation ($jk \rightarrow l$)

jk:	11	22	33	23,32	13,31	12,21
l:	1	2	3	4	5	6

We can rewrite the polarization in a matrix form,

$$\begin{pmatrix} P_x(\omega_m+\omega_n) \\ P_y(\omega_m+\omega_n) \\ P_z(\omega_m+\omega_n) \end{pmatrix} = \epsilon_0 k(\omega_m+\omega_n;\omega_m;\omega_n) \times \begin{pmatrix} d_{11} & d_{12} & d_{13} & d_{14} & d_{15} & d_{16} \\ d_{21} & d_{22} & d_{23} & d_{24} & d_{25} & d_{26} \\ d_{31} & d_{32} & d_{33} & d_{34} & d_{35} & d_{36} \end{pmatrix} \times \begin{pmatrix} E_x(\omega_m)E_x(\omega_n) \\ E_y(\omega_m)E_y(\omega_n) \\ E_z(\omega_m)E_z(\omega_n) \\ E_y(\omega_m)E_z(\omega_n)+E_z(\omega_m)E_y(\omega_n) \\ E_x(\omega_m)E_z(\omega_n)+E_z(\omega_m)E_x(\omega_n) \\ E_x(\omega_m)E_y(\omega_n)+E_y(\omega_m)E_x(\omega_n) \end{pmatrix} \tag{2.4}$$

where k is $\frac{1}{2}$ for the degenerate fields $\omega_m = \omega_n$ and 1 otherwise. If the radiation fields involved in the nonlinear process are far away from any atomic resonances of the crystal i.e. a lossless transparent medium, the coefficients can be further reduced by evoking Kleinman symmetry [74, 76]. For the crystals and radiation fields used in the experiment in the thesis, the Kleinman symmetry is valid, which further reduces the coefficients to 10 non-zero coefficients with $d_{21} = d_{16}, d_{24} = d_{32}, d_{31} = d_{15}, d_{14} = d_{36} = d_{25}, d_{32} = d_{24}, d_{12} = d_{26}, d_{13} = d_{35}$

2.2 Second-Harmonic Generation: Theory

SHG is a process that converts a radiation field of frequency ω to 2ω: $E(\omega)E(\omega) \rightarrow E(2\omega)$, when an appropriate crystal with non-zero $\chi^{(2)}$ is pumped with a strong radiation field. Commonly used green laser pointers exploit the SHG process to convert 1064nm infra-red (IR) radiation to 532nm green light. To get more insight about the SHG process, we can solve Maxwell's equations for plane waves traveling in a transparent nonlinear medium. From Maxwell's equation one can obtain an electromagnetic wave equation,

$$\nabla^2 E - \frac{1}{c^2}\frac{\partial^2 E}{\partial t^2} = \frac{1}{\epsilon_0 c^2}\frac{\partial^2 P}{\partial t^2} \tag{2.5}$$

where E is the electric field of the radiation. Separating the polarization to linear ($P^{linear} = \epsilon_0 \chi^{(1)}$) and nonlinear components (P^{NL}) and substituting in (2.5) we get

a driven wave equation where the source is on the right hand side,

$$\nabla^2 E - \frac{1+\chi^{(1)}}{c^2}\frac{\partial^2 E}{\partial t^2} = \frac{1}{\epsilon_0 c^2}\frac{\partial^2 P^{NL}}{\partial t^2} \tag{2.6}$$

Without a driving source term, the solution of equation (2.6) is a plane wave,

$$E(r,t) = E_0(r)e^{i(\omega t - k.r)} + E_0(r)^* e^{-i(\omega t - k.r)} \tag{2.7}$$

where $k = \frac{n(\omega)\omega}{c}$ is the wave-vector and $n^2(\omega) = (1+\chi^{(1)}(\omega))$ is the index of refraction of the medium through which radiation is propagating. From equation (2.2), second-

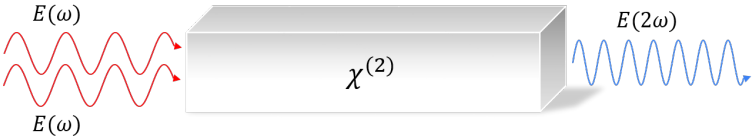

Figure 2.3: Cartoon of SHG generation.

order polarizibility that generates SHG is

$$\begin{aligned} P^{(2)}(2\omega) &= \epsilon_0\chi^{(2)}(E_F e^{i(\omega t - k_F.r)} + E_F^* e^{-i(\omega t - k_F.r)})(E_F e^{i(\omega t - k_F.r)} + E_F^* e^{-i(\omega t - k_F.r)}) \\ &= \epsilon_0\chi^{(2)}(2|E_F|^2 + E_F^2 e^{2i(\omega t - k_F.r)} + (E_F^*)^2 e^{-2i(\omega t - k_F.r)}) \end{aligned} \tag{2.8}$$

The first term generates a static electric field, whereas the second term is a source term that oscillates at twice the original frequency (also called the fundamental frequency). Assuming that the fundamental field ($E_F(\omega)$) and the generated field ($E_{SHG}(\omega_{SHG} = 2\omega)$) are propagating in the z-axis, the equation of motion for the fields can be obtained by substituting modified eq. (2.8) in to eq. (2.6). After some algebra,

$$\frac{\partial^2 E_{SHG}(\omega_{SHG},z)}{\partial z^2} + 2ik_{SHG}\frac{\partial E_{SHG}(\omega_{SHG},z)}{\partial z} = -\frac{4d_{eff}\omega_{SHG}^2}{c^2}E_F^2(\omega,z)e^{i\Delta kz} \tag{2.9}$$

where $\Delta k = 2k_F - k_{SHG}$ is wave-vector mismatch between the fundamental field and the second-harmonic field, commonly referred to as a phase mismatch, and $d_{eff} = \frac{\chi^{(2)}}{2}$. The phase mismatch is non-zero due to the dispersion relationship, details of which will be given in the next section. Assuming $E(z)$ slowly varies across z, we can drop the higher order derivative terms in z,

$$\frac{\partial E_{SHG}(2\omega, z)}{\partial z} = \frac{8id_{eff}\omega^2}{k_{SHG}c^2} E_F^2(\omega, z)e^{i\Delta kz} \tag{2.10}$$

Similarly for the fundamental field,

$$\frac{\partial E_F(\omega, z)}{\partial z} = \frac{2id_{eff}\omega^2}{k_F c^2} E_F^*(\omega, z)E_{SHG}(2\omega, z)e^{-i\Delta kz} \tag{2.11}$$

We have 2 coupled differential equations that can be solved numerically to obtain the intensity profile of the SHG field. To get more insight about the solution, let us assume that the fundamental does not deplete much within the crystal length L [75],

$$\frac{\partial E_F(\omega, z)}{\partial z} \to 0 \tag{2.12}$$

The electrical field of the SHG becomes,

$$E_{SHG}(2\omega, z) = \frac{8id_{eff}\omega^2}{k_{SHG}c^2} E_F^2(\omega) \int_0^L e^{i\Delta kz} dz = \frac{8id_{eff}\omega^2}{k_{SHG}c^2} E_F^2(\omega) \frac{e^{i\Delta kL} - 1}{i\Delta k} \tag{2.13}$$

The intensity of the SHG field is given by,

$$I = 2n\epsilon_0 c|E|^2 \tag{2.14}$$

Substituting the electric field,

$$\begin{aligned} I_{SHG}(2\omega, L) &= \frac{128 n_{SHG}(2\omega) d_{eff}^2 \omega^4}{k_{SHG}^2 c^3} |E_F(\omega)|^4 |\frac{e^{i\Delta k L} - 1}{\Delta k}|^2 \\ &= \frac{128 n_{SHG}(2\omega) d_{eff}^2 \omega^4}{k_{SHG}^2 c^3} |E_F(\omega)|^4 L^2 Sinc^2(\frac{\Delta k L}{2}) \end{aligned} \tag{2.15}$$

The intensity of the SHG field is proportional to the square of the length of the crystal and square of the interaction coefficient. The length dependence of the result is valid only when the crystal is pumped with a loosely focused beam, in other words the fundamental field can be approximated as a plane wave. Boyd and Kleinman solved the problem by assuming the fundamental to be a Gaussian beam and obtained a more realistic result where the power grows linearly with the crystal length [76]. Under the large depletion regime, the second-harmonic intensity grows linearly for a small crystal length and then saturates to some steady state value. The intensity distribution of the SHG field as a function of phase mismatch is plotted in figure 2.4. The exact form of the intensity distribution for a tightly focused beam is somewhat complicated and depends on the Gaussian beam parameters.

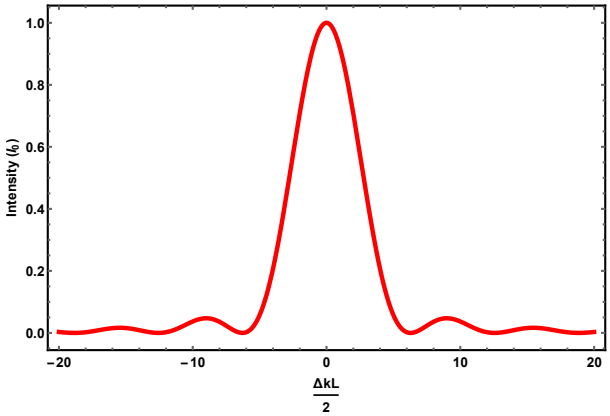

Figure 2.4: Intensity distribution of SHG field as a function of phase mismatched

With proper crystal selection one can convert most of the fundamental beam into twice its frequency, contingent on proper phase matching. For a focused beam,

the phase matching is complicated by Gouy phase [77]. As SHG is quadratically dependent on the crystal length, one could increase the field intensity by increasing the length of the crystal; however, phase mismatching prohibits the SHG field from building up. For the undepleted fundamental field case, SHG intensity as a function of length for different phase mismatching is plotted in figure 2.5. As evident from figure 2.5, without proper phasematching, increasing the crystal length beyond $L_c = \frac{\pi}{\Delta k}$ has no net gain on the SHG intensity. This length is called the coherence length. Sometimes coherence length is defined as $L_c = \frac{2\pi}{\Delta k}$, which is the length after which the field phase changes its sign. Without proper phase matching one usually is limited to employing a very thin crystal length for SHG, which is often impractical. In the next section we discuss in detail about phase matching.

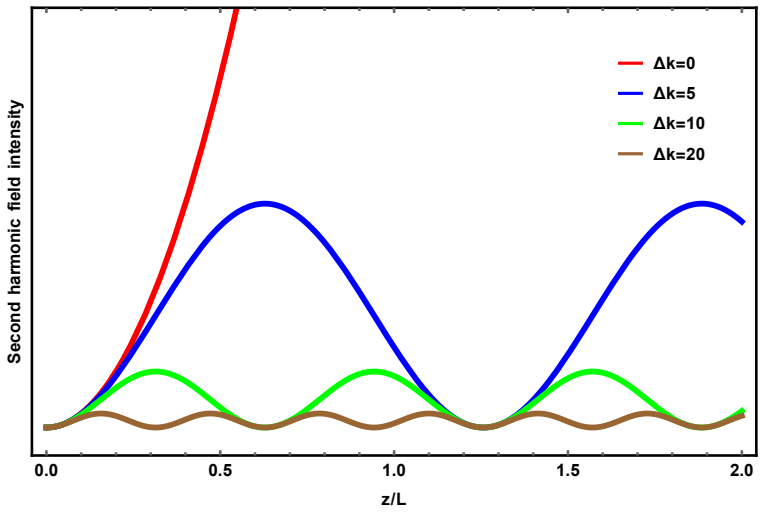

Figure 2.5: Second-harmonic intensity vs. phase mismatching as a function of crystal length

2.3 Phase Matching in Nonlinear Crystal

As with any other closed system, conservation of energy has to be strictly satisfied between the input and the output fields generated in a crystal for the nonlinear interaction to happen. Assuming the fields involved in the interactions are plane waves, momentum conservation gives

$$\vec{k}_1^{in} + \vec{k}_2^{in} + ...\vec{k}_n^{in} = \vec{k}_1^{out} + \vec{k}_2^{out} + ...\vec{k}_n^{out} \tag{2.16}$$

For SHG, the phase mismatch between the fundamental and second-harmonic field is

$$\begin{aligned} \Delta k &= 2k_F - k_{SHG} \\ &= \frac{2n_F(\omega_F)\omega_F}{c} - \frac{n_{SHG}(\omega_F)\omega_{SHG}}{c} = \frac{2\omega_F}{c}(n_F(\omega_F) - n_{SHG}(2\omega_F)) \end{aligned} \tag{2.17}$$

In most materials with normal dispersion, the index of refraction decreases monotonically with increasing wavelength, i.e. $\frac{\partial n}{\partial \lambda} < 0$ (see figure 2.6 for an example). The fields involved in the nonlinear processes of interest to us often have very different wavelengths, thus one cannot obtain perfect phase matching. To minimize the phase mismatch one can employ the ordinary and extraordinary axes of the birefringent crystal, that is typical of the nonlinear crystal, such that the fundamental and second-harmonic field propagate in different crystal axis. However birefringence of a crystal is often not enough to obtain perfect phase matching. For instance, in this thesis the SHG process in KTP, a biaxial crystal, is utilized to generate blue light by pumping with near-IR pulsed laser. As it is evident from the figure 2.6 there are no two points spaced at $\lambda/2$ where the value for ordinary and extra-ordinary index have the same value.

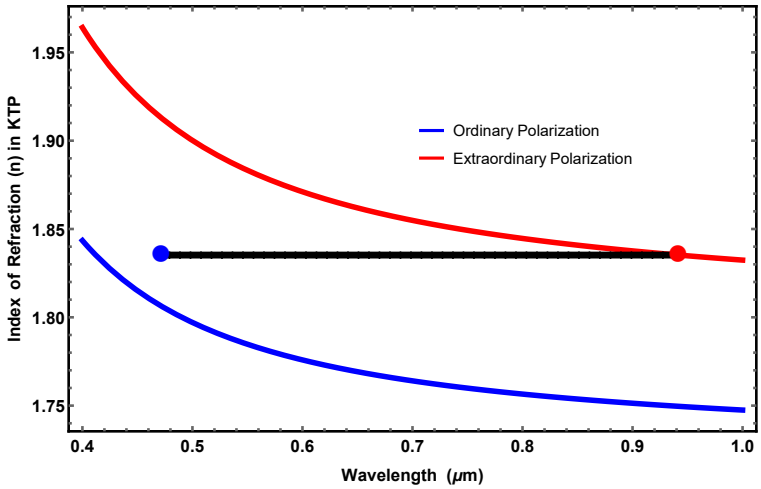

Figure 2.6: Index of refraction for KTP crystal as a function of wavelength. The red and blue dots correspond to the fundamental and second-harmonic wavelength needed for the experiment. Once can see from the plot that the ordinary polarization falls short from the desired number to obtain a perfect phase matching at the wavelength of our interest.

The index of refraction can be tuned by changing the temperature or by changing the angle between the propagation vector and the crystal axis. In the former case, the temperature dependence of the indices is weak and in the later case angle tuning does not always satisfy the phase matching conditions and is often impractical.

2.3.1 Quasi-Phase Matching

In 1962 Armstrong et. al. proposed an alternative technique to achieve quasi-phase matching in a crystal for $\chi^{(2)}$ processes [78]. In their proposal, instead of using a homogenous crystal, they use a spatially modulated crystal to achieve phase matching. As one can see from figure 2.5, the field builds up to the coherence length. By resetting the phase of the crystal at the appropriate length–i.e. flip crystal axis which results change in the sign of the nonlinear susceptibility–one can built the

intensity of the non-linearly generated field.

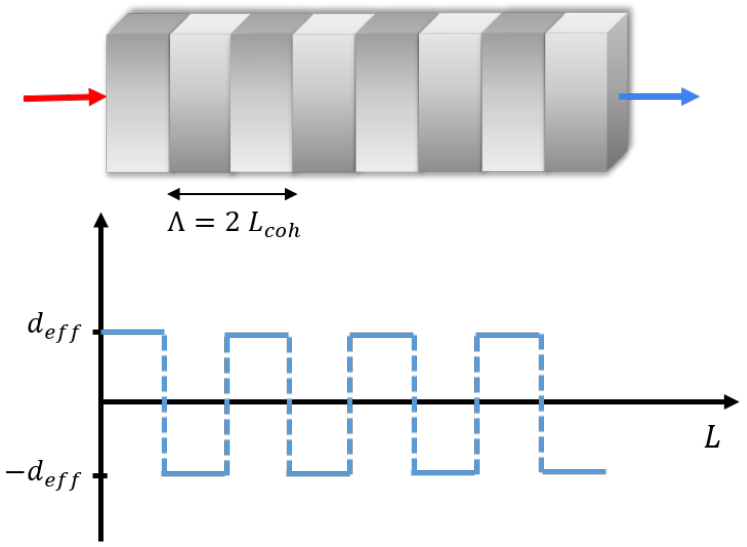

Figure 2.7: Cartoon of a periodically poled crystal and the spatial distrubtion of index

This can be achieved in a nonlinear crystal with a ferroelectric property. Ferroelectric crystals have electric polarization generated spontaneously, which can be flipped by applying an external electric field. One can flip the domain of a ferroelectric material by applying a mask with an alternative electrodes of fixed periodicity and applying large voltage pulses. With periodic poling and temperature tuning, phase matching can be achieved for any wavelength combination within the transparency window of the crystal. See figure 2.8 for the effect of quasi-phase matching on the second-harmonic field intensity. In figure 2.8 the circle of the red arrows represent twice the coherence length ($2L_c = \frac{2\pi}{\Delta k} = \Lambda$). Without proper phase matching, after twice the coherence length the second-harmonic field transfers back to the fundamental field making the process very inefficient.

To mathematically describe the second-harmonic field generated in a periodically poled crystal, one can model the spatially modulated nonlinear tensor coefficient as

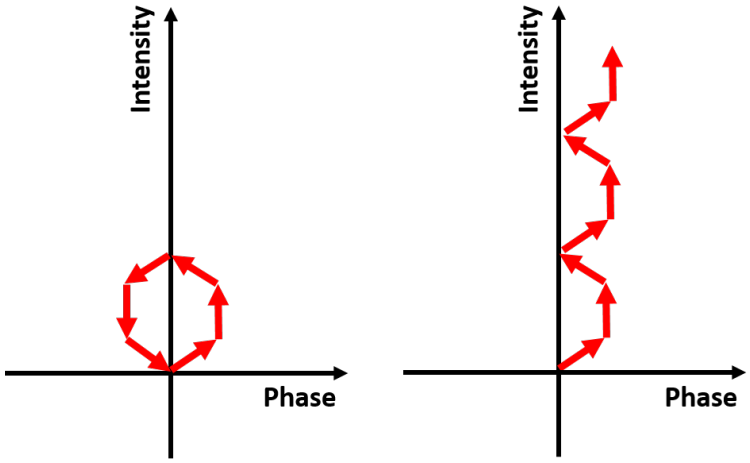

Figure 2.8: Phasor diagram of the second-harmonic field intensity generated in a nonlinear crystal as a function of crystal length without periodic poling (L) and with periodic poling (R). The arrow represents the complex amplitude of the field, where the circle of arrows represent twice the coherence length ($2L_c = \frac{2\pi}{\Delta k}$). For a phase matched crystal, the intensity of the second-harmonic field builds up over the length of the crystal.

a square wave

$$d(z) = d_{eff} \cdot \sum_{m=-\infty, m\in odd}^{\infty} G_m e^{\frac{-2i\pi mz}{\Lambda}} \tag{2.18}$$

where,

$$G_m = G_{-m} = |\frac{2}{m\pi}|, m \in odd \tag{2.19}$$

With periodical poling, the coupled fundamental and second-harmonic fields in equation (2.10) and (2.11) become,

$$\frac{\partial E_{SHG}(2\omega, z)}{\partial z} = \frac{8i\omega^2}{k_{SHG}c^2} E_F^2(\omega, z) d \sum_{m=-\infty}^{\infty} |\frac{2}{m\pi}| e^{i(2k_F - k_{SHG} - \frac{2\pi m}{\Lambda})z} \tag{2.20}$$

$$\frac{\partial E_F(2\omega, z)}{\partial z} = \frac{2i\omega^2}{k_F c^2} E_F^* E_{SHG}(\omega, z) d \sum_{m=-\infty}^{\infty} |\frac{2}{m\pi}| e^{-i(2k_F - k_{SHG} + \frac{2\pi m}{\Lambda})z} \tag{2.21}$$

where,

$$\begin{aligned}\Delta K &= 2k_F - 2k_{SHG} - k_{\frac{2\pi}{\Lambda}} \\ &= 2\pi\left(\frac{2n_F(\omega,T)\omega_F}{c} - \frac{2n_{SHG}(2\omega,T)2\omega}{c} - \frac{1}{\Lambda}\right)\end{aligned} \tag{2.22}$$

ΔK is the phase mismatching for the SHG process and $d = \frac{2}{\pi}d_{eff}$ is the effective nonlinearity for a crystal with periodic poling. With poling spacing

$$\Lambda = \frac{2\pi}{2k_F - K_{SHG}} = 2L_{coh} \tag{2.23}$$

one can obtain perfect phase matching. With perfect phase match the field equations for fundamental and second-harmonic can be solved with some algebra.

In this thesis, we used Potassium Titanyl Phosphate ($KTiOPO_4$) (also referred to as KTP) to generate 471nm blue light through SHG process, which is then used to pump another periodically poled KTP crystal (PPKTP) to generate a pair of polarization correlated photons through an SPDC process. SPDC is the reverse of the SHG process, where a pump photon interacts with the nonlinear medium creating a pair of down-converted photons, $\omega_{pump} \rightarrow \omega_{signal} + \omega_{idler}$, where the down-converted photons are referred to as signal and idler photons. In the next chapter, a mathematical description of the SPDC photons is given in detail.

Phasematching type	Pump Polarization	Signal Polarization	Idler Polarization
Type-0	o	o	o
Type I	e/o	o/e	o/e
Type II	e/o/o	o/e/o	e/o/e
Type III	e	e	o
Type IV	e	e	e

Table 2.1: Various phase-matching types by input and output fields polarization where e and o refers to extraordinary and ordinary polarization propagating in a birefriengence crystal.

As seen in table (2.4), second-order nonlinear processes happen for a specific po-

larization combination of the fundamental field(s) and the generated field(s). The most common second-order nonlinear processes are Type I where the input (output) fields are of the same polarization for SHG (downconversion) process and Type II if the fields are orthogonally polarized. See table 2.1 for different phase-matching types. As derived earlier for a non-linear process in Eq. 2.4, interaction due to $\chi^{(2)}$ can be quantified with 18 coefficients given by a 3×6 matrix with coefficients d_{ij}. A KTP material has 5 non-zero d_{il} coefficients [79],

$$\begin{pmatrix} 0 & 0 & 0 & 0 & \mathrm{d}_{15} & 0 \\ 0 & 0 & 0 & \mathrm{d}_{24} & 0 & 0 \\ \mathrm{d}_{31} & \mathrm{d}_{32} & \mathrm{d}_{33} & 0 & 0 & 0 \end{pmatrix}$$

where different coefficients result in different phase matching conditions. For a z-cut KTP crystal with the fields propagating along the x-axis, the $E_F^y E_F^y \rightarrow E_{SH}^z$ (Type I) process can be obtained by exploiting the d_{33} coefficient to generate a second-harmonic field. Coefficients d_{15} and d_{24} give rise to polarization entangled photons of Type II. In KTP, $d_{24} = 7.6 Pm/V$ is larger than $d_{15} = 6.1 Pm/V$ [79]. We exploit the d_{24} coefficient in a z-cut PPKTP crystal with the fields propagating along the x-axis to obtain Type II polarization correlated photons $E_{SH}^y \rightarrow E_{signal}^y E_{idler}^z$, where the pump is polarized along the y-axis and the signal and idler photons are polarized along the y- and z-axes respectively.

2.3.2 Sellmeir Equations and Temperature Tuning of Refractive Indices

As mentioned previously, to obtain perfect phase matching, in addition to growing a crystal with periodic poling, one can tune the temperature of the crystal.

So far we have discussed the wavelength dependence of the index of refraction, without giving an exact mathematical form for it. The wavelength dependent index of refraction for a KTP crystal can be empirically expressed as a set of Sellmeier

equations for x, y, and z polarized fields. Using refractive index value measured by Zeng et al.[80] and Shen et al. [81], Kato et al. [82] extracted the parameters of Sellmeier equations for flux-grown KTP crystal, resulting in the following equations,

$$\begin{aligned} n_x(\lambda) &= \sqrt{3.291 + \frac{0.0414}{\lambda^2 - 0.03978} + \frac{9.35522}{\lambda^2 - 31.4557}} \\ n_y(\lambda) &= \sqrt{3.45018 + \frac{0.04341}{\lambda^2 - 0.04597} + \frac{16.9883}{\lambda^2 - 39.438}} \\ n_z(\lambda) &= \sqrt{4.59423 + \frac{0.06206}{\lambda^2 - 0.04763} + \frac{110.807}{\lambda^2 - 86.1217}} \end{aligned} \tag{2.24}$$

Similarly, the index of refraction is dependent on the temperature of the crystal. The temperature dependence part can be expressed by by Taylor expanding the index around temperature $T_0 = 25°C$, which gives

$$n(\lambda, T) = n(\lambda, T_0) + n_1(\lambda, T_0)(T - T_0) + n_2(\lambda, T_0)(T - T_0)^2 \tag{2.25}$$

where, n_1 and n_2 are third-order polynomials of inverse wavelength given by

$$n_{1,2}(\lambda, T_0) = \sum_{m=0}^{3} \frac{a_m}{\lambda^m} \tag{2.26}$$

The above holds for all three polarizations n_x, n_y, n_z, where the coefficient a_m for y and z polarizations are taken from Shai et al.'s work [83], listed in the Table 2.2 Here

	z-polarization		y-polarization	
	$n_1(\times 10^{-6})$	$n_2(\times 10^{-8})$	$n_1(\times 10^{-6})$	$n_2(\times 10^{-8})$
a_0	9.9587	-1.1882	6.2897	-0.14445
a_1	9.95228	10.459	6.3061	2.2244
a_2	-8.9603	-9.8136	-6.0629	-3.5770
a_3	4.1010	3.1481	2.6486	1.3470

Table 2.2: Table of temperature dependent coefficients for index of refraction empirically extracted by Shai Emanueli and Ady Arie.

in eq. (2.24) (2.25) wavelengths are expressed in micrometers.

In this thesis work, a 10 mm long PPKTP crystal is pumped with a 942 nm pulsed laser to generate 471 nm blue light. The near-IR pulses are generated by a 76 MHz repetition rate, 50 ps pulse duration, mode-locked, Ti:sapphire laser built by Spectra-Physics (Tsunami). The 50 ps pulse width is selected for two reasons: it is within the accepted bandwidth of the second-harmonic crystal that ensures most of the fundamental beam is converted to the second-harmonic beam, and the emission timing jitter of the down-conversion photon, which becomes important when performing two-photon interference measurements, is set by the pump pulse duration. The 50 ps timing jitter is within the best commercially-available single photon detectors. The beam parameters of the fundamental beam are set to ensure maximum blue light generation, which is dictated by the Boyd-Kleiman parameter [76]. The crystal is mounted in a temperature stabilized oven that maintains the temperature within an accuracy of 10 mK. Figure 2.9 and 2.10 are experimental data that shows the intensity profile of the second-harmonic beam generated as a function of the crystal temperature.

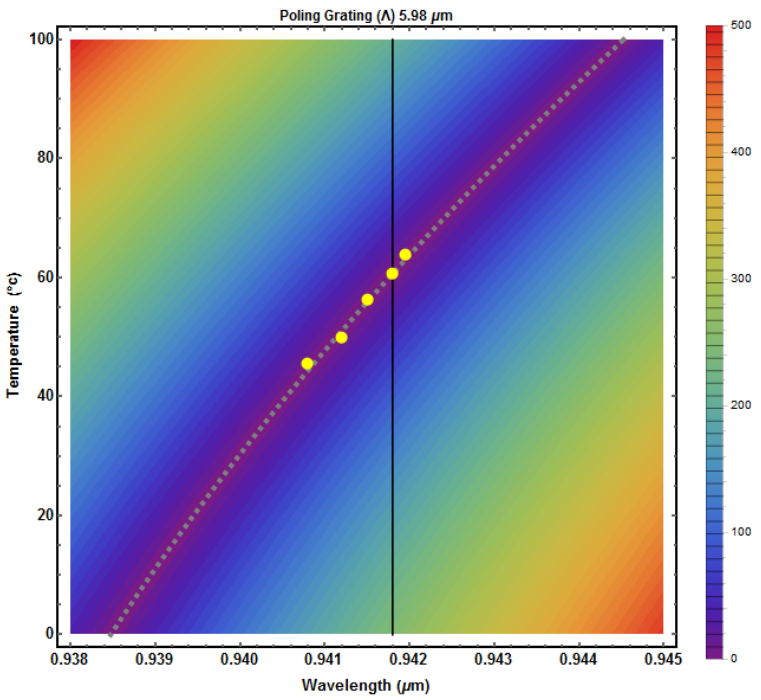

Figure 2.9: Contour plot of the theoretical prediction of the phase mismatch in second-harmonic generation as a function of the crystal temperature and fundamental wavelength. The gray dash line is the contour line along which the phase mismatch is zero. The yellow dots are experimental data. For the theoretical plot the poling of the crystal is adjusted from the manufacture provided number $5.95\mu m$ to $5.988\mu m$ in order to match the theoretical fit with the experimental data.

The theoretical prediction and the measured second-harmonic field as a function of temperature for a fixed fundamental wavelength can be seen in figure 2.10. The deviation in the fit arises due to the assumption we have made about the fundamental pump beam. As we mentioned earlier, the measured profile of the second-harmonic intensity depends on the profile of the fundamental beam, which deviates from the Sinc function [76].

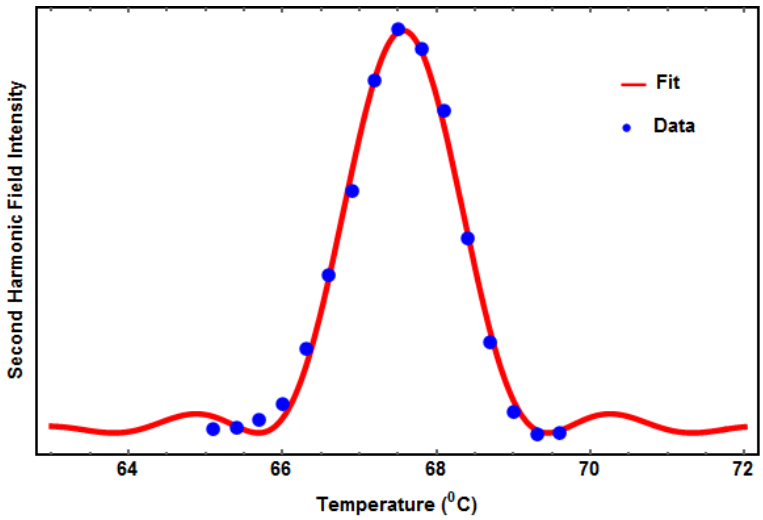

Figure 2.10: Experimental data of intensity of the second-harmonic field as a function of the crystal temperature and a theoretical fit.

2.4 Chapter Summary

In this chapter we briefly discussed nonlinear optics and its application for second-harmonic generation processes. We gave a detailed explanation of quasi phase matching for SHG processes, which naturally extends to the down-conversion process that will be discussed in the next chapter. Using the theoretical calculations derived in the chapter for SHG processes, we successfully explained the experimental data, which works as a controlled test bench to verifying both the conceptual and experimental understanding of the system. This will be of utmost importance in understanding SPDC, which is more cumbersome than the SHG process.

CHAPTER III

Theory of Spontaneous Parametric Down-Conversion

Entanglement is one of the most unique features of quantum mechanics, the analog of which is absent in the classical world. The influential thought experiment by Einstein and his colleagues, also known as the Einstein-Podolsky-Rosen paradox [84], generated much interests in testing quantum mechanics. It inquires about the reality of the quantum wavefunction, specifically speaking whether the quantum wavefunction is the complete description of a system. In order to preserve local realism[1] with the assumption that a particle must objectively have a pre-existing value, EPR proposed that quantum mechanics must be an incomplete description of nature, thus there must be a local hidden-variable-type scenario which gives a more complete description of nature [84]. After the EPR paradox was identified, several hidden variable theories were proposed that preserved local realism [85, 86]. Later in 1951, using spin entangled electrons, John Bell theoretically showed that the correlation predicted by quantum mechanics is stronger than with hidden variable theorems by deriving the famous Bell's inequality [87]. Violation of Bell's inequality, which implies quantum description is more complete than hidden-variable theories, was experimentally shown using entangled photons emitted by calcium atoms by Stuart Freedman and John

[1] The cause-and-effect are limited to the speed of light and a system has a well defined pre-existing value independent of measurements.

Clauser in 1972 [88] and by Alain Aspect *et al.* in 1981 [1]. All these measurements make several assumptions about the experimental setup, which are also referred to as loopholes, thus testing loophole free Bell's inequality has been a holy grail for the fundamental physics community.

Despite the early success of atomic systems for generating correlated photons, they came with several issues, one being the reduction of correlation due to the recoil of the atoms when photons are not emitted back-to-back [48]. In 1970, D. C. Burnham and D. L. Weinberg experimentally demonstrated the generation of pairs of photon by pumping an ammonium dihydrogen phosphate crystal with a 325-nm He-Cd laser [89]. Later, in 1987, R. Ghosh and L. Mandel showed that down-converted photons generated using a non-linear crystal had the desired "non-local correlation" [90] that circumvented the existing problems. Since then there have been several experiments testing Bell's inequality using entangled photons generated by spontaneous parametric down-conversion (SPDC) [91, 3]. Polarization entangled photons using a single Type-II crystal or two stacked Type-I crystals are two of the most customizable and accessible sources presently being used for such quantum mechanical tests [67].

Over the past few decades, SPDC has generated much interests from quantum optics and quantum information science communities [92, 93], specifically for quantum secure communication such as quantum key distribution [94, 95] and even for linear quantum computing [96]. As the process is exploited in our laboratory for the first time, we will go through the derivation of SPDC wavefunction, review the basic formalism for calculating Heisenberg operators of fields generated inside an optical cavity and justify the use of cavity-SPDC in the thesis work.

3.1 Theoretical Description of the Spontaneous Parametric Down-Conversion Process

Before we get into the experimental details, it is important to understand the origin of various rich physical properties that arises in a SPDC system. Most of such phenomena can be understood by analyzing the structure of the SPDC wavefunction, which otherwise might not be evident from the Hamiltonian itself. When a pump

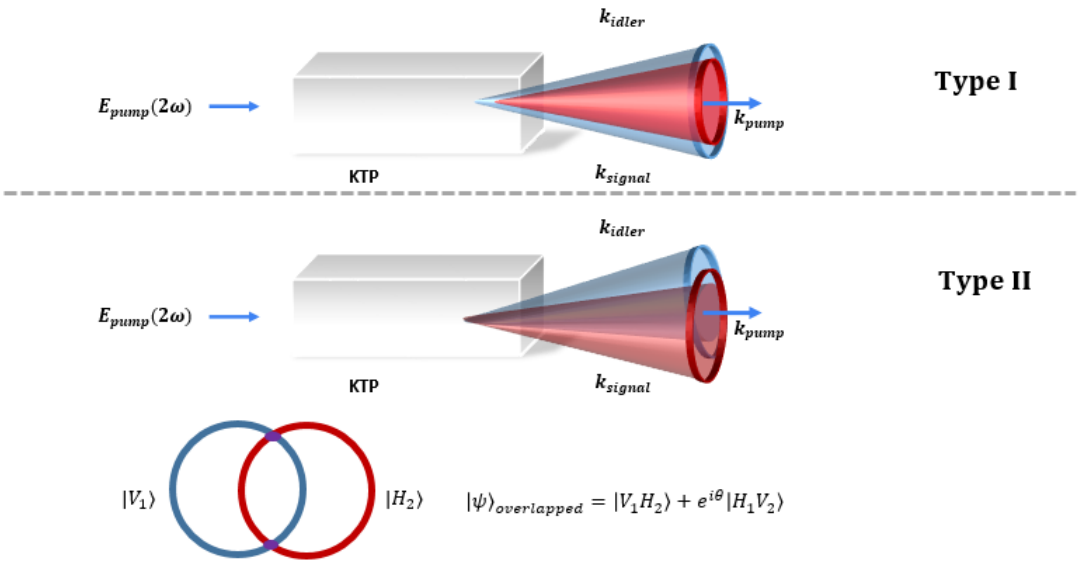

Figure 3.1: Ordinary and extraordinary polarization generated from a KTP crystal via spontaneous down-conversion process (Top) Type I (Bottom) Type II.

radiation of energy E_p is focused on a crystal, the second-order polarization gives rise to various non-linear phenomena. For new fields to emerge out of a finite size crystal, appropriate phase-matching needs to happen, which is explained extensively in the previous chapter. As one can recall from Eq. (2.4) and non-zero nonlinear coefficients for Potassium titanyl phosphate (KTP) crystal, both Type I and Type II phase matching for second-harmonic generation (SHG) and SPDC processes can take place depending on the pump polarization and the phase matching conditions [97].

The following are the down-conversion processes that can happen in a KTP crystal:

$$\begin{aligned} E_p^z &\xrightarrow{d_{32}} E_{signal}^y E_{idler}^y \qquad (TypeI) \\ E_p^z &\xrightarrow{d_{33}} E_{signal}^y E_{idler}^y \qquad (TypeI) \\ E_p^y &\xrightarrow{d_{24}} E_{signal}^y E_{idler}^z \qquad (TypeII) \end{aligned} \tag{3.1}$$

where d_{ij} are element of the polarizability tensor given by Eq. (2.4). If the down-converted photons are emitted in the same crystal axis, they are referred to as Type I processes. As a result, the down-converted photons have same polarizations and are emitted symmetrically along the propagation axis of the pump beam [48]. Whereas if the photons are emitted in two different crystal axes, the process is referred to as Type II processes. For Type II process, the down-converted photons are polarized orthogonal to each other and are emitted in two different cones [98]. By adjusting the angle between the pump beam and the crystal for Type II processes, the two cones can be made to intersect in two lines (see figure 3.1). At the intersection, the ambiguity of the origin of the photons' propagation axis leads to the polarization entangled two-photon state given by [67, 48],

$$|\psi\rangle = \frac{1}{\sqrt{2}}(|H_{K_1}\rangle|V_{K_2}\rangle + e^{i\theta}|V_{K_1}\rangle|H_{K_2}\rangle) \tag{3.2}$$

where H_k, V_k are horizontal and vertical polarizations with momentum k and θ is the phase relationship between the two states obtained by inserting a medium in one of the collection path. In the following section, the wavefunction of the down-converted two-photon state, assuming the fields are collinear and in the absence of the cavity, is derived by loosely following M. Rubin *et al.* and A. Ling's work [97, 99]. Though there are several distinctions from their calculations, e.g. our calculation uses square-modulated nonlinear coefficients and derives an explicit mode function of the down-conversion under some approximation regime. For the following calculations,

we take the crystal face to be in the yz-axes, where the pump and the down-converted fields propagate in the x-axis. The interaction Hamiltonian for Type II spontaneous down-conversion can be written as [100],

$$H^I = \int_{Vol} d^3r d(x) E_p^{(+)}(\vec{r}) E_s^{(-)}(\vec{r}) E_i^{(-)}(\vec{r}) + h.c. \tag{3.3}$$

where d(x) is the periodically poled non-linear interaction coefficient and $E_{p/s/i}$ are electric field operators given in Eq. 3.5, 3.10 . Ignoring higher order terms [101],

$$d(x) = |\frac{2d_{24}}{\pi}| e^{\frac{-2i\pi x}{\Lambda}} + c.c. \tag{3.4}$$

For simplicity we assume that the pump beam is a weakly focused Gaussian beam with a narrow band frequency spectrum centered at ω_p. The crystal used for the down-conversion has length L is X-cut thus the lengthwise orientation will be taken along the x-axis. The electric field for the pump field propagating along the x-axis can be written as [99],

$$E_p^{(+)}(r,t) = \frac{1}{2} E_p^0 \hat{e_p} g_p(r) e^{-i\omega_p t} \tag{3.5}$$

where

$$g_p(r) = e^{ikx} U(y,z) = e^{ikx} e^{-\frac{y^2+z^2}{W_p^2(x)}} \tag{3.6}$$

is the spatial mode of the pump beam. $W_p(x)$ is the spot size for the Gaussian beam at length x from the focus spot given by,

$$W_p(x) = w_{0p} \sqrt{1 + \left(\frac{x\lambda_p}{\pi w_{0p}^2} \right)^2} \tag{3.7}$$

and w_{0p} is the beam spot at the focus and λ_p is the center wavelength of the pump

beam. The coefficient E_p^0 can be expressed as a function of pump power (P),

$$|E_p^0|^2 = \alpha_p^2 \frac{2P}{\epsilon_0 n_p c} \tag{3.8}$$

where

$$\alpha_p = \sqrt{\frac{2}{\pi w_{0p}^2}} \tag{3.9}$$

and n_p is the index of refraction for the pump in the medium. Above we assume that the transverse momentum of the pump beam is negligible, i.e. $k_T = 0$ and we ignored the Gouy phase by assuming the Rayleigh length of the pump beam is comparable to the crystal length [99]. In order to calculate the two-photon wavefunction of the down-converted photons, we need to work with the fully quantized fields. In the following calculation we follow the quantization scheme given by Loudon [102], where the fields are assumed to satisfy a periodic boundary condition imposed by the quantization volume. As the down-converted fields are produced within the pump beam waist, the quantization volume is written in terms of some length L_q and the beam waist. When the problem is treated properly, the measured spectrum should not depend on the quantization volume. With this, in SI units, the quantized electric field modes of the signal and idler photons with frequencies ω_s and ω_i generated in the down-conversion process can be written as [99],

$$E_{s,i}^{(+)}(r,t) = \frac{i}{2} \sum_{k_{s,i}} \sqrt{\frac{\hbar\omega_{s,i}}{n_{s,i}^2 \epsilon_0}} \frac{\alpha_{s,i}}{\sqrt{L_q}} \hat{e_{s,i}} U_{s,i}(y,z) e^{-i\omega_{s,i}t + ik_{s,i}x} a_{k_{s,i}}(0) \tag{3.10}$$

The $\alpha_{s,i}$, $U_{s,i}$ are defined same as the pump field and $a_{k_{s,i}}$ is an annihilation operator for mode k.

The initial state-vector of the SPDC system before the down-conversion happens

can be expressed as the products of two "empty" vacuum modes and a Glauber state,

$$|\psi(0)\rangle = |0_s\rangle|0_i\rangle|\alpha\rangle \tag{3.11}$$

The time evolution of the above state-vector in the interaction picture can be treated perturbatively. For a small interaction coefficient d_{24}, the state-vector becomes

$$\begin{aligned}
|\psi(t)\rangle &= |0_s\rangle|0_i\rangle|\alpha\rangle + \frac{1}{i\hbar}\int_t H^I(t\prime)dt\prime|\psi(0)\rangle + .. \\
&= |0_s\rangle|0_i\rangle|\alpha\rangle + \frac{1}{i\hbar}\int_t\int_{Vol} d^3r d_{24}(x)E_p^{(+)}(\vec{r},t\prime)E_s^{(-)}(\vec{r},t\prime)E_i^{(-)}(\vec{r},t\prime)dt\prime|0_s\rangle|0_i\rangle|\alpha\rangle + .. \\
&= |0_s\rangle|0_i\rangle|\alpha\rangle + \sum_{k_s,k_i}\frac{id_{24}\alpha_s\alpha_i}{2\pi n_s n_i\epsilon_0 L_q}\int_0^t \sqrt{\omega_s\omega_i}e^{-i(\omega_p-\omega_s-\omega_i)t\prime}dt\prime \\
&\times \underbrace{\int_{-\infty}^{\infty}\int_{-\infty}^{\infty} dydzU_p(y,z)U_s^*(y,z)U_i^*(y,z)\int_0^L dx e^{i(k_p-k_s-k_i-\frac{2\pi}{\Lambda})x}}_{\Phi(r,\Delta k)} a_{k_s}^\dagger a_{k_i}^\dagger|0_s\rangle|0_i\rangle|\alpha\rangle + ..
\end{aligned} \tag{3.12}$$

For a large time limit the first integrand gives a delta function that enforces energy conservation,

$$E_p = E_s + E_i \tag{3.13}$$

Similarly, the second integrand gives spatial envelope of the signal and idler fields and the last integrand yields a *Sinc* function with phase mismatch as its argument. Collectively the second and third integrals are defined as $\Phi(r,\Delta k)$, which can be expanded as

$$\Phi(r,\Delta k) = \int_{-\infty}^{\infty}\int_{-\infty}^{\infty}\int_0^L dxdydz e^{-(y^2+z^2)(\frac{1}{W_p^2(x)}+\frac{1}{W_s^2(x)}+\frac{1}{W_i^2(x)})}e^{i\Delta Kx} \tag{3.14}$$

where,

$$\Delta K = k_p - k_s - k_i - \frac{2\pi}{\Lambda} \tag{3.15}$$

is the phase mismatch as derived in chapter 2 for the SHG process. In order to obtain a maximum count rate emitted from the crystal, the phase matching condition needs to be satisfied. This can be achieved by tuning the index of refraction of the PPKTP crystal. The spot sizes $W_{p,s,i}(x)$ are function of x which makes it harder to analytically solve the integral. One can obtain an exact spatial envelop by numerically solving the integration. The detailed solution to a Type-I down-conversion without periodical poling is calculated in references [103] [104]. By making a few assumptions about the system, we can simplify the problem and obtain an analytical solution. Assuming that the crystal length is shorter than the Rayleigh length ($x_R = \frac{\pi w_0^2}{\lambda}$) of the pump beam, we can Taylor expand the exponent,

$$e^{-\frac{(y^2+z^2)}{w_{0_p}^2(1+(x/x_R)^2)}} \simeq e^{-\frac{(y^2+z^2)}{w_{0_p}^2}(1-(x/x_R)^2)} \tag{3.16}$$

Let us assume that the factor $(x/x_R)^2$ makes only a small contribution to the solution, thus can be dropped from rest of the calculation,

$$\begin{aligned} \Phi(r, \Delta k) &= \int_{-\infty}^{\infty}\int_{-\infty}^{\infty}\int_{0}^{L} dxdydz e^{-(y^2+z^2)(\frac{1}{w_{0_p}^2}+\frac{1}{w_{0_s}^2}+\frac{1}{w_{0_i}^2})} e^{i\Delta K x} \\ &= \pi L Sinc(\frac{\Delta k L}{2}) e^{i\Delta k L/2} (\frac{1}{w_{0_p}^2} + \frac{1}{w_{0_s}^2} + \frac{1}{w_{0_i}^2})^{-1} \end{aligned} \tag{3.17}$$

Substituting 3.17 in 3.12 and converting the discrete modes to a continuum state in 1D with following prescriptions [65]

$$\sum_k \rightarrow \frac{L_q}{2\pi}\int dk_x, \qquad a_k(t) \rightarrow \sqrt{\frac{2\pi}{L_q}} a(k,t) \tag{3.18}$$

we obtain

$$|\psi\rangle_{SPDC} = |0_s\rangle|0_i\rangle|\alpha\rangle + i\int\int d\omega_s d\omega_i \frac{d_{24}E_p^0 L}{2\pi w_{0s} w_{0i} n_s n_i \epsilon_0 c}\sqrt{\omega_s\omega_i}\delta(\omega_p - \omega_s - \omega_i) \\ \times Sinc(\frac{\Delta KL}{2})e^{i\Delta KL/2}(\frac{1}{w_{0_p}^2} + \frac{1}{w_{0_s}^2} + \frac{1}{w_{0_i}^2})^{-1}a^\dagger(\omega_s)a^\dagger(\omega_i)|0_s\rangle|0_i\rangle|\alpha\rangle + ... \tag{3.19}$$

From the two-photon state-vector derived above, one can calculate the absolute photon count rate, which is done in section 3.2.1 for a single mode SPDC field generated inside a cavity. The calculation shows that the count rate is proportional to the spectral density of the two-photon state-vector. As the state-vector is proportional to the crystal length, naively it seems that the count rate is quadratic in the crystal length. However, the dependence is more complex. For a thin down-conversion crystal where the crystal length is short relative to the Rayleigh length of the pumped beam, the absolute count rate is linear in crystal length [99]. This is because an additional L appears in the denominator from the length dependence of the phase-matching terms. After a critical thickness, the count rate is independent of the crystal length. A detailed analysis of the count rate as a function of focusing parameters and crystal length is given in reference [99]. Similarly, one can see from the Eq. 3.19 that the count rate is linear in the pump power.

The two-photon state-vector given in 3.19 is rich in physics with interesting features that one can identify immediately. The state-vector is a linear combination of Fock state photon pairs with decreasing probability for multiple pairs emission. The majority of the pump photons pass through the crystal without any interaction and are blocked using a long-pass filter. The probability of generating a pair of downconverted photons from the pump is a small number dictated by the magnitude of the polarizability tensor coefficient d_{eff}. The phase matching factor is non-factorizable in the signal and idler fields state-vectors, which leads to the polarization state entangled for the two different momentum states. The frequency-dependent factors results in

frequency correlations between the two photons. By engineering the phase matching conditions in different crystal geometries one can generate two-photon entanglement in various degrees of freedom as mentioned earlier in the chapter.

One important feature of the above state-vector is the generation of a heralded photon source. In our case, the signal and idler photons are correlated in polarization, even though we did not explicitly write the polarization of the emitted modes, thus can be split with a polarizing beam splitter. By detecting an idler photon one can immediately herald a photon state in the signal mode. Such heralded photon sources are of great importance for many basic and applied science experiments.

3.2 Cavity-Enhanced Spontaneous Parametric Down-Conversion

Most quantum information applications requires one to have single or entangled photons with a narrow frequency bandwidth. Despite the flexibility allowed by SPDC sources in tuning and modifying the photon properties, energy conservation allows the photons to be emitted in a broad frequency spectrum. The typical spectral bandwidth is in a Terahertz range, which is beyond the temporal resolution of current detectors and electronics technology. For photon interference measurements to be temporally resolved, the SPDC bandwidth needs to be on the order of the detector timing jitter. In addition to the detector timing resolution, another constraint for SPDC bandwidth comes from the bandwidth of the source to be interfaced with. Most atomic and solid-state systems have sub-GHz bandwidth. To interface SPDC photons with such atomic or solid-state systems, the bandwidth of the down-conversion needs to be reduced dramatically. Often in the SPDC community the spectral property of the down-conversion photons are quantified using a term "coherence time", with SPDC photons having a pico-second coherence time. The term coherence is used in many different contexts in quantum mechanics and often prone to abuse, often ends up implying more than what it means. The quoted pico-second coherence time is nothing but the inverse

of the spectral bandwidth $\tau_{coherence} \approx \frac{1}{\delta\omega} \approx \frac{1}{10^{12}Hz} \approx 1ps$. Such small coherence times are highly undesirable for quantum information application, as the photon will interfere with other photons only within the coherence time. One can circumvent the short coherence time problem using a narrow spectral filter. However, such passive filtering gets rid of a large portion of the down-converted photon's spectrum, making the source weak and hardly useable.

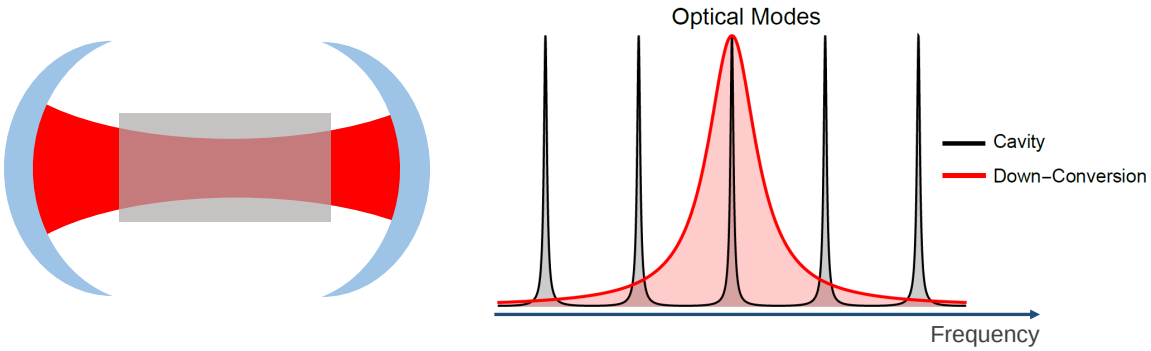

Figure 3.2: A down-conversion crystal placed inside an optical cavity (L). Modes of a hypothetical optical cavity is super-imposed over the down-conversion bandwidth (R)

To get over such passive filtering problems, one could place a SPDC crystal inside a cavity that has modified vacuum DOS, see figure 3.2. With modified DOS inside the cavity, the down-conversion can happen only withing a narrow bandwidth that could be engineered as desired. In additional to filtering the bandwidth, such cavity configuration can modify the spectral density making the source brighter [50]. As it is important to the thesis work, we will go through Ou and Collett *et al.*'s derivation [105, 106] to calculate the enhancement factor for such an optical cavity. In the next chapter, we will demonstrate the design and successful implementation of such cavity-enhanced SPDC source that mode matches with quantum dot photons.

3.2.1 Theoretical Calculations of the Field Enhancement Factor in Cavity-SPDC

In order to calculate the field spectrum and the enhancement factor for a cavity SPDC source, we need to calculate the field spectrum, which requires an appropriate Hamiltonian. The microscopic nature of the down-conversion Hamiltonian is still not fully understood. However much of the physics can be captured with the following Hamiltonian [106, 107],

$$H = \hbar\omega a^\dagger a + i\hbar\chi^{(2)}(\beta^* e^{i\omega_p t} a^2 - \beta e^{-i\omega_p t} a^{\dagger 2}) \tag{3.20}$$

where a is the field operator for the down-converted photons centered at ω_0 and $\beta e^{-i\omega_p t}$ is the pump field centered at $\omega_p = 2\omega_0$. We will assume the down-conversion fields are collinear and degenerate in frequency and occupy a single-mode of the cavity. This significantly simplifies the calculation. We will use cavity input-output formalism to relate the output (a_{out}) and input fields (a_{in}) with the internal field (a) of the cavity generated through the down-conversion process [106]. See Appendix A for the detailed theoretical description of the cavity input-output formalism. The field operators are defined in Eq. A.8 and Eq. A.12. Using the above Hamiltonian along with Eq. A.10 from Appendix A, we can solve for the intra-cavity field [106].

$$\begin{aligned} \dot{a}(t) &= -i\omega_0 a(t) + \epsilon e^{-i\omega_p t} a^\dagger(t) + \sqrt{\gamma} a_{in}(t) - \gamma/2 a(t) \\ \dot{a^\dagger}(t) &= i\omega_0 a^\dagger(t) + \epsilon^* e^{i\omega_p t} a(t) + \sqrt{\gamma} a^\dagger_{in}(t) - \gamma/2 a^\dagger(t) \end{aligned} \tag{3.21}$$

where $\epsilon = \chi^{(2)}\beta$ is the field interaction strength and we will assume it to be real. The above equation can be rewritten in a matrix form and can be solved by taking its Fourier transformation with equation A.11. With some algebra we obtain [106],

$$
\begin{aligned}
a_{out}(\omega_0+\omega) &= g(\omega)a_{in}^{\dagger}(\omega_0-\omega) + G(\omega)a_{in}(\omega_0+\omega) \\
a_{out}^{\dagger}(\omega_0-\omega) &= g(\omega)a_{in}(\omega_0+\omega) + G(\omega)a_{in}^{\dagger}(\omega_0-\omega)
\end{aligned}
\tag{3.22}
$$

where

$$
g(\omega) = \frac{4\epsilon\gamma}{(\gamma-2i\omega)^2-4|\epsilon|^2}, \qquad G(\omega) = \frac{\gamma^2+4\omega^2+4|\epsilon|^2}{(\gamma-2i\omega)^2-4|\epsilon|^2} \tag{3.23}
$$

Fourier transformation of the first-order field correlation gives the spectrum of the field. In order to compare the spectral density of the cavity field, we can calculate the spectrum for signal and idler fields using [50, 108],

$$
S_{s,i}(\omega) = \frac{1}{2\pi}\int_{-\infty}^{\infty} d\tau e^{i\omega\tau} G_{s,i}^{(1)}(\tau) \tag{3.24}
$$

where

$$
G_{s,i}^{(1)}(\tau) = \langle\psi|E_{s,i}^{-}(x,t)E_{s,i}^{+}(x,t+\tau)\underbrace{|\psi\rangle}_{\text{Time independent Bi-photon wavefunction}} \tag{3.25}
$$

is the correlation function. Calculating two-time correlation functions can often be cumbersome. To simplify the above calculation we can use the relationship [108],

$$
\langle a^{\dagger}(\omega_1)a(\omega_2)\rangle = 2\pi\delta(\omega_1-\omega_2)\int_{-\infty}^{\infty} d\tau e^{i\omega_2\tau}\langle a^{\dagger}(t_1)a(t_1+\tau)\rangle \tag{3.26}
$$

With the above relationship,

$$
\langle a_{out}^{\dagger}(\omega_0+\omega)a_{out}(\omega_0+\omega')\rangle = S_{s/i}(\omega)\delta(\omega-\omega') \tag{3.27}
$$

where we assumed $\omega_0 = \omega_s$. The correlation function can be written as,

$$\langle a^{\dagger}_{out}(\omega_0+\omega)a_{out}(\omega_0+\omega')\rangle = \\ \langle (g(-\omega)a_{in}(\omega_s-\omega)+G(-\omega)a^{\dagger}_{in}(\omega_s+\omega))(g(\omega')a^{\dagger}_{in}(\omega_s-\omega')+G(\omega')a_{in}(\omega_s+\omega'))\rangle \tag{3.28}$$

Taking the initial wavefunction to be $\psi(0)\rangle = |\alpha\rangle_p|0_s, 0_i\rangle$ and keeping the non-zero terms, we obtain the spectrum to be,

$$S_{s,i}(\omega) = \frac{16|\epsilon|^2\gamma^2}{((\gamma-2i\omega)^2-4|\epsilon|^2)((\gamma+2i\omega)^2-4|\epsilon|^2)}\langle a_{in}(\omega_s-\omega)a^{\dagger}_{in}(\omega_s-\omega')\rangle \tag{3.29}$$

As we are interested in finding the enhancement rate for the cavity-SPDC, assuming the field coupling is small ($\epsilon \to 0$), the photon count rate is given by [50]

$$R_{cavity} = \frac{1}{2\pi}\int d\omega S_{s1}(\omega) = \frac{2\epsilon^2}{\gamma} \tag{3.30}$$

We can rewrite the count rate in terms of the finesse of the cavity ($\mathcal{F} = \frac{2\pi}{\gamma\Delta t}$)[50],

$$R_{cavity} = \frac{|r|^2\mathcal{F}}{\pi\Delta t} \tag{3.31}$$

where $r = \epsilon\Delta t$ is the single pass gain parameter and Δt is the cavity round-trip time. The down-conversion bandwidth of a single-pass SPDC is typically much larger than the cavity bandwidth. In order to calculate the enhancement factor we need to compare the down-conversion spectrum within the cavity bandwidth γ which is obtained by placing a narrow band passive filter after the cavity $\Delta\omega_{filter}$. Assuming the normalized DOS of the down-conversion spectrum is constant within the filter bandwidth, single-pass count rate without a cavity is [50]

$$R_{single-pass} = \frac{|r|^2\Delta\omega_{filter}}{2\pi} \tag{3.32}$$

With the count rate calculated for both cases, the average enhancement per mode γ is given by [50]

$$Enhancement = \frac{R_{cavity}}{R_{single-pass}} = \frac{\mathcal{F}^2}{2\pi} \tag{3.33}$$

The calculation shows that the enhancement per mode due to a cavity is roughly square of the finesse of the cavity. By placing a SPDC crystal inside a cavity with finesse 100 we can obtain an enhance of around 1600 which is a significant improvements in the count rate.

3.2.2 Wavefunction of the Cavity-SPDC photons

So far we have assumed the fields are collinear and occupy a single spectral mode. In a realistic cavity, due to the finite free-spectral range (FSR) of the cavity, there exist multiple cavity modes. In our experimental case, the FSR of the cavity is about 10 GHz and the SPDC down-conversion bandwidth is about 600 GHz, which results in many modes to be occupied by the down-converted fields. Herzog *et al.*, have done a detail calculation of the cavity-SPDC and the multimode spectrum of the downconverted photons [109]. The multimode electric field of the signal and idler photons are the sum of the Lorentzian functions, as derived in Eq.3.22, separated by the FSR of the cavity $\Omega_{s,i}$. With the appropriate electric fields, we can find the wavefunction of the down-conversion fields by re-solving the SPDC Hamiltonian with the modified electric fields. Following reference [109], the wavefunction of the bi-photon generated from the cavity-SPDC can be written as

$$|\psi_{s,i}\rangle \propto \sum_{m=-\infty}^{\infty} \int_{-\infty}^{\infty} d\omega \frac{\Phi_m(\omega)}{\gamma/2 - i\omega} a^\dagger(\omega_s + m\Omega_s + \omega) b^\dagger(\omega_i - m\Omega_i - \omega)|0\rangle \tag{3.34}$$

where $a^\dagger$ and $b^\dagger$ are creation operators for signal and idler photons occupying modes $+m$ and $-m$, the sum of which satisfies energy conservation. $\Phi_m(\omega)$ is the phase

mismatching for mode m (similar to Eq. 3.17 derived earlier), given by

$$\Phi_m(\omega) \propto \frac{1}{L} \int_{-L}^{0} dx e^{i(\omega + m\Omega)\tau_0 x/L} \tag{3.35}$$

$\tau_0 = L(1/v_{g,i} - 1/v_{g,s})$ is the relative transit times between the signal and idler photons in the cavity, given by the group velocity for signal ($v_{g,s}$) and idler ($v_{g,i}$) photons in the crystal with length L. The phase mismatching function $\Phi_m(\omega)$ gives a Sinc function and sets the bandwidth of the down-conversion as derived in section 3.1. This bi-photon wavefunction will be of importance for explaining the cavity-SPDC data in the next chapter.

3.3 Chapter Summary

In this chapter, we discussed the importance of SPDC sources in basic physics and gave a brief motivation for cavity-SPDC. We derived the wavefunction of the down-converted field and examined its structure carefully. Following Ou's calculation, we calculated the field enhancement factor for the cavity-SPDC system. We discussed the multimode nature of the cavity fields and the bi-photon wavefunction of the down-converted photons. The theoretical treatment of the topic will be useful in the next chapter to describe the cavity-SPDC experiment.

CHAPTER IV

Experimental Realization of Cavity Spontaneous Parametric Down-Conversion

The ability to generate an on-demand single photons with customized temporal and spectral properties is of utmost importance for many quantum information protocols. Here we have implemented a customizable single photon source with spontaneous parametric down-conversion (SPDC). Through the use of an optical cavity, the down-converted photons are modified to be mode matched with the quantum dots photons. In this chapter we will give a detailed description of the cavity-SPDC setup and the measurements performed to characterize the system. The original design and preliminary implementation for the cavity based SPDC was done by collaborators at UIUC (Prof. P. Kwiat). The theoretical analysis and testing of the system along with optimization was done by me. Along with the performance of this system and an understanding of the physical origin of the behavior we have observed, a primary result of this section is a recommendation for the redesign of an SPDC system appropriate for teleportation to a quantum dot electron spin.

4.1 Experimental Setup for Cavity-SPDC

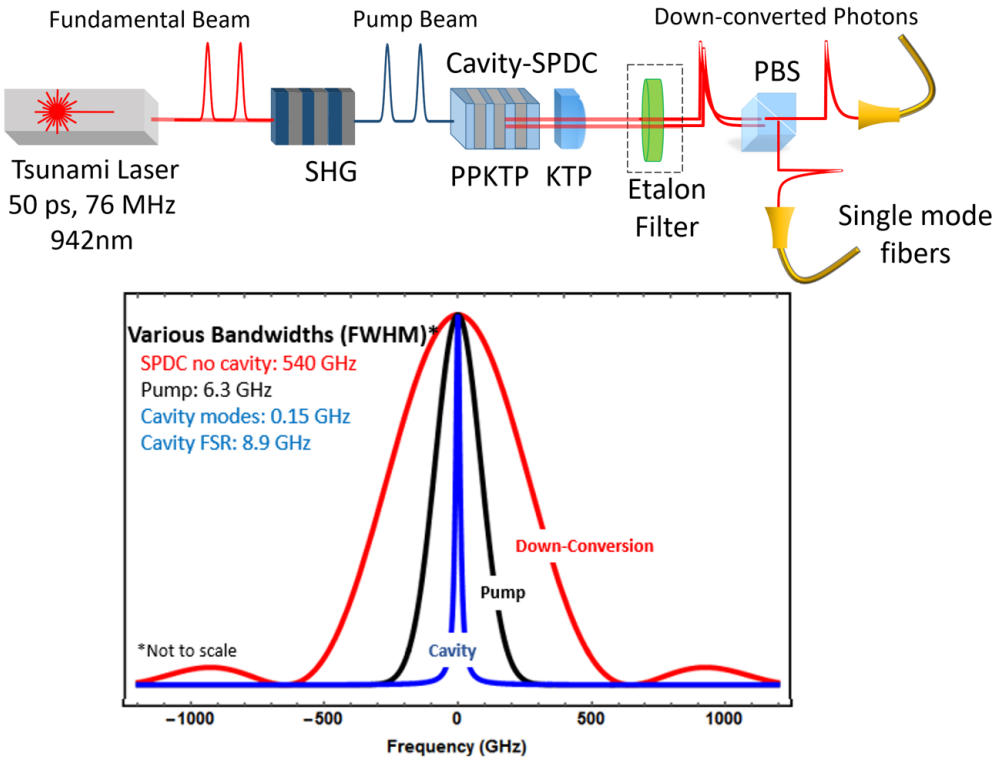

Figure 4.1: Schematic of the cavity SPDC setup and the characteristic frequency bandwidths involved in this chapter. The bandwidths are not to scale.

As described in Ch. 3, Type-II parametric down-conversion processes give rise to a pair of polarization entangled photons, where the polarization of the signal and idler photons are orthogonal to each other. When a non-linear crystal placed inside an optical cavity is pumped with a laser, within the down-conversion bandwidth, the down-converted fields emitted from the source defined by the field modes of the cavity. In addition, the intensity of the field per mode is enhanced proportional to the square of the finesse of the cavity [105]. Here, we have implemented such a Type-II cavity-SPDC source operating at around 942 nm and the details of which are given

in the following subsections.

4.1.1 Crystal Selection, Cavity Parameters, and the Optical Setup

We use an X-cut, periodically-poled 5mm long KTP crystal for down-conversion and a 2 mm long KTP crystal to correct the birefringence mismatch between the signal and idler fields. As given by the Sellemier equations, described in Eq. 2.24, for a KTP crystal, the index of refraction for the ordinary and extraordinary polarization are 1.83 and 1.75 respectively at 940 nm. This results in a different free spectral range (FSR) between the signal and idler photons in a cavity. However, we are interested in obtaining degenerate operation between the signal and idler fields in the cavity. This is one of the primary reasons for the KTP crystal in the cavity. The optical axis of the KTP crystal is rotated by 90° with respect to the PPKTP crystal. To obtain perfect degeneracy between the the two polarization modes of the cavity, the KTP crystal's length needs to be equal to the PPKTP crystal's length. However, we are interested in obtaining degeneracy only at the central frequency component, thus we have selected a shorter KTP crystal. This way the FSRs for the signal and idler photons remain unequal, resulting in suppression of unwanted cavity modes. The crystals are custom grown by Raicol Crystals Ltd. and coated by TwinStar as per our design requirements.

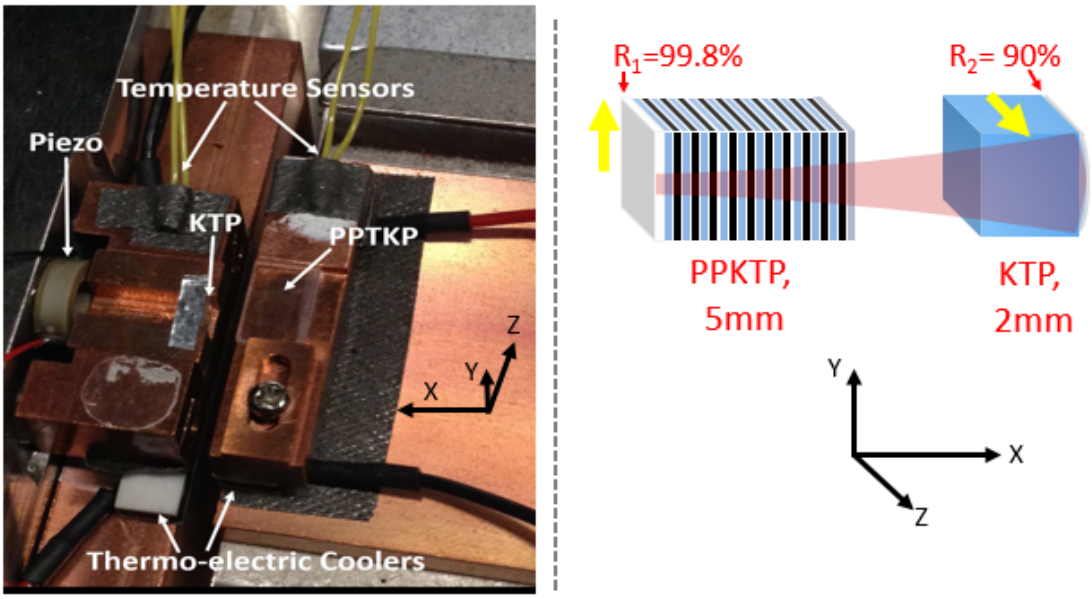

Figure 4.2: Cavity SPDC setup. (L) Image of the experimental setup of the cavity-SPDC source. A semi-concave cavity is formed using a flat PPKTP and a curved KTP crystals. A piezo is mounted to the KTP crystal to allow changing the cavity length by several free spectral ranges. (R) A cartoon of the cavity setup. The cavity is formed by HR coating the two ends of the PPKTP and KTP crystals. The optical axis of the KTP crystal is rotated by 90° with respect to the PPKTP crystal. This allows us to obtain a double resonance for signal and idler fields in the cavity. The black arrows define the Cartesian coordinate system used in this chapter and the yellow arrows represent the crystal's optical axes.

We built a semi-confocal cavity using the flat end of the PPKTP and the curved end of the KTP crystals as seen in Fig. 4.1. A confocal cavity is generally more stable and robust against small misalignment. The two ends of the crystals are commercially coated with high-reflective mirrors. Finesse is an important parameter given by the reflectivity of the mirrors of the cavity. A cavity formed with two mirrors

with reflectivity R_1 and R_2 has a finesse of

$$\text{finesse} = \frac{\pi(R_1 R_2)^{0.25}}{1-(R_1 R_2)^{0.5}} \tag{4.1}$$

Similarly, free spectral range is another important cavity parameter given by the length of the cavity. In our case, the FSR for signal and idler fields are given by,

$$\begin{aligned} FSR_s &= \frac{c}{2(n_y(\lambda,T)\times d_1 + n_z(\lambda,T)\times d_2 + l_{ca})} \\ FSR_i &= \frac{c}{2(n_z(\lambda,T)\times d_1 + n_y(\lambda,T)\times d_2 + l_{ca})} \end{aligned} \tag{4.2}$$

where c is the speed of light, l_{ca} is the distance between the crystals and $n_{y,z}(\lambda,T)$ are the indices of refraction for the ordinary and extra-ordinary polarized lights given by Eqs. 2.24, 2.25 and 2.26. As previously mentioned, the FSRs of the signal and idler are different due to different crystal lengths. However, as the birefringence of the crystals are temperature dependent, they can be brought to degeneracy at a single cavity mode frequency by tuning the temperature of the crystals. This will be of importance for obtaining degenerate operation. Another important cavity parameter is the cavity bandwidth, given by the ratio of the FSR to the finesses of the cavity. By selecting the FSR and finesse of the cavity appropriately, the down-converted photons properties are designed to match with the quantum dot's photons.

While designing the cavity-SPDC setup, it is important to consider the geometry of the excitation and collection paths. The cavity is pumped from the high reflectance end of the PPKTP crystal and the down-converted photons are collected in the forward geometry through the KTP crystal. This has several advantages: first, the focus parameters of the lenses for the pump and the collection beams can be controlled independently; second, it provides more space to place optical components making the experiment less cluttered. Considering these two points, we designed an asymmetric single-sided cavity by unbalancing the reflectivity of the crystals. The

two outward facing sides of the PPKTP and KTP crystals are coated to give 99.8% and 90% reflectivity respectively. From Eq. 4.1, 4.2, we can calculate the finesse, FSR and bandwidth of our cavity to be $\sim$ 58, 8.93 GHz and $\sim$ 160 MHz respectively. The designed crystal parameters are given in Table 4.1.

PPKTP crystal dimension	1 x 8 x 5mm(L)
KTP crystal dimension	3 x 3 x 2mm(L)
PPKTP radius of curvatures	S1: $\infty, S2: \infty$
KTP radius of curvatures	S1:$\infty, S2: 19.3mm$
PPKTP coating	S1: AR @ 471 nm and HR @ 942 nm,
	S2: AR @ 942 nm and 471 nm
KTP coating	S1: AR @ 942 nm and 471 nm,
	S2: AR @ 471 nm (S2)
PPKTP reflectivity	S1: 99.8% @ 942 nm
KTP reflectivity	S2: 90% @ 942 nm
Finesse	58
Cavity FSR(Ω)	$\sim 8.9GHz$
DownConversion Bandwidth	$\sim 540GHz$
Fundamental Pulse width ($\delta\omega$)	50 ps Sech^2
Fundamental Pulse bandwidth (δt)	6.3 GHz ($\delta\omega\delta t \sim 0.315$)

Table 4.1: Experimental parameters of the cavity-SPDC setup. S1 and S2 correspond to surface-1 and surface-2 of the crystals as given in Fig. . HR and AR stands for high-reflecting and anti-reflecting coatings.

As per the design, the both ends of the PPKTP crystals are flat whereas one end of the KTP crystal has a finite radius of curvature. Even though only a single KTP crystal is used for the cavity setup, we bought two KTP crystals with 19.3 mm and 12mm radius of curvatures, which allows flexibility in designing the cavity parameters. In order to obtain stable cavity operation, the wavefront of the down-converted fields has to match well with the curvature of the KTP crystal. Using an ABCD matrix for Gaussian beams optics, cavity parameters are calculated and the setup is built accordingly such that the cavity bandwidth matches with the quantum dot's photons. Another important parameter to be considered while designing a cavity-SPDC setup is the pump beam's confocal parameter. For a down-conversion crystal of length L,

the optimal focusing parameter can be calculated using Boyd-Kleinman's criteria [76],

$$\zeta = \frac{L}{b} = 2.8 \tag{4.3}$$

where b is the confocal parameter given by twice the Rayleigh range. The Rayleigh range (z_R) of a focused Gaussian beam is given by,

$$z_R = \frac{n\pi w_0^2}{\lambda} \tag{4.4}$$

where w_0 is waist (radius) of the beam at the focus. For our crystal, the optimal focus diameter for the pump and the down-converted fields are $\sim 17\mu$m $\sim 26\mu$m respectively. To obtain stable cavity operation, the down-converted fields' radi of curvature need to match well with the curvature of the crystal. Figure 4.3 is a contour plot of the beam waist vs the distance between the two crystals l_{ca} calculated theoretically, that matches the radi of curvature of the down-converted field with the KTP crystal.

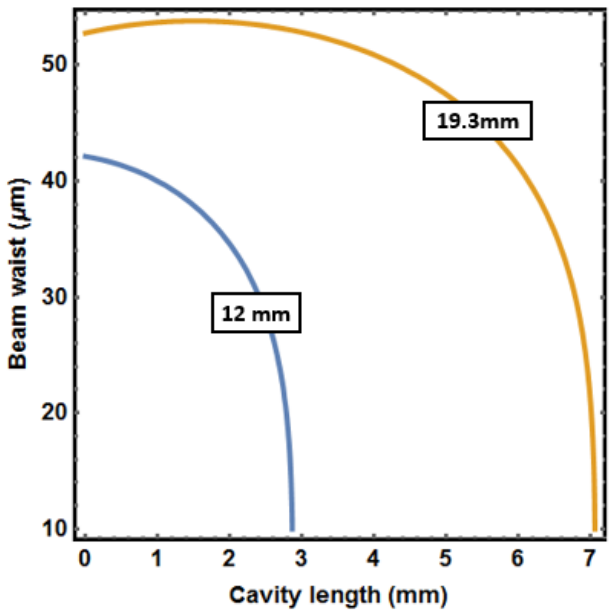

Figure 4.3: Contour plot of the beam waist vs the distance between the two crystals that matches the radi of curvature of the KTP crystal calculated using Gaussian beam optics. The number in the box corresponds to the radi of curvature of crystals that is available in the lab.

The PPKTP crystal is mounted on an XYZ-stage that has pitch and yaw (tip-tilt) degrees of freedom. The KTP crystal is securely placed on a copper piece with a piezo mounted to it. The piezo is driven with a ramp voltage generated by a Keithley function generator along with a voltage amplifier (PI E836) that can output -30V to 130V signal. The piezo allows the cavity length to be stabilized using a Pound-Drever-Hall locking technique, which will be discussed in detail later in the chapter. Both PPKTP and KTP crystal holders are mounted on top of separate temperature sensors to read out the crystal temperature and thermo-electric coolers (TEC) manufactured by TE Technology to adjust the temperature. The TECs are capable of tuning the crystal temperatures from $10° - 60°$C. The TECs and the sensors are connected to two independent PID controllers (LFI-3751 manufactured by Wave Electronics) that

can stabilize the temperature within a few mK accuracy. Such ability to tune and stabilize the crystal temperature individually will be of importance for degenerate operation.

A rough alignment procedure of the cavity is as follows. As the KTP crystal is placed on the piezo mount and doesn't have much freedom for fine alignment, the blue pump beam is aligned normal of the KTP crystal with the beam focus several mm before the KTP crystal. The reflections of the blue beam from the crystal surfaces are used as guidance for ensuring the pump is impinging on the KTP crystal on axis. Then, the PPKTP crystal is roughly placed at the distance determined from the Gaussian beam calculation. The pump beam focus is adjusted to be roughly at the beginning of the PPKTP crystal. A fraction of the fundamental beam at 942 nm is sent to the cavity through the PPKTP end and is aligned to be collinear with the pump beam (see Figure 4.4). As the cavity length is changed periodically by scanning the piezo, when the 942 nm laser's frequency is in resonance with the cavity modes, the reflected intensity of the beam drops, forming multiple dips in the reflection. The reflected beam is monitored using a photo-detector and an oscilloscope. By monitoring the reflection profile, the cavity is further fine-tuned to maximize the TEM_{00} modes that are separated by the FSR of the cavity. With the same 942 nm beam transmitted through the cavity, the collection path for the down-converted photons are aligned. As per the calculation, a 60 mm-long focal-length lens is mounted in front of the KTP crystal that is used to collect the down-converted photons. The collection lens is mounted on a linear stage which allows the focus to be fine controlled. A polarizing beam splitter is mounted after the lens to split the signal and idler photons. Two 0.16 NA aspheric lenses are mounted at the two output ports of the beam splitter to focus and collect the down-converted fields into two single-mode fibers. The collection packages are mounted on two XYZ-stages, and two pairs of mirrors allow maximizing the field coupling.

After the collection and the pump path are set, a high power fundamental beam is back-propagated from the collection fibers to the cavity. For an appropriate fundamental polarization, the down-conversion crystal generates a weak blue light through an SHG process that is propagated towards the pump beam. The cavity and the collection paths are optimized to maximize the intensity of the blue light generated by the down-conversion crystal. This forward and reverse alignment processes are repeated until both the pump and the blue light generated by the down-conversion crystal converge to the same beam parameters and are spatially overlapped. Once a satisfactory alignment is achieved, the down-converted photons are measured using two single-photon detectors. The whole alignment process is repeated until the single photons and the coincidence counts are maximized.

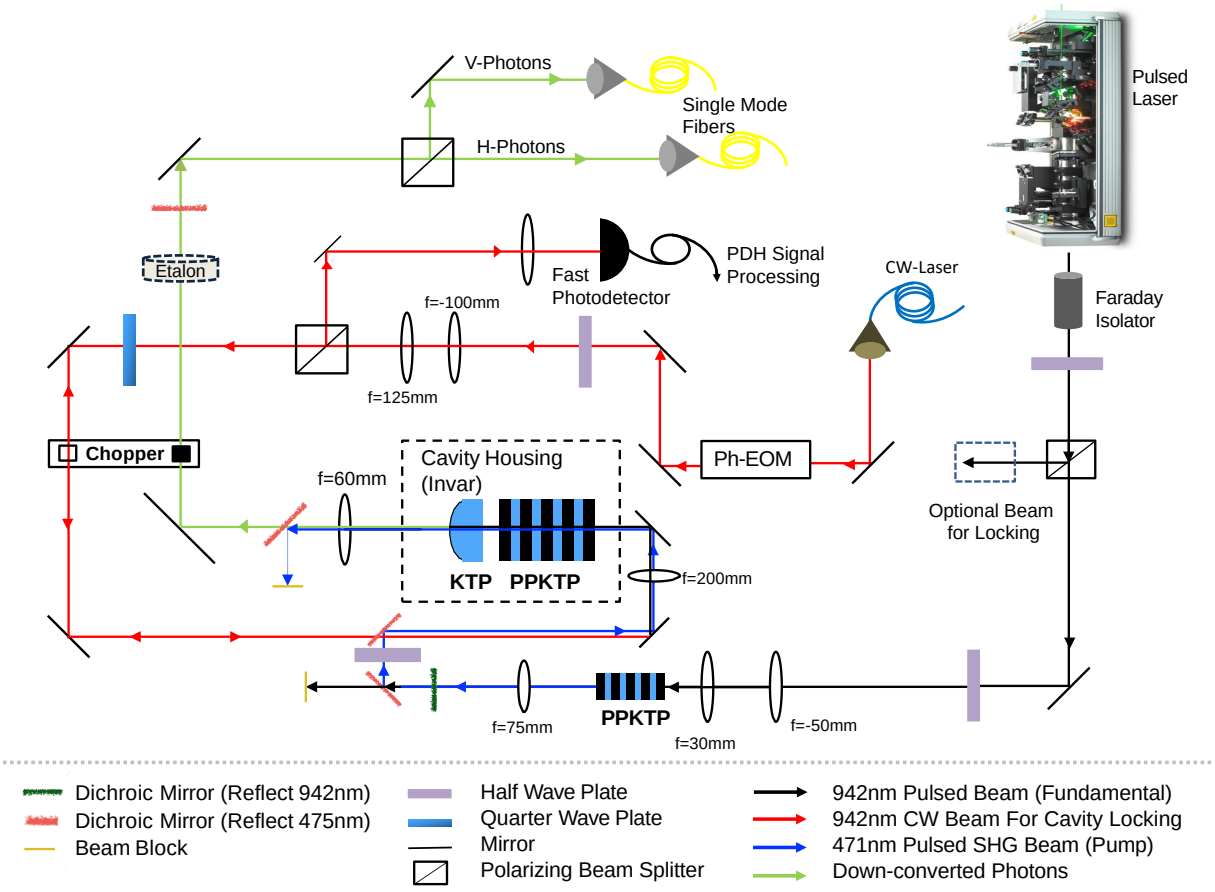

Figure 4.4: Practical schematic of the experimental setup for SHG and the cavity-SPDC operation.

The experimental setup for the second-harmonic generation and the cavity-SPDC is given in Figure 4.4. The setup can be split into four main parts: the blue light generation through the SHG process, the cavity-SPDC setup, the collection setup for the down-converted fields, and the cavity locking setup. A 941-942 nm beam (fundamental) with 50 ps pulse width and 76 MHz repetition rate denoted by a black line is focused to the first PPKTP crystal for SHG. A HWP and polarizer is used before the SHG crystal to clean the polarization and control the incident power as desired. The SHG crystal is temperature stabilize at 68° C using a PID-controlled

oven. The crystal generates linearly polarized blue light at 471 nm with up to 500 mW power. A dichroic mirror and a short-pass filter is used to block the fundamental beam and the blue light, denoted by a blue line, is focused onto the cavity-SPDC setup. A HWP is used before the cavity to rotate the polarization of the pump beam. The pump is linearly polarized along the y-axis of the PPKTP crystal, which is the axis along which the crystal is poled. The signal and idler fields are polarized along the y- and z-axis respectively (see Figure 4.1 for coordinates). The cavity lifetime is 1.06 ns, which is much smaller than the inverse repetition rate of the pump laser (13 ns). This guarantees that there is a very little stimulated emission and pileup forming in the cavity. The collection path of the down-converted fields are denoted by the green lines. Multiple long-pass filters are placed in the collection path to remove the 471 nm pump beam. The red lines represents the optical paths used to lock the down-conversion cavity using the PDH technique (see Section 4.1.4 below). As the cavity locking beam could blind the single photon detectors, a mechanical chopper is introduced along the locking and the collection paths. This ensures the collection arm is blocked while the locking beam is in the cavity. The cavity is locked at a rate of 50 Hz. The cavity is originally designed to be locked with the fundamental beam. However, as the spectral bandwidth of the fundamental beam (6.3 GHz determined by 50 ps sech square pulse) is much larger than the cavity bandwidth (160 MHz), and the cavity is asymmetric, the majority of the incident beam gets reflected from the highly reflecting surface of the PPKTP crystal without entering the cavity. This results in a large unwanted DC component in the photo-detector that monitors the reflectivity of the cavity which results in a small lock signal. To get around the small lock signal, a narrow-band (< 100KHz)) CW beam mode-locked at the fundamental wavelength is used for locking the cavity. This additional tunable CW beam allows us to fine-tune the cavity lock set-point for degenerate operation. The setup is designed such that either the fundamental or the CW beam can be used to lock the cavity.

4.1.2 Phase Matching for Degenerate Operation and SPDC Spectrum

As previously discussed in Ch. 2 for the second-harmonic generation case, proper phase-matching between the signal, idler and the pump field is necessary for the new fields to propagate. One can obtain such phase-matching by angle tuning the pump beam. However, as the down-conversion crystal is embedded inside a cavity, we want the signal and idler field to be collinear with the pump field, which makes angle tuning not a viable option. Similar to the second-harmonic crystal, the down-conversion crystal is periodically poled to obtain degenerate operation at the desired wavelength. Here we write the phase mismatching as described in Ch. 2 but by explicitly writing the bandwidth of the fields,

$$\Delta K(\omega_s+\Delta\omega_s,\omega_i+\Delta\omega_i,\omega_p+\Delta\omega_p) = k_p(\omega_p+\Delta\omega_p)-k_s(\omega_s+\Delta\omega_s)-k_i(\omega_i+\Delta\omega_i)-\frac{2\pi}{\Lambda} \tag{4.5}$$

where the k's are the wave-vector of the fields with center frequencies and frequency bandwidths ($\Delta\omega$) written out explicitly and Λ is the periodic poling length of the crystal. To get perfect phasing matching ($\Delta K = 0$), Λ is set to an appropriate value calculated using the Sellmeier equations (Eqs. 2.24, 2.25 and 2.26). The perfect phase matching condition is achieved assuming the down-conversion bandwidth is negligible $\Delta\omega = 0$. However in a more realistic scenario, the involved fields have finite bandwidth and energy conservation allows the down-conversion to happen in a large wavelength region with a broad bandwidth. Energy conservation requires, $\Delta\omega_p = \Delta\omega_s + \Delta\omega_i$. Knowing *a priori* that the down-conversion bandwidth is much larger than the pump bandwidth (6.3GHz), we will solve the problem in the limit of zero pump bandwidth, which gives $\Delta\omega_s = -\Delta\omega_i$. Taylor-expanding Eq. 4.5 around the center frequency,

$$\Delta K(\omega_s+\Delta\omega_s,\omega_i+\Delta\omega_i,\omega_p) = k_p(\omega_p)-k_s(\omega_s)+\frac{\partial k_s}{\partial\omega}\Delta\omega_s-k_i(\omega_i)+\frac{\partial k_i}{\partial\omega}\Delta\omega_i-\frac{2\pi}{\Lambda} \tag{4.6}$$

The terms can be rearranged to get

$$\Delta K(\omega_s + \Delta\omega_s, \omega_i + \Delta\omega_i, \omega_p) = \Delta K(\omega_s, \omega_i, \omega_p) + (\frac{\partial k_s}{\partial \omega} - \frac{\partial k_i}{\partial \omega})\Delta\omega \qquad (4.7)$$

The first term on the RHS is simply the phase mismatch for the single frequency components which is tuned to be zero, and the second term gives the down-conversion bandwidth. The partial derivatives in the second term can be calculated from Eq. 2.24.

As calculated in Section 3.1, the intensity profile of the down-converted field is given by a $Sinc^2$ function. The profile is the same as the intensity profile calculated and measured in Ch. 2 for the SHG field. The second term in Eq. 4.7 is the argument of the $Sinc^2$ function, from which we can calculated the down-conversion bandwidth by calculating the FWHM of the intensity profile. The bandwidth of the down-conversion field can be calculated to be [98],

$$\Delta\omega = 2\frac{2 \times 1.39}{2\pi L(\frac{\partial k_s}{\partial \omega} - \frac{\partial k_i}{\partial \omega})}, \qquad (4.8)$$

where L is the length of the crystal. The bandwidth is inversely proportional to the length. As the crystal length increases, the phase matching condition gets restricted to a smaller wave-vector spread, as a result the phasematching bandwidth drops. In our experiment, we use 5 mm long PPKTP crystal, which results in 540 GHz down-conversion bandwidth. The bandwidth is significantly larger than the cavity FSR. As a result, a large number of cavity modes are occupied with the down-conversion and the down-conversion is highly multi-mode in nature.

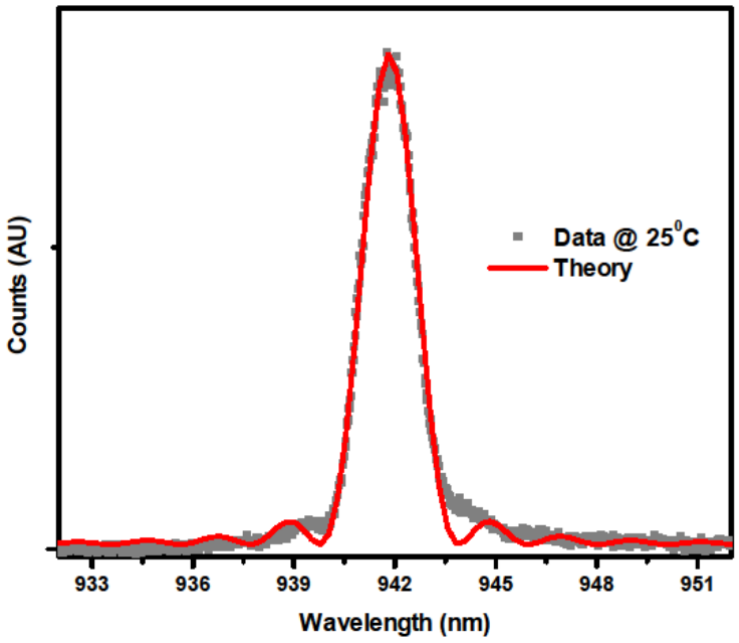

Figure 4.5: Spectrum of the signal photons. Gray dots are the experimental data measured at 25^0C temperature using a spectrometer. The red curve is a theoretical fit obtained using the calculation done in Section 3.1.

To verify the theoretical prediction, we measured the spectrum of the cavity-SPDC fields using a spectrometer. Figure 4.5 is the wavelength dependent intensity profile of the signal field measured using a spectrometer. We use HR-640 spectrometer with 1200 lines/mm grating and a nitrogen-cooled CCD camera to record the spectrum. The individual modes of the cavity($\sim 9GHz$) aren't visible as the spectrometer resolution is similar to the FSR of the cavity. The data is fitted with a $Sinc^2$ function given by the red curve and the extracted bandwidth is consistent with the theoretical prediction of ~ 540. The deviation of the data points around the wings from the theoretical calculation could be due to the effective pump beam profile deviating from the assumed Gaussian modes.

To understand the temperature tuning behavior of the down-converted fields, we

measured the spectrum of the signal and idler fields by tuning the PPKTP crystal temperature and recording them with the spectrometer. Figure 4.6 (left) is the spectrum of the signal and idler photons measured as a function of the PPKTP crystal temperature. As described previously, the signal and idler photons become degenerate at 27° C. Figure 4.6 (right) is the theoretical prediction made using the Sellemeir equations given in Chapter 2 (Eqs. 2.24, 2.25 and 2.26). As the efficiency of the spectrometer changes by up to a factor of 5 times for s- and p-polarized photons, data in Figure 4.6 were measured separately for the signal and idler photons and later scaled with an appropriate correction factor. It is important to note that our theoretical understanding, thus the prediction agrees well with the tuning behavior of the down-converted fields.

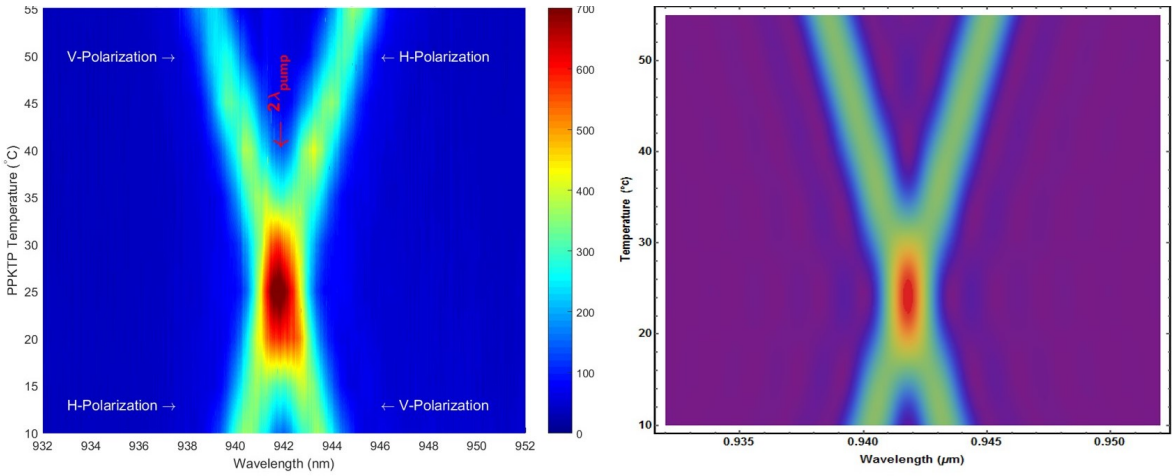

Figure 4.6: (L) Experimental data and (R) theoretical calculation for the spectrum of the down-converted photons as a function of PPKTP temperature. As predicted theoretically, at around 25° C the signal and idler spectra are degenerate in wavelength with the fundamental beam. The temperature bandwidth for degenerate operation is $\sim$ 10° C which agrees with the theoretical calculation.

During the design of the experiment, the wavelength of the quantum dots to be

interfered with the SPDC photons was uncertain, thus the PPKTP crystal was grown with several domains with different poling periods to allow degenerate operation at various wavelengths. As seen in Figure 4.7 (left), the PPKTP crystal is designed with six domains with different periodic poling period to allow the emission wavelength to be tuned from 939 nm-947 nm by changing the PPKTP crystal temperature by 60° C. The degenerate operation temperature seen in Figure 4.7 (right) for various polling length is calculated using Sellmeier equations written in Chapter 2. The degenerate down-conversion operation points for domain 3 is designed to be slightly above room temperature for 942 nm.

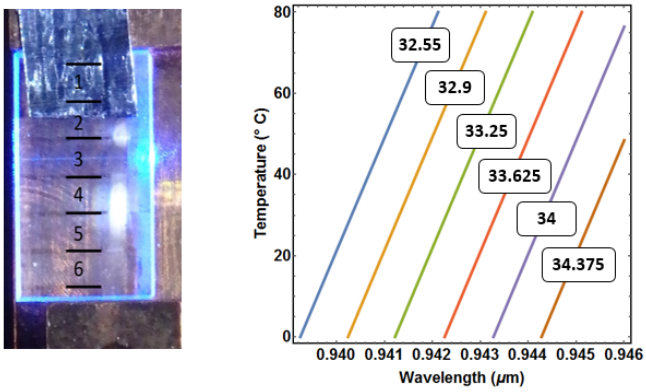

Figure 4.7: (L) PPKTP crystal with six different domains that have different periodic poling. The period of the corresponding poling is given in the right plot (R) PPKTP temperature versus signal/idler wavelength for degenerate down-conversion calculated using the Sellmeir equations for various poling periods. The numbers inside the box are poling periods with micrometer lengths and correspond to the poling represented on the left crystal image.

4.1.3 High Resolution Spectrum of the Down-Conversion Field

As the cavity FSR is $\sim$ 9GHz and the down-conversion bandwidth is 540 GHz, $\sim$ 50 non-degenerate modes of the cavity are available for the down-conversion fields to be emitted within the bandwidth. This results in highly multi-mode emission from the cavity. If we define the mode (m) of the fundamental laser to occupy the central mode, $m = 0$, energy conservation requires the signal and idler fields to be emitted on opposing sides of the central mode. This feature is encapsulated in the bi-photon wavefunction of the signal and idler field given by Eq. 3.35. If the cavity is pumped with a narrow-band field such that the pump bandwidth is smaller than the FSR mismatch between the signal and idler fields, conservation of energy would have suppressed most of these modes. However, in this thesis work, we are interested in generating heralded single photons with well defined emission time. As a result, we use the fundamental beam with 50 ps pulse duration, resulting in 6.3 GHz frequency bandwidth for the pump beam. This finite pump bandwidth allows energy conservation to be satisfied for most of the cavity modes (both degenerate and non-degenerate) that lie within the bandwidth of the down-conversion emission, resulting in a broad emission.

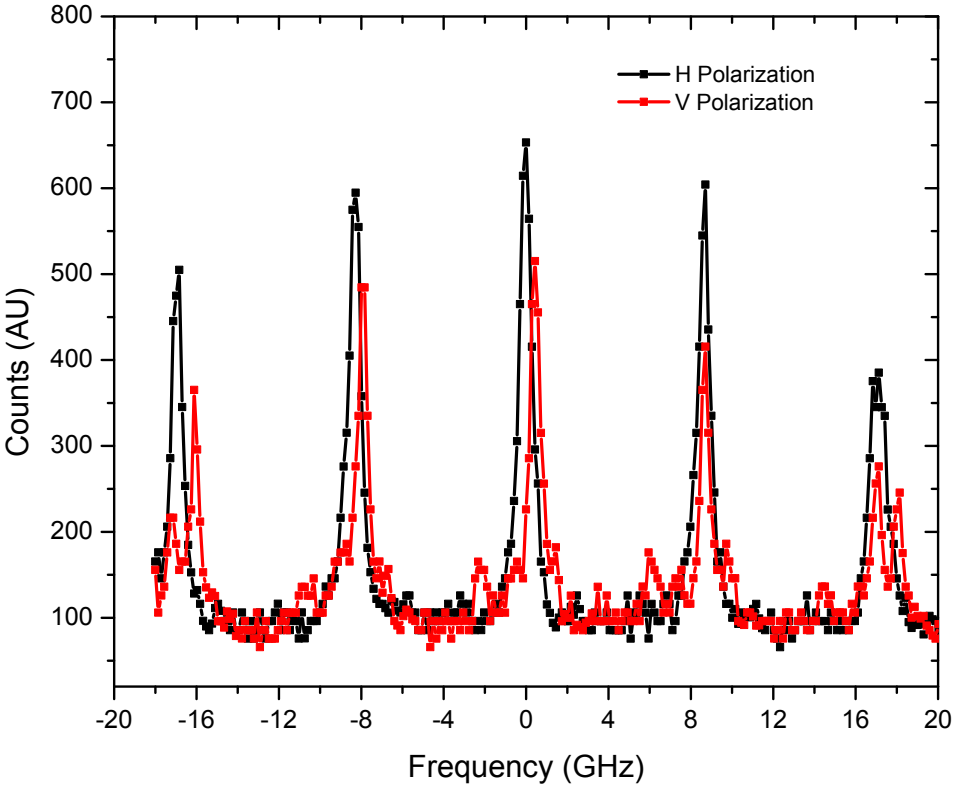

Figure 4.8: Signal and idler field spectra of the down-converted photons centered at 941.8 nm obtained by scanning the pressure tuned etalon. The peaks are separated by the FSR of the cavity, which is 8.9 GHz. The linewidth of the individual peaks are limited by the scanning etalon' bandwidth. As the down-conversion bandwidth is 540 GHz and the FSR of the cavity is much smaller that the bandwidth, most of the cavity modes are occupied.

The emission spectrum of the cavity modes is measured using a pressure tuned Fabre-Perot cavity. A commercially manufactured air-spaced etalon with 45 GHz free-spectral range and $\sim$ 400 MHz bandwidth is mounted in an airtight glass housing. The glass housing is connected to a dry nitrogen gas cylinder through a solenoid valve. A PID controller controls the solenoid to hold the pressure constant. The

system is computer controlled and can set a desired pressure inside the housing on command. Because the etalon is not sealed, by changing the pressure of gas inside the housing and thereby changing the gas pressure inside the etalon, the resonance frequency of the etalon cavity can be tuned. The pressure-tuned cavity setup is built on a separate platform equipped with fiber in-coupling and out-coupling, where the output is monitored with single photon detectors and counting modules.

The pressure-tuned etalon setup is designed and build by Aaron Ross and Colin Chow. We send the signal and idler photons separately through the pressure tuned cavity and record the integrated counts while scanning the pressure.

Figure 4.8 is the high resolution signal and idler field spectrum of the down-converted photons from the cavity-SPDC source. The emission is centered at around 942 nm and is filtered with a $\sim$ 40 GHz FWHM etalon with 10 nm FSR. The filtered data is sent to the pressure-tuned etalon and the spectrum is recorded by tuning the pressure. As predicted, the peaks are separated by the FSR of the SPDC cavity, which is 8.9 GHz. The individual peak's linewidth is limited by the pressure tuned etalon's bandwidth. We are interested in obtaining degenerate operation between the signal and idler photons to form a doubly-resonant cavity operation. For Type-II cases the signal and idler can be emitted into any modes, as long as the sum of the energy of the two photons is equal to the pump energy. This results in frequency correlations between the two photons as one can see from Equation 3.35. However, when the signal and idler frequencies are degenerate, for the center mode ($m = 0$) such frequency entanglement is removed between the modes to the left and right of the center mode. To achieve this experimentally, first, the PPKTP crystal is temperature tuned to obtain a degenerate operation between the signal and idler photons within the down-conversion bandwidth as seen in Fig. 4.6. Then the KTP temperature is finely tuned until the down-conversion modes at the fundamental frequency are doubly resonant with the cavity modes. For the rest of the data presented in the

thesis, the cavity is operated at the doubly degenerate regime.

4.1.4 Pound-Drever-Hall Technique for Stabilizing the Frequency of the Down-Converted Fields

Due to the mechanical coupling of the cavity with the surrounding and the room temperature fluctuations, the length of the cavity is susceptible to low frequency noise that cause the length of the cavity to drift over time. Such drift in cavity length causes the down-conversion spectrum to drift in frequency. One can stabilize the cavity length by locking to the cavity transmission fringes. However, this comes with a few caveats. As the transmission peak is symmetric around the center there is no way to tell in which direction the cavity has drifted, which results in a very narrow cavity locking range. In addition, such a locking protocol is very sensitive to laser intensity fluctuation. Pound, Drever and Hall proposed an elegant technique, known as PDH locking, to stabilize an optical cavity that overcomes the above mentioned limitations [110], [111]. In PDH locking, a reference laser beam is phase modulated to generate sidebands and is reflected through the cavity that needs to be stabilized. Whenever the cavity length gets modified due to some mechanical vibration, the relative intensity of the reflected sidebands changes. This results in an unbalanced reflectance profile for different frequency components. When the reflected beam is beat with itself and is measured with a fast photodetector, after some signal processing, one can generate an error signal that is odd Lorentzian in frequency (or cavity length). This can be used to lock the cavity. The electric field profile of a continuous-wave beam of frequency ω after passing through a phase modulator can be written as

$$\begin{aligned} E_{inc} &= E_0 e^{i(\omega t + \beta sin\Omega t)} \\ &\approx E_0[J_0(\beta)e^{i\omega t} + J_1(\beta)e^{i(\omega+\Omega)t} - J_1(\beta)e^{i(\omega-\Omega)t}] \end{aligned} \tag{4.9}$$

where Ω is the modulation frequency, β is the modulation degree, and J_n is the nth coefficient of the Bessel functions of the first kind. The above equation ignores the higher-order sidebands which is a valid approximation when driven with a small modulation depth. Note that the sidebands are π out of phase, thus one would not detect the modulation frequency by simply measuring the intensity of the field. Following E. Black [111], the electric field profile of the reflected beam from a cavity can be related to the incident beam by using a transfer function $R(\omega)$,

$$\frac{E_{ref}(\omega)}{E_{inc}(\omega)} = F(\omega) = \frac{-r_1 + r_2(t_1^2 + r_1^2)e^{-i\omega/\omega_{fsr}}}{1 - r_1 r_2 e^{-i\omega/\omega_{fsr}}} \tag{4.10}$$

where r_1, r_2, t_1, t_2 are reflection and transmission coefficients of the cavity mirrors and ω_{fsr} is the free spectral range of the cavity. With the transfer function in hand, we can calculate the frequency-dependent electric field profile of our modulated incident field reflected from the cavity, which is

$$E_{ref} = E_0[F(\omega)J_0(\beta)e^{i\omega t} + F(\omega+\Omega)J_1(\beta)e^{i(\omega+\Omega)t} - F(\omega-\Omega)J_1(\beta)e^{i(\omega-\Omega)t}] \tag{4.11}$$

The reflected beam is detected using a fast photodetector. After some algebraic simplification, the power of the reflected beam can be written as

$$\begin{aligned} P_{ref} \propto & |E_0|^2(|F(\omega)|^2|J_0(\beta)|^2 + |F(\omega+\Omega)|^2|J_1(\beta)|^2 + |F(\omega-\Omega)|^2|J_1(\beta)|^2 .. \\ & - 2Re[\chi(\omega)]\cos\Omega t - 2Im[\chi(\omega)]\sin\Omega t + O(2\Omega)) \end{aligned} \tag{4.12}$$

with [111]

$$\chi[\omega] = F[\omega-\Omega]F^*[\omega] - F^*[\omega+\Omega]F[\omega] \tag{4.13}$$

The detected signal is mixed with a fraction of the radio-frequency field that drives the EOM and is detected after sending through a low-pass filter. The detected signal,

also referred as the error signal, is given by

$$V_{ErrorSignal} \propto Re[\chi(\omega)] \sin\phi + Im[\chi(\omega)] \cos\phi \tag{4.14}$$

where ϕ is the relative phase between the photodetector signal and the radio-frequency field. χ is an odd Lorentzian function, the detailed shape of which is highly dependent on the modulation frequency (Ω), cavity bandwidth and the relative phase (ϕ).

To PDH lock our cavity SPDC we used an independent frequency locked continuous-wave laser modulated using a New Focus Electro-Optic phase modulator driven at $250MHz$. A mode-locked CW-laser tuned to the fundamental beam's wavelength is used for locking the cavity.

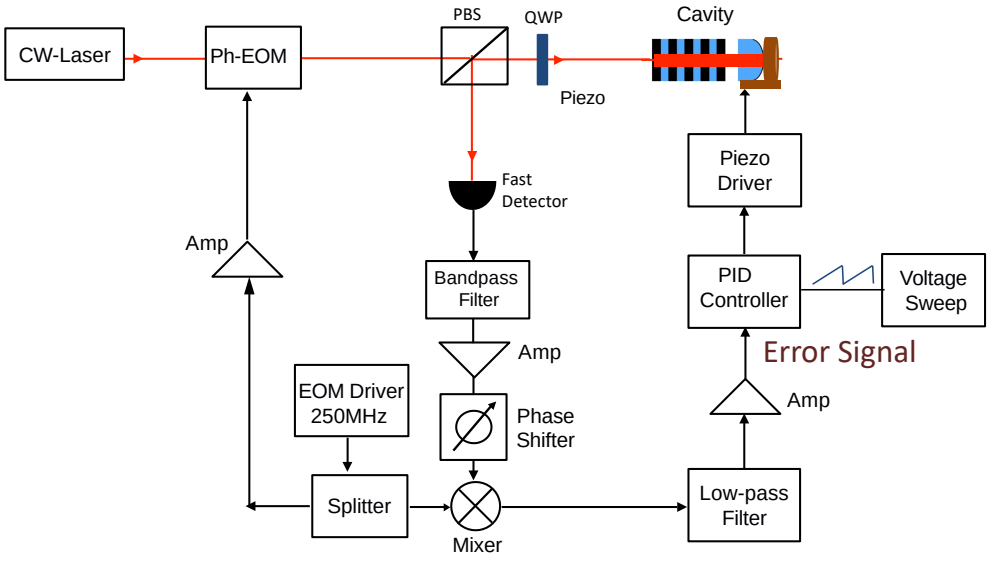

Figure 4.9: Experimental setup for PDH locking. The red arrow line corresponds to the cw-laser beam and black arrow corresponds to the electronic signal. The KTP crystal is mounted on a piezo ring and is swept with a triangular wave at 50 Hz. A snapshot of the error signal obtained from the PDH locking measured using an oscilloscope is given in Figure 4.10.

The experimental setup for cavity locking is given in Fig. 4.9, where the reflectance signal (red) and the error signal (blue) are plotted as a function of the sweep voltage. As the modulation frequency is comparable to the cavity bandwidth the error signal is simply an odd Lorentzian without any features.

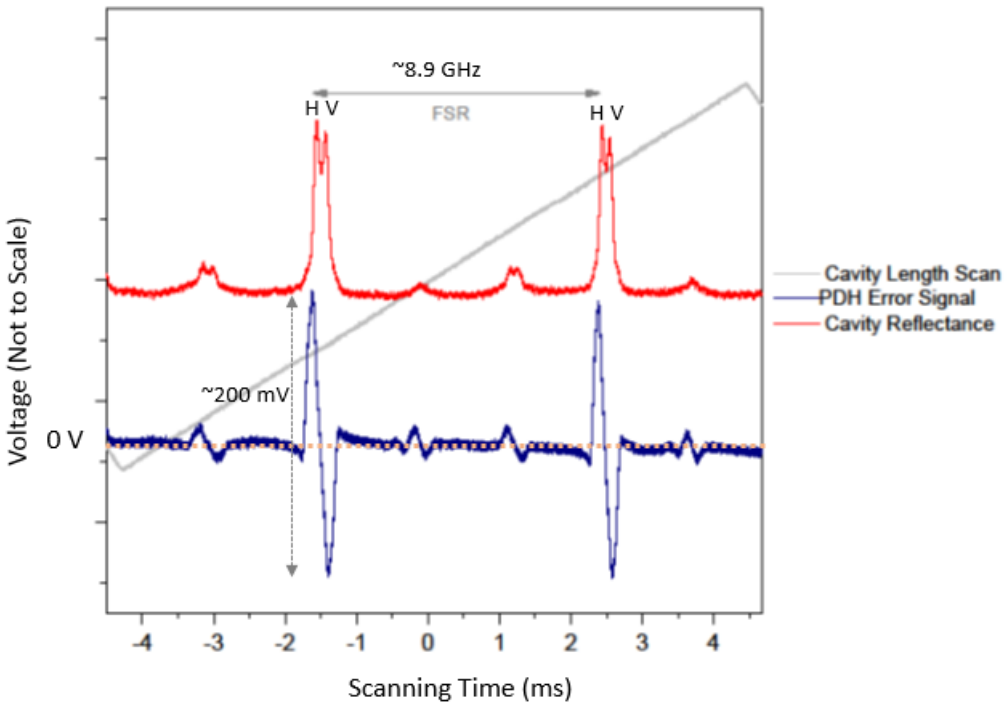

Figure 4.10: Cavity reflectance signal (red) and error signal from PDH locking (blue) as a function of cavity length. Cavity length is scanned by moving the KTP crystal, where the KTP is glued to a piezo stack driven with a low frequency ramp voltage (gray). The PHD error signal is centered around 0 V. As the voltage size are different for reflectivity and the error signal, they are plotted in different scale. The nearly degenerate peaks correspond to the H and V polarization with respect to the lab frame, the relative position of which can be changed by tuning the crystals' temperature. The gray arrow indicates the free spectral range of the cavity, which is ~ 8.9 GHz. The small peaks corresponds to the higher-order transverse cavity modes. Through further alignment, the higher order modes can be suppressed.

To obtain degenerate operation, the PPKTP crystal temperature is tuned while measuring the signal and idler photons using an spectrometer. Once degenerate

down-conversion is obtained within the spectrometer resolution ($\sim 10GHz$), the cavity length is locked to the zero-crossing of the error signal using a NewFocus PID controller. As the slope is linear in voltage, it is robust against small perturbations. Once the cavity is locked, the KTP crystal temperature is slowly tuned until the signal and idler frequencies are overlapped with the fundamental field. The degeneracy of the signal and idler mode with the fundamental beam (central mode $m = 0$) is verified by measuring the down-conversion spectrum with the pressure tuned Fabry-Pérot etalon. When the signal and idler photons are degenerate with the fundamental beam, the coincidence count rate increases.

4.2 Temporal Properties, First- and Second-Order Coherence and Heralded Photon Statistics of the Cavity-SPDC Photons

So far we have discussed the spectral properties of the down-converted fields from the cavity-SPDC source. It is equally important to fully understand the temporal properties and the coherence of the down-converted fields. Several time-domain measurements that are complimentary to each other are performed and reported in the following sub-sections that fully characterize the cavity-SPDC source. Most of these measurements can be explained through correlation measurements between fields in the second and fourth orders. A detailed example of the fourth order field coherence is given in Ch. 6 with quantum dot photons. Here, we will cite important theoretical results when necessary and focus on the experimental data.

4.2.1 First Order Coherence with Michelson Interferometry

The first-order coherence of a field is defined as

$$g^{(1)}(\tau) = \frac{\langle E^{-}(t)E^{+}(t+\tau)\rangle}{\langle E^{-}(t)E^{+}(t)\rangle} \tag{4.15}$$

where $E^{-}(t)$ and $E^{+}(t)$ are the negative and positive frequency components of an electric field [65]. The first-order temporal coherence of a field can be measured using a Michelson interferometer as drawn in Fig. 4.11. Unlike the second-order intensity correlation measurement, a Michelson interferometer measurement is independent of the detectors and electronic's speeds. This allows one to directly measure the first-order temporal coherence of a field with sub-femtosecond resolution.

The basic idea behind the experiment is that when a radiation is sent through the interferometer, as seen in Fig. 4.11, the electric field of the radiation splits into two optical paths and acquires different phases between the paths. When the two arms are combined at a beam splitter, the field exits through different ports of the beam splitter, depending on the relative phase differences. For a monochromatic classical field, the intensity at the output port of a 50:50 beam splitter is given by the simple relationship [65]

$$I_{D1} = 1 - \cos^2\left(\frac{\omega\Delta L}{2c}\right) \tag{4.16}$$

where ΔL is the relative path length difference between the two arms of the interferometer. As the relative path length difference is changed, the counts in detector 1 varies from 0 to 1. The interference fringe contrast can be defined as [65]

$$\zeta = \frac{\bar{I}_{max} - \bar{I}_{min}}{\bar{I}_{max} + \bar{I}_{min}} \propto |g^{(1)}(\tau)| \tag{4.17}$$

For an input field with a Lorentzian frequency profile, the visibility decays exponen-

tially [112, 65],

$$|g^{(1)}(\tau)| \sim e^{-\frac{|\tau|}{\tau_c}} \tag{4.18}$$

where τ_c is defined to be the coherence time of the field given by the full-width half-maximum (Γ) of the input field's profile, $\tau_c = 1/(2\Gamma)$.

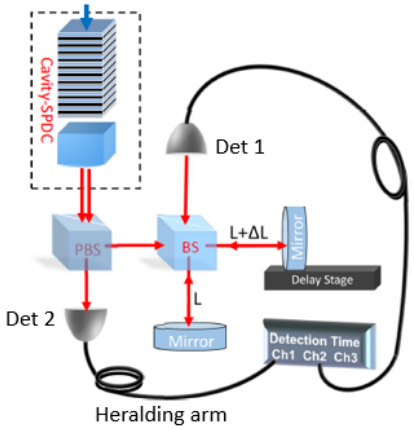

Figure 4.11: Schematic of an experimental setup for Michelson interferometry with heralded signal photons.

A Michelson interferometer setup is built by sending single signal photons through a fiber out-coupler to a non-polarizing beam splitter. A schematic of the experiment is given in Fig. 4.11. The presence of a single photon in the interferometer is heralded by detecting an idler photon in the Detector 2. The two ports of the beam splitter are sent through two arms and recombined back to the same beam splitter. One of the arms is equipped with a mechanical stage (Newport) that allows the relative time difference between the two paths to be adjusted by up to 1.2 nanoseconds with a precision of a few hundred femtoseconds. As the beams are sent collinear to each other, only a single output port of the beam splitter is accessible for detection. The output port is collected in a single mode fiber and is detected using a single photon

detector.

We monitor the photon detection rate with Detector 1 for 10 seconds while changing the relative path delay length (ΔL). The count rate is acquired in 10 ms time bin widths. As the interferometer is not phase stabilized, thermal and mechanical fluctuations in the laboratory cause the relative phase difference in the interferometer to change rapidly. As a result, the count rate fluctuates due to constructive and destructive interference between the two paths. The data is analyzed to look for the maximum and minimum counts at each delay stage point. Using Eq. 4.18, the interference visibility fringe is calculated and is plotted as seen in Fig. 4.12. The visibility for the central peak is less than one, the ideal case scenario, due to the background counts which is not subtracted in the plotted data. The data shows a periodic interference visibility which is exponentially decaying as the relative delay path is changed.

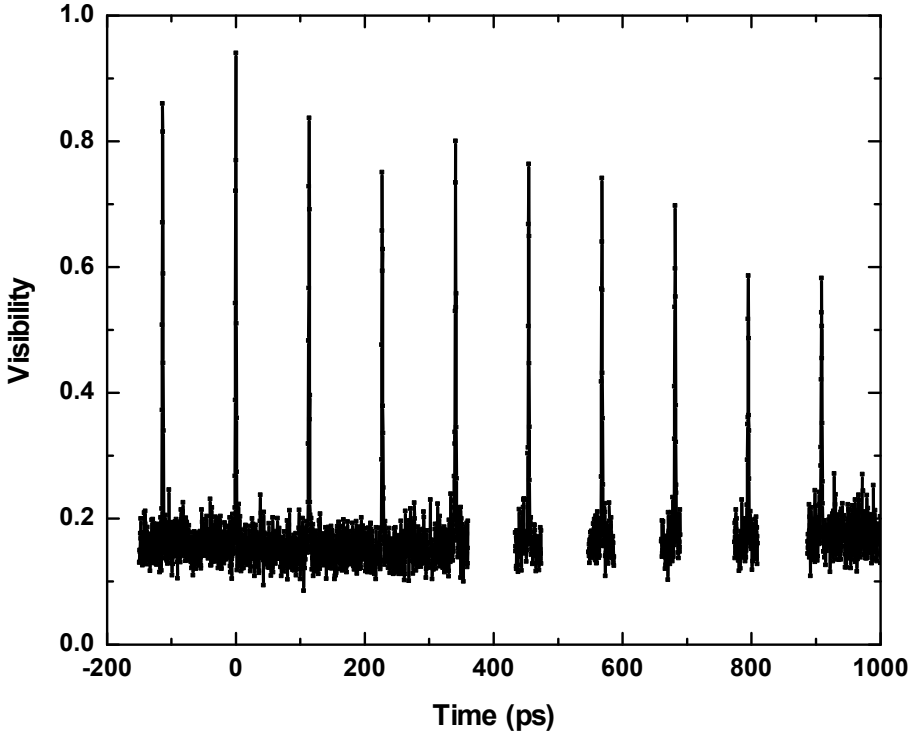

Figure 4.12: First-order interference visibility of heralded single photons measured using the Michelson interferometer as seen in Fig. 4.11. The y-axis is the visibility calculated using Eq. 4.18, and the x-axis is the relative time difference between the two interferometer paths given by $\Delta L/c$. The peaks are separated by 1/FSR $\sim$ 115 ps of the cavity. The envelope decays with lifetime of $\sim$ 1 ns corresponding to the lifetime of the cavity. The decay is modulated with $\sim$ 3 GHz oscillation, this is due to the higher order modes as seen in Fig. 4.8.

There exist two characteristic coherence times in the data, 0.93 ps decay time of individual narrow peaks and a long decay of $\sim$ 1 ns. The coherence time of the narrow peaks corresponds to the inverse of the down-conversion bandwidth (538 GHz), which is consistent with the our earlier prediction of 540 GHz. The long coherence time of 1

ns corresponds to the coherence time of the individual cavity modes. In other words, it gives the spectral width of the individual cavity modes. The peaks are separated by ~ 115 ps, which corresponds to the inverse of the free-spectral range of the cavity. Figure 4.13 is the zoomed-in data from the central peak near $\Delta L = 0$ fitted with a double sided exponential decay.

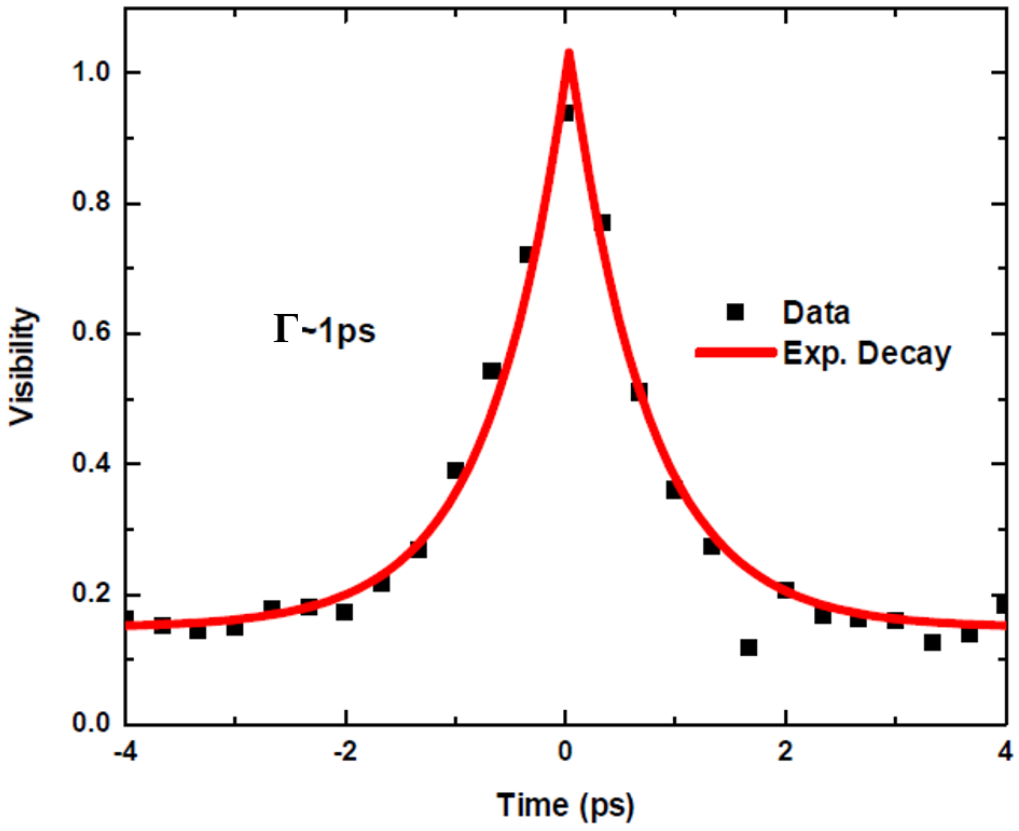

Figure 4.13: Zoomed-in interference visibility data centered at $\Delta L = 0$ obtained with measurements done with heralded signal photons. The data is fitted with exponential decays.

Similarly, we performed time-tagged photon counting measurements of the signal photons. The measurement is done by syncing the electrical pulse generated by the pulsed laser and recording the relative emission time of the down-converted photons

detected by a single-photon detector and an electronic counter [113]. Figure 4.14 (a) is the experimental data of the time emission histogram of the signal photons and the red solid line is an exponential fit to the data. Similar to the first order coherence measurements, there exist two characteristic times in the data, individual narrow peaks separated by 115 ps and a long decay time of 840 ps. The long decay time corresponds to the cavity lifetime, which is mapped to the down-converted photons. The oscillation with a period of 115 ps corresponds to the temporal beating between different frequency components of the cavity modes. The width of the individual peaks is given by the inverse of the down-conversion bandwidth. Individual peak widths in Fig. 4.14 (a) are detector resolution limited. The timing jitter of the detectors used in this thesis are plotted in 4.14 (c). See ref [114] for details about the superconducting nanowire detectors used in the study as single-photon detectors.

Figure 4.14(d) shows the fast Fourier transformation (FFT) power spectrum density of the residual to the exponential fit to the data. To extract the exact power distribution between different modes, the FFT needs to be take for the whole data instead of the residual. As, the FFT of the whole data masks the peaks making them less prominent, we have plotted the residual of the fit. The dash red lines corresponds to the frequency components centered at 3.1 GHz and 8.77 GHz.

The detailed mode analysis for a confocal cavity formed with finite length crystals requires a full treatment of boundary conditions with Maxwell equations and is beyond the scope of this section. However, some insights into the mode structure can be obtained by following Boyd and Kogelnik's calculation of resonant frequencies for a confocal cavity built with two spherical mirrors. For such a cavity, the FSR is given by [115, 116]

$$\begin{aligned} f &= \pi^{-1} cos^{-1}[(1-\frac{L}{b_1})(1-\frac{L}{b_2})]^{\frac{1}{2}} \\ \text{FSR} &= \frac{c}{2L}[q+(1+m+n)f] \end{aligned} \tag{4.19}$$

where q is the longitudinal mode number, m, n are transverse mode numbers that can take $0, 1, 2, ..$ values, L is the distance between the two mirrors, and b_1 and b_2 are curvatures of the cavity mirrors. In our case $b_1 \rangle \infty$ and $b_2 = 19.3$ mm. The measured 8.77 GHz peak in 4.14 corresponds to the temporal beating between the TEM_{000} FSR modes of the cavity, and the 3.1 GHz peak corresponds to the higher order cavity modes $\text{TEM}_{q\neq 0, n\neq 0, m\neq 0}$. The separation between the modes is given by [115, 116]

$$\delta\nu_{\Delta(m+n)} = \frac{c}{2L}[f\Delta(m+n)] \tag{4.20}$$

The $\text{TEM}_{n\neq 0, m\neq 0}$ modes can be seen in the high resolution spectrum plotted in Fig. 4.8, where the higher order mode is separated by ~ 3 GHz from the TEM_{000} mode. The cavity emission is primarily dominated by the TEM_{000} modes. The power ratio between different modes heavily depends on the pump alignment to the cavity-SPDC and varies from experiment to experiment.

Without a cavity, the down-conversion would have happened within the excitation laser pulse time, which is 50 ps in the experiment. As per the design, the cavity lifetime is close to the typical excited state lifetime of InAs/GaAs quantum dots. The cavity lifetime can be tuned from 800 ps to 1.2 ns by changing the cavity length. The reported lifetime in this measurement is lower (840 ps) than the rest of the measurements ($\sim$ 1.06 ns). This is due to the reduction in the cavity length to shorten the SPDC lifetime, so that it matches with the typical QDs.

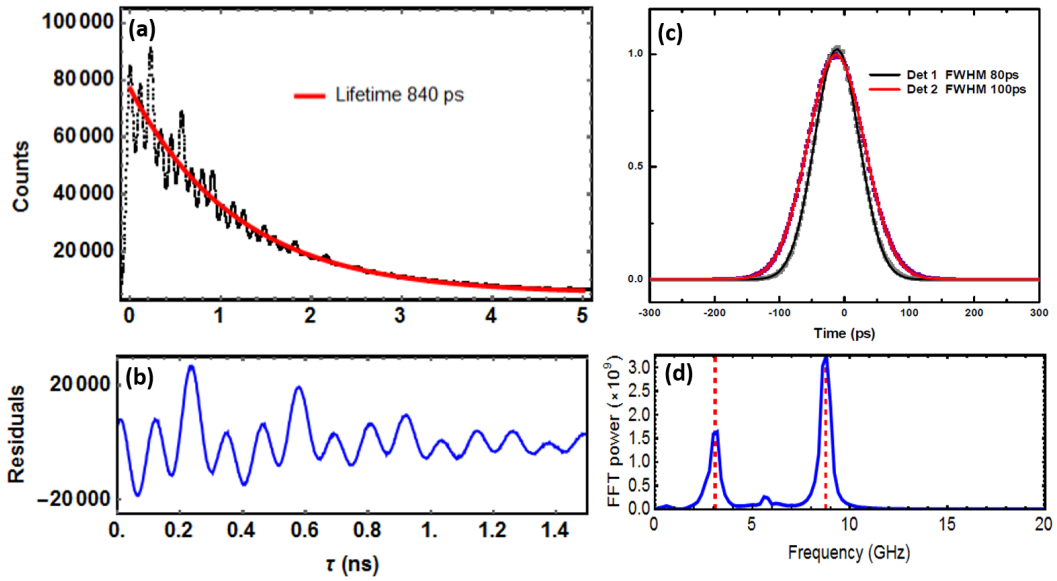

Figure 4.14: (a) Time emission of the signal photons with a exponential fit (b) Residue of the fit zoomed. (c) Instrument response function (IRF) of the detectors and the time-tagged electronic. The detector response is measured with a 2 ps pulses MIRA laser, beside this all the measurements are done with the Tsunami laser. The solid lines are Gaussian fits to the data. The detectors used in the study have 80 ps and 100 ps timing jitter resolution. (d) Fast Fourier transformation (FFT) power spectrum density of the residual to the fit. The dash red lines show peaks centered at 3.1 GHz and 8.77 GHz. The 8.77 GHz peak corresponds to the FSR of the cavity for TEM_{00} modes, the 3.1 GHz peak corresponds to the higher order cavity modes $TEM_{n\neq 0,m\neq 0}$[116]

4.2.2 Intensity Correlation of the Down-converted Photons

Second-order intensity correlation measurement is an important experimental technique that will be exploited frequently through out the thesis. With the in-

tensity correlation measurement, we can infer the second-order temporal coherence of the down-converted fields. In addition, it allows us to measure the relative emission time between the signal and idler photons with a very high precision that otherwise is not accessible through the previous measurements. For a quantized field, the intensity correlation between the signal and idler photons can be defined mathematically as

$$G^{(2)}_{s,i}(\tau) = \frac{\langle \psi_{s,i}|E^-_i(t)E^-_s(t+\tau)E^+_s(t+\tau)E^+_i(t)|\psi_{s,i}\rangle}{\langle \psi_{s,i}|E^-_i(t)E^+_s(t)|\psi_{s,i}\rangle^2} \tag{4.21}$$

where $|\psi_{s,i}\rangle$ is the bi-photon wavefunction of the cavity-SPDC fields given by Eq. 3.35 and $E^-_{s,i}(t)$ are an electric field operators of the detection event for the signal and idler photons, given in Chapter 3.

Scholz *et al.* [117] derived the second-order intensity correlation between the signal and idler photons with different cavity parameters for the signal and idler photons. The intensity correlation function becomes [117, 109],

$$G^{(2)}_{s,i}(\tau) \propto \begin{cases} |\sum_{m_s,m_i} \frac{\sqrt{\gamma_s\gamma_i\omega_s\omega_i}}{\Gamma_s+\Gamma_i} e^{-2\pi\Gamma_s(\tau-\tau_0/2)} sinc[i\pi\tau_0\Gamma_s]|^2 & \tau \geq \frac{\tau_0}{2} \\ |\sum_{m_s,m_i} \frac{\sqrt{\gamma_s\gamma_i\omega_s\omega_i}}{\Gamma_s+\Gamma_i} e^{+2\pi\Gamma_I(\tau-\tau_0/2)} sinc[i\pi\tau_0\Gamma_i]|^2 & \tau < \frac{\tau_0}{2} \end{cases} \tag{4.22}$$

where $\Gamma_i = \gamma_i/2 + im_i\Omega_i$, $m_i \in \mathbb{N}$ and Ω_i is the FSR of the fields with i representing signal and idler fields. As evident from these equations, the correlation function decays exponentially where the decay rate is given by the inverse of the cavity lifetime. The exponential decay oscillates with the FSR of the cavity.

We measure the second-order temporal coherence of the cavity-SPDC fields using two fast detectors and an electronic counter (Hydraharp). Photons emitted from the cavity setup are sent through the polarization beam splitter and are collected in two single-mode fibers. The electronic counter stores the absolute detection times

between the two detectors and the data is stored in the computer. Using a custom written MatLab code, the data is analyzed in real time. A histogram of relative time differences between the detection events for signal and idler photons is build and plotted, as seen in Fig. 4.16 [113].

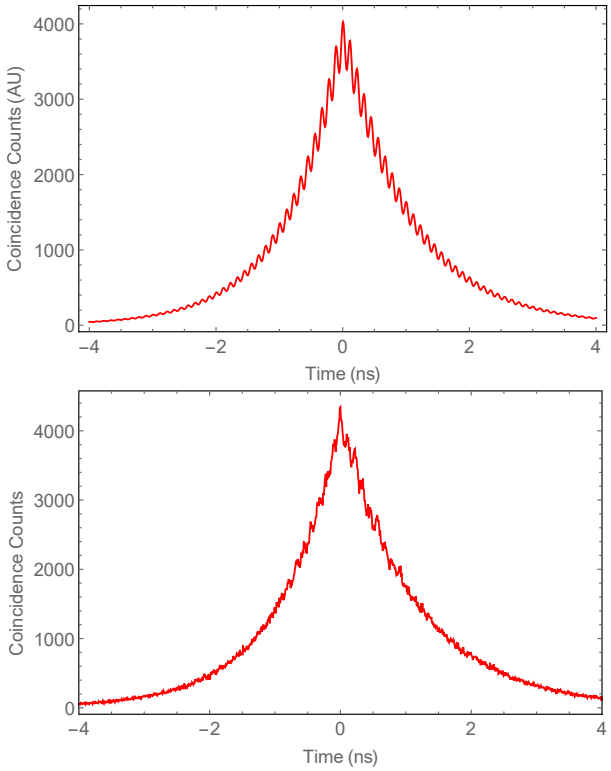

Figure 4.15: (Top). Theoretical plot of the intensity correlation between the signal and idler photons calculated using Eq. 4.22 for the designed cavity parameter of $\Omega \sim 9$ GHz and $\Gamma_s = 150$ MHz and $\Gamma_i = 180$ MHz. (Bottom) Experimental plot of the intensity correlation between the signal and idler photons measured using two fast single-photon detectors. The saw-tooth oscillation is due to the beating between different FSR modes of the cavities as predicted by Eq.4.22, which is visible in the measured data.

The measured intensity correlation between the signal and idler as seen in Eq.

4.16 (bottom) is well explained by the theoretical description given in Eq. 4.22. The theoretical fit is obtained with the designed cavity parameter given in the Table 4.1. Consistent with the previous measurements, the envelop of the signal and idler photons decay with rate of $\sim$ 150 MHz. The lifetime of the cavity is given by $(2\pi 150\text{MHz})^{-1}$, which give 1.06 ns. There exists additional feature in the decay profile that are separated by the FSR of the cavity, which is $\sim$ 9 GHz, consistent with the previous measurements. As the individual peak widths are the convolution of the real width with the detector timing resolution, the theoretical prediction given in Fig. 4.16 (top) is convolved with the IRF given in Fig. 4.14(d).

In order to achieve single-mode operation, a 650 GHz FSR with 5 GHz bandwidth etalon is placed before the polarizing beam-splitter. The etalon is pre-aligned using the fundamental beam. When the signal and idler photons are degenerated in wavelength within 5 GHz of the fundamental wavelength, the photons pass through the etalon, resulting in single mode operation. Figure 4.16 (c, d) is an intensity correlation measurement between the signal and idler photons after an additional spectral filter is introduced in the setup. Figure 4.16 (a, b) is an intensity correlation measurement without any spectral filtering and the Fourier transformation of the correlation data plotted for comparisons. The peak at $\sim$ 9 GHz corresponds to the FSR of the cavity. Unlike in the unfiltered spectrum, the frequency components disappear for the filtered case as seen in Fig. 4.16 (d), indicating a single-mode operation.

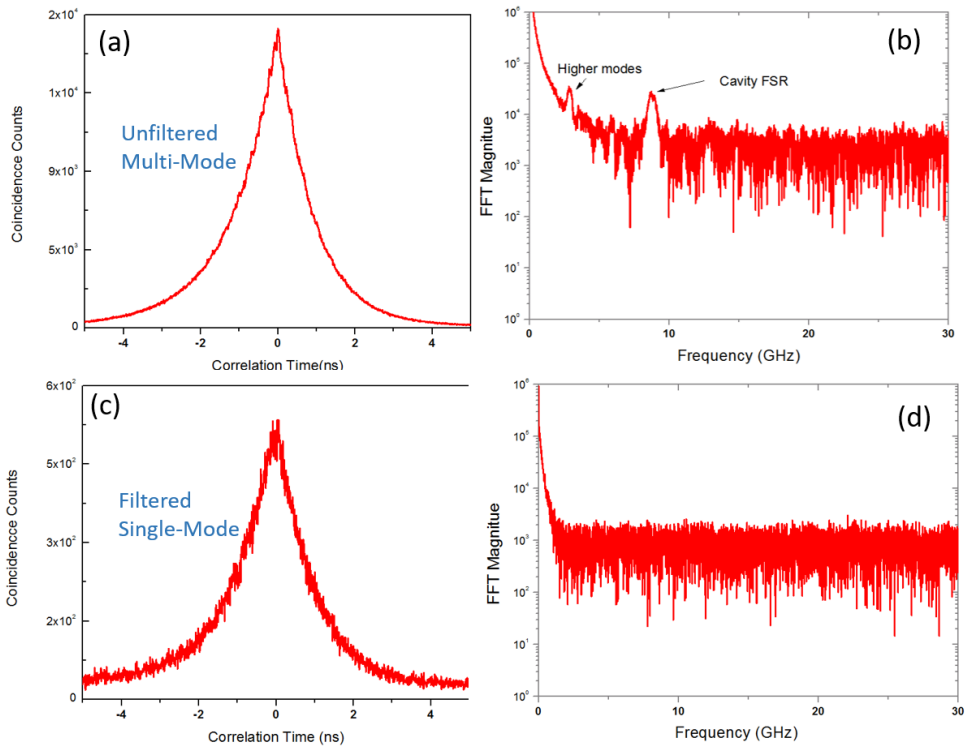

Figure 4.16: (a) Intensity correlation between the signal and idler photons for an un-filtered case. (b) A semi-log plot of power spectrum density of the Fourier transformation of the intensity correlation data for the un-filtered case. The peak at around 9 GHz corresponds to the FSR of the cavity. The additional peak is due to the higher order transverse modes of the cavity [115, 116]. The additional peak can be reduced or completely eliminated in some measurements though additional realignment. (c) Intensity correlation between the signal and idler photons for the filtered case. (d) A semi-log plot of power spectrum density of the Fourier transformation of the intensity correlation data for the filtered case. Lack of any additional peaks in the Fourier transformation of the intensity correlation data indicates that the the additional frequency modes are suppressed and the detected photons are single-mode in nature.

Here, the expression single-mode operation does not correspond to a true single mode in frequency but one mode (peak) of the cavity field out of many FSR modes. This filtering process selects 1 mode out of many (passive filtering) and results in the loss of photon counts. In many other previous cavity-SPDC setups, the fundamental/pump beam is quasi-CW. As the signal and idler photons have different free-spectral ranges only a few cavity modes satisfy the energy conservation. However, in our case, the original design of the experiment was to perform quantum teleportation measurement between the SPDC and QD [118]. The successful transfer of information from the SPDC photons to the QD spin requires one to perform two-photon interference measurement for which the perfect temporal overlap between the SPDC and QD photons is required. Once the photons are successfully interfered in the beam splitter, verification of the faithful transfer of the quantum state to the QD is done by reading the spin-state of the QD electron. Such an experiment requires a well-defined emission timing from the down-conversion process. However, the down-conversion process is probabilistic and accurate timing information of the down-converted photons can not be known within the pump pulse width. To address the problem, the experiment was designed with a narrow pulse width, which means more cavity modes satisfy the energy conservation requirement. One can circumvent such timing limitations by post-processing the data, i.e. by binning the heralded time information and discarding the data where heralded photons falls outside the QD's pulse width. However, such post-processing causes reduction in the usable photon counts.

4.2.3 Pair-Product Rate

When the cavity-spdc is operated under a low power, the pair generation rate (measured as the coincidence counts) should be linear in the pump power. The blue points in Fig. 4.17 are the measured coincidence counts as a function of pump power.

The data is fitted with a linear equation (red curve). The experimental data confirms that we are operating at the linear cavity regime. With further alignment, higher count rates were achieved. The plotted coincidence rate is integrated across the whole down-conversion bandwidth which is 540 GHz in our case, and is collected with 60% detector efficiency. The data was taken with a 70:30 non-polarizing beam splitter in the collection path, which reduces the coincidence rate further. With further alignment, we were able to obtained a maximum raw counts of 400,000/sec/channel and 40,000 coincidence counts/sec when pumped with a 5mW blue light. This results in ~ 80 pairs $s^{-1}mW^{-1}(150MHz)^{-1}$ collection for single-mode fibers without correcting for the detector efficiency. This does not account the loss in the collection setup. In addition, as the down-converted photons are collected in a single-mode fiber, not all the emitted modes are collected, which results in further drop in the heralding rate.

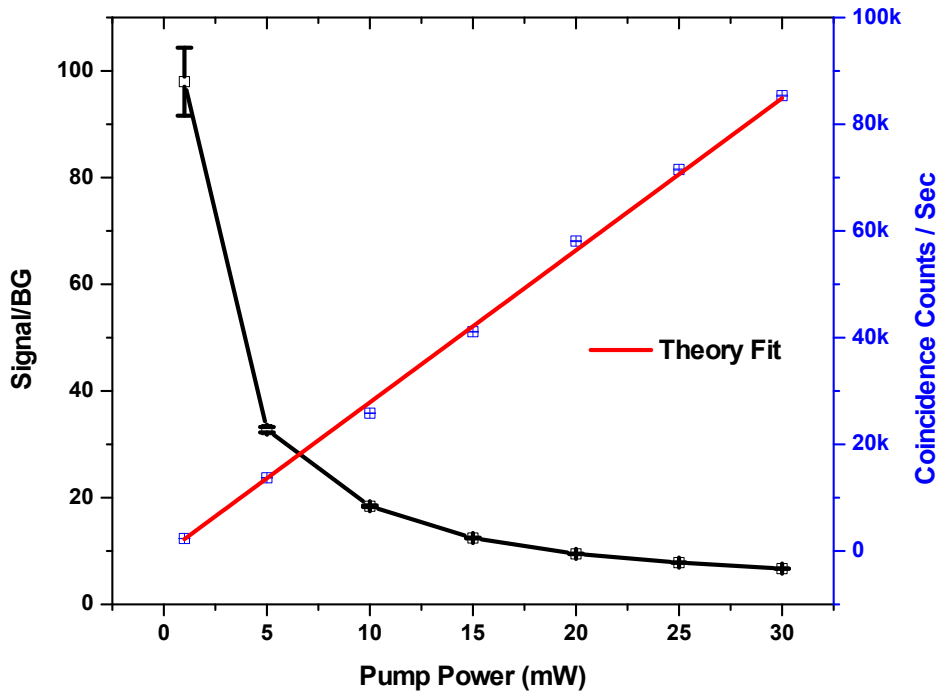

Figure 4.17: Signal to background ratio (black) and coincidence counts (blue) as a function of second harmonic pump power. As theoretically predicated in Ch 3 (see Eq. 3.19) the signal size grows linearly with the pump power. The red line is a linear fit to the experimental data.

The pair production happens at the same shot of the experiment, as a result the coincidence counts about $\tau = 0$ is finite, whereas is close to zero between two different shots (such accidental/uncorrelated coincidence counts will be referred to as background). Background light and detector dark counts contribute to the accidental coincidence counts. However, as we increase the pump power, multipare emission process becomes equally dominated in the experiment and the long decay tail of the pump beam causes an additional down-conversion to happen at longer time delay. The black points in Fig. 4.17 are the measured signal-to-background ratio for coincidence

counts as a function of pump power. The signal is defined as the integrated counts measured within the same shot of the pulse by both detectors, whereas the background is the accidental counts. The accidental counts is measured by looking for events when a detector fires at shot 0 of the pulse and the second detector fires at shot 1. We obtain as high as 100:1 signal-to-background ratio for low pump power. The ratio drops significantly for higher pump powers. However as the heralded $g^{(2)}$ also goes above the quantum limit for high powers, the interest region is limited to the lower power.

4.2.4 Photon Statistics of the Heralded Field

To generate pairs of single photons with very low higher pair generation rate, it is important to pump the cavity with low power. When the cavity is pumped with high enough power, the field generation rate and the leak rate balance out, forming an optical-parametric-oscillation (OPO). The photons emitted by an OPO source has a Poissonian statistics [119]. Here we are interested in investigating the heralded field's statistics when operated far below the threshold. When the system is pumped with low power, as solved in Eq. 3.12, the state of the down-converted photons can be expanded perturbatively in the number basis as [98]

$$|\psi\rangle \approx (1 - |\eta|^2/2)|0\rangle + \eta|1_S, 1_I\rangle + \eta^2|2_S, 2_I\rangle + \eta^3|3_S, 3_I\rangle + ... \tag{4.23}$$

where η is the coupling parameter proportional to the product of $\chi^{(2)}$ and the pump amplitude (b). As discussed in the earlier chapter, the state-vector $|n_S, n_I\rangle$ represents a state containing n signal and idler fields summed over multi-mode frequency, spatial and polarization degrees of freedom. The non-linear interaction causes a small fraction of the pump field to spontaneously convert into a pair of photons, where the emission process is random. The emitted pairs are chaotic in nature, resulting in thermal

photon statistics for the individual signal and idler modes [120]. As we are interested in a single-photon source, by detecting an idler photon in one port of the polarizing beam splitter using a single-photon detector, a single photon state can be heralded in the other port of the beam splitter. The heralded state can be expressed as,

$$\psi_{Heralded} = \langle 1_I|\psi\rangle \propto (1-|\eta|^2/2)\langle 1_I|0\rangle + \eta\langle 1_I|1_S,1_I\rangle + \eta^2\langle 1_I|2_S,2_I\rangle + \eta^3\langle 1_I|3_S,3_I\rangle + ...$$
$$\psi_{Heralded} \propto \eta|1_S\rangle \tag{4.24}$$

This ideal state results in a perfectly anti-bunched source [121], $g^{(2)}(0) = 0$. Such a heralding process assumes the photon detector is a number resolving detector. However, most commercially available detectors operator in a Geiger counter mode and can not resolve the photon numbers. This results in a more complicated state for the heralded photon,

$$\psi_{Herladed} = \eta|1_S\rangle + \eta^2|2_S\rangle + \eta^3|3_I\rangle + ... \tag{4.25}$$

which results in $g^{(2)}(0) > 0$, making the SPDC source far from an ideal Fock state generator. However, the higher-order pair production can be suppressed by operated the system at a small η regime ($\ll 1$). This results in the heralded photon to be an approximate single-photon state. One important distinction of such a state from a weak coherent state is that the vacuum component is removed and one can use it to obtain a "on-demand" single-photon source (within the lifetime of the photon packet).

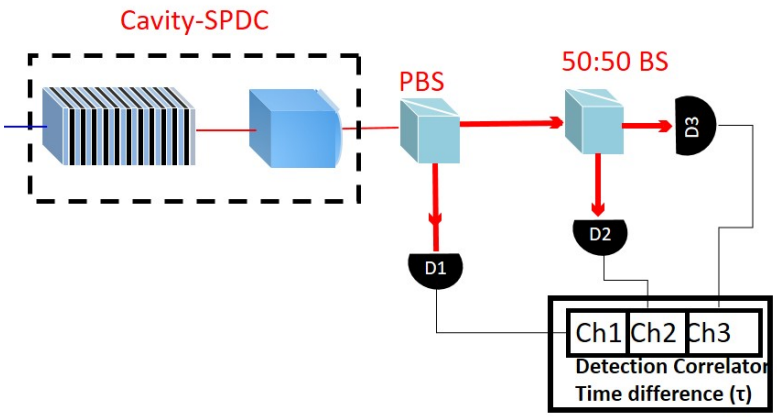

Figure 4.18: Experimental setup for three photon correlation measurements

To study the photon statistics of the heralded signal, we performed a three-detector intensity correlation measurement. The emitted signal and idler photons are sent through a polarizing beam-splitter. The idler photon is immediately collected in a single-mode fiber, whereas the signal photon is sent through a 50:50 non-polarizing beam splitter and is collected with two single-mode fibers. The output of the fibers are measured using two superconducting nanowire detectors and a tau-spad detector. The absolute detection time for all detectors is recorded using fast time-tagged electronics (Hydraharp). An schematic of the experimental setup is given in Fig. 4.18.

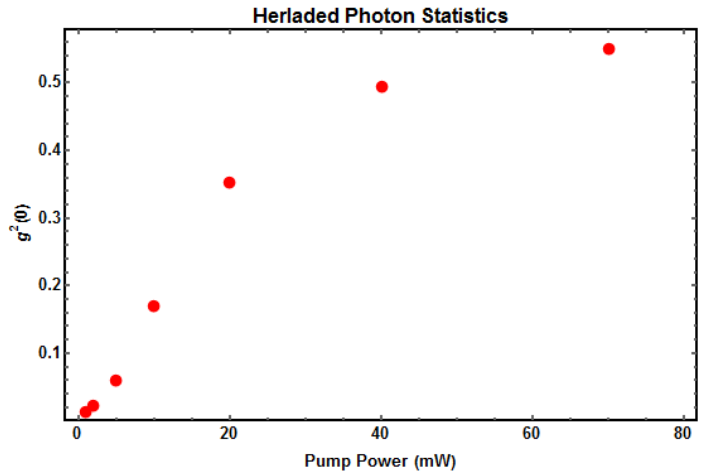

Figure 4.19: Photon statistics of a Heralded signal photon as a function of pump power.

The collected data is analyzed by first searching for events in the idler detector. If a detection event is found, then we look for activities in the other two detectors within a few nanoseconds time window. If the source emits a single pair of signal and idler photons, the probability of all three detectors firing simultaneously goes to zero. The total counts of all three detectors firing (counts_{123}) is recorded as a function of the pump power. The recorded number is meaningless unless it is properly normalized. The data can be normalized by dividing by the joint detections events between Detectors 1-2 (counts_{12}) and 1-3 (counts_{13}) and scaling with the total heralding photons (counts_{1}). With this, the normalized $g^{(2)}(|\tau| < 3\text{ns})$ of the heralded signal photon becomes [121],

$$g^{(2)}(|\tau| < 3\text{ns}) = \frac{counts_{123} \times counts_1}{counts_{12} \times counts_{13}} \tag{4.26}$$

We performed several three-detector correlation measurements by varying the pump power. As evident from Eq. 4.25, increasing the pump power causes the multi-pair emission rate to increase. This results in a reduced $g^{(2)}$ value. The experimental data of heralded $g^{(2)}$ measurements as a function of pump power is plotted in Fig. 4.19.

For reasonably high pump power, we can still obtain $g^{(2)} < 0.5$, below the classical limit.

4.3 Chapter Summary

In this chapter, we gave a detailed explanation of the cavity-SPDC setup and demonstrated the successful implementation of such a system in our laboratory. We performed a thorough spectral and temporal characterization of the cavity-SPDC photons and compared the experimental data with the theoretical predictions. We showed that the implemented cavity-SPDC source is capable of emitting heralded single photons with $g^{(2)} \ll 0.5$, making it a bright multi-mode single-photon source. Through the use of additional filtering, we obtained single mode operation from the setup that matches the properties of the quantum dot photons.

CHAPTER V

Optical Properties of InAs Quantum Dots

Gallium arsenide (GaAs) is a III-V zinc blende semiconductor material with a direct band gap of 1.424 eV at room temperature [122]. GaAs is a versatile semiconductor material that is used for a wide range of applications. The direct bandgap allows the material to be optically manipulated. This makes it a good candidate for solar cell applications. For high frequency electronic applications, GaAs is superior over silicon due to its higher electronic mobility, low sensitivity to heating and creates lower noise at high frequencies [123].

Type III-V materials provide a wide selection of elements for alloying purpose. Alloying allows one to tune the lattice constant and band gap, which is important for growing heterostructures and designing materials for particular applications, e.g. solar cells and light-emitting diodes (LED). Since indium arsenide (InAs) and GaAs have the same crystal structure but different lattice constants, by growing them together on top of each other one can grow thin films or semiconductor nanostructures, such as quantum dots (QDs) through the Stranski-Krastanov growth method. Conversely, as the lattice constants for GaAs and aluminum arsenide (AlAs) are the same but the band gap is different, one can grow relatively complicated heterostructures to exploit difference in the band gap without having to worry about the lattice mismatch. This ability will be of importance to grow a distributed Bragg reflector (DBR)

structure, such as the one in our sample.

5.1 Confinement in Semiconductor Material, Sample Structure and Electronic Properties

The quantum dots studied in this thesis are nanoscopic pancake-shaped structures with dimensions of approximately 20 nm base radius and 3 nm height formed with Stranski-Kranstanov-grown GaAs and InAs semiconductor materials. Molecular beam epitaxy allows atomically thin layers of material to be grown on top of a substrate. GaAs and InAs are type III-IV semiconductor with similar properties but with a small lattice constant mismatch of 7%. When a thin layer of InAs is deposited on top of a GaAs surface, the lattice mismatch between the two materials causes strain to build up on the surface. After a critical thickness, the material self assembles on top of the thin InAs layer (also referred to as the wetting layer) to form small island-like structures. The radius of the nanostructure can be altered by changing the growth parameters. The nano-structures are capped with layers of epitaxially-grown GaAs that can form an electronic barrier, resulting in zero-dimensional (0D) structures. Similar to an optically active bulk semiconductor, pairs of electron-holes can be excited to the conduction band of these nanostructures. If the Coulomb attraction between the excited electron and hole is stronger than the thermal energy, they form a bound state acting as a quasi-particle. Such quasi-particles are referred to as excitons.

If the size of nanostructure is comparable to the Bohr radius of a single exciton, the available density of states for excitons to occupy in the nanostructure gets modified, forming discrete atomic-like energy levels. Such 0D confined nanostructures are referred to as quantum dots (QDs). In a single QD, the optically excited exciton wavefunction is confined within a few lattice sites, in contrast to a bulk material where it

is spread out across numerous sites. Such a localization of the excitonic wavefunction results in suppression of most of the many-body effects[1], making it close to an isolated atom-like structure. The total energy of such bound excitons can be calculated with the following equation,

$$E_{\mathbf{total}} = E_{\mathbf{bandgap}} + E_{\mathbf{confinement}} + E_{\mathbf{exciton}} + E_{\mathbf{strain}} \tag{5.1}$$

where the total energy of the system is the sum of various factors as written in the subscripts. The band gap energies of bulk InAs and GaAs at room temperature are 0.35 eV and 1.42 eV respectively. The 3D confinement of the nanostructure can be loosely modeled as a particle in a box (though it is by no means a complete explanation), with energy given by the size of the box. Similarly, the binding energy can be calculated by modeling the exciton as a Rydberg-like system. With these assumptions, we can estimate the confinement and binding energy as

$$\begin{aligned} E_{\mathbf{confinement}} &= \frac{\hbar^2 \pi^2}{2\mu a^2} \\ E_{\mathbf{exciton}} &= -\frac{\mu R_y}{\epsilon_r^2 m_e} \end{aligned} \tag{5.2}$$

where a is the radius, μ is the reduced mass given by the electron (m_e) and hole (m_h) masses, ϵ_r is the dielectric constant, and R_y is the Rydberg energy. As Eq. 5.2 suggests, the total energy of the exciton increases as the confinement size decreases. This allows tuning of the emission energy for commercially applications that use the nanostructure as lighting material.

In this thesis, we will be studying isolated single QDs formed with InAs/GaAs materials as a source of single photons and spin qubit systems for the purpose of quantum information science. The InAs QDs are embedded in the GaAs host material,

[1] A single exciton sits in a host material with $\sim 10^5$ atoms which have non-zero nuclear spin values. This results in many interesting dynamics between the single exciton and nuclei, making the system much more complex and richer than stated here.

with the emission energy of the QDs centered at around 1.32 eV (920-970 nm).

5.1.1 Sample Structure

Due to a large index mismatch between the top GaAs layer and the air surface, a large fraction of the light emitted by a QD is lost inside the structure. To overcome this problem, the QDs are grown inside an asymmetric optical cavity that modifies the directional emission of the light generated inside the cavity, while enhancing the field emission rate. The asymmetric cavity is formed with alternative layers of AlAs and GaAs materials that have indices of refraction of 3.66 and 2.96 respectively. Such alternating layers of materials with different indices of refraction form a distributed Bragg reflector (DBR) that can act as a highly reflecting surfaces. An optical cavity can be formed by growing DBR structures at the front and back of the sample. The reflectivity of the DBR "mirrors" can be modified by modifying the thickness and the number of material layers.

The sample used in this study has an asymmetric DBR cavity designed such that the photons from the QDs are emitted preferentially from the front end of the sample. The bottom part of the sample consists of 10 periods of AlAs and GaAs alternate layers with 82 nm and 69 nm thicknesses respectively, grown on top of an n-doped GaAs substrate. The top part consists of 4 periods of AlAs/GaAs layers. The cavity is 10.6 nm in width centered around 950 nm. This results in the DBR cavity operating at a weak cavity-limit with a Q-factor of around 90[2].

As derived in the cavity-SPDC case in the previous chapter, the enhancement in the count rate due to the DBR structure is approximately the finesse of the cavity [124]. In addition, the bottom DBR reflects more light, giving two times more counts that the Schottky diode samples that were studied by the previous generation of students. Overall, the DBR sample design should yield roughly 200X photons collections

[2]This number is based on reflectivity measurements performed by Aaron Ross on a different sample from the same wafer. The measurement is made at 6K.

that the Schottky sample, which is consistent with the experimental data. For details on collection efficiency and maximum sample brighness for QDs, see Ref. [125].

The sample structure used in this thesis study is given in Fig. 5.1.

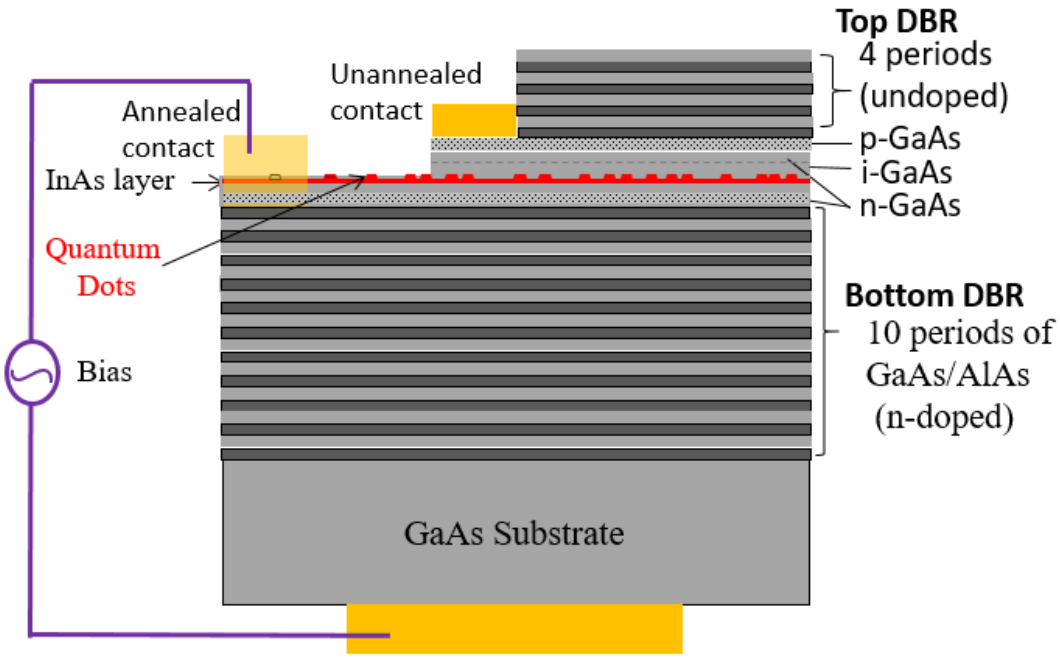

Figure 5.1: Schematic of the DBR sample structure with embedded QD nanostructures used in this thesis.

A single exciton inside a QD can be charged with an additional electron or a hole by embedding the sample in a diode structure. When a bias is applied on the diode, it raises the Fermi level of the QD, allowing an additional electron (e) or hole (h) to tunnel into the QD, forming a three-particle state (1-eh pair + 1-e or 1-eh pair + 1-h), also referred to as a trion state. Coulomb interactions between electrons allow only a single exciton or a single trion to be trapped inside a single QD. This phenomena is known as Coulomb blockade and is used to deterministically form a single charged

state inside a single QD [126, 127]. For selective charging of a single QD to form a trion state, a PIN-diode structure is formed in the sample by using the p- and n-dopped layers of GaAs around the wetting layer. In addition to charging a single QD by applying a bias voltage, the transition energy of the QDs can be Stark-shifted by several wave numbers. Also, Stark shift allows voltage modulation spectroscopy to be performed with single QDs [128].

We studied several generations of QD samples, transitioning from a Schottky diode to a delta-doped DBR structure to a PIN-junction structure and eventually converging to the current PIN sample with the DBR structures, each had its own strength and weakness. The Schottky diode samples had excellent optical and electronic properties and were used extensively by the previous generation of students that ultimate lead to the demonstration of the spin-photon entanglement [43]. However, for performing two-photon interference measurements and the proposed teleportation experiment, the sample suffered from low collection efficiency. This was caused by a large total internal refraction due to the index of refraction mismatch between the GaAs layers and the air surface. In addition, a semi-transparent titanium surface fabricated on top of the GaAs surface for applying a bias voltage accross the sample result in a further loss in the photon count.

The collection efficiency was enhanced by embedding the QD sample inside a DBR structure. With a δ-doped DBR structure, we were able to get photon counts 10 times larger than the Schottky sample. However, the sample was limited by several issues. Due to probabilistic charging of QD from the δ-doped surface, we had to rely on luck to find a trion state, which was labor intensive–often most of the experiment time was taken away finding a suitable state to study. Despite their bright emission rate, the majority of the QDs found through non-resonant excitation (photoluminescence) were not optically active when addressed resonantly. In addition, the QDs suffered from large spectral dephasing, resulting in linewidths of single excitons to be 10-40 times

larger than their Fourier limited linewidths. The broadening was suspected to be caused by spectral wandering due to trap states surrounding the dots. We were able to reduce the spectral wandering of QD transitions by applying a weak 532 nm He:Ne laser to the sample in addition to the resonant laser. However, the lines remained several GHz at best even with the He:Ne laser. We also studied several generations of PIN-diode structures that suffered from multiple issues. Some were dimmer than the Schottky sample, some couldn't trap an additional electron to form a charged trion state, other had too large or too small of a Stark shifts, making it hard to find a trion state. The PIN-diode sample with DBR structure suffered from slow transition frequency wandering on the order of several GHz within a few second time window. This was suspected due to be due to charge trapping inside the DBR layers, as a bias is applied across the sample. The investigation of these various samples lead to a better understanding of various sample designs, identifying each structure's weakness and strength, ultimately leading to a design and growth of sample that solved most of the issues.

After studying almost 10 samples, we converged on the sample described above that solved most of the previous issues and yet is capable of emitting a bright photon count rate. The brightness is increased by forming a single sided DBR structure and removing the semi-transparent titanium surface. The unwanted charge trapping issues that caused spectral wandering is resolved by forming contacts above (below) the bottom (top) layers of the DBR structures such that the bias is applied only through the few layers with embedded QDs, excluding the DBR layers (see Fig. 5.1). The QDs are embedded inside the two intrinsic layers of GaAs in order to reduce the effective electric field seen by the dots. This solved the problem of dots seeing too large electric field, causing unstable charge behavior. With the additional intrinsic layers, negatively charged trion states can be found within a 500-800 mV bias voltage range.

The samples used in this thesis are grown and generously provided to us by Dan Gammon and Allan Bracker from the Naval Research Laboratory (NRL). We are very grateful for their continuous support and collaboration with our laboratory.

5.1.2 Trion Optical Dipole Selection Rules

Even though QDs have millions of atoms, since the crystal structure is periodic, we can approximate the wavefunction of the exciton with the slowly varying part of the lattice wavefunction, also referred to as the envelope function. This is given by Bloch's theorem [122]. The exciton's envelope solutions are hydrogen atom-like. However, it is important to note that, unlike a hydrogen atom, an exciton in a semiconductor is the excited state of the QD crystal. The optical selection rules for an exciton can be calculated with the knowledge of the angular momentum part of the excitonic wavefunction. However, unlike atomic states, an exciton in the QD exhibits a discrete rotational symmetries given by the crystal's point group, thus lacks a 3D rotational symmetry. As rotational symmetry gives rise to the law of conservation of the angular momentum. Such lack of 3D rotation symmetry in a QD makes angular momentum not to be a "good" quantum number to describe the wavefunction of the system. Nonetheless, at gamma points ($\vec{k} = 0$), the electron in the conduction band and the holes in the valance bands can be approximated by the orbitals of the atomic states. With this information, the wavefunction of the electrons in the conduction band and the holes in the valence band can be approximated to be s-like ($L = 0$) and p-like ($L = 1$) respectively. Once the angular momentum of the electron and hole states are determined, we can calculate the optical selection rules for excitons using the Wigner-Eckart theorem. The optical selection rules for a neutral exciton and trion state have been discussed extensively in the previous lab members' theses [113, 118]. Here, we will give a brief summary of the relevant results without going into the theoretical details.

A trion state can be generated inside a single QD by optically exciting an exciton while simultaneously biasing the sample. When operated in an appropriate bias region, a single electron can be tunneled inside the QD, forming a negatively charged trion state. At zero magnetic field, a trion state forms two degenerate two-level systems. The transition energy levels and selection rules for a single trion state at zero magnetic field are given in Fig. 5.2. The box with dash-lines encloses the energy levels of a trion state.

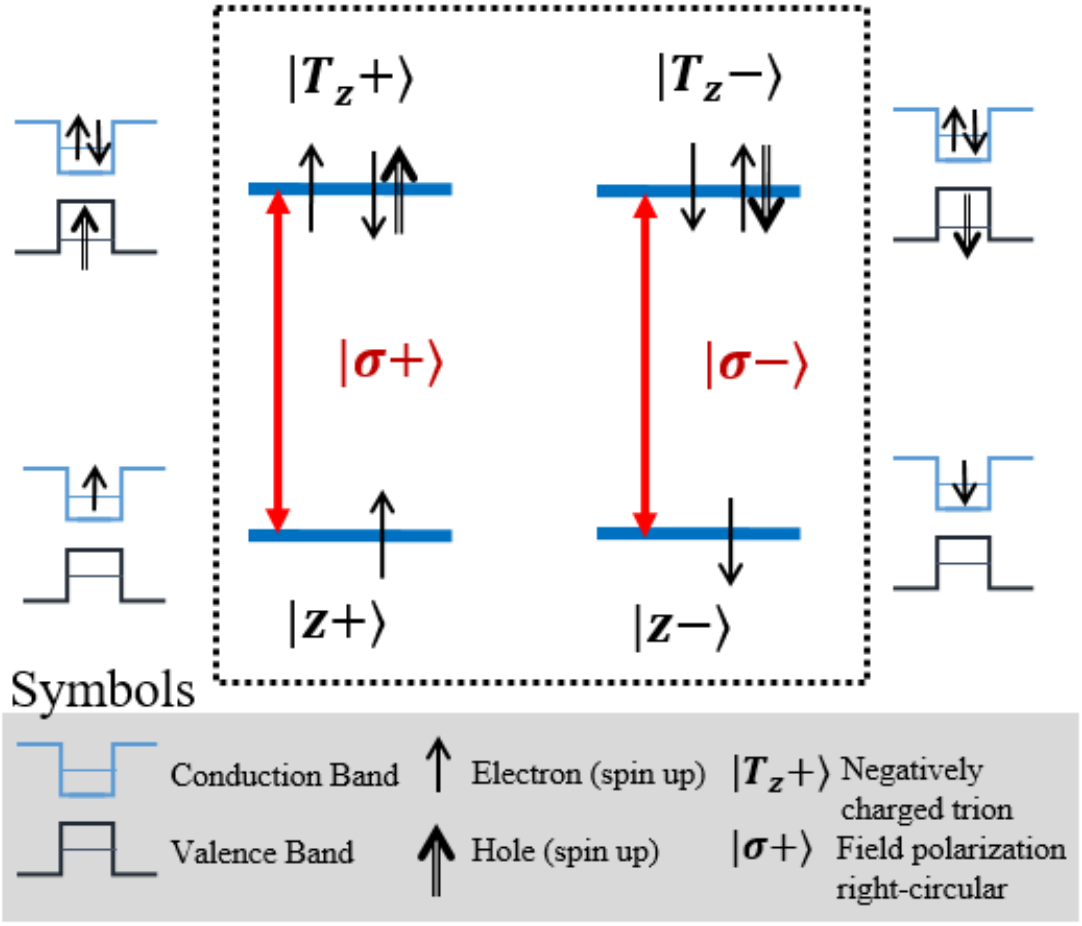

Figure 5.2: Transition energy levels and selection rules for a single trion state at zero magnetic field.

As seen in the figure, the excited trion state ($|T_z\rangle$) is composed of a pair of electrons with opposite spins living in the conduction band and a hole in the valence band. Trion states in the InAs/GaAs material have a typically lifetime of around one nanosecond, within which an excited state electron and the hole recombine back, emitting a single photon packet and leaving a single electron in the conduction band. The single electron state in the conduction band forms the ground state of our system. As given in Fig. 5.2, the two vertical transitions can be excited with circularly polarized light. At zero magnetic field, the two cross-transitions are dipole-forbidden [113].

The degeneracy between the two ground states can be broken by applying an external magnetic field [129]. The cryostat is equipped with a superconducting magnets that is capable of applying 7 Tesla magnetic field. When applying a magnetic field in the transverse plane of the QD sample, the trion state breaks into two Lambda-systems (four non-degenerate levels), with all states optically accessible. The transverse magnetic field, also referred to as the Voigt geometry, sets the quantization axis in which the new states can be expressed as a linear sum of the old states at zero magnetic field.

The ground state of a negatively charged dot containing one extra electron comprised of two spin states. When prepared in a coherent superposition state, the coherence time of the trion state in InAs/GaAs QD at 4 K temperature is shown to be a few ns (T_2^*), with the intrinsic coherence time (T_2) exceeding a few μs [37, 36]. Previous studies have shown that the ground state spin can be initialized within nanoseconds and rotated to an arbitrary superposition state within a few picoseconds [34, 35], forming a single electron spin qubit. Such arbitrary manipulation of a spin qubit, along with fast optical initialization, allows more than 1000 gate operations to be performed within the coherence time. This satisfies an important criteria for using trions as spin qubits for building quantum computers [38]. Such single electron spin

qubits are at the heart of many quantum information protocols, as described in the introduction chapter [39, 38, 40, 41, 42].

For the rest of the thesis study, unless otherwise explicitly state, we will use a negatively charged trion state at zero magnetic field.

5.2 Spectroscopy of a Single Quantum Dot

In this section, we will investigate the optical properties of single QDs using various spectroscopy techniques at 4 K temperature. All the measurements reported in this section are done with a single trion state at zero magnetic field. Without an external magnetic field, much of the physics and spectroscopic features of an isolated trion state can be explained by treating it as a two-level system. Before we get into the experimental details, we will visit the density matrix formalism to describe the light-matter interaction for a two-level system.

5.2.1 Light Matter Interaction For Two-level Systems

In this section, we give a brief theoretical treatment of semi-classical field matter interaction for an optically active two-level system driven near-resonantly with a classical field. The theoretical treatment will be followed from Ch. 3 of Principles of Laser Spectroscopy and Quantum Optics by P. Berman and V. Malinovsky [65]. The semi-classical treatment is important for understanding light-matter interaction. In the dipole approximation, interaction between a two-level system and an electric field is can written as the interaction Hamiltonian [65]

$$\hat{V}_{AF}(R,t) = \hat{\mu} \cdot \mathrm{E(R,t)} \tag{5.3}$$

where E(R,t) is the electric field of the laser with polarization $\hat{\epsilon}$ and $\hat{\mu}$ is the dipole moment operator of the two-level system, and R is the position of the atom. Assuming

the transition frequency of the two-level system is ω_0 and the electric field of the laser is approximated as a plane-wave centered at ω, the system Hamiltonian in the field interaction representation can be written as

$$H(t) = \frac{\hbar}{2}\begin{bmatrix} -\delta & \Omega_0^*(t) \\ \Omega_0(t) & \delta \end{bmatrix} \tag{5.4}$$

where $\Omega_0(t) = -\hat{\mu} \cdot \hat{\epsilon} E_0(t)/\hbar$ is the Rabi frequency and $\delta = \omega_0 - \omega$ is the detuning between the excitation laser and the transition energy of the two-level system.

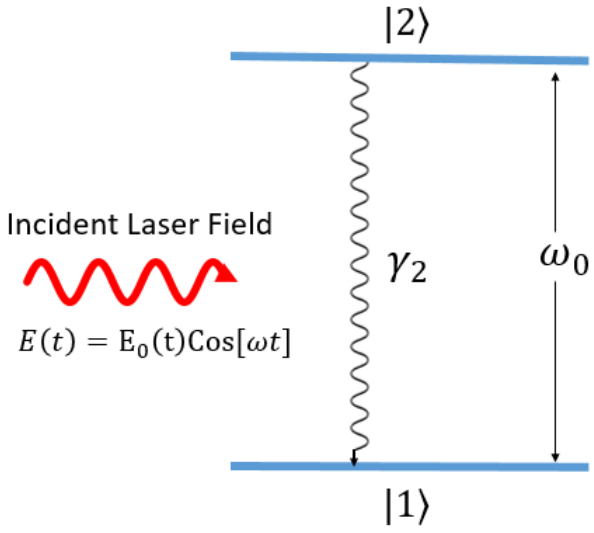

Figure 5.3: Energy level diagram of a two-level quantum system with ω_0 transition frequency interacting with an electric field of the excitation laser centered at ω. γ_2 is the excited state decay rate cause by spontaneous emission.

Once the Hamiltonian for the system of interest is defined, one can calculate the time dependent wavefunction of the system $|\psi(t)\rangle$ using the Schrödinger equation. A measurement performed in the laboratory can be expressed as an expectation value

of an appropriate Hermitian operator $\mathbf{O}$, given by

$$\langle \mathbf{O} \rangle = \langle \psi(t) | \mathbf{O} | \psi(t) \rangle \tag{5.5}$$

With a time dependent density matrix operator $\rho(t)$ in the Schrödinger picture defined as

$$\rho(t) = |\psi(t)\rangle\langle\psi(t)| \tag{5.6}$$

Density matrix formalism allows one to naturally include the relaxation terms given by spontaneous emission and environmental dephasing present in the system with a very little mathematical complexity. With this, the expectation value can be re-written in the trace form, given by

$$\langle \mathbf{O} \rangle = Tr[\rho(t)\mathbf{O}] \tag{5.7}$$

Including the relaxation terms, the time evolution of the density matrix operator can be calculated using the master equation

$$i\hbar \frac{d\widetilde{\rho}(t)}{dt} = [H(t), \widetilde{\rho}(t)] + \text{relaxation terms} \tag{5.8}$$

where $\widetilde{\rho}(t)$ is in the field-interaction picture defined as

$$\widetilde{\rho} = e^{-i\omega\sigma_z t/2} \rho e^{i\omega\sigma_z t/2} \tag{5.9}$$

with

$$\sigma_z = \begin{pmatrix} 1 & 0 \\ 0 & -1 \end{pmatrix}. \tag{5.10}$$

For a two-level system given in Fig. 5.3, $\rho_{22}, \rho_{11}, \rho_{12}$ represents the excited state population, ground state population, and the coherence between the two levels re-

spectively. Using Eq. 5.8, we can solve for the time evolution of the density matrix operators,

$$\frac{d\widetilde{\rho}_{22}(t)}{dt} = -\gamma_2\widetilde{\rho}_{22}(t) - i\chi(t)\widetilde{\rho}_{12}(t) + i\chi^*(t)\widetilde{\rho}_{21}(t) \tag{5.11a}$$

$$\frac{d\widetilde{\rho}_{11}(t)}{dt} = \gamma_2\widetilde{\rho}_{22}(t) + i\chi(t)\widetilde{\rho}_{12}(t) - i\chi^*(t)\widetilde{\rho}_{21}(t) \tag{5.11b}$$

$$\frac{d\widetilde{\rho}_{12}(t)}{dt} = -(\gamma - i\delta)\widetilde{\rho}_{12}(t) - i\chi^*(t)(\widetilde{\rho}_{22}(t) - \widetilde{\rho}_{11}(t)) \tag{5.11c}$$

$$\frac{d\widetilde{\rho}_{21}(t)}{dt} = -(\gamma + i\delta)\widetilde{\rho}_{21}(t) + i\chi(t)(\widetilde{\rho}_{22}(t) - \widetilde{\rho}_{11}(t)) \tag{5.11d}$$

with $\chi(t) = \Omega_0(t)/2$ and the decay rate of the coherence $\widetilde{\rho}_{12}$ defined as $\gamma = \gamma_2/2 + \Gamma$. γ_2 is the spontaneous decay rate of the excited state population and Γ is the dephasing decay rate. The above equations can be solved numerically for an arbitrary electric field profile of a laser. Taking the field amplitude to be time independent, in the steady state limit the above equations can be solved to obtain

$$\widetilde{\rho}_{22} = \frac{2\gamma}{\gamma_2}\frac{|\chi|^2}{\gamma^2 + \delta^2 + \frac{4\gamma}{\gamma_2}|\chi|^2} \tag{5.12a}$$

$$\widetilde{\rho}_{11} = 1 - \widetilde{\rho}_{22} \tag{5.12b}$$

$$\widetilde{\rho}_{12} = \frac{i\chi^*}{\gamma - i\delta}\frac{\gamma^2 + \delta^2}{\gamma^2 + \delta^2 + \frac{4\gamma}{\gamma_2}|\chi|^2} \tag{5.12c}$$

In the following sections, we will use absorption and fluorescence spectroscopy to resonantly study the property of single QDs. The key idea behind both of the measurements is that when a electric field of a laser is in resonance with a single QD approximated as a two-level system, it gets scattered in 4π direction. We can either collect the scattered field directly, often referred to as Rayleigh scattering, or monitor the change in the incident laser intensity due to the scattering process, also referred to as absorption spectroscopy.

When a laser frequency is scanned across a resonance of a two-level system, the

profile of the scattered field intensity can be expressed as the population term derived for the steady state case,

$$I(\chi, \delta) = \eta\tau\gamma_2\rho_{22}(\chi, \delta) \tag{5.13}$$

where η and τ are the detection efficiency of the scattered field and integration time. ρ_{22} can be rewritten to obtain a familiar Lorentzian form,

$$\rho_{22} = \frac{2\gamma}{\gamma_2} \frac{|\chi|^2}{\gamma_B^2 + \delta^2} \tag{5.14}$$

where

$$\gamma_B = \gamma\sqrt{1 + \frac{4|\chi|^2}{\gamma\gamma_2}} \tag{5.15}$$

is a term that gives rise to the power-broadening in the decay rate. Thus, through a linear resonant excitation one can measure the total decay rate of the system.

To identify the contribution of the radiative and pure dephasing decay rates, one needs to perform more complicated experiments. Pump-probe spectroscopy with two or more fields is commonly performed in our laboratory to study the detailed features of a dephasing broadened two-level system. See Ref. [71, 72, 130] for details on the pump-probe measurements. But for our purpose, as the InAs QDs have excellent spectral properties, the steady state solutions to the density matrix will be sufficient to describe most of the spectroscopic features that will be measured in the subsequent sections.

5.2.2 Experimental Method and Excitation Geometry

The sample is mounted inside a liquid helium flow cryostat (Janis) cooled to 4 K. A high numerical aperture aspheric lens with 0.65 NA is mounted in front of the sample, allowing the incident laser beam at 940 nm to be focused onto the sample with a micron spot size. The same incident aspheric lens is used to collect the emitted photons in the reflection geometry. In order to access both the excitation and emission

paths a 90:10 (R:T) beam-splitter is used in front of the cryostat. This gives access to the 90% of the collected photons by the aspheric lens. An optical telescope is used before the aspheric lens outside the cryostat to compensate for any misalignment in the reflected spatial mode.

The detailed schematic of the experimental setup for various spectroscopy measurements that will reported in this section is given Fig. 5.4. The short green dash lines represents optional beam paths used for different studies. The zoomed top inset shows a mounted sample with a high NA aspheric lens aligned to it.

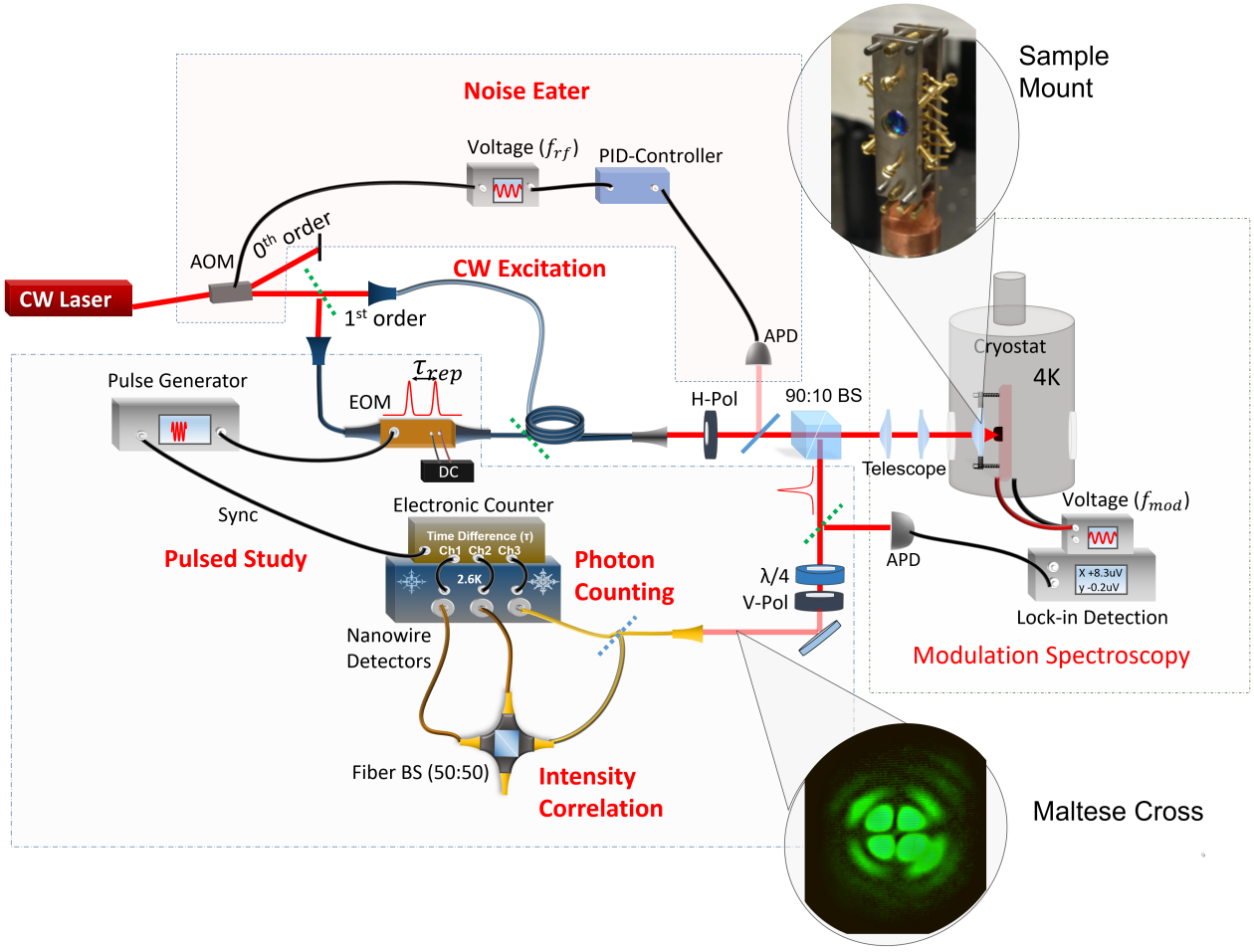

Figure 5.4: An schematic of an optical setup for performing various spectroscopic measurements to study the optical properties of a single QD.

The QDs are excited with a tunable, CW-laser with linewidth less than 100 kHz. At zero magnetic field, a negatively charged trion state forms a degenerate two two-level system [35]. The cross transitions are dipole forbidden. The allowed individual transitions can be excited with left and right circularly polarized light due to the selection rules. When excited with linearly polarized light, the scattered photons are circularly polarized. By projecting the scattered photons to the polarization orthogonal to the polarization of the incident excitation beam, most of the unwanted laser light can be suppressed while collecting single photons scattered by a QD. In addition, a single mode fiber with a core of $\sim 5\mu$m along with a 0.16 NA aspheric lens is used to collect the photons that pass through the cross-polarization setup. All optical elements used in the experiment along with the windows of the cryostat are anti-reflectance coated for 780-1000 nm wavelength range to minimize any unwanted scattering from the optical surfaces.

As the collection arm has a polarizer aligned perpendicular to the input polarizer, a large fraction of the reflected laser beam gets rejected. However, due to birefringence in the sample, the cryostat windows, and the optical components such as the lenses, the reflected beam's polarization has some elliptical components. With an addition of quarter-wave plate (QWP) before the polarizer, a large fraction of the beam is blocked. The curvatures of high NA lenses in the optical path causes polarization aberrations as s- and p-polarized beam acquire different phases through the surfaces [131]. This results in a cross-shape dark region (Maltese cross) in the reflected beam after the waveplates and polarizer as seen in the lower inset in Fig. 5.4, where the reflected beam is blocked with an extinction ratio of $10^5 : 1$. In order to further suppress the laser beam, an aspheric lens with NA $0.14 - 0.20$ is used to image the core of the Maltese cross into a single mode fiber with a core size of 5μm. The combination of the aspheric lens and the fiber acts as a spatial filter that further rejects the laser light, ultimately yielding a $10^7 : 1$ extinction ratio of the unwanted background. The

single photons are detected using superconducting nanowire detectors.

5.2.3 Identifying Quantum Dots Excitonic States with Non-Resonant Excitation

We survey the emission energy and the charge states of individual quantum dots using a non-resonant excitation. The laser spot focused on the sample is approximately a micron diameter. Within the focus spot, tens of QDs are present. The sample is optically excited by a 890 nm CW-laser centered at the wetting layer of the sample. This injects multiple electron and holes to the continuum of conduction and valence bands. The electrons and holes from multiple QDs decay non-radiatively to the lowest states of the QD energy levels. Pairs of single electron and holes form a bound state also referred to as neutral excitons in multiple QDs. After a nanosecond time, the excitons recombine, emitting photon packets centered at the excitons energy. This method of obtaining single photons from non-resonantly excited QDs is often referred to as photoluminescence (PL) spectroscopy. A cartoon of the PL spectroscopy for InAs QDs is given in Fig. 5.5. See Ref. [132] for complete energy levels calculated for self-assembled QD excitons.

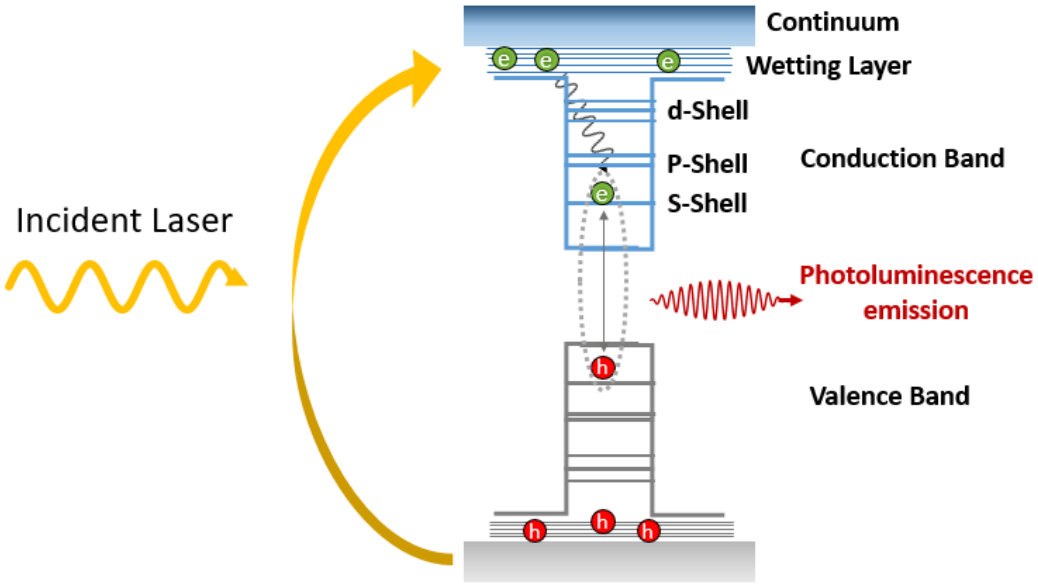

Figure 5.5: A cartoon of the energy levels of self-assembled InAs QDs and the PL technique without any Stark shifts. See Ref. [132] for a complete energy levels diagram calculated using band theory.

The photoluminescence spectrum emitted from the QDs is collected using the same excitation aspheric lens and is collected in the reflection geometry as shown in Fig. 5.4. The photoluminescence is sent through a HR-640 spectrometer with 1200 lines/mm gratings and is detected with a nitrogen-cooled CCD camera.

A bias voltage-dependent PL map is constructed to identify the charge states of the QDs and their respective emission energies. The diode structure is designed such that individual QDs can be charged with an electron or holes. This results in charge complexes, with a well defined region of existence for neutral and charged excitons. The bias dependent photoluminescence plotted in Fig. 5.6 shows discrete charging patterns seen in the sample, with positive trions (X^+) at low biases, neutral excitons

(X^0) at 200 - 600 mV range, negative trions (X^-) at 550-700 mV, and X^{2-} (1 exciton + 2 electrons) states above 700mV.

The neutral excitons have fine-structure splittings of 1-10 GHz at zero magnetic field. The splitting is dictated by the symmetry of the dots, where the splitting is smaller for more symmetric dots [129]. The splitting is not always visible in the PL spectroscopy due to the resolution of the spectrometer ($\sim$ 8 GHz). As the bias is increased, a neutral exciton gets charged with an additional electron. This results in the emission energy of a negative trion shifting down by approximately 6 meV as seen in Fig. 5.6. The negatively charged trions have relatively shorter existence ranges than neutral excitons, as can been seen in the Fig. 5.6. For the sample in study, the negatively charged trions are clustered at around 550-800 mV bias range. Fig. 5.6 (top) shows a slice of a PL map at 620 mV bias, where the tall peak corresponds to a negatively charged trion state. With further realignment optical coupling with the nearby dots can be suppressed.

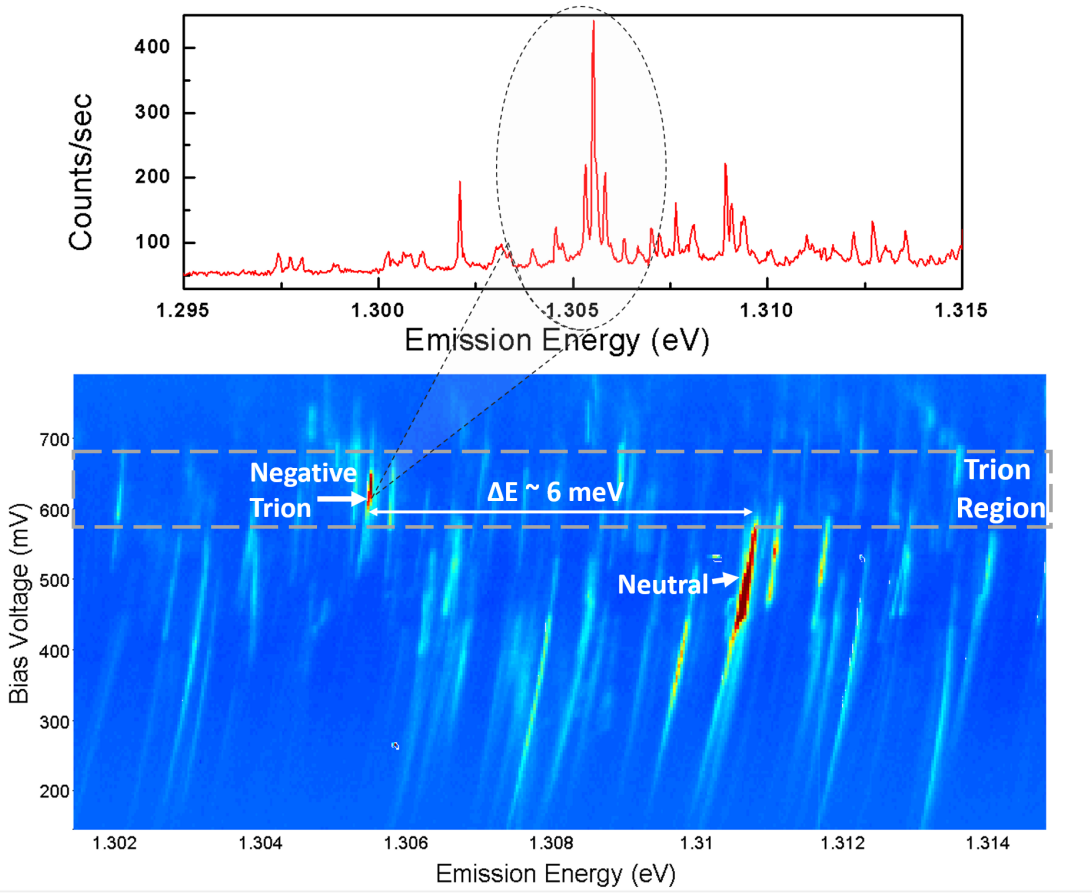

Figure 5.6: Bias dependent photoluminescence map from multiple quantum dots. The top inset is the zoomed in spectrum at 620 mV bias. The charge states are labeled. A discrete charging pattern can be seen in the PL map.

The charge state of excitons can also be determined through Magneto-photoluminescence spectroscopy by exploiting their optical selection rules.

5.2.4 Resonant Spectroscopy with a Single QD

With an external static field applied across a QD exciton, the transition energy of the exciton can be changed due to the Stark shift. The shift in the transition energy

is given by [133]

$$\Delta E = -\vec{\mu}_0 \cdot \vec{F} - \beta |\vec{F}|^2 \tag{5.16}$$

where $\vec{\mu}_0$ is the zero-field dipole moment, $\vec{F}$ is the external static electric field and β is the polarizability of the exciton.

Once the exciton states of interest are determined through PL measurements, we exploit the Stark shift effect to perform high resolution modulation spectroscopy of the individual QDs. When a QD exciton is brought into resonance with the excitation laser by applying an appropriate DC voltage, the QD scatters the incident field. The scattered field interferes with the reflected beam, resulting in a decrease of the laser intensity [65]. The drop in laser intensity is typically of around 0.1-1%. This signal is often smaller than the laser power fluctuation in the experiment.

The signal sensitivity can be increase significantly by performing phase-sensitive modulation spectroscopy using a lock-in detection technique. A DC bias is applied to the sample along with a few kHz square wave voltage with amplitude of 50 mV. A narrow-band (<100 kHz) wavelength tunable CW-laser is incident on the sample, tuned to the wavelength of an exciton identified through the PL measurement. The power of the laser beam incident on the sample is stabilized within 0.1% using a PID controller and an acousto-optic modulator through a noise-eater setup. The reflected beam is focused to a Hamamatsu avalanche photodiode (APD). The APD is operated with a high gain of ∼50-100X while keeping it in the linear regime. The output of the APD is sent to the lock-in detector with a 10 K shunt resistor and is integrated for 100-500 ms. The kHz square modulation brings the QD in and out of the resonance, causing periodic reduction in the reflected laser intensity. This periodic drop in the reflected intensity (R) can be detected with a high signal-to-noise ratio using the APD and lock-in detector (signal measured in the reflection will be denoted by dR). The signal obtained from such a measurement is often referred to as Stark modulation spectroscopy. Once a non-zero signal is found for a QD of interests, using

the telescope in front of the cryostat the signal is optimized by fine tuning the overlap between the single QD's dipole and the mode of the excitation laser.

With the Schottky sample, a single QD would yield <0.1% dR/R signal [113]. With the DBR sample in study, we obtain almost 10 times larger dR/R signal. The enhancement is due to the increase in the field density, resulting in a stronger interaction between the laser and the QD's dipole. See Fig. 5.4 for the modulation spectroscopy and noise-eater setup.

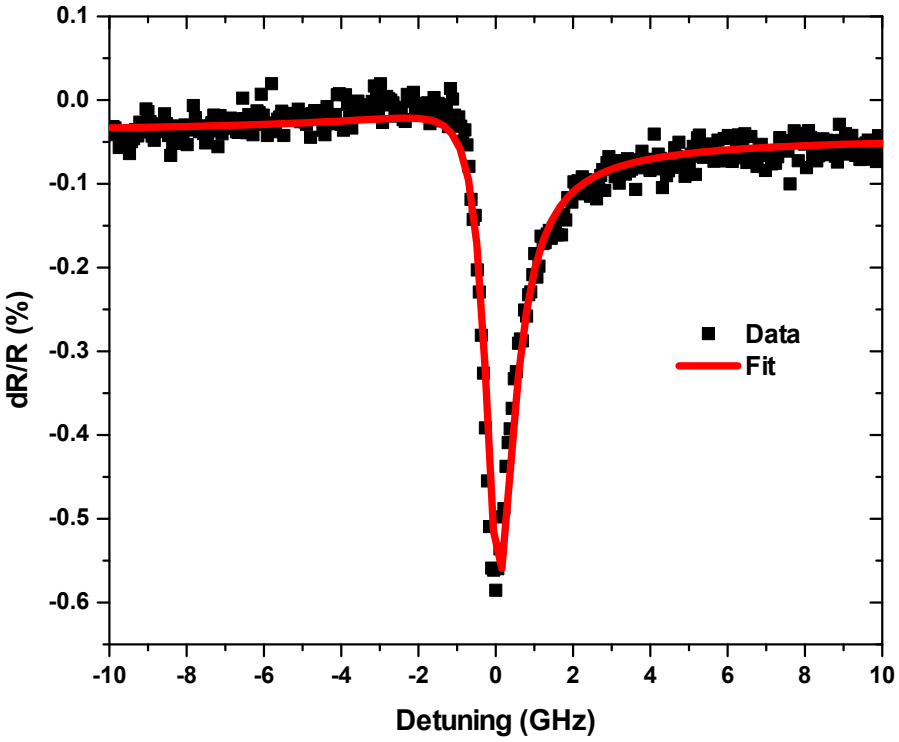

Figure 5.7: Differential reflection as a function of the detuning from a single trion state. The data is taken by square modulating the sample at a fixed DC voltage and scanning a narrow band CW-laser across the trion resonance polarized linearly. The incident power is approximately 10 nW and the reflected beam is 1 mW. For smaller excitation powers, the dR/R values increases up to 1.5%. The red line is the dispersive Lorentzian lineshape fitted to the data.

Figure 5.7 is the dR/R signal as a function of laser wavelength measured for a single negatively charged trion state. The data is obtained by scanning the laser across the transition energy, while modulating the sample with a fixed DC bias and a modulation voltage larger than the trion linewidth. As the QD is embedded inside

the material, the emitted field and the reflected laser from the surface of the sample acquire different optical phases [134]. This results in an asymmetric Lorentzian linewidth, as seen in the data. The red solid line is the fit to the data obtained by fitting a dispersive lineshape, with linewidth of 400 MHz.

Single photons emitted from an isolated single QD are of interest for most quantum information protocols. InAs QDs form an excellent source of single photons. Below we will discuss on the single photons generation from a resonantly excited single QD.

Instead of measuring the drop in the intensity of the laser field due to the interference between the reflected field and the scattered field, we can directly measure the Rayleigh scattered photons from a single quantum dot. Similar to the differential reflection measurements, a tunable CW-laser's wavelength is scanned around the transition of a single trion state. As described in the experimental methods subsection, the scattered photons are detected in a cross-polarization setup. The experimental setup is given in Fig. 5.4 enclosed in the lower dash box. We obtain a signal to background ratio exceeding 100:1 for the photon counting experiments. The scattered photons are collected in a single mode fiber and are detected using a single-photon detector. Similar to the absorption case, as derived in Eq. 5.12, the scattering profile is given by a Lorentzian function. We will often use RF for resonant fluorescence to denote the data.

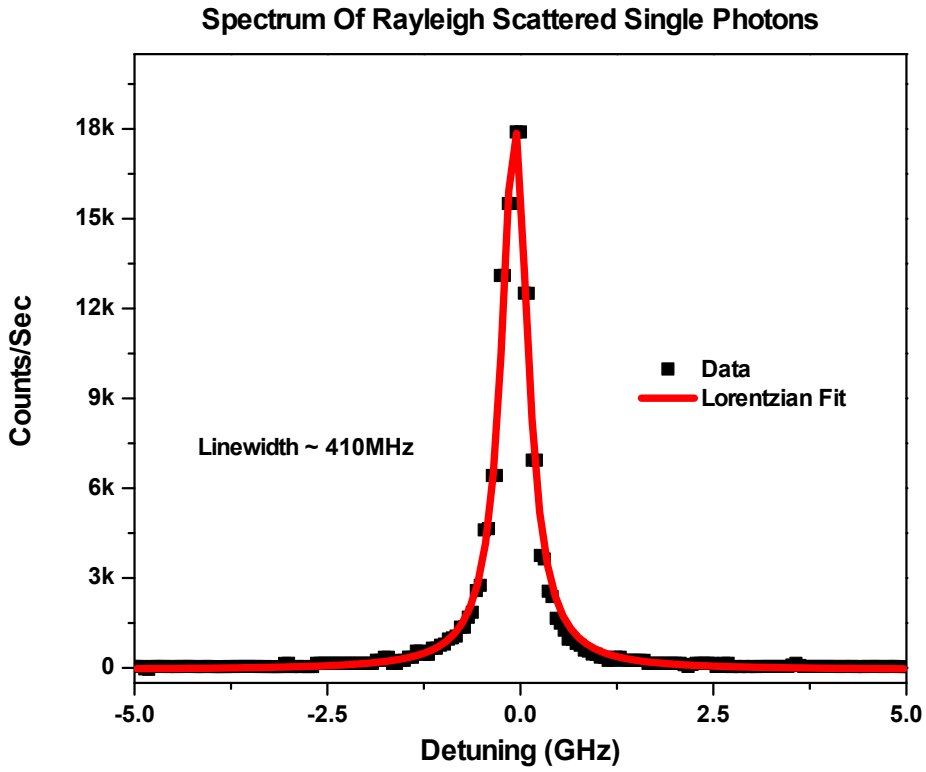

Figure 5.8: Intensity profile of a single trion state measured through resonant Rayleigh scattering. The line is a Lorentzian fit obtained with Eq. 5.12. The power broadened linewidth extracted from the fit is 410 MHz.

Figure 5.8 is the intensity profile of a single trion state measured through resonant Rayleigh scattering process. The data is fitted with the population term of the density matrix derived early for the steady state case, given by Eq. 5.12. The fit gives a 410 MHz power-broadened linewidth. For the typical QDs in this sample, the Rayleigh scattering linewidths range anywhere from 450 MHz to 1 GHz. The broadening of the linewidth from the natural linewidth in some dots could be caused by spectral wandering. The reported linewidh is the narrowest resonance that is observed in this thesis work. At saturation, we obtain the single photon rate as high as 4 million per

second in the same sample.

5.2.5 Time Resolved Study of a Single Trion State

The transient behavior of a single quantum dot can be studied through pulse excitation measurements. The direct observation of time-resolved Rabi oscillation between the two-level system of a single QD has been recently demonstrated in our laboratory [135] using a resonant pulse excitation scheme. Resonant pulse excitation allows one to measure the optical coherence of a QD. In addition, one can directly measure the spontaneous emission time (excited state lifetime) of a single QD. The time-correlated single photon counting measurements can be performed by resonantly exciting a single QD with laser pulses, with a well-defined pulse width and repetition rate, and recording the emission time through a fast detector and time tagging electronics. The single photons emitted through the spontaneous emission process are often referred to as resonant fluorescent photons. The detail of the time-correlated measurement technique is given in J. Schaibley's thesis [113].

Time domain experiments are of interest in quantum information applications for two fold reasons: first, it allows one to manipulate the electronic/excitonic state through optical pumping and initialize the system in a desired state; second, it can be used to generate on-demand single photons emission from a single QD. By exciting a single QD with a narrow pulse (pulsewidth smaller than lifetime) with a π-pulse, the QD can be kicked to the excited state. This starts the clock for the decay of the QD to happen, making the QD a so called "on-demand" single photon source [136]. It is important to note that the emission and collection process is probabilistic and the photons get emitted within the lifetime of the QD, which is typically a ns.

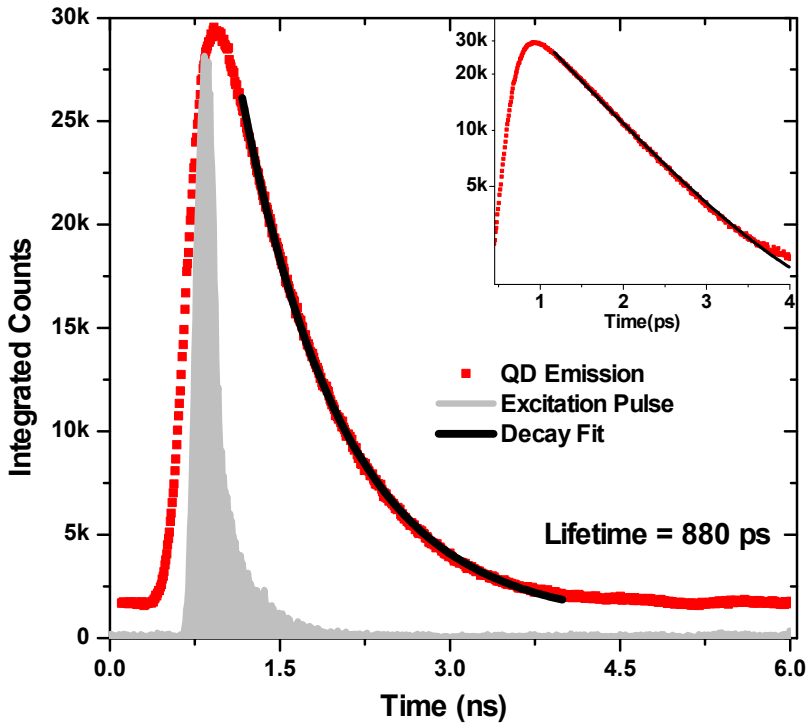

Figure 5.9: Time resolved resonant fluorescence photons from a single QD. The inset is a semi-log plot of the data to show the decay feature of the dot. The data is fitted with a single exponential curve. At long time the data deviates from the fit. Such deviation could be due to the slow decaying trap states. The instrument response function is 80ps, much smaller than the trion lifetime, thus the data is not deconvolved.

Here, we resonantly excite a trion state using 175 ps pulses at 76 MHz repetition rate and the emitted photons are detected with fast nanowire superconducting detectors with timing resolution of 80 ps. The pulses are generated by time gating a CW-laser using an amplitude electro-optics modulator and the laser tuned to the transition energy of a trion state. The gray area is the time profile of the excitation

pulse. The emission time is recorded using Picoquant HydraHarp 400 (HH400) time-tagged electronics and a histogram is built with the integrated count rate. The data in Fig. 5.9 is one example of the time-resolved resonant fluorescence measurement performed with a single trion state. The red line is an exponential fit to the data. We extract the trion lifetime to be 890 ps, where lifetime is given by $1/\gamma_2$. The typical trions lifetimes in the sample are anywhere from 600 ps to 900 ps.

5.2.6 Photon Statistics of a Resonantly Excitd Single QD

Second-order intensity correlation, commonly referred to as $g^{(2)}$, is an important experimental technique that allows one to study the statistics of the photons. As discussed in the earlier chapter, photons emitted by a single two-level system exhibit sub-Poissonian statistics. Kimble *et al.* performed the first intensity correlation measurement of single photons emitted by an atom and showed the anti-bunching behavior of the emitted field [66], linking the anti-bunching property to the quantum mechanical property of an excited atom. Similar, Grangier *et al* performed a heralded intensity correlation measurement with an atomic cascade decay to show the anti-bunching behavior of the single photons, the explanation of which required treating atomic radiation as a quantized field [121]. Since then, intensity correlation has been used as a hallmark experimental technique for identifying the single photon nature of a single emitter.

An intensity correlation measurement can be performed in a Hanbury, Brown, and Twiss (HBT)-type setup using a 50:50 non-polarizing beam splitter and two fast single-photon detectors. Mathematically, the intensity correlation of a scattered field by a two-level system can be defined as

$$g^{(2)}(\tau) = \lim_{t\to\infty} \frac{\langle E^-(R,t)E^-(R,t+\tau)E^+(R,t+\tau)E^+(R,t)\rangle}{\langle E^-(R,t)E_s^+(R,t)\rangle\langle E^-(R,t+\tau)E_s^+(R,t+\tau)\rangle} \tag{5.17}$$

where $E^{-}(R,t)$ is the electric field operator of the emitted radiation field at location R and time t. In the fully quantized picture, the scattered field by a two-level system can be calculated using the source-field formalism [65]. When the initial field is polarized along the z direction, the scattered radiation at angle θ can be expressed in terms of the atomic operator,

$$E^{+}(R,t) = -\left(\frac{\omega^2 \mu_{12} sin\theta}{4\pi\epsilon_0 c^2 R}\right)\sigma_{-}(t - R/c) \tag{5.18}$$

where σ_{-} is a lowering operator that lowers the atom from the excited state to the ground state and, similarly, $E^{-}(R,t)$ is proportional to the raising operator σ_{+}. It is important to note that the radiation field emitted by a two-level system looks similar to a dipole oscillating in z-direction, analogous to what one gets from a classical dipole oscillator. However, the emitted field has several important distinctions from the classical dipole, such as anti-bunching behavior. Substituting Eq. 5.18 to Eq. 5.17 we obtain,

$$g^{(2)}(\tau) = \lim_{t\to\infty} \frac{\langle \sigma_{+}(t)\sigma_{22}(t+\tau)\sigma_{-}(t)\rangle}{\rho_{22}^2} \tag{5.19}$$

where σ_{22} is the product of $\sigma_{+}\sigma_{-}$ and ρ_{22} is the steady state population term derived in Eq. 5.12. At $\tau = 0$ the numerator is zero, as one can not re-excite the atom twice at t = 0, giving $g^{(2)}(0) = 0$. This results in the well known anti-bunching property of a single atom.

The expectation values of the two-time operator can be calculated using the quantum regression theorem. With some insight into the problem[3], it can be shown that the numerator in Eq. 5.19 can be rewritten as $\rho_{22}\langle\sigma_{22}(\tau)\rangle$, where the expectation value of $\langle\sigma_{22}(\tau)\rangle$ is equal to the $\rho_{22}(\tau)$, which can be calculated using the density matrix equations given by Eq. 5.11. See App. C for a detailed calculation. For a constant Rabi frequency and zero detuning ($\delta = 0$), Eq. 5.19 can be written as

[3]This calculation is adopted from Paul Berman's lecture notes

[65, 137],

$$g^{(2)}(\tau) = 1 - [cos(\lambda|\tau|) + \frac{\gamma + \gamma_2}{2\lambda} sin(\lambda|\tau|)]e^{-\frac{1}{2}(\gamma+\gamma_2)|\tau|} \tag{5.20}$$

where

$$\lambda = \sqrt{(\Omega_0^2 - \frac{(\gamma - \gamma_2)^2}{4})} \tag{5.21}$$

and as expected $g^{(2)} = 0$ at $\tau = 0$

Physically, $g^{(2)}(\tau)$ is the chance of detecting a photon at $t = \tau$ if another photon was detected at $t = 0$. For an ideal single photon source, the properly normalized $g^{(2)}(\tau = 0) = 0$ since if it emitted a photon at $\tau = 0$, the emitter is now in the ground state and cannot emit again until it is re-excited. Thus it is not surprising that the intensity correlation function reduces to the transient behavior of an excited state population [66].

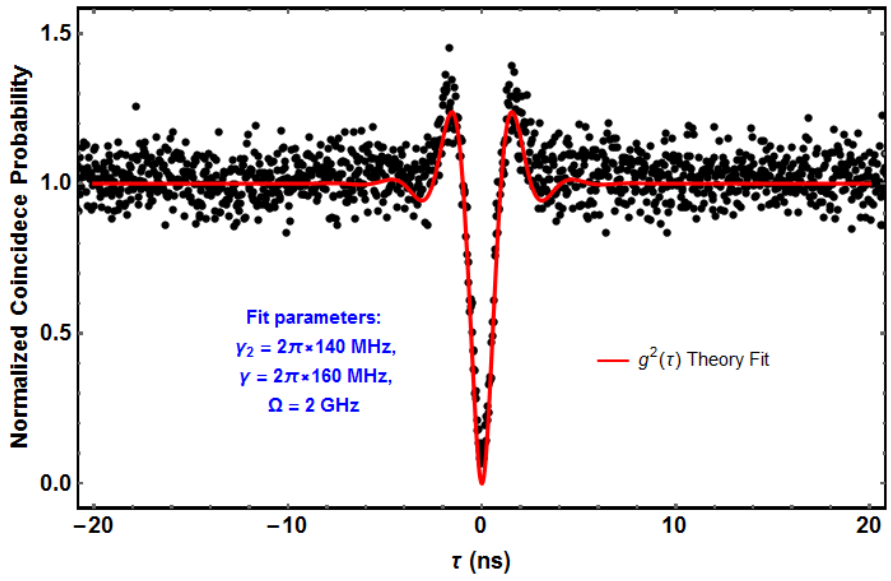

Figure 5.10: Second order intensity correlation with a single QD resonantly excited with a CW-laser. The fit is done using the theoretical equation for $g^{(2)}$ given in Eq. 5.20. The fit parameters are given in the plot

We performed both CW and pulsed intensity correlation measurements with a single QD. Single photons emitted by a resonantly excited trion state are collected and sent through a fiber beam splitter with 50:50 R:T. The two outputs of the fiber beam splitter are sent to two nanowire detectors. The absolute detection timing is recorded using an electronic time-tagger (Hydraharp) that can record emission timing with a resolution of 2 ps. And the data is analyzed to look for coincidence counts between the two detectors within several hundreds nanosecond time window as done in the previous studies [113]. The coincidence counts are normalized by taking the steady state value of $g^{(2)}(\tau \to \infty) = 1$.

Figure 5.10 is the normalized raw data [4] and a theoretical fit to the data using Eq. 5.20. The fit parameters are given in the plot. The oscillation at the two sides of the

[4]The $g^{(2)}$ measurement shown here is done with a different dot than the one used in the earlier studies

$\tau = 0$ correspond to the Rabi oscillation of the two-level system. The deviation from the fit at $\tau = 0$ is due to the finite detector resolution, which smooths the dip holding it from going to zero. As evident from the data at $\tau = 0$ the coincidence counts drops close to zero. At $\tau = 0$, $g^{(2)}(0) = 0.06 \pm 0.02$, and is limited by the detector timing resolution. In the quantum optics community, a photon source with $g^{(2)}(0) < 0.5$ is referred to as a single photon emitter. The data indicates that the QD in the study is an excellent single photon source.

As for demonstrating two-photon interference measurement that will be discussed in the next chapter, a trion state is resonantly excited with a pulsed laser. This allows us to obtain single-photon packets with well defined temporal information and emission time that can be interfered with another QD photon or an SPDC photon. For such measurements, pulsed excitation is vital, thus it is important to verify that a single shot of the QD emission still holds the single-photon nature. In addition, the pulsed $g^{(2)}$ measurement is not limited by the detectors' timing jitters as long as the jitters are comparable to the lifetime of the QD.

We excite a single trion with stream of 175 ps pulses separated by 13.1 ns as described in the previous subsection. The emitted resonant fluorescence photons are sent through the same HBT type setup and the correlation histogram is built. Figure 5.11 is the histogram of the normalized coincidence counts obtained for the intensity correlation. The data is normalized by taking the $\tau \neq 0$ shots of the measurement to be one.

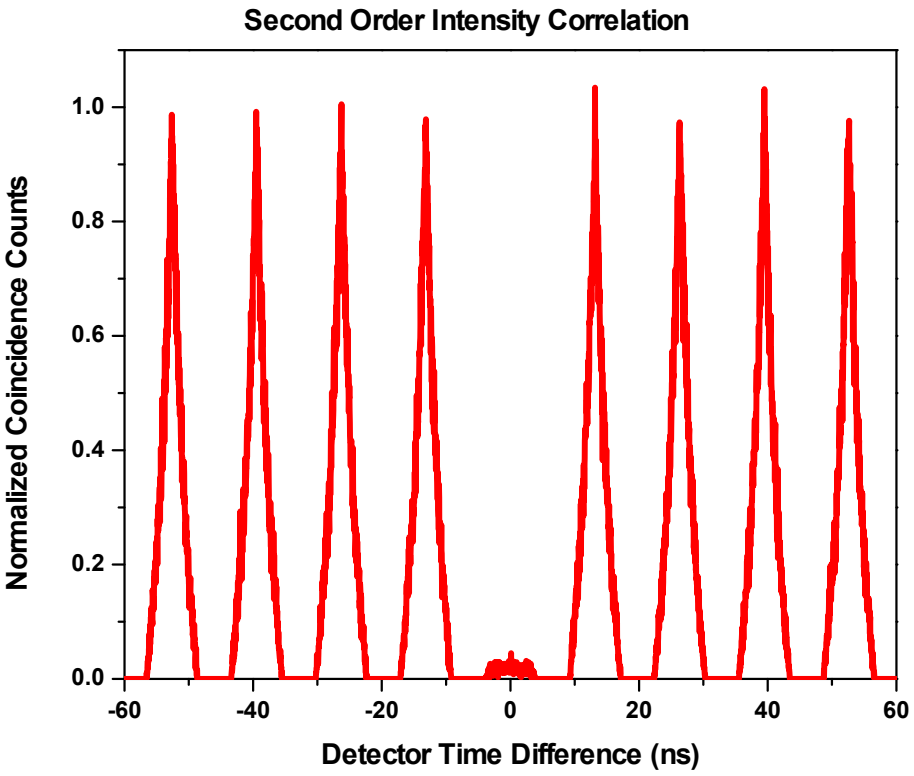

Figure 5.11: Pulsed second-order intensity correlation of a single QD.

Due to the single photon nature of the source, at $\tau = 0$ the normalized coincidence probability is highly suppressed, similar to the CW data show in Fig. 5.10. From the normalized data we obtain $g^{(2)}(\tau = 0) \leq 0.02$, indicating that the probability of multiple photons emission is less than 2%. The residual count could be due to dark counts of the detectors. Such a high purity single photon source would be of interests for various quantum key distribution protocols.

5.3 Chapter Summary

In this chapter, we discussed confinement in a semiconductor material. We gave a brief overview of the sample growth techniques to obtain semiconductor nanostruc-

tures. We showed that the nanostructures, also referred to as quantum dots, have discrete energy levels. We gave a brief semi-classical theoretical treatment for light-matter interactions. We discussed the spectroscopy techniques for a single QD and way to identify a trion state. We showed that the QDs in the study are an excellent single photon source. These studies lay the foundation for more complicated quantum information-type experiments that will be reported in the next chapters.

CHAPTER VI

Two-Photon Interference: Theory and Experiment

Quantum communication protocols require faithful transport of quantum information over a long distance. Photons form an excellent candidate for such flying qubits but with a caveat: they interact weakly. Due to the lack of a photon-photon interaction vertex in QED, two photon interactions are possible only in the high-energy regime through the generation of virtual electron-positron pairs. The cross-section for such interactions is on the order of $\alpha^4 \sim \frac{1}{137^4}$ [138] which is hard to observe in an ordinary experimental setting for low energy photons. For optical fields, the elastic scattering cross-section is 10^{-64}cm^2, which is 39 orders of magnitude smaller than Thomson scattering cross-section [139]. Despite the lack of direct interaction between two low-energy photons, one can exchange information between atoms via photons through a detection process. Such experiments often require simple linear optical elements such as a beam splitter and an appropriate measuring device. A proper quantum mechanical description of a single photon detection process is yet to be solved completely [65]. Nonetheless, as Glauber suggested [140], most of the quantum optics phenomena can be explained by simply assuming that a photon detector acts as a destruction operator that subtracts a single quanta mode from the state-vector of the photon being detected.

Following Glauber's proposal [140], the transition amplitude of a single photon

detection process can be written as,

$$\langle f|E_{\mu}^{+}(r,t)|i\rangle \tag{6.1}$$

where the field in an initial state $|i\rangle$ transits to a final state $|f\rangle$ through the absorption of a single photon with polarization μ at position r. A positive component of the quantized electric field operator in a free-space can be written as [63, 64],

$$E^{+}(r,t) = -\sum_{k,\mu} \sqrt{\frac{\hbar\omega_0}{2\epsilon_0}} f_{k,\mu}(r) a_{k,\mu}(t) \tag{6.2}$$

where $f_{k,\mu}(r)$ is the spatial mode distribution and the electric field is summed over all polarization (μ) and momentum states (k).

To find the detection probability one needs to sum over all the final states,

$$\sum_{f} |\langle f|E_{\mu}^{+}(r,t)|i\rangle|^2 = \langle i|E_{\mu}^{-}(r,t)E_{\mu}^{+}(r,t)|i\rangle \tag{6.3}$$

The above equation 6.3 is the basis for all quantum optics experiments where photons are detected using a Geiger counter also referred to as a single photon detector. This formalism will be used frequently throughout the thesis.

When two nearly identical yet independent photon packets are sent through the two input ports of a beam-splitter such that all the modes of the two photons are overlaped (temporal, polarization, spectral, spatially, etc.), they coalesce, exiting together from the same output port of the beam-splitter[141]. This phenomena was first experimentally demonstrated by Hong-Ou-Mandel (HOM) in 1988 using SPDC photons. Such HOM interference is the demonstration of the fourth-order field interference between two photons[142, 143, 141] through a second-order intensity correlation measurement. In ref [142] Z.Y. Ou calculates the fourth-order field interference effect for both classical waves and quantum fields to demonstrate the quantum-mechanical

nature of the Hong-Ou-Mandel interference, which otherwise cannot be explained by simply evoking a classical theory. This two-photon interference phenomenon is of great interest in quantum communication experiments [144].

In this chapter, a theoretical description of two-photon interference is given and is demonstrated experimentally using quantum dot photons. Legero *et al.* have given a theoretical treatment for two-photon interference measurement assuming that the spectral mode of the input photons are Gaussian [145]. Their calculation is in the Schródinger picture and the key mathematical parts that deal with the operators is not given in the paper. As we would like to extend the two-photon calculation for various different scenarios [1], we redid the calculation in the Heisenberg picture following the formalism given by Ou in Ref. [98]. Our calculation has several important distinctions from Ou's calculation: Ou integrates over the temporal profile of the photon and calculates the coincidence probability as a function of time delay between the two photons, as the temporal profile of the SPDC photons ($\sim$ ps) are much smaller than the available detector resolutions ($\sim 100 - 500$ ps). Whereas we are interested in the time resolved dynamics of the two-photon interference measurements. Also, Ou's calculation does not include spectral jitter. We follow both Ou and Legero *et al.*'s calculations when suitable and derive two-photon interference result for single photons emitted by a single QD. The results we obtain in this chapter agrees well with both of their calculations.

[1] A theory paper on two-photon interference between two single photons with multiple sidebands is current under preparation.

6.1 Theory Of Two-Photon Interference

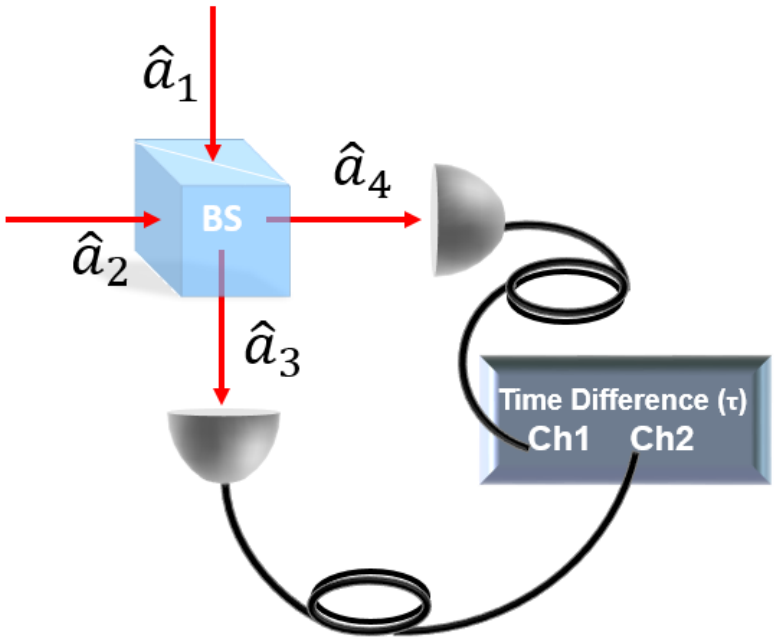

Figure 6.1: Schematic of the experimental setup for two-photon interference measurement. $\hat{a}_i$ is the ith mode of the beam splitter, where $\hat{a}_1$ and $\hat{a}_2$ are the input modes and $\hat{a}_3$ and $\hat{a}_4$ are the output modes equipped with two single detectors operating at a Geiger count mode and a fast electronic to record the timing information of the detection events.

Hong-Ou-Mandel type measurements require a conceptually simple setup, where photon packets are sent through the two input ports of a beam splitter and are detected by two single photon detectors on the output ports (see figure 6.1). The earlier HOM measurements were done using detectors with response time slower than the wavepacket of the interfering photons. In the original experiment, the joint detection counts between the two detectors for a specified time window was recorded as a function of the photon packets overlap timing at the beam-splitter. However, devel-

opments in the detector technology over the past decade have allowed several HOM experiments to be done with time resolved measurements[146, 147, 148, 147, 149]. In those measurements the relative photon packet delay time is fixed to be zero and the experiment is done by measuring the relative detection time between the two detectors. This made additional features, such as frequency beatings, spectral jitters, etc[146, 145], to be visible in the interference measurement that were not easily accessible through the original method. For such experiments to be performed the detectors and the electronics need to be faster than the photon wavepacket, which is the case with our experiment.

An ideal lossless beam-splitter can be described by a unitary transformation matrix that relates the input spatial-temporal electric field modes to the output modes. In the Heisenberg picture, the transformation of the electric field operators[2] is given by [141]

$$\begin{pmatrix} \hat{E}_3^+(t) \\ \hat{E}_4^+(t) \end{pmatrix} = \begin{pmatrix} \sqrt{T} & i\sqrt{R} \\ i\sqrt{R} & \sqrt{T} \end{pmatrix} \begin{pmatrix} \hat{E}_1^+(t) \\ \hat{E}_2^+(t) \end{pmatrix} \tag{6.4}$$

where R, T are reflection and transmission coefficient of the beam-splitter such that $R + T = 1$ and E^+ is defined in Eq. 6.2. The minus sign arises from the requirement of time-reversal symmetry. Assuming the electric field is a plane wave propagating in free space along the z-direction and is continuous with center frequency ω_0, we can rewrite equation 6.2 as

$$E^+(z,t) = -\hat{\mu}\sqrt{\frac{\hbar\omega_0}{2\epsilon_0 cA}} \int d\omega e^{i(kz-\omega t)} a(\omega) \tag{6.5}$$

where A the area of the mode function. Let us consider that two photon packets are impinged on a beam-splitter and are detected by two single photon detectors

[2]There exist several different unitary matrices in use for a BS, each derived with a different argument. All such transformations ultimately result to the same result in our calculation. See Ref. [150] for a detailed analysis on the subject matter.

on the output ports. In order for the following calculation to hold, the two photon packets do not necessarily have to be of single photon nature. However, in the next section we will solve the problem assuming the photon packets are multimode single-photon packets. Following Glauber [140], the process of detecting a single photon by a detector 3 at time t and another photon by a second detector 4 at time $t + \tau$ can be written as,

$$G^{(2)}(t, t+\tau) = Tr[\rho_{12} E_3^{(-)}(t) E_4^{(-)}(t+\tau) E_4^{(+)}(t+\tau) E_3^{(+)}(t)] \tag{6.6}$$

where,

$$\rho_{12} = |\psi\rangle\langle\psi| \tag{6.7}$$

where $|\psi\rangle$ is the initial state-vector of the two input states. Substituting the density matrix for the input state-vectors,

$$G^{(2)}(t, t+\tau) = \langle\psi| E_3^{(-)}(t) E_4^{(-)}(t+\tau) E_4^{(+)}(t+\tau) E_3^{(+)}(t) |\psi\rangle \tag{6.8}$$

The time correlation is an unnormalized second-order intensity correlation. Assuming the detectors are faster than the temporal profile of the single-photons, which is the case in our experiments, we can calculate the joint photon detection probability from the second-order correlation function. Even though the correlation function is a function of t and τ, in an experiment we only care about the relative time difference between the two detected events. Thus by integrating the correlation function over all time, we can calculate the joint photon detection probability [145],

$$P_{34}(\tau) \propto \eta_1 \eta_2 \int dt G^{(2)}(t, t+\tau) \tag{6.9}$$

where η_i is the detection efficiency of the detector i. As the input photons are in the ports 1 and 2 and the detectors are in 3 and 4, we can solve for the correlations

by using the Heisenberg pictures, in which the operators can be evolved through the beam-splitter and transformed using eq 6.4. To further simplify the problem, we can insert an identity operator $\sum_{n_1 n2} |n_1 n_2\rangle\langle n_2 n_1| = 1$. With this eq 6.9 becomes,

$$\begin{aligned} P_{34}(\tau) \propto \int dt \sum_{n_1 n_2} |\langle n_2 n_1|(i\sqrt{RT}E_1^+(t+\tau)E_1^+(t) + i\sqrt{RT}E_2^+(t+\tau)E_2^+(t) \\ - RE_1^+(t+\tau)E_2^+(t) + TE_2^+(t+\tau)E_1^+(t)|\psi\rangle|^2 \end{aligned} \tag{6.10}$$

The calculated joint detection probability is written in a general form without making any assumptions about the input states. Let us further examine the integrand of the joint detection probability by substituting the electric field operators.

$$\begin{aligned} \text{1st Term} &: \frac{i\sqrt{RT}\hbar\omega_{01}}{4\pi\epsilon_0 cA} \sum_{n_1 n_2} \langle n_2 n_1| \int_{-\infty}^{\infty}\int_{-\infty}^{\infty} d\omega_1 d\omega_1' e^{i\omega_1(z_1/c-(t+\tau))+i\omega_1'(z_1/c-t)} a_1(\omega_1)a_1(\omega_1')|\psi\rangle \\ \text{2nd Term} &: \frac{i\sqrt{RT}\hbar\omega_{02}}{4\pi\epsilon_0 cA} \sum_{n_1 n_2} \langle n_2 n_1| \int_{-\infty}^{\infty}\int_{-\infty}^{\infty} d\omega_2 d\omega_2' e^{i\omega_2(z_2/c-(t+\tau))+i\omega_2'(z_2/c-t)} a_2(\omega_2)a_2(\omega_2')|\psi\rangle \\ \text{3rd Term} &: \frac{-R\hbar\sqrt{\omega_{01}\omega_{02}}}{4\pi\epsilon_0 cA} \sum_{n_1 n_2} \langle n_2 n_1| \int_{-\infty}^{\infty}\int_{-\infty}^{\infty} d\omega_1 d\omega_2 e^{i\omega_1(z_1/c-(t+\tau))+i\omega_2(z_2/c-t)} a_1(\omega_1)a_2(\omega_2)|\psi\rangle \\ \text{4th Term} &: \frac{T\hbar\sqrt{\omega_{01}\omega_{02}}}{4\pi\epsilon_0 cA} \sum_{n_1 n_2} \langle n_2 n_1| \int_{-\infty}^{\infty}\int_{-\infty}^{\infty} d\omega_1 d\omega_2 e^{i\omega_2(z_2/c-(t+\tau))+i\omega_1(z_1/c-t)} a_1(\omega_1)a_2(\omega_2)|\psi\rangle \end{aligned} \tag{6.11}$$

where z_1 and z_2 are the path length of the two photon packets before they enter the beam splitter.

The first two operators annihilate the two single photon modes in each input ports. For an experimental case where two single photons are sent through the two input modes of a $50:50$ beam-splitter, the first two terms result in zero amplitude, as neither of the inputs have two photons going through them. The remaining two terms annihilate single photon in each input modes. For identical input photon packets the

remaining two terms destructively interfere, resulting in a zero joint photon detection probability. This is the idea behind the famous Hong-Ou-Mandel experiment. In an actual experimental setup, single photons are often not identical and have a finite temporal spread resulting in a partial interference between the two photons. In the subsequent sections, we will derive the detailed structure of the joint photon detection probability for two single-photon packets emitted by a QD.

6.2 Two-photon interference With QD Photons: Theory

A single photon packet emitted by a trion state at zero magnetic field through a spontaneous emission process can be written as [151],

$$|\psi\rangle = \int_{-\infty}^{\infty} d\omega g(\omega) a^{\dagger}(\omega)|0\rangle \tag{6.12}$$

where

$$g(\omega) = \frac{\sqrt{\Gamma}}{\sqrt{2\pi}[\omega - \omega_0 + i\Gamma/2]} \tag{6.13}$$

is the spectral distribution of the photon packets centered at frequency ω_0 with linewidth Γ and we ignored the polarization degree of freedom. Here, we assume that the photons are Fourier limited. In the full treatment of the spontaneous emission from a two-level system, the integrand is multiplied with a Heavyside function that limits the integral to $0 \rightarrow \infty$ and the integration results in energy shift [151].

In order to calculate an analytical solution for the two-photon measurement, we start with two photon packets with the same spatial mode with identical polarization but with different center frequencies $(\omega_{01}, \omega_{02})$ and linewidths (Γ_1, Γ_2). The joint input state can be written as,

$$|\psi\rangle = |\psi_{qd1}\rangle \otimes |\psi_{qd2}\rangle = \int_{-\infty}^{\infty}\int_{-\infty}^{\infty} d\omega_1 d\omega_2 g_{01}(\omega_1) g_{02}(\omega_2) a^{\dagger}(\omega_1) a^{\dagger}(\omega_2)|0_1 0_2\rangle \tag{6.14}$$

where the spectral mode function g_{01} is same as eq. 6.13 with the subscript indicates the center frequency and decay rate of each photon packet.

Now that we have written the input wavefunction explicitly, we can calculate the joint detection probability by using equation 6.10. As mentioned earlier, for two single photons input only the 3rd and 4th terms from equation 6.11 contribute to our solution and the sum reduces to the vacuum terms. Substituting the state-vector for the 3rd term of eq 6.11,

$$\begin{aligned}\text{3rd Term}: &\frac{-R\hbar\sqrt{\omega_{01}\omega_{02}}}{4\pi\epsilon_0 cA}\langle 0_2 0_1| \int_{-\infty}^{\infty}\int_{-\infty}^{\infty} d\omega_1 d\omega_2 e^{i\omega_1(z_1/c-(t+\tau))+i\omega_2(z_2/c-t)}.. \\ &.. \int_{-\infty}^{\infty}\int_{-\infty}^{\infty} d\omega_1' d\omega_2' a(\omega_1)a(\omega_2)a^\dagger(\omega_1')a^\dagger(\omega_2')g(\omega_1')g(\omega_2')|0_1 0_2\rangle\end{aligned} \tag{6.15}$$

evoking the commutation relationship $[a(\omega_i), a^\dagger(\omega_j)] = \delta(\omega_i - \omega_j)$, we can further simplify the integration.

$$\text{3rd Term}: \frac{-R\hbar\sqrt{\omega_{01}\omega_{02}}}{4\pi\epsilon_0 cA} \int_{-\infty}^{\infty} d\omega_1 e^{i\omega_1(z_1/c-(t+\tau))} g_1(\omega_1) \int_{-\infty}^{\infty} d\omega_2 e^{i\omega_2(z_2/c-t)} g_2(\omega_2) \tag{6.16}$$

Equation 6.16 consists of two complex integrals that can be solved using Cauchy's integral formula. Similarly, following the above steps we can solve the 4th term. Substituting the solutions to the 6.9, we obtain the joint detection probability,

$$\begin{aligned}\int_{-\infty}^{\infty} dt \frac{\hbar^2\omega_1\omega_2\Gamma_1\Gamma_2}{4\epsilon_0^2 c^2 A^2} |&- Re^{(i\omega_1+\Gamma_1/2)(z_1/c-(t+\tau))+(i\omega_2+\Gamma_2/2)(z_2/c-t)}\Theta(-z_2/c+t)\Theta(-z_1/c+t+\tau) \\ &+ Te^{(i\omega_1+\Gamma_1/2)(z_1/c-t)+(i\omega_2+\Gamma_2/2)(z_2/c-(t+\tau))}\Theta(-z_1/c+t)\Theta(-z_2/c+t+\tau)|^2\end{aligned} \tag{6.17}$$

where Θ, the Heaviside step function, is a result of the pole of the complex integral that ensures causality. To find the joint detection probability we need to integrate the

equation 6.17 over all time [145]. This can be done by first expanding the integrand, which results in three different terms: the squares of each term, the sum of which results in frequency independent envelope function, and a cross-term that is a function of the relative frequency difference between the two photon pulses. After some algebra we obtain,

$$P_{12}(\tau) \propto \frac{\hbar^2\omega_{01}\omega_{02}\Gamma_1\Gamma_2}{4\epsilon_0^2c^2A^2(\Gamma_1+\Gamma_2)}(R^2[e^{\Gamma_2(\Delta t+\tau)} + (e^{-\Gamma_1(\Delta t+\tau)} - e^{\Gamma_2(\Delta t+\tau)})\Theta(\Delta t+\tau)] + T^2[e^{\Gamma_1(-\Delta t+\tau)} + (e^{-\Gamma_2(-\Delta t+\tau)} - e^{\Gamma_1(-\Delta t+\tau)})\Theta(-\Delta t+\tau)] - 2RT[e^{-\Gamma_1(|\Delta t|+|\tau|/2)-\Gamma_2|\tau|/2}cos\Delta\omega\tau]) \tag{6.18}$$

To simplify the calculation, we substitute the relative time difference between the two input photon packets to be $(z_2 - z_1)/c = \Delta t$, where Δt is assumed to be positive and the frequency detuning between the two photons is defined as $\Delta\omega = \omega_{01} - \omega_{02}$. The solution we obtained reduces to a similar result that reference [145] derived using a Schrodinger picture for two input photons with Gaussian profile. The first two terms in the above equation 6.18 gives a convolution of the two input pulses and the third term gives rise to the famous Hong-Ou-Madel interference. For two input photon packets with identical bandwidths overlapped at the beam-splitter simultaneously ($\Delta t = 0$), equation 6.18 simplifies to

$$P_{12}(\tau) \propto (T^2 + R^2 - 2RTcos\Delta\omega\tau)e^{-\Gamma|\tau|} \tag{6.19}$$

For a 50:50 beam-splitter with zero detuning, the probability goes to zero! Our result reduces to the well known HOM interference form given by Ou [98, 141]. Notice that the two photons do not need to have identical frequencies in order for them to interfere at $\tau = 0$. The joint detection probability oscillates as a function of the frequency detuning between the two photons ($\Delta\omega$), which is always zero within a

narrow time window $\tau_{window} \sim \frac{1}{\Delta\omega}$ about $\tau = 0$. Figure 6.2 is a contour plot of the joint detection probability theoretically predicted for various frequency detunings obtained from the above calculations. It assumes that the input photons have the same bandwidth and are temporally overlapped at the beam-splitter. As one can see from the plot, when performed a measurement with infinitely fast detectors, at time zero, the two input photons always exit through the same port of the beam-splitter.

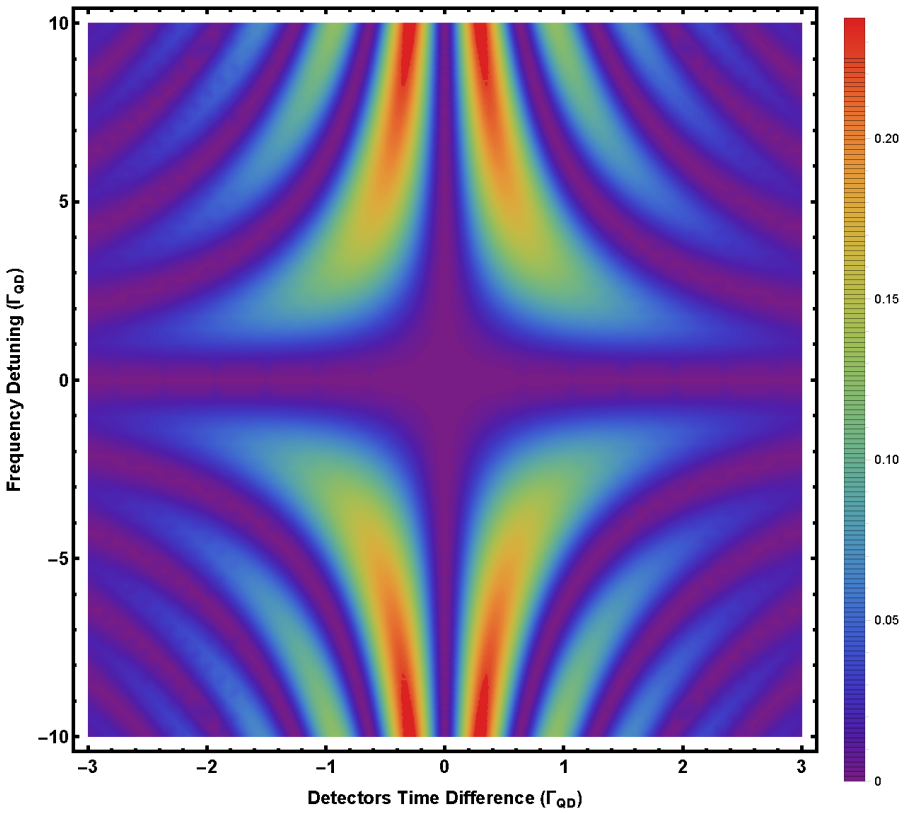

Figure 6.2: Contour plot of theoretical calculation of joint photon detection probability as a function of frequency difference between the two input photons and the relative time difference between the two detectors. The x axis is the the relative detection time between the two detectors defined to be dimensionless time by normalizing it with the bandwidth of the input photons. The plot legend on the right of the figure corresponds to the un-normalized joint detection probability. At $\tau = 0$ the probability is always zero for all frequency detunings.

So far we have not performed any normalizations in our coincidence detection probability, which is essential to obtain any meaningful conclusion from the data. In order to obtain a proper normalization of the data, one needs to perform an

additional control measurement and compare the relative probability between the two measurements. The most common way to normalize the result is by performing a similar experiment but with two cross-linearly polarized input photons. In the case of the cross-linearly polarized input photons, we need to sum over all the polarization terms that results in the mod of the 3rd and 4th term, which causes the cross term in equation 6.18 to vanish [145], thus resulting in a finite joint detection probability at zero time. Figure 6.3 is an example of joint detection probability theoretically predicted for co-polarized and cross-polarized input photons with various detuning obtained from the above calculations. The x axis is the the relative detection time between the two detectors defined to be dimensionless time by normalizing it with the bandwidth of the input photons. For identical photons (red curve), the coincidence probability goes to zero. For distinguishable input photons (cross-polarized) plotted in figure 6.3 (dash black curve), the coincidence probability goes to a finite value. And one can see beats in the coincidence probability when the input photons have finite frequency detuing (purple curve).

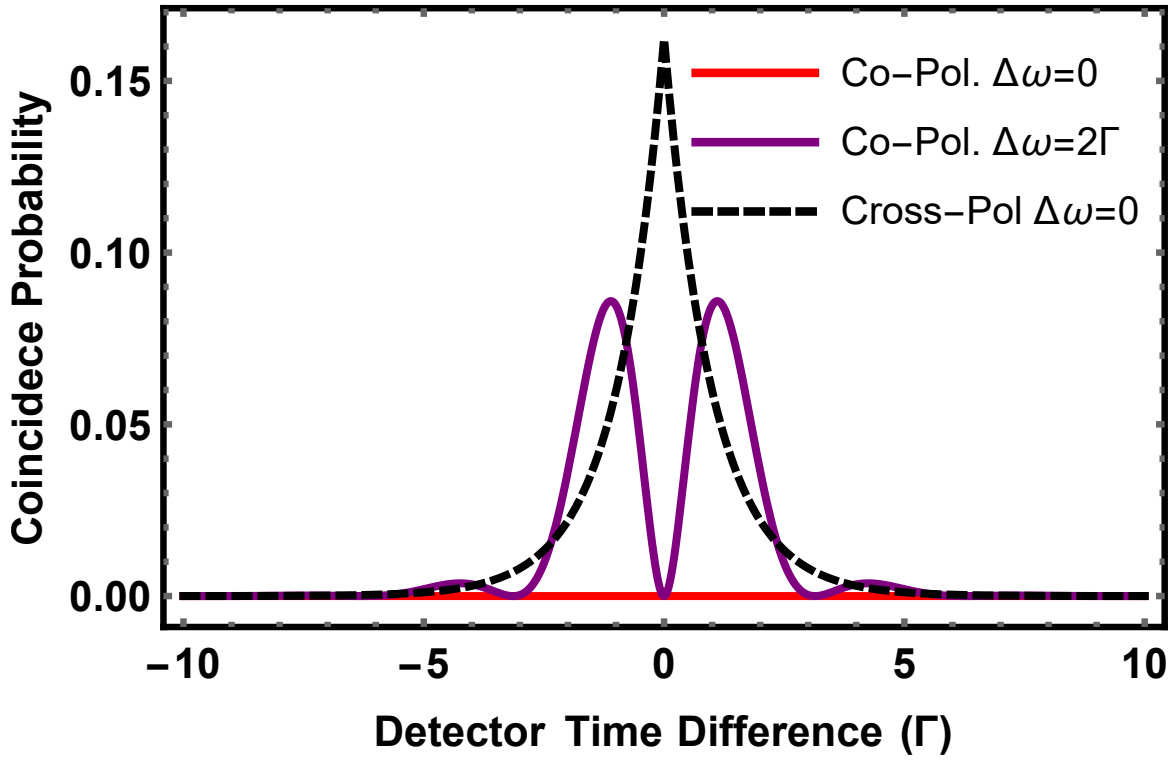

Figure 6.3: Theoretical calculation of joint photon detection probability as a function of frequency difference between the two input photons for co-polarized and cross-polarized photons.

So far we have assumed the interfering photons are Fourier limited. If we assume the input states have some frequency jitter resulting in the frequency detuning with a Gaussian distribution of width $\delta\omega$ given by,

$$f(\Delta\omega) = \frac{1}{\sqrt{\pi}\delta\omega} e^{-\Delta\omega^2/\delta\omega^2} \tag{6.20}$$

the joint detection eq. 6.18 gets modified as,

$$P_{12}(\tau, \delta\omega) = \int_{-\infty}^{\infty} d\Delta\omega P_{12}(\tau) f(\Delta\omega) \tag{6.21}$$

which results in the $cos(\Delta\omega\tau)$ getting replaced with $e^{-\delta\omega^2\delta\tau^2/4}$. Thus, any non-zero spectral jitter in the emitted photons cause the interference visibility to be reduced. $T2 = 2/\delta\omega$ can be defined as the interference coherence time [145] for a system with a non-zero spectral jitter. This result will be used later in the chapter to fit the experimental data. One can extend the calculation to include a temporal jitter in the emission process. This could happen due to the uncertainty in the emission time of the photons with respect to the excitation laser or fluctuation in the relative path delay between the two arms. As long as such temporal jitters are much smaller than the temporal length of the photon wavepacket, it does not affect the interference visibility.

6.3 Two-photon interference with QD Photons: Experiment

In this section we report on the two-photon interference measurement performed in our laboratory. The two-photon interference with resonantly excited pulsed QD photons have been reported previously [149, 21]. Nonetheless, it is important to perform the measurement for two fold reasons. First, as we are interested in interfacing the cavity-SPDC photons with a QD, it is important to verify that the QD photons are indistinguishable. And secondly, it is important to understand the experimental techniques and be able to perform the two-photon interference measurement in the laboratory.

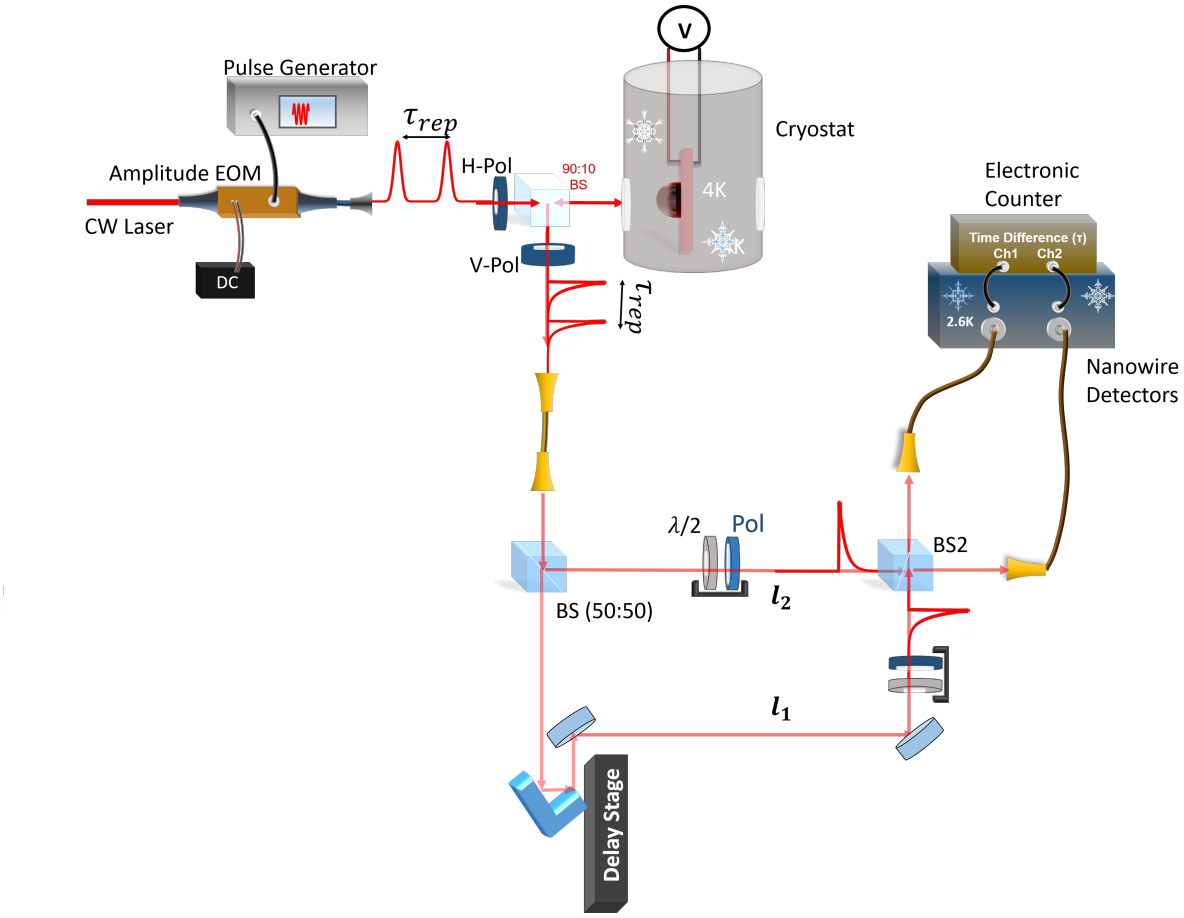

Figure 6.4: Experimental schematic of the two-photon interference with quantum dots photons. The relative arms length of the interferometer is adjusted such that $\frac{l_1 - l_2}{c} = \tau_{rep}$

A trion state at zero magnetic field is resonantly excited with a stream of 200ps $\pi-$pulses separated by 11 nanoseconds. The resonant Rayleigh emission and the time resolved resonant fluorescence emission from the trion in the study are given in Fig. 5.8 and Fig. 5.9respectively. The pulses are created by time-gating a CW-laser using an electro-optical modulator and a fast pulse generator. The spontaneously emitted photons, also referred to as resonance fluorescence, are collected in a single mode fiber in a cross-polarization setup and are sent through a free-space 50:50

non-polarizing beam-splitter to form two arms. The two arms are later combined in a second free-space 50:50 non-polarizing beam-splitter. The overall setup forms an unbalanced Mach-Zehnder interferometer. The relative length between the two arms is set to be the repetition rate of the excitation laser. As the relative pulse separation is about 11ns (7.5ns) for QD-1 (QD-2)–which is much longer than the first-order coherence length of the photon packets–there is little to no second-order field interference of an individual photon with itself. In order to get good interference visibility it is important for the input photons to be nearly identical in frequency, bandwidth, temporal, spatial, and polarization degrees of freedom. As we are using subsequent photon packets emitted by a single QD that has an excellent optical property with a very little spectral jitter, the frequency and bandwidth of the two consecutive photons are guaranteed to be nearly identical. Similarly to ensure the photon packets meet at the beam-splitter simultaneously, we send the excitation laser pulses through the HOM setup and monitor the relative time difference between the two arms using a fast detector with timing jitter of 40ps. One of the arms is equipped with a Newport delay stage that has a sub-ps delay precision. The delay stage is finely adjusted until the two excitation pulses temporally overlap at the second beam-splitter. As the excitation pulse sets the emission time of the resonance fluorescence photons within the lifetime of the excited state, this technique ensures the temporal overlap of the emitted photons within 10's of ps. Figure 6.4 is a schematic of the experimental setup.

Once the delay stage's position is set to the desired value, the spatial overlap is performed by using the following procedure. We send a nearly monochromatic CW-laser tuned to the emission wavelength of a QD through the interferometer and monitor the output ports of the second beam-splitter. Due to the long first-order coherence length of the laser, the laser fields split between the two arms interfere at the output ports of the second beam-splitter. Due to air turbulence and me-

chanical vibrations the relative phase between the two arms changes, which results in the changing interference fringes at the output of the second beam-splitter. The interference fringes are monitored with a CCD camera. We use single mode fibers mounted with aspherical lenses at the input and output ports of the interferometer. This ensures the beams before and after the second beam-splitter have well-defined TEM_{00} transverse modes. Any asymmetries in the spatial alignment at the second beam-splitter causes the fringes to have slanted dark and bright strips. The interferometer is iteratively aligned until the fringes become completely symmetric. When the spatial modes are well overlapped in the second beam-splitter, the fringes beat at a sub-Hz rate forming a completely dark and bright spot. Once the spatial mode for the interferometer is well overlapped, the two fiber inputs at the output of the second beam-splitter are realigned to maximize the output coupling of the beams. The two arms of the interferometer are equipped with half-wave plates and polarizers. This allows one to change the input polarization right before the second beam-splitter to make the input states to be co-polarized or cross-polarized as needed.

As we are interested in performing a time resolved two-photon interference measurement, it is crucial to use detectors with timing jitter better than the photon packets' temporal spread. We used two superconducting nanowire detectors with temporal jitter of 100ps to perform the measurement along with a fast electronic counter (Hydraharp 2.0) that has resolution of 2ps. An absolute detection time for the two detectors are recorded by the Hydraharp counter and is stored in the computer. Once the measurements of interests are performed, the relative detection time between the two detectors is plotted in a histogram. We performed two-photon interference measurements with several different QDs with co-linearly (indistinguishable) and cross-linearly polarized (distinguishable) input photons.

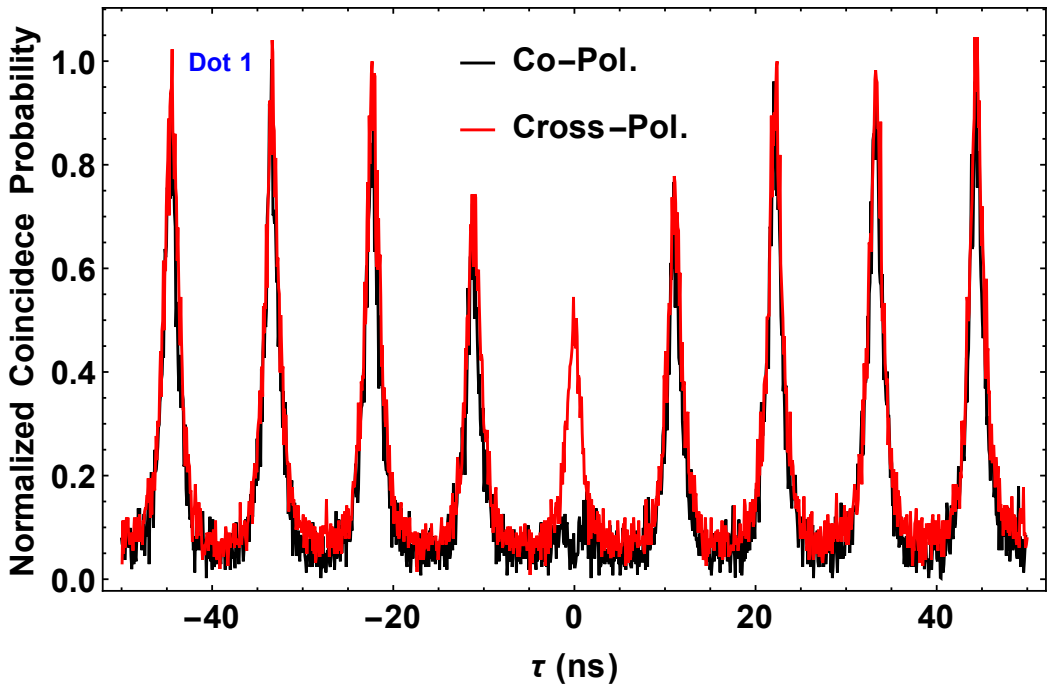

Figure 6.5: Experimental data of the two-photon interference measurement done with photons from QD-1 for the co-linearly polarized (black) and cross-linearly polarized input photons (red). The x axis is the relative time difference between the two detectors and the y axis is the normalized coincidence counts between the two detectors. At $\tau = 0$, for co-linearly polarized input photons (indistinguishable), the coincidence probability is highly suppressed close to the background level, whereas for cross-linearly polarization photons (distinguishable) the coincidence probability is finite. As there should be no interference between the photons emitted in the past and the future, there is a finite probability of detecting a photon in detector 2 at time $t + n\tau_{rep}$ after the detection of the first photon by detector 2 at time t, where n is the pulse number. The measured data is normalized by averaging the peaks away from the center to be one.

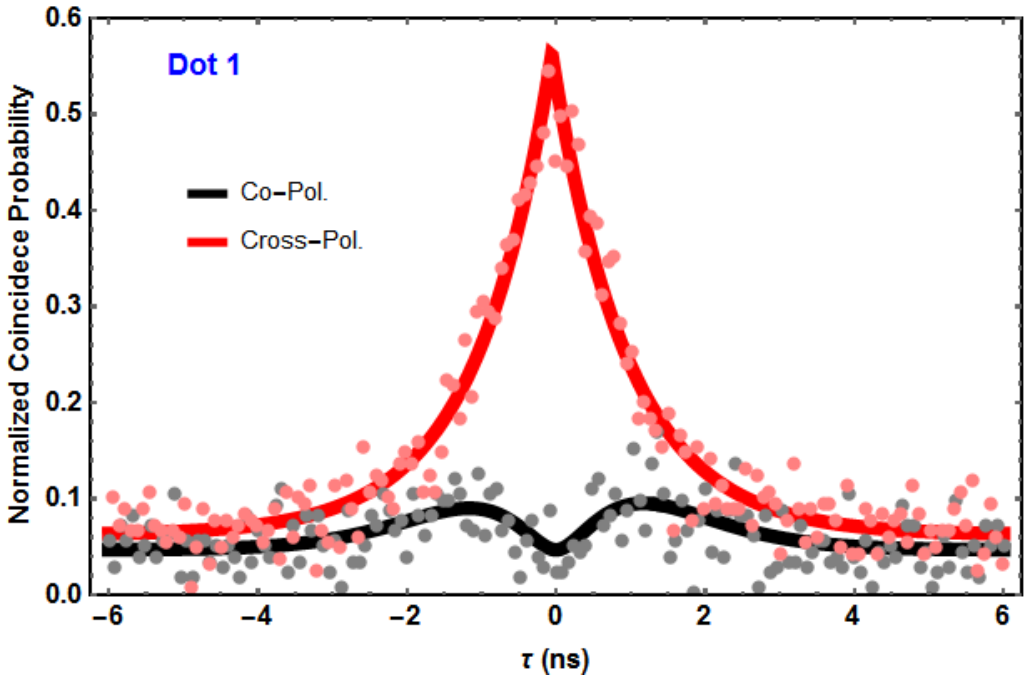

Figure 6.6: Detail plot of the two-photon interference measurement data shown in fig. 6.5 along with a theoretical fit for the co-linearly (black) and cross-linearly polarized (red) input photons. The non-zero peak for co-linearly polarized photons at $\tau \sim \pm 1$ could be caused by a spectral diffusion or mode-mismatch between the the emitted photons. The fit is obtained with $\Gamma = 2\pi * 210$ MHz and $\delta\omega = 500$ MHz.

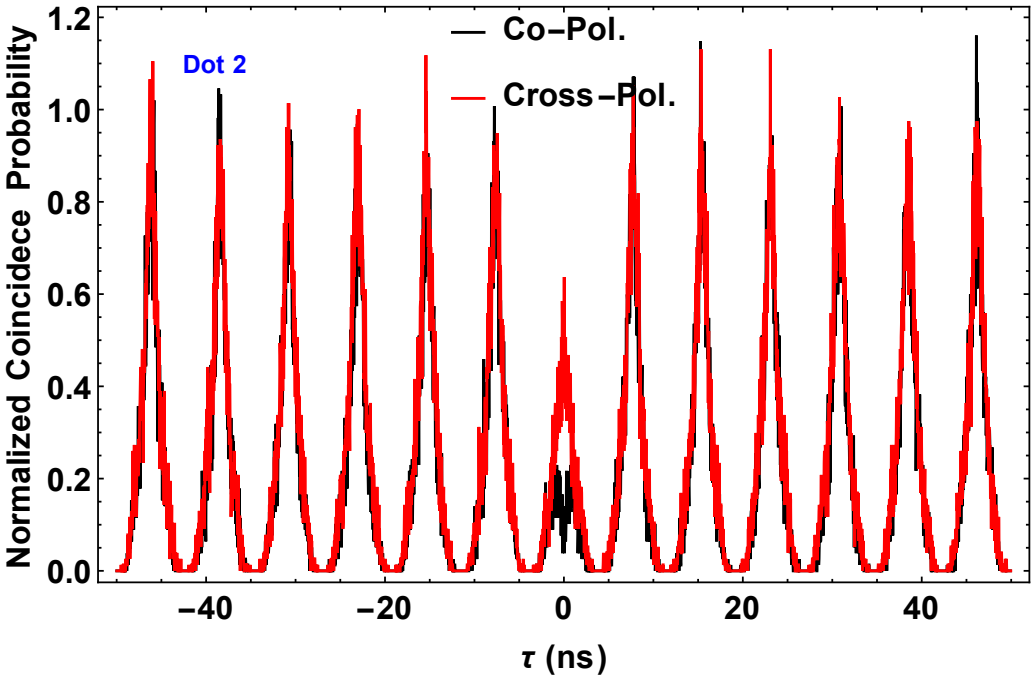

Figure 6.7: Experimental data of the two-photon interference measurement done with photons from QD-2 for the co-linearly (indistinguishable) and cross-linearly polarized (distinguishable) input photons. Similar to QD-1, the emitted photons interfere well. The repetition rate of the excitation laser and the relative delay arm is about 7 ns in this measurement such that two photon packets meet at the beam splitter (HOM setup) simultaneously.

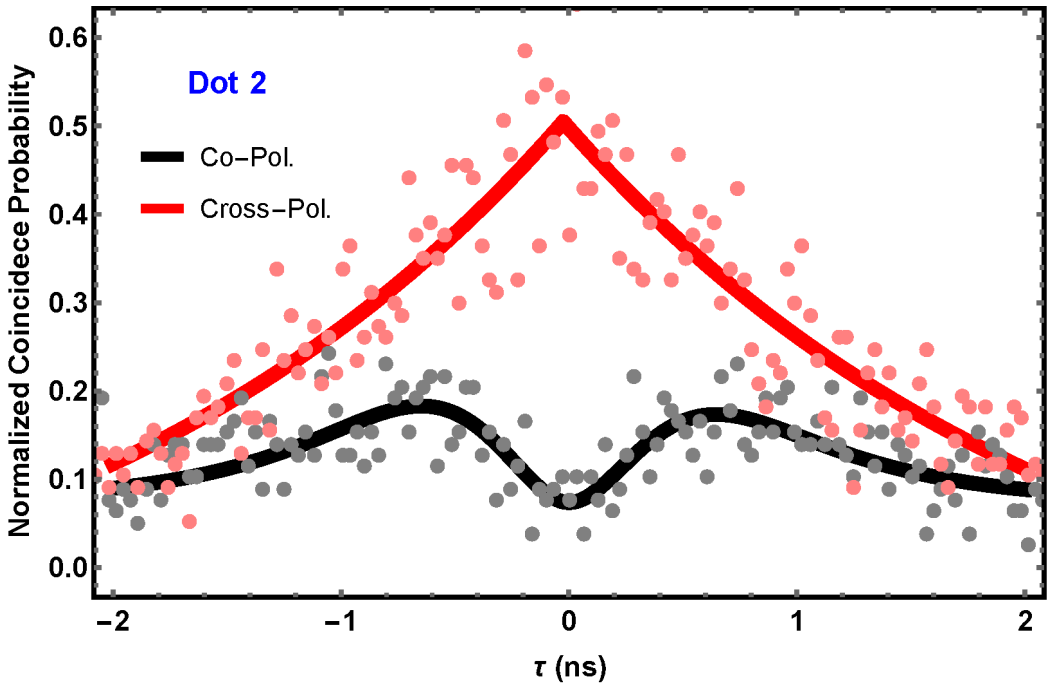

Figure 6.8: Detail plot of the two-photon interference measurement data shown in 6.7 along with a theoretical fit for the co-linearly (black) and cross-linearly polarized (red) input photons. The coincidence probability is reduced at $\tau = 0$. In comparison to fig. 6.6 for co-linearly polarized photons the coincidence probability is slightly higher. This could be caused by a spectral diffusion or mode-mismatch between the the emitted photons. The fit gives coherence time $T2 = 2/\delta\omega = 0.63ns$. The interference features are well captured for the case with non-zero spectral jitter.

Figures 6.5, 6.6, 6.7, and 6.8 are the normalized coincidence counts from the two-photon interference measurement performed with QD-1 and QD-2 for the co-linearly (indistinguishable) and cross-linearly polarized (distinguishable) input photons cases. The plots are normalized histograms of the relative time difference between detection events in each of the two detectors for various input polarization configurations. The data is normalized by averaging the peaks away from the center to be one. When

the input photons are identical, as the theory suggests, the photons should bunch together resulting in zero coincidence detection at $\tau = 0$. In all of the above plots for co-linear polarization case, the coincidence probability is significantly suppressed close to the background level at $\tau = 0$ indicating the emitted photons are nearly identical. When the input polarizations are set to be cross-polarized to each other, the photons become distinguishable resulting in no interference between the two photons beyond the classical counting probability of 1/2. The experimental data indeed verifies that for cross-polarized input photons, the coincidence probability increases to the classical correlation level. As there should be no interference between the photons that reach the second beam-splitter at different times, there is a finite probability of detecting a photon in detector 2 at time $t + n\tau_{rep}$ after the detection of the first photon by detector 1 at time t, where n is the photon shot number. This results in the multiple peaks separated by the repetition rate of the excitation pulses. Figure 6.6 and 6.8 is the zoomed-in plot for the data to show the detail features of the interference along with the theoretical fits. The theoretical fit explains the data very well. For QD-1 the coincidence counts at $\tau = 0$ is close to the background level indicating the photons are nearly indistinguishable. For QD-2, the interference visibility for parallel photons is reduced. The reduction in the interference visibility is captured by the fit when we assume the photons emitted by QD-2 have a small spectral diffusion or possibly due to the loss in mutual coherence at long times. The fit to the HOM data with QD1 gives spectral jitter 500 ± 100 MHz, which is close to the linewidth measured for the QD 410 MHz. The typical linewidths for the quantum dots in this sample range from 400 MHz to 1.5 GHz.

6.4 Chapter Summary

In this chapter we gave a detailed theoretical treatment for Hong-Ou-Mandel type interference with an arbitrary field input state. Using two multimode single photon

packets emitted by two single emitters with different center frequency and bandwidth, we theoretically solved the exact analytical form of the two-photon interference profile. We examined various theoretical scenarios that would give rise to the reduction in the interference visibility. In the last section, we discussed an experimental realization of two-photon interference measurement with subsequent single photon pulses emitted by resonantly driven QDs. The experimental data demonstrated the photons emitted by our QD sample are nearly indistinguishable. The experiment realization of such two-photon interference measurement is of importance for many quantum information protocols. In the next chapter we perform similar two-photon interference measurements between QD and SPDC photons.

CHAPTER VII

Interfacing SPDC Photons with a Single Quantum Dot: An Elementary Building Block for Quantum Networks

The basic building blocks of a quantum network can be broken into two parts: matter nodes for storing and manipulating information locally and photonic qubits to link the distant nodes. The basic idea behind a quantum network is to form quantum nodes confined in space that are locally interacting and are in connection with other nodes at a distance. This way one can form quantum non-local connections, forming a network between a large number of nodes. With a quantum network, one can faithfully transfer quantum information.

Quantum nodes can be linked several different ways. By bringing the two matter qubits in proximity, they can be entangled with each other through the local Coulomb interaction [18, 19]. Alternatively, by performing HOM type interference between the flying qubits emitted by the two matter nodes of interest, one can interface distant nodes [20, 149, 21]. If the emitted photons are entangled with the nodes, with a Bell state's analysis, the distant nodes can be entangled with each other [20]. Similarly, there exists a third class of protocols where the nodes separated by some distance can be connected with each other through the direct absorptions of single photons [23, 24].

Cirac *et al.* developed a protocol where two atoms of interest for quantum linkage are embedded inside two high-Q cavities [27]. One of the atoms is optically manipulated using lasers and is prepared in a desired state. In the process, the atom emits a packet of photons with the internal state of the atom mapped on to the photon. The photon packet propagates to a nearby atomic site through a waveguide or a transmission channel and gets absorbed by the second atom. Through the absorption process, the internal state of the first atom can be mapped to the second atom, creating direct links for the exchange of quantum information between two spatially separated atoms [26, 22, 25].

A realistic quantum network could be composed of several different systems, each with different electronic and optical properties. To envision such a hybrid network that could utilize the best features of each system, one needs to build a highly flexible photon pairs source that can form links between two disparate systems [47]. A type II spontaneous parametric down-conversion (SPDC) source could form a flexible link that can be either used as a heralded single photon source or a source of polarization entangled photons [48]. By engineering the phase matching conditions, SPDC sources are shown to emit highly non-degenerate photons and are wavelength-tunable by several hundred nanometers [49]. This allows one to link two systems at very different wavelengths. In addition, by placing the down-conversion crystal inside an optical cavity, it is shown that the emitted photons' temporal and spectral properties can be modified as desired while enhancing the count rates of the down-conversion photons [50]. Such large wavelength tunability, along with the customizable spectrum, makes cavity-SPDC an excellent source to generate highly flexible entangled photon sources.

In the previous chapters, we gave a detailed account of such cavity-SPDC sourcse built to mode match with a single InAs QD. In this chapter, we will report on two classes of measurements done to link cavity-SPDC sources with QDs thorough two-photon interference between the SPDC and QD photons, and through direct excita-

tion of single QD using the SPDC photons.

7.1 Two-Photon Interference Between Signal Photons and QD Photons

For two different photons to optimally interfere with each other, the spatial, temporal, polarization, and spectral modes of the photon wave functions need to overlap perfectly. We have successfully designed and implemented a cavity-SPDC source that emits a pair of polarization-correlated photons at 942 ± 2 nm. The cavity parameters are designed such that the emitted photons are mode-matched with the QD photons.

A mode-locked Ti-sapphire laser (Tsunami laser by Spectra Physics) with 50 ps pulse width, and 76 MHz repetition rate operating at 941.85 nm is used to pump a PPKTP crystal to generate blue light at 470.98 nm through a SHG process. The second-harmonic crystal is temperature-tuned to obtain phase-matching for maximum blue light generation. The 941.85 nm beam will be referred to as the fundamental beam and the 470.98 nm beam will be referred to as the pump beam. As described in Ch. 4, the main component of the cavity-SPDC setup is composed of a 5 mm long PPKTP crystal and 2 mm long KTP crystals. A semi-confocal cavity is formed by using the two ends of the crystals that are HR-coated at 942 nm with reflectivites 99.8% and 90 %. The PPKTP crystal is used for Type II down-conversion and the KTP crystal is used for compensating the birefringence mismatch between the signal and idler photons. The down-conversion crystal is periodically poled with length of $\Lambda = 33.25\mu$m to achieve degenerate operation at 941.85 nm. This is achieved by tuning the PPKTP crystal to 27°C.

Due to the free-spectral range (FSR) mismatch between the signal and idler photons in the cavity, the cavity modes are mismatched. Both the signal and idler photons are brought to degeneracy with the mode of the cavity, overlapping at the fundamen-

tal frequency, by further tuning the temperature of the KTP crystal. The PPKTP and KTP crystals are mounted on two separate copper blocks, each equipped with a thermoelectric heater and a temperature sensor. The temperature of the crystals are stabilized to the desired value within 10 mK accuracy using a PID controller. At the degenerate operation point, the signal and idler photons are co-linearly emitted, both centered on the fundamental beam. The down-converted photons are linearly cross-polarized.

The finesse of the cavity is designed to be ~ 58 and the FSR is 8.9 GHz. This results in a cavity bandwidth of 153 MHz, which is designed to match the Fourier-limited linewidth of InAs QDs. As the FSR of the cavity is much smaller than the emission bandwidth of the down-conversion crystal (540 GHz), the down-conversion crystal emits into several modes of the cavity. This results in a a highly multi-mode photon emission. The mode degenerate to the fundamental beam will be referred to as the $m = 0$ mode. To obtain a single-mode operation, a 6 GHz solid etalon with a 695 GHz FSR is mounted at the collection arm and is aligned to pass photons centered at 941.85 nm (10617.35cm^{-1}). The output of the etalon is sent to a polarizing beam splitter that splits the signal and idler photons into two arms. The signal and idler photons are collected in a single mode fiber. The collected photons occupy the $m = 0$ mode of the cavity centered at 10617.35cm^{-1} with a bandwidth of 150 MHz.

For the two photons to interfere with each other, the spectral, temporal, spatial, and polarization modes between the two photons need to be identical. The temporal and spectral bandwidth of the SPDC source is designed to match with the QD photons. It is important that the central frequencies of the QD and the SPDC photons are identical. Once the cavity-SPDC central frequency is determined, we search for a trion state with emission within a wavenumber of 10617.35 cm^{-1}. Once an isolated QD is found, the QD's transition frequency is finely tuned by Stark-shifting the QD with an external bias voltage. The emission energy of the QD is matched with

the SPDC source. This is verified by sending the QD and SPDC photons through a pressure-tuned Fabry-Perot etalon. With the etalon, we can determine the emission frequency within a few hundred MHz. Once an appropriate QD matching the SPDC photons is found, we excite the single QD using a fraction of the power ($\sim$ 10 nW) from the Tsunami laser, which emits 50 ps pulses at a 76 MHz repetition rate. As both the QD and the SHG crystal are excited with the same laser, any drift in the energy will be mutual, thus the QD and SPDC photons are always within the bandwidth of the laser pulse frequency bandwidth ($\sim$ 6 GHz).

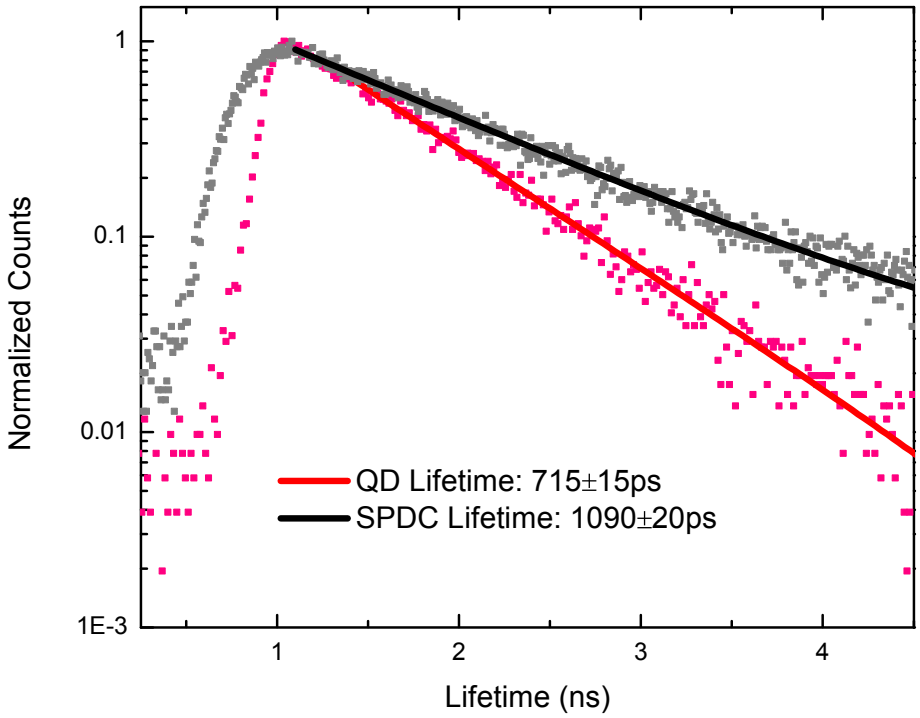

Figure 7.1: Lifetime comparisons between SPDC and QD photons.

The temporal profiles of the signal photons from cavity-SPDC and the QD photons are given in Fig. 7.1. The data is obtained by exciting a single QD with the same laser that pumps the SHG crystal. The temporal profile is obtained by time-tagging

the SPDC and QD photons by electronically syncing the detection time with the pulses from the Tsunami laser. The SPDC emission lifetime and the QD lifetime are fitted with a single exponential function. From the fit, we obtain the SPDC and QD lifetimes to be 1090 ps and 710 ps respectively. The QD lifetime varies anywhere from $600 - 1000$ ps in the sample. The lifetime of the cavity-SPDC can be tuned from 800 ps to 1300 ps by changing the cavity length. Even though the lifetime is different by almost 40%, the difference is not significant enough to degrade the interference visibility between the QD and the SPDC photons. See Dyckovsky and Olmschenk's work for mode mismatch and its impact on the two-photon interference visibility [152].

We perform two-photon interference measurement as described in the previous chapter between the signal photons emitted from the cavity-SPDC source and the QD photons. A schematic of the experimental setup is given in Fig. 7.2. The filtered cavity-SPDC photons and the QD photons are sent to a free-space 50:50 beam-splitter (BS) and the outputs of the beam-splitter are monitored with two superconducting nanowire detectors that has timing jitters of 80 ps and 100 ps. The photon packets are temporally and spectrally overlapped at the BS with techniques described in Ch. VI. The detection time is recorded using a fast electronic counter that has 2 ps timing resolution.

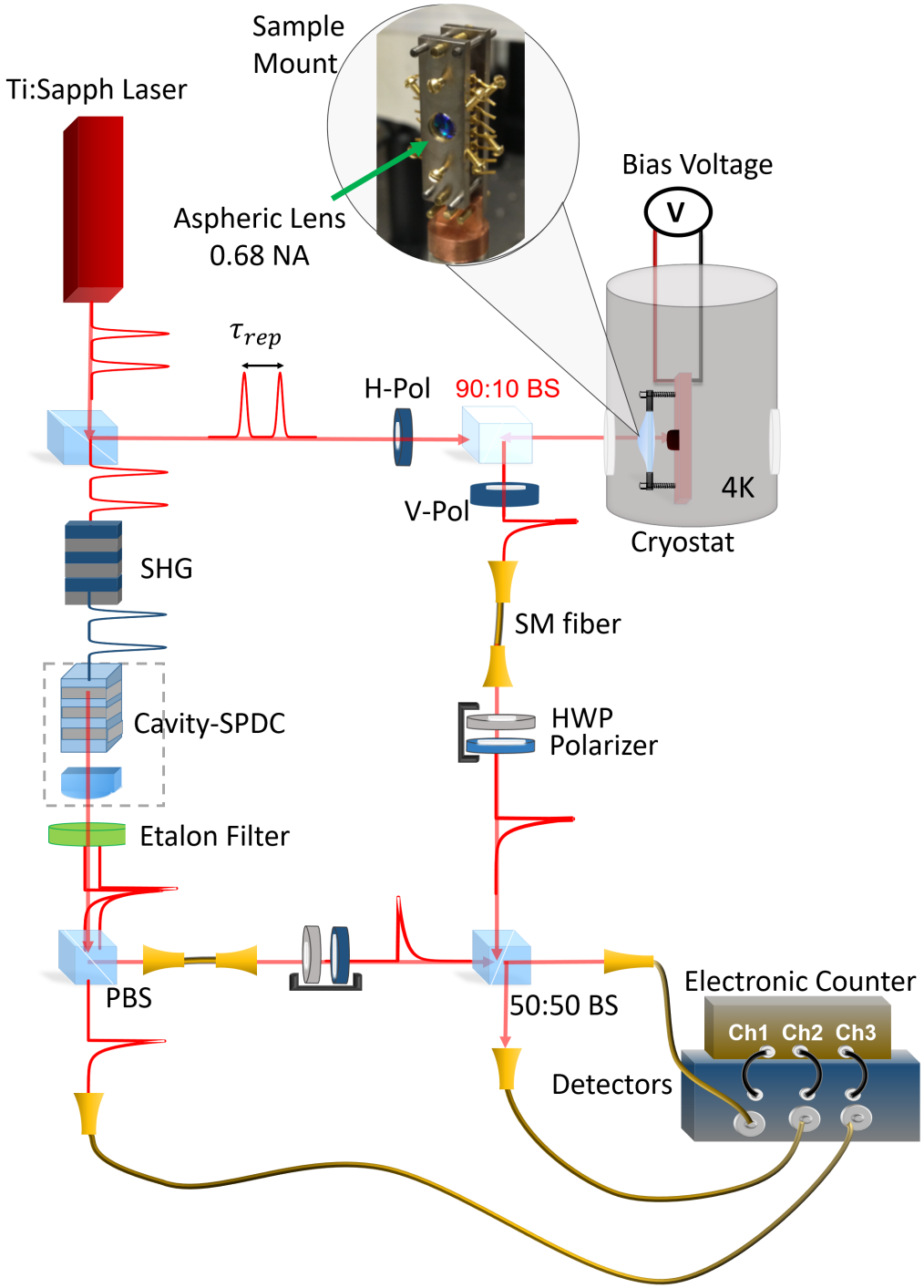

Figure 7.2: Experimental setup for two-photon interference between the cavity-SPDC and QD photons.

The experiment is performed, with the setup given in Fig. 7.2. Once the measurement is performed, the data is analyzed to search for the coincidence counts between two detectors within a 100 ns time window. The resulting data is plotted in a histogram as seen in Fig. 7.3, where the x-axis is the relative time difference between the two detectors and the y-axis is the normalized coincidence counts between the two detectors.

Figure 7.3 is the experimental data of the two-photon interference measurement between the signal photons from the cavity-SPDC source and the QD photons for linearly co-polarized and cross-polarized incident photons in the 50:50 BS. If the photons are indistinguishable, which results in the interference between the two photons, then the coincidence counts at $\tau = 0$ drop. This is due to the Hong-Ou-Mandel effect discussed extensively in Ch. VI. To quantify the interference between the QD and SPDC photons, two separate measurements are done: one with the input photons in the $50:50$ beam-splitter to be co-linearly polarized (black curve in Fig. 7.3) and the second with the photons to be cross-linearly polarized (red). Each measurements are done by integrating for an hour. At time zero, for co-linearly polarized input photons (indistinguishable), the coincidence probability is suppressed relative to the cross-linearly polarized photons (distinguishable). As there should be no interference between the photons emitted in the past and the future, there is a finite probability of detecting a photon in detector 2 at time t + n τ_{rep} after the detection of the first photon by detector 1 at time t, where τ_{rep} is the repetition rate of the excitation laser (13.25 ns) and n is the pulse number. The measured data is normalized by averaging the peaks away from the center to be one.

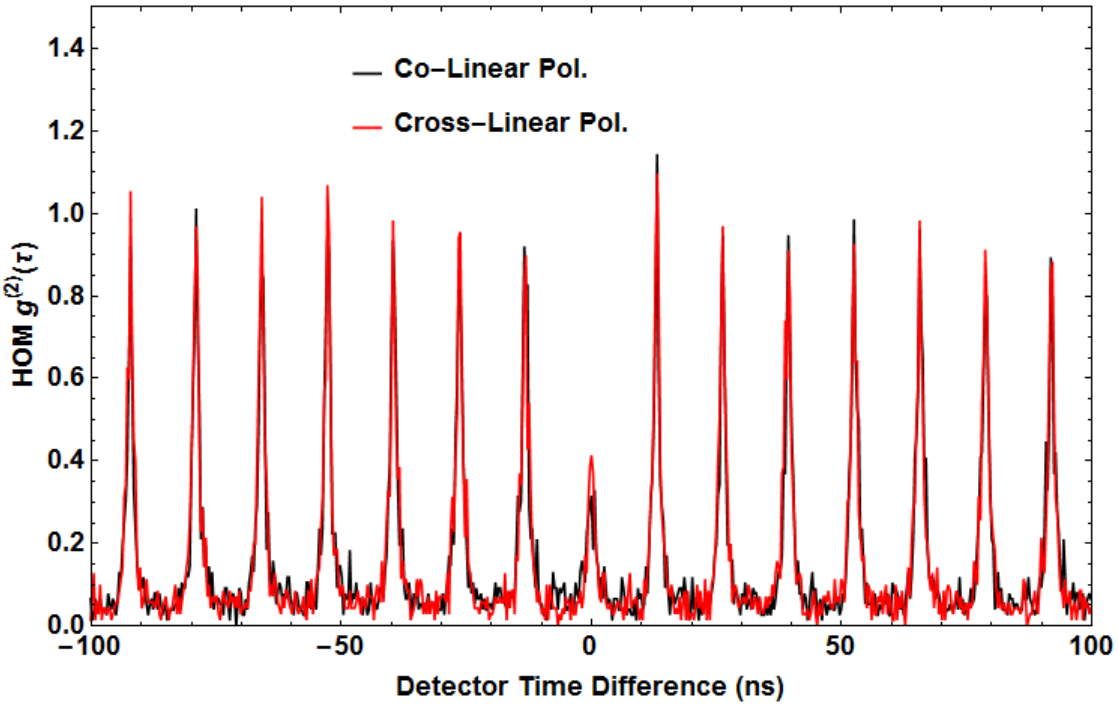

Figure 7.3: Experimental data of the two-photon interference measurement between the signal photons from the cavity-SPDC source and the QD photons. Two separate measurements are done, with the SPDC and QD photons at the input ports of the 50 : 50 BS linearly co-polarized (black) and linearly cross-polarized (red). The x-axis is the relative time difference between the two detectors and the y-axis is the normalized coincidence counts between the two detectors. At time zero, for co-linearly polarized input photons (indistinguishable), the coincidence probability is suppressed relative to the cross-linearly polarization photons (distinguishable). As there should be no interference between the photons emitted in the past and the future, there is a finite probability of detecting a photon in detector 2 at time t + n τ_{rep} after the detection of the first photon by detector 1 at time t, where n is the pulse number. The measured data is normalized by averaging the peaks away from the center to be one.

Figure 7.4 is the detailed plot of the two-photon interference measurement data shown in Fig. 7.3 along with a theoretical modeling for the co-linearly (black) with infinite detector timing response and cross-linearly polarized (red) input photons. The dashed-blue line modeled for the co-linear case is obtained by convolving the theory given in Eq. 6.21 with the instrument-response function (IRF) given in Fig. 4.14 and the dashed-gray line is for a large frequency jitter. (c). The theoretical modeling of the data with the spectral jitter (mismatch between SPDC and QD) of 6 GHz can be attributed to the linewidth of the external filter cavity, as the frequency overlap was determined within the filter bandwidth. This is due to the drift in the cavity length, resulting in the frequency drift of the SPDC photons relative to the QD photons. Even though the modeling to the data with large spectral jitter and expected 6 GHz spectral jitter is not significantly different, a presence of a possible interference can be calculated by integrating the area under the curve and comparing them for the distinguishable and indistinguishable cases.

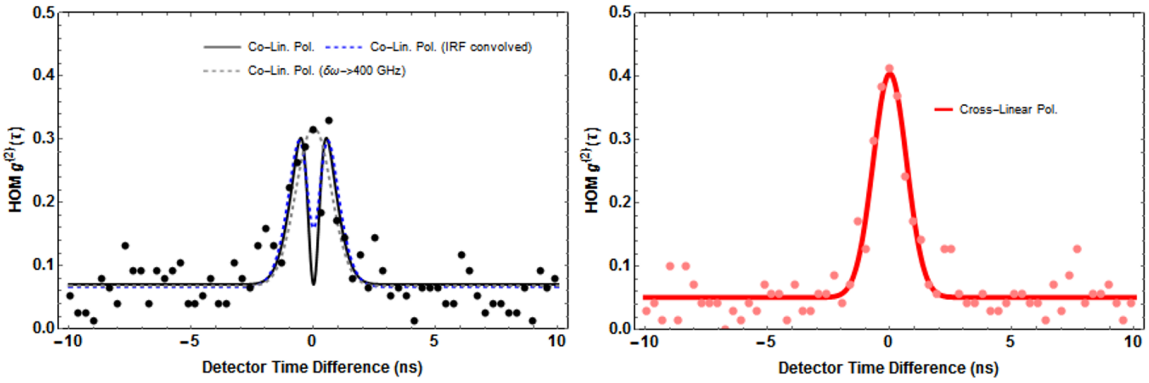

Figure 7.4: Detailed plot of the two-photon interference measurement data shown in Fig. 7.3 along with theoretical fits for the co-linearly (black) and cross-linearly polarized (red) input photons. For the co-linear case, the lines are modeling of the data from the theory with infinity detector timing resolution (black), convolved with the IRF (dashed-blue) given in Fig. 4.14 and a large frequency jitter (dashed-gray). The theory is obtained from the convolution of Eq. 6.21 with IRF. (c) The drop in the coincidence counts for co-linear case relative to the cross-linear case can be attributed due to the two-photon interference between the QD and SPDC photons.

To quantify the indistinguishability between the QD and SPDC photons, we can define the interference visibility as

$$\text{visibility} = \frac{A_{cross-lin.} - A_{co-lin.}}{A_{cross-lin.}} \tag{7.1}$$

where $A_{cross-lin.}$ and $A_{co-lin.}$ are the normalized areas at the $\tau = 0$ bins from the two-photon interference raw data, where the input photons in the 50 : 50 BS are cross-linearly and co-linearly polarized. If there is no interference between the two

photons, the visibility goes to zero. If they interfere perfectly, $A_{co-lin.}$ goes to zero, resulting in a visibility of one.

From the reported two-photon interference measurements between the SPDC and QD photons, we obtain an interference visibility to be 0.32 when looked within a 500 ps time window about $\tau = 0$. This post-processed visibility number of 32% indicates that the SPDC and QD photons are closely identical. The interference visibility is reduced for several reasons. The experiment was performed with ~ 40 mW pump power, at which the heralded $g^{(2)}(0) \sim 0.4$. Such non-zero $g^{(2)}$ implies a finite multi-photon emission probability, which reduces the interference visibility. One could perform the experiment with a low pump power for which $g^{(2)}(0) \sim 0$, however lower pump power means lower photon counts. This would require long integration time to obtain any meaningful data. In additional, the interference visibility would increase further if the experiment were performed with heralded photons. Due to the SPDC cavity stability issue and the limited photon count, we couldn't integrate the data for sufficiently long time to obtain heralded two-photon interference.

7.2 Direct Excitation of a QD with SPDC Single Photons

As discussed in the introduction section, distant nodes can be connected with each other through a cascade excitation system, where the first node is excited with a laser pulses and then the photon emitted by the first node is sent to the second node where the single photon gets "absorbed". Through such a cascaded excitation process, the internal state of the first node gets mapped on to the second node [26]. A successful transfer of information from the first node to the second node can be verified by reading out the photons emitted by the second node and the spin states of the node. Such cascaded quantum systems have been recently demonstrated between SPDC photons and a single ion [22], between two QDs [26], and between a QD and an ion [25].

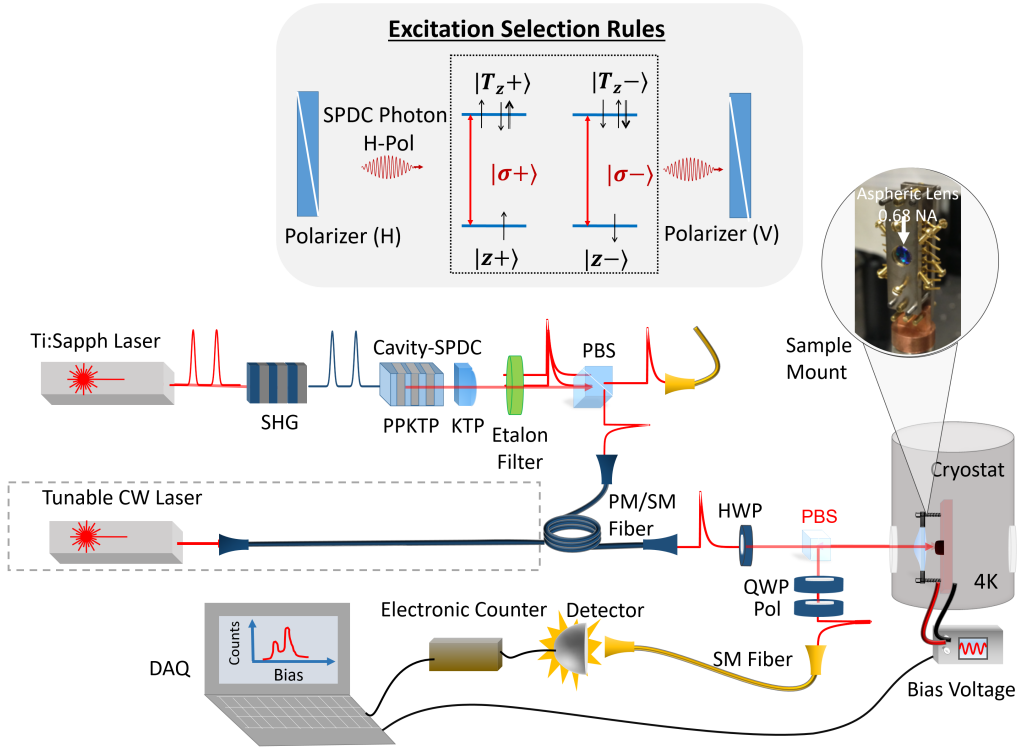

Figure 7.5: Experimental setup for direct excitation of a single QD with SPDC photons. The dash box is a removable setup used to find the single QD in study. Once a single QD is identified at the wavelength degenerate with the down-conversion photons, the fiber connecting the CW-laser to the setup is disconnected and connected to the photons collected from the cavity-SPDC source.

Here, we use the photons emitted from the cavity-SPDC source to directly excite a single QD. As described in the previous section, the PPKTP and KTP crystals' temperatures are tuned to obtain a degenerate operation at 10617.48 cm^{-1} wavenumber, where the signal and the idler photons are degenerate with the fundamental beam. The emission energy is slightly shifted from the previous measurement. The output of the cavity-SPDC is filtered with a 6 GHz solid etalon centered at the fun-

damental beam, sent through a polarizing beam splitter, and coupled to two single mode fibers. The collected photons occupy the $m = 0$ mode of the cavity centered at 10617.48 cm^{-1} with a bandwidth of $\sim$ 150 MHz. A single trion state with the same transition frequency is found using a CW-laser. The trion in this study is different than the one used in the previous experiment. First, the trion state at zero magnetic field is studied resonantly in a cross-polarization setup by counting single photons scattered by the QD. As given in the top inset of Fig. 7.5, at zero magnetic field, a trion state forms two degenerate two-level system that can be excited with circularly polarized light. Instead of using a 90:10 BS before the cryostat, a 50:50 polarizing beam-splitter (PBS) is used before the cryostat. A quarter-wave plate is introduced after the PBS to compensate for any birefringence rotation of the excitation field. By exciting the trion with linearly polarized light and projecting the scattered single photons onto the polarization orthogonal to the excitation beam, we can collect single photons scattered by a QD with 100 : 1 signal to background ratio. Figure 7.6 (a) is the intensity profile of a single trion state used in the study measured through resonant Rayleigh scattering by scanning the sample bias for a fixed excitation laser frequency. The details of the excitation protocol are given in Fig. 7.5.

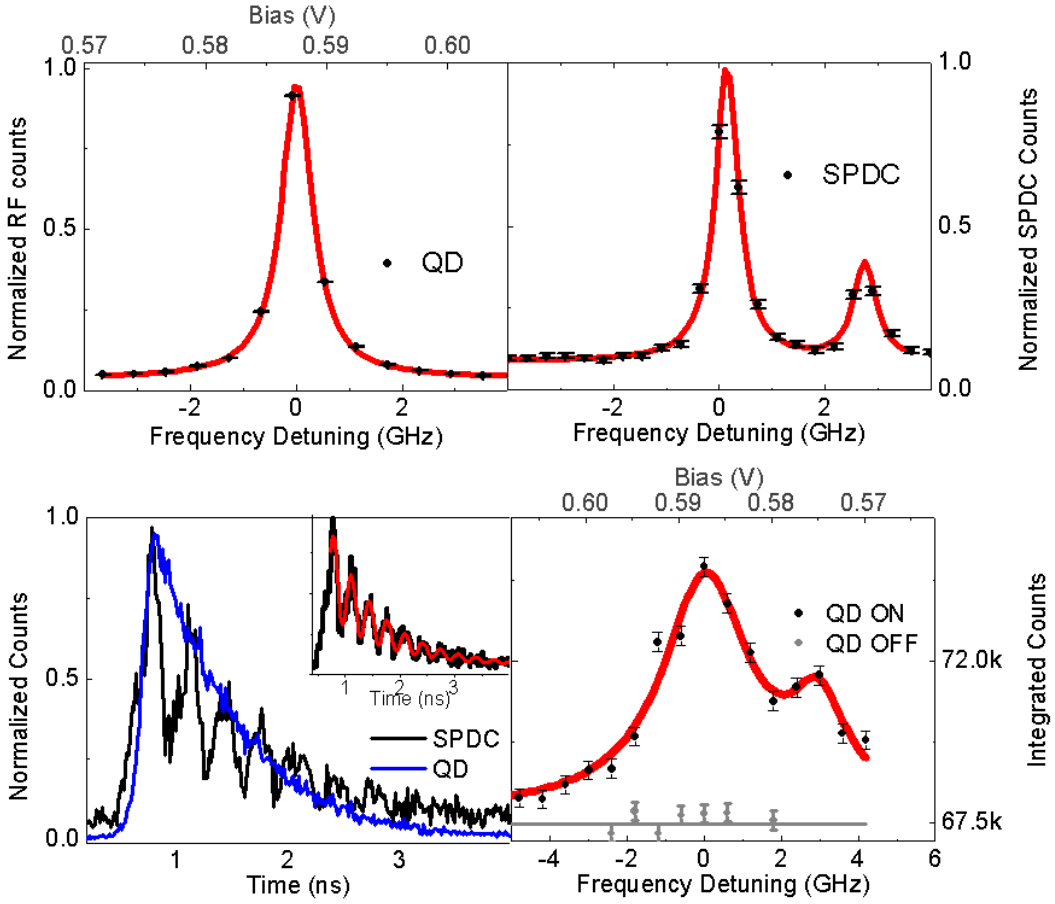

Figure 7.6: Schematic of the experimental setup for exciting a single quantum dot directly with SPDC photons. (a) Integrated photons scattered from a single QD as a function of bias scan. The spectrum is obtained by tuning a CW-laser to the resonance of the QD trion. (b) SPDC spectrum where the x-axis corresponds to the Fabry-pérot etalon detuning and (c) time-tagged photon emissions from a single trion state (blue) and SPDC signal photons (black). The inset is the spdc signal fitted with 3 GHz oscillation which is due to the beating between the $\mathrm{TEM}_{m=0,n=0}$ and $\mathrm{TEM}_{m\neq 0,n\neq 0}$ modes. (d) SPDC single photons scattered by a single QD. The gray dots are the data with the QD bias off. For all the spectral plots, the x-axis is detuning from the center frequency 10617.48 cm^{-1}.

Figure 7.6 (b) is the spectrum of the cavity-SPDC signal photons (after the filter etalon) used to excite the QD. The spectrum of the signal photons is obtained by using a pressure-tuned etalon and the x-axis corresponds to the Fabry-pérot etalon detuning. The center peak is due to the $\text{TEM}_{m=0,n=0}$ mode of the cavity and the smaller peak on the left is due to the $\text{TEM}_{m\neq 0,n\neq 0}$ mode of the cavity, which are separated by $2.8 \pm .2$ GHz [115, 116]. Due to the finite bandwidth of the filter etalon, both peaks are used to excite the QD. Figure 7.6 (c) is the temporal profile of the cavity-SPDC signal photons (black) and the QD photons (blue) obtained by exciting with the Tsunami laser and building time-tagged emission by syncing the emission time with the laser pulse. The QD in the study has a lifetime of 751 ps and the SPDC has a lifetime of 932 ps. The inset shows the oscillation of the temporal profile of the cavity-SPDC photons due to the beating between the two cavity modes. The red curve is an exponentially decaying curve with sinusoidal oscillation fit to the integrated counts of cavity-SPDC signal photons right before they sent to interact with the QD. The oscillation frequency is $3.06 \pm .1$ GHz, consistent with the spectral profile of signal photons given in Fig. 7.6 (a).

The cavity-SPDC source is excited with 40 mW of blue light and the collected signal photons are sent through the QD setup. With a half-wave plate before the PBS, the polarization of the signal photons is rotate to obtain maximum transmission through the beam-splitter. The QD is excited with 60,000 signal photons per second, utilizing the same setup as given in Fig. 7.5. The fiber from the CW-laser is detached in the experiment. When linearly polarized input cavity-SPDC photons are in resonance with the QD transition energy, the QD is excited and emits circularly polarized single photons. By collecting the photons cross linearly polarized to the incident photons, we can ensure the collected photons are emitted by the QD. We detected the emitted photons with high-efficiency superconducting nanowire detectors (efficiency of 70%) while changing the resonance energy of the QD transition with

Stark-shift effect. The black dots in Fig. 7.6 (d) correspond to the total photon count integrated for 10 minutes at each bias voltage. And the gray dots correspond to the background counts when the QD is turned off by unplugging the bias. As we tune the bias voltage, the two different frequency components of the cavity-SPDC photons separated by 3 GHz come in and out of resonance with the QD transition. As a result, more photons are scattered and detected at the resonances. As one would expect from the Stark shift of the trion, the higher frequency peak shows up at lower bias, consistent with the measured data. All the important features of the SPDC photons are mapped on to the direct excitation data seen in Fig. 7.6 (d). The red curve is a fit to the data with two Voigt peaks where they are split by 3 GHz, consistent with the cavity-SPDC spectral modes used to excite the QD. The broadening of the linewidth is due to the cavity-SPDC drift over time, which is not locked for the measurements performed in this chapter.

When the QD is turned off, there should be no scattering events detected and the counts should be dominated by the detector dark count. The dark count for the detector is 110 counts per second. For 10 minutes integration time, we expect 66 thousands dark counts, which is consistent with the background counts measured when the bias is off. From the resonant fluorescence and absorption measurements performed with the dots, we expect the excitation efficiency to be $\sim 2\%$ excitation efficiency and 1% collection efficiency for the sample; for 60,000 incident photons per seconds, we expect to obtain ~ 12 scattered events per second, with 7200 events for the integration time. This number is consistent with the signal counts above the dark counts obtained in Fig. 7.6 (d) when the QD bias is on. With this data, we have successfully demonstrated a cascaded quantum system where a single QD is excited with spectral engineered photons emitted from a cavity-SPDC source.

7.3 Chapter Summary

In this Chapter, we have given a brief overview of different ways to link distant nodes to build a quantum network. We demonstrated the photons emitted by the cavity-SPDC source are closely mode matched with the QD photons. Through two-photon interference measurements, we showed the cavity-SPDC photons interfere with the QD photons. Also, by using the cavity-SPDC photons, we were able to directly excite a single QD. This demonstration serves as an alternative method to map quantum states between two distant nodes through cascaded quantum systems.

The reduction in the two-photon interference visibility between the QD and cavity-SPDC is limited by the cavity-SPDC photons. In the previous chapters we were able to demonstrate two-photon interference between two distant shots from a single QD with visibility exceeding 90%. The low interference visibility can be improved by performing the experiment with heralded signal photons and with a low pump power. Due to the limitations in the photon count rate and the instability issue with the cavity, we were not able to perform a heralded interference measurements. This could be addressed through a redesign of the cavity-SPDC setup. One major improvement can be made by mounting the crystals in the more stable housing that allows a fine tuning of the cavity length, as the cavity stability was a major issue in the experiment. In addition, a thin etalon with bandwidth smaller than the cavity-FSR but with a FSR larger than the down-conversion bandwidth could be inserted inside the cavity. If the FSR of the SPDC cavity and the thin etalon are mismatched, the down-conversion happens only at the degenerate mode (the down-conversion, cavity-SPDC, and the thin etalon are degenerate), which will actively suppress the emission from the unwanted modes (non-degenerate to the fundamental beam), while increasing the brightness of the source.

The reported measurements should lay a foundation towards building quantum repeaters [16], which will be an integral part of a hybrid quantum network.

CHAPTER VIII

Spectral Modification of Single Photons with a Phase Modulator

Generation and manipulation of the quantum state of a single photon is at the heart of many quantum information protocols. It has been experimentally shown that the temporal profile of a single photon can be post-modified through time-gated modulation techniques [153, 154]. Similarly, the frequency of a single photon can be changed with parametric processes [155]. In this chapter, we will give a theoretical description of the state-vector of a single photon packet modified with a phase-modulator. Then, we will demonstrate the modification of the single photon packet emitted by a quantum dot using an electro-optic phase modulator and generate new frequency components (modes) where the new modes have well-defined phases relative to the central mode. Through two-photon interference measurements, we show that for an output consisting of three modes (the original mode and two side bands on either side) the indistinguishability of the spectral modified single photons are well-preserved. The sideband generation technique can be employed to generate a frequency qubit or qutrit out of a single photon and also for encoding information in the frequency sidebands for quantum cryptography [56, 59, 156, 157, 55].

8.1 Classical Description of Phase Modulation

Phase modulators are widely used for various communication applications [158]. They exploit the linear electro-optic effect to modulate the index of the material. When a monochromatic electric field with amplitude E_0 and frequency ω_c is sent through a phase modulator, the input and output fields can be written as

$$\begin{aligned} E_{in} &= E_0 e^{i\omega_c t} \\ E_{out} &= E_0 e^{i\omega_c t - i\phi} \end{aligned} \tag{8.1}$$

where $\phi = \frac{2\pi}{\lambda} n_x L$ is the phase factor gained by the field of wavelength λ traveling through a medium with index n_x and length L. When the modulator is driven with a sinusoidal voltage $V = V_m \sin(\Omega t + \theta)$, the index of refraction is modified due to the applied electric field,

$$\phi = \frac{2\pi}{\lambda}(n_x + \Delta n_x)L \tag{8.2}$$

For a transverse modulator, where the microwave field is applied transverse to the optical field propagation, the change in the phase factor becomes [158]

$$\Delta n_x = -\frac{1}{2} n_x^3 r \left(\frac{L}{d}\right) V_m \sin(\Omega t + \theta) \tag{8.3}$$

Where r is the interaction coefficient and d is the thickness of the crystal across which the voltage is applied. With the modified phase, the output field can be rewritten as

$$E_{out} = E_0 e^{i\omega_c t - i\phi_0 - i\beta \sin \Omega t} \tag{8.4}$$

where $\phi_0 = \frac{2\pi}{\lambda} n_x L$ is the time-independent phase factor and $\beta = \frac{\pi}{2} n_x^3 r (\frac{L}{d}) V_m$ is the modulation index, proportional to the applied voltage. The constant phase factor can be absorbed into the electric field amplitude and the exponential can be expanded as

a sum of the coefficients of the Bessel functions of the first kind (J_n),

$$E_{out} = E_0 \sum_{n=-\infty}^{\infty} J_n(\beta) e^{in(\theta-\pi/2)} e^{i(\omega_c+n\Omega)t}. \tag{8.5}$$

The result is the well known result for the phase modulation of a classical electric field, where multiple sidebands are created at the harmonics of the applied microwave field. The Bessel coefficients are a function of the applied microwave voltage and the relative amplitude of the sidebands can be changed by changing the voltage.

8.2 Quantum Mechanical Modeling of Phase Modulation

There are several theoretical papers that explore the quantum nature of the phase modulator [159, 160]. From its classical behavior, one can derive a very simplistic phenomenological picture of a phase modulator: a birefringent crystal driven with a microwave field of frequency Ω. When a temporally and spatially localized single photon-packet is sent, the interaction process destroys a single quanta of the optical photon at frequency ω and creates a new photon of frequency $\omega \pm \Omega$.

Such an interaction falls under the category of parametric interactions, which are well-understood in non-linear optics. We will draw closely from WH. Louisell, *et. al's* quantum mechanical description of parametric processes in [161] and use Hamiltonian for phase modulators as the one described by G. P. Miroshnichenko *et al.* [159].

Let us assume that the phase modulator is built of a non-linear crystal of length L. The surfaces are anti-reflectance coated. At 0 K temperature, we can quantize the fields inside the crystal, where the wall sets the periodic boundary condition [97, 161, 162] and define the quantized modes of the crystal as

$$k_m = \frac{2\pi m}{L}, \quad m \in \mathbb{Z} \tag{8.6}$$

The center frequency (ω_c) of the input optical photonpacket can be expressed as the modes of the modulator cavity:

$$\omega_c = \frac{2\pi m}{L} v_{opt} = \Omega_{opt} m,$$

where $\Omega_{opt} = \frac{2\pi}{L} v_{opt}$ and m is of order 10^5 for the optical photons.

Following reference [159] and analogous to Eq. 19 (b) in Ref. [161], we write the Hamiltonian for the modulator to be

$$H = \underbrace{\hbar\Omega_{opt} \sum_m m a_m^\dagger a_m}_{H_0} + \underbrace{\sum_m (\gamma_0 a_{m+1}^\dagger a_m b e^{-i\Omega t} + \gamma_0^* a_m^\dagger a_{m+1} b^* e^{i\Omega t})}_{V(t)} \tag{8.8}$$

where a_m is an annihilation operator that destroys an optical field at mode m of the cavity, $be^{-i\Omega t}$ is a strong microwave field treated classically [97, 163] and γ_0 is the coupling constant between the microwave field and the optical field related to the $\chi^{(2)}$ of the non-linear medium [164]. γ_0 contains the spatial mode structure of the quantized field. However as done in Ref. [161, 163], we assume it varies very little over the interaction region and treat it as a complex constant for the rest of the calculation. The interaction Hamiltonian destroys a photon in mode $m+1$ while creating a photon in mode m and vice-versa [159, 160].

To solve for the state vector of the radiation field of a single photon packet after the phase modulator, we need to solve the time-dependent Schrödinger equation. In the interaction picture,

$$i\hbar \frac{\partial}{\partial t} |\psi_I(t)\rangle = V_I(t) |\psi_I(t)\rangle \tag{8.9}$$

where $|\psi_I(t)\rangle$ is the state-vector of the single photon after the phase modulator that

is of interest and

$$
\begin{aligned}
V_I(t) &= e^{iH_0t/\hbar}V(t)e^{-iH_0t/\hbar} \\
&= \sum_m (\gamma e^{+i\Omega_{opt}(m+1)t}e^{-i\Omega_{opt}mt}e^{-i\Omega t}a^\dagger_{m+1}a_m + \gamma^* e^{+i\Omega_{opt}mt}e^{-i\Omega_{opt}(m+1)t}e^{i\Omega t}a^\dagger_m a_{m+1}) \\
&= \sum_m (\gamma e^{-i\delta t}a^\dagger_{m+1}a_m + \gamma^* e^{i\delta t}a^\dagger_m a_{m+1})
\end{aligned}
\tag{8.10}
$$

is the interaction part of the Hamiltonian in the interaction picture. Above, we define $\gamma = \gamma_0 b$ and $\delta = \Omega - \Omega_{opt}$ is the frequency mismatch between the microwave mode and optical mode. This frequency mismatch results in a delta function when integrated over some large time T that enforces energy conservation. Here we will look at the resonant case, which is often denoted as the phase-matching condition in non-linear optics. With this, the interaction Hamiltonian in eq. 8.10 becomes

$$
V_I(t) = \sum_m (\gamma a^\dagger_{m+1}a_m + \gamma^* a^\dagger_m a_{m+1}) \tag{8.11}
$$

Assuming there is no loss in the system, with proper phase matching the interaction Hamiltonian satisfies energy conservation. The new wavefunction can be expressed in the free-Hamiltonian basis,

$$
|\psi_I(t)\rangle = \sum_q c_q(t)|1_q\rangle, \quad q \in \mathbb{Z} \tag{8.12}
$$

where q are all modes of the quantization cavity. Before the interaction, the initial state vector of the single photon packet emitted by a two-level system through spontaneous emission process with center frequency ω_c and decay rate Γ is

$$
|\psi(t=0)\rangle = \sum_q \frac{\sqrt{\Gamma}}{\sqrt{2\pi}[\omega_q - \omega_c + i\Gamma/2]} a^\dagger(\omega_q)|0\rangle \tag{8.13}
$$

We will assume the initial single-photon packet is linearly polarized and the polarization does not get affected throughout the phase modulator, thus the polarization degree of freedom will be dropped from the calculation.

Combining Eqs. (8.9, 8.10, 8.12, 8.13), Eq. (8.9) becomes

$$\begin{aligned} i\hbar\frac{\partial}{\partial t}\sum_q c_q(t)|1_q\rangle &= \sum_q\sum_m(\gamma a^\dagger_{m+1}a_m + \gamma^* a^\dagger_m a_{m+1})c_q(t)|1_q\rangle \\ i\hbar\frac{\partial}{\partial t}c_q(t) &= |\gamma|(e^{-i\theta}c_{q-1}(t) + e^{i\theta}c_{q+1}(t)) \end{aligned} \tag{8.14}$$

where γ is written as $|\gamma|e^{i\theta}$ and the second equation is obtained by projecting the state into $|1_k\rangle$. We have q coupled differential equations for q coefficients, where each level is coupled with the modes immediately above and below it.

$$i\hbar\frac{\partial}{\partial t}c_q(t) = |\gamma|(e^{-i\theta}c_{q-1}(t) + e^{i\theta}c_{q+1}(t)) \tag{8.15}$$

The solution to the above coupled differential equations is given by infinite sums of Bessel coefficients. Using [165],

$$\frac{\partial}{\partial t}J_q(t) = \frac{1}{2}(J_{q-1}(t) - J_{q+1}(t)) \tag{8.16}$$

We can use this relationship to find the solution to Eq. 8.15:

$$c_q(t) = \sum_j \alpha_j J_{q-j}(2|\gamma|t/\hbar)e^{i(\theta-\pi/2)(q-j)} \tag{8.17}$$

where α_j are the initial conditions of the differential equation given by the quantum dot single-photon packet. At $t = 0$, the state should be the state of a photon emitted by a QD through a spontaneous emission process. With this initial condition, the

final wavefunction of the single-photon packet after a phase modulator becomes,

$$|\psi_I(t)\rangle = \sum_q \sum_j J_{q-j}(2|\gamma|t/\hbar) e^{i(\theta-\pi/2)(q-j)} \frac{\sqrt{\Gamma/2\pi}}{[\omega_j - \omega_c + i\Gamma/2]} a_q^\dagger |0\rangle \tag{8.18}$$

At $t = 0$, the Bessel coefficients go to zero for all q and j except at $q = j$, when J_0 become 1. At $q = j$, the phase term θ goes to zero. Now assuming that the interaction between the single-photon packet and the modulator happens for a finite time T (given by the length of the modulator), redefining the coefficients inside the Bessel as $\beta = 2|\gamma|T/\hbar$, where β is equivalent to the classical modulation index, and shifting the sums of the Bessel function ($q - j = n$), the ω_q in the denominator becomes $\omega_j = \omega_{q-n} = \omega_q - n\Omega$ and we obtain the final form of the wavefunction,

$$|\psi_{\text{after interaction}}\rangle = \sum_q \sum_n J_n(\beta) e^{i(\theta-\pi/2)n} \frac{\sqrt{\Gamma/2\pi}}{[\omega_q - n\Omega - \omega_c + i\Gamma/2]} a_q^\dagger |0\rangle \tag{8.19}$$

As the sums are both running from $-\infty$ to ∞, shifting the sum is equivalent to the given result. The state we derived agrees with the form given in Ref. [166, 160].

The spectrum of the modified single photon packet is simply a Lorentzian function centered around $\omega_c + n\Omega$.

$$S(\omega) = \sum_n |J_n(\beta)|^2 \frac{\Gamma/2\pi}{(\omega - n\Omega - \omega_c)^2 + \Gamma^2/4} \tag{8.20}$$

We have retained the form that one gets classically when performing a phase modulation of a field.

8.3 Experimental Realization of Spectral Modification of Single Photons with Phase Modulator

To demonstrate the ability to change the frequency state of single photons emitted from a cw-driven isolated quantum dot, a single QD is resonantly excited with a CW-laser. The scattered photons are sent through a polarization-maintaining single mode fiber and are sent through a commercial electro-optic phase modulator built by EOSpace (part number: PM-5S5-20-PFU-PFU-940-LV-UL Serial 299203) driven with 5 GHz modulation frequency (Ω). As the theory for phase modulation suggests, the single photons at the output of the modulator should develop additional peaks that are separated by the driving frequency. To resolve the frequency spectrum of the spectral modified photons, they are sent through a pressure-tuned air-spaced etalon with 400 MHz bandwidth and 45 GHz free-spectral range, and are detected with single photon detectors. To ensure the spectrum is not cluttered by the free-spectral combs, the emission is centered at the center of the scan range. The pressure inside the cavity is stabilized by a PID controller and can be tuned on demand with a computer command.

The spectrum of the single photons after the modulator are plotted in Fig. 8.1. The QD is driven at saturation. The x-axis is the etalon detuning and y-axis is the integrated counts obtained by integrating for a second at each point. The bottom curve in Fig. 8.1 is the spectrum of the unmodulated photons. The remaining curves show the modified spectrum of a single photon packet after the phase modulator driven by a 5 GHz microwave field at various modulation indices (β). The integrated total counts remain constant for all modulation indices, including the unmodulated case. The data is fitted with multiple Lorentzian peaks with weighted coefficients, as predicted by the theory derived in the previous section.

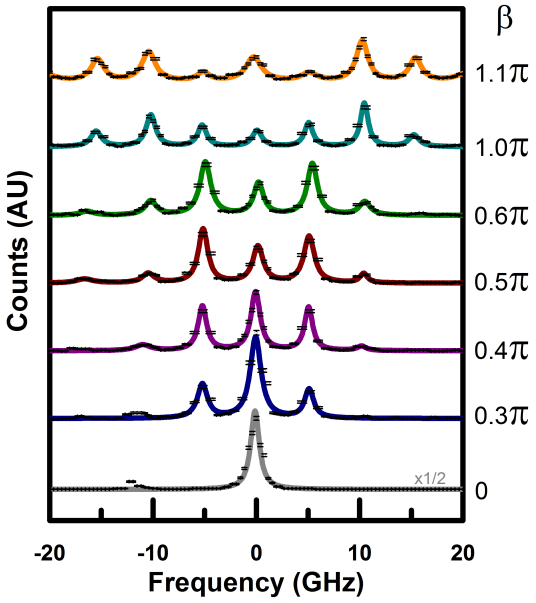

Figure 8.1: Scanning Fabry-Pérot spectrum of single photons after sending through the electro-optic phase modulator for various modulation indices (β). The bottom curve is the spectrum when the modulation is turned off. The solid lines are the Lorentzian fits to the data. The phase modulator is driven with a 5 GHz sinusoidal voltage.

Figure 8.2 shows the integrated counts for the central peak ω_c and the average of the first two sidebands ($\omega_c \pm \Omega$ and $\omega_c \pm 2\Omega$), obtained from the fit for various modulation indices (β). The data is normalized by taking the integrated counts for the unmodulated case to be one. The solid lines are the square of the first three Bessel coefficients ($|J_n(\beta)|^2$ for n = 0,1,2) plotted as a function of the modulation index. As one can see from Fig. 8.2, the single photons are modulated up to the π modulation index, which corresponds to a π phase shift. The blue fit to the carrier peak shows that the carrier component (ω_c) of the photon is almost completely suppressed at

$3\pi/4$ modulation index. The bandwidths of the sidebands are same as the bandwidth of the unmodulated carrier field, within the margin of error. As one would expect, the sidebands are generated at the harmonics of the driving field. The linewidth of the primary and side band peaks, assuming monochromatic excitation, would also be monochromatic; however, in these experiments we are operating at powers where the Rabi frequency is close to the natural linewidth. Under these conditions, the Mollow theory shows the line broadens considerably compared to the near delta function behavior associated with quasi-monochromatic ($<$ 100 KHz) excitation [167].

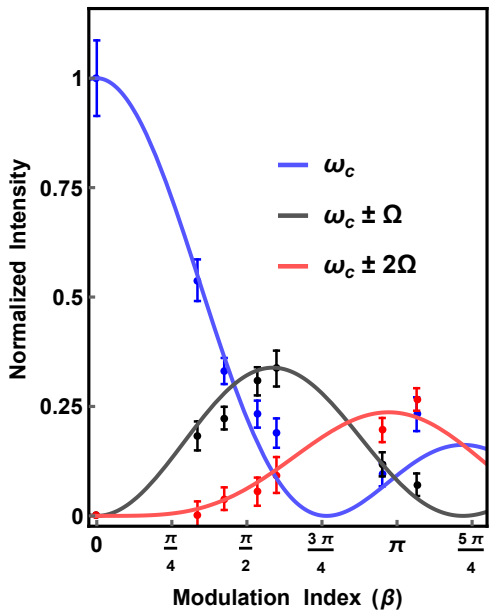

Figure 8.2: Integrated counts as a function of modulation index for the central peak and the average of the first two sidebands obtained for the fit. The data is normalized by taking the integrated count for the unmodulated case to be one. The solid lines are the square of the zeroth, first and second order Bessel coefficients plotted as a function of the modulation index.

8.4 Single Photons Indistinguishability with Two-Photon Interference

In this section, first we will perform two-photon interference measurements using a stream of single photons emitted by a CW-excited QD. Then we will repeat the measurements with the photons with a modified spectrum due to the the phase modulator. We will demonstrate that the indistinguishability of the photons remains preserved after the spectral modifications. The results in this section will be adapted from the draft of the paper that is currently under preparation for publication.

8.4.1 Two-Photon Interference with Unmodulated Photons

The QD is resonantly excited by a CW-laser and the emitted single photons are collected in a cross-polarization setup. We perform CW Hong-Ou-Mandel-type two-photon interference measurements with a single QD [168, 169] in an unbalanced fiber Mach-Zehnder interferometer by exciting the QD at around saturation power. One arm of the interferometer is delayed 35 ns relative to the other arm to ensure there is no second-order field interference and photons from two different shots of the measurement arrive at the beam-splitter simultaneously. The experimental setup for the two-photon interference measurement is given in Fig. 8.3. The phase modulator is turned off for this measurement.

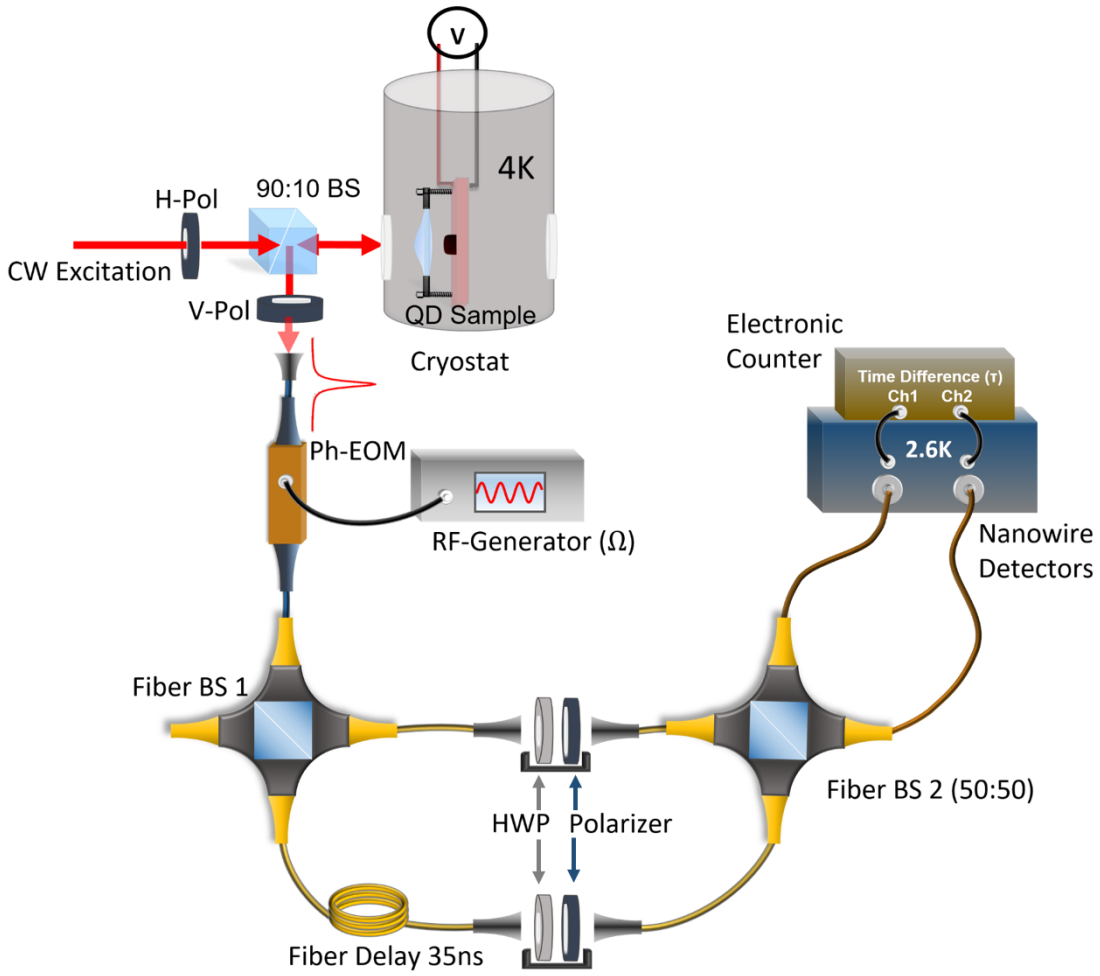

Figure 8.3: Two-photon interference experimental setup. The quantum dot is resonantly excited by a CW-laser and the emitted single photons are collected in a cross-polarization setup. The collected photons are sent through a fiber phase modulator (turned off for this measurement) and then sent through an unbalanced fiber Mach-Zehnder interferometer.

When the incident photons are identical in all degrees of freedom, the input photons exit through the same port of the beam splitter (BS2 in Fig. 8.3). This results in a drop in coincidence counts between the two detectors. The two photon interference

measurements can be described with the second-order intensity correlation function and can be related to the $g^{(2)}$ function. The normalized coincidence probability for the two-photon interference measurements are given by [168]

$$\begin{aligned} g_{\parallel}^{(2)}(\tau) &= \frac{1}{2}g^{(2)}(\tau) + \frac{1}{4}(g^{(2)}(\tau-\Delta\tau) + g^{(2)}(\tau+\Delta\tau))(1 - v_c e^{-2\frac{|\tau|}{\tau_c}}) \\ g_{\perp}^{(2)}(\tau) &= \frac{1}{2}g^{(2)}(\tau) + \frac{1}{4}(g^{(2)}(\tau-\Delta\tau) + g^{(2)}(\tau+\Delta\tau)) \end{aligned} \tag{8.21}$$

where $g_{\parallel}^{(2)}$ and $g_{\perp}^{(2)}$ correspond to the cases where the input photons in BS2 are linearly co-polarized and linearly cross-polarized respectively, and $g^{(2)}$ is the intensity correlation function calculated in Ch. V given by [65, 137]

$$g^{(2)}(\tau) = 1 - [\cos(\lambda|\tau|) + \frac{\gamma+\gamma_2}{2\lambda}\sin(\lambda|\tau|)]e^{-\frac{1}{2}(\gamma+\gamma_2)|\tau|} \tag{8.22}$$

where

$$\lambda = \sqrt{(\Omega_0^2 - \frac{(\gamma-\gamma_2)^2}{4})} \tag{8.23}$$

and γ_2 and γ are the excited state population decay rate and the dephasing rate of the QD. The two beam-splitters (BS1 and BS2) used in the setup are 50:50 (R:T), $\Delta\tau$ is the relative time difference between the two arms of the interferometer, τ_c is the first order coherence time of the photons, and v_c is the overlap of all the modes of the two incident photons that takes the value from 0 (no overlap) to 1 (perfect overlap). The overall indistinguishability of the photons is quantified by a visibility function defined as [168]

$$V_{\mathrm{HOM}}(\tau) = \frac{g_{\perp}^{(2)} - g_{\parallel}^{(2)}}{g_{\perp}^{(2)}} \tag{8.24}$$

For completely indistinguishable photons, the visibility goes to 1 at $\tau = 0$, whereas it goes to 0 for distinguishable photons.

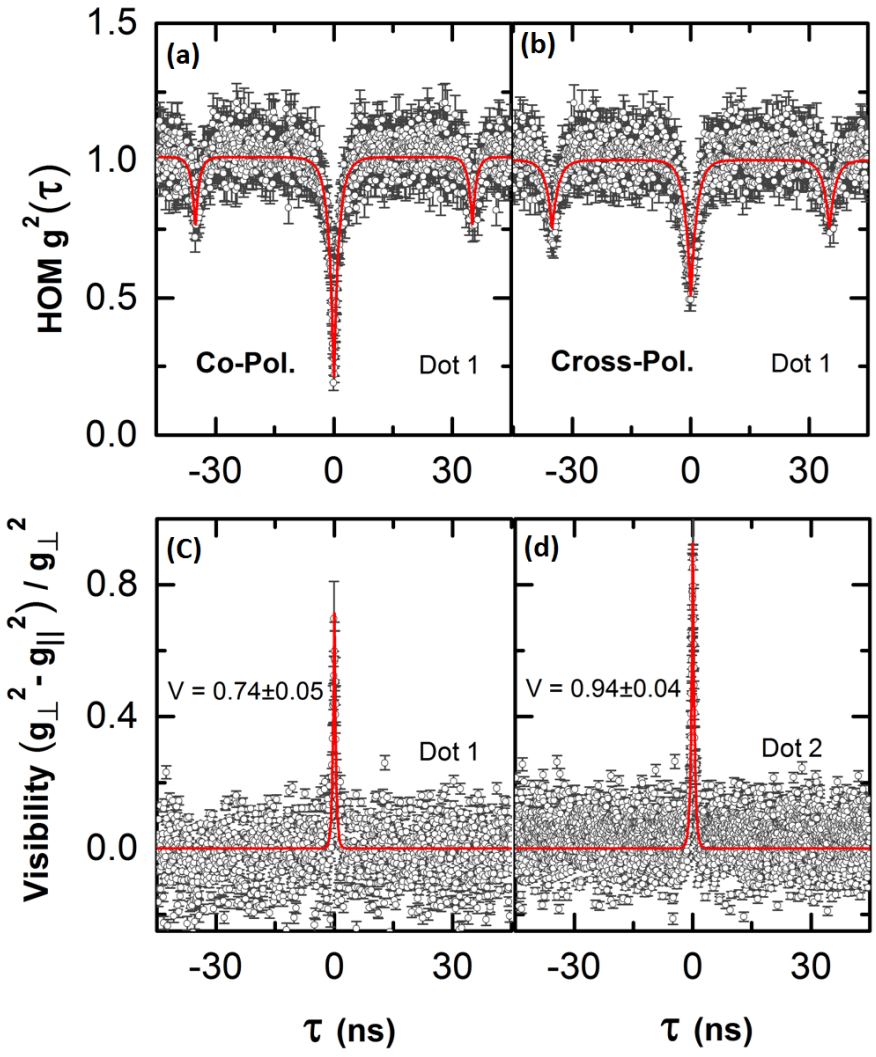

Figure 8.4: Continuous-wave two-photon interference experimental data. (a) Two-photon interference measurements with dot 1 for linearly co-polarized and (b) linearly cross-polarized photons with the phase modulator off. For co-polarized photons, the $g^{(2)}_{\mathrm{HOM}}(\tau = 0)$ goes to $0.19 \pm .01$. In the case of the cross-polarized photons, the value is 0.5, which is the classical correlation value. Figure (c) and (d) are interference visibility measured for dot 1 and dot 2. The red curve on plots (a)-(b) and (c)-(d) are obtain from the theoretical fit given by Eq. 8.21 and 8.24 respectively.

Figure 8.4 (a) and (b) are the normalized two-photon interference raw data for dot 1 performed with the phase modulator off for linearly co-polarized and cross-polarized photons respectively. The red lines are the theoretical fit to the data obtained from Eq. 8.21. At $\tau = 0$, for the co-polarized case, the coincidence counts goes to $0.19 \pm .01$ (Fig. 8.4a), much below the classical correlation limit of 0.5, whereas for the cross-polarized case, the coincidence is 0.5 (Fig. 8.4b). The two side dips at $\tau = \pm 35$ ns correspond to the relative path length difference of the Mach-Zehnder interferometer, where the coincidence count is reduced due to the classical counting probability for a single photon source, and not due to the interference. Therefore, the magnitude of these dips are equal for the co-polarized and cross-polarized cases. We obtain a visibility of $0.74 \pm .04$ with the dot (dot 1) used in the study. A different dot (dot 2) from the same sample has a two-photon interference visibility of up to $0.94 \pm .04$ (Fig. 8.4d). As of our knowledge, this is the highest raw visibility seen in CW two-photon interference measurements reported to date. The reduction in visibility (Fig. 8.4c) from the ideal value of 1 is possibly due to the spectral diffusion of the QD emission frequency, and uncontrolled polarization rotation of the fiber before the second beam splitter.

8.4.2 Two-Photon Interference with Phase Modulated Photons

After the photon packets are processed through the phase modulator, it is important to verify that the coherence properties of the photons are not degraded substantially. While the bandwidths of the sideband peaks remain close to that of the carrier frequency, it is important to verify that the modified photons remain indistinguishable.

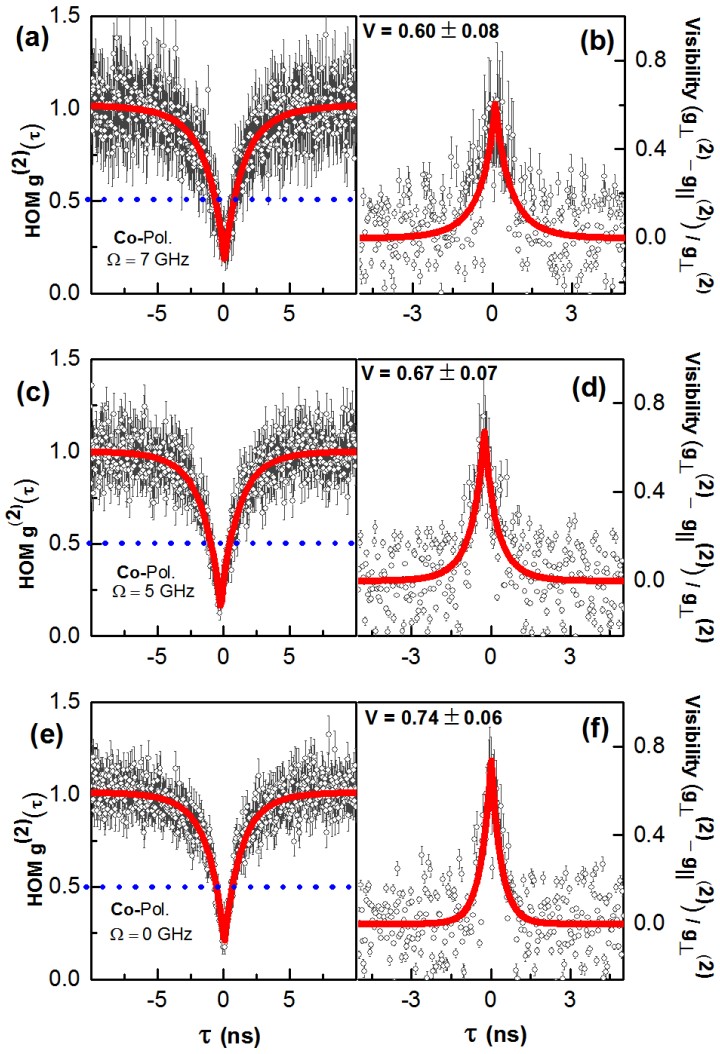

Figure 8.5: Two-photon interference measurements for linearly co-polarized photons performed with the spectral modified photons driven with the modulator at (a) 7 GHz (c) 5 GHz and (e) unmodulated case. The interference visibility for each driving frequency is plotted with the same order in the right column. For Fig. (a-d), the photons' spectrum are modified with a modulation index of $\beta \sim \pi/3$ and all frequency components are used in the HOM measurements.

We repeat the two-photon interference measurements between subsequent photons in the same setup with the phase modulator turned on and driven by a sinusoidal microwave source. The phase modulator is driven at the modulation index of $\beta \sim \pi/3$ (blue curve in Fig. 8.1), at which the ratio of the intensity of carrier mode to the first sidebands is $2.7 : 1$. The output of the phase-modulator with all the frequency components is sent through the two-photon interference setup. Several two-photon interference measurements are performed with various driving frequencies ranging from 2 to 7 GHz and the data is analyzed and plotted using the same procedure as for the unmodulated case above. The two-photon interference for the linearly co-polarized photons with the modulated spectra and the interference visibility are plotted in Fig. 8.5 (a-d). The red curves are the theoretical fit to the data given by Eq. 8.21 and 8.24 for the unmodulated case. Figure 8.5 (e,f) are the detailed plot of Fig. 8.4 (a,b), showing two-photon interference visibility for the unmodulated photons plotted together for comparison. The dashed blue lines in the left figures are the classical correlation limit; the normalized coincidence counts below the line indicates the quantum interference between the two photons. As seen in the Fig. 8.5 (a-d), the visibility of the modulated photons remain within the error bars of the unmodulated case. This demonstrates that the spectral modified single photons maintain their indistinguishability to a high degree, resulting in an excellent interference visibility.

8.5 Chapter Summary

In this Chapter, we have demonstrated that the frequency spectrum of single photons emitted from a cw-excited single quantum dot can be modified near-arbitrarily to generate well defined frequency sidebands using a phase modulator. We have shown that the sidebands inherit the properties of the unmodulated photon. Through two-photon interference measurements, we have demonstrated that the indistinguishability of individual photons emitted by a quantum dot is fully preserved in the presence

of additional frequency sidebands generated via a phase modulator for a range of modulation frequencies. These results demonstrate the suitability of this approach for use in the development of frequency qubits from narrow-band single photons.

By filtering the carrier frequency and a single sideband through a fiber Bragg grating and a circulator, we can construct a photonic frequency qubit [56, 59, 156] [157, 55]. In addition, there exist proposals to use the carrier component and the first pair of sidebands ($\omega_c, \omega_c \pm \Omega$) as the basis for BB84 protocols [59]. As the modulator is embedded in a single mode fiber, all of the frequency components are in the same spatial mode. This allows the transferring of such qubit states over a long distance using fiber optics networks without the problems that characterize polarization qubits [56].

CHAPTER IX

Future Directions

The original goal of constructing the cavity-SPDC source was to encode a frequency qubit with cavity-SPDC photons and teleport it to the spin states of a trion state (the details of the proposed experiment can be found in Ref. [118]). The major steps of the experiment are the generation of frequency qubits with the SPDC photons and Hong-Ou-Mandel (HOM) type interference that will be used for performing the Bell state measurement. In this thesis, we have demonstrated the generation of frequency qubit with the radiation generated from a continuous-wave excited single quantum dot. We also performed HOM interference measurement between quantum dots and SPDC photons. The post-process interference visibility is 32% when the data is analyzed to look for coincidence counts within a 500 ps time window. For the proposed teleportation measurement, visibility near unity is desired. As discussed in Ch. 7, the reduction in the interference visibility is limited by the cavity-SPDC photons. Due to the instability issues with the cavity, we were not able to get any meaningful heralded interference data, as it requires more integration time. To address the problem, we propose a redesign of the cavity-SPDC setup. One major improvement can be made by mounting the crystals in a more stable housing that allows fine tuning of the cavity length and re-doing the wiring work such that the cavity is isolated from any external mechanical vibration. The redesign of the cavity

housing is not limited by any physics, and thus can be done as a first step to improve the setup. However, it will require some detailed machining work and careful re-alignment and re-characterization of the experimental setup, which could be labor intensive and time consuming.

In addition, we propose adding an intra-cavity thin etalon with a bandwidth smaller than the SPDC cavitys free-spectral range (FSR) ($<$ 8.9 GHz) but with an FSR larger than the down-conversion bandwidth ($\sim$ 540 GHz). If the FSR of the SPDC cavity and the thin etalon are mismatched, the down-conversion happens only at the degenerate mode (i.e. when the down-conversion, cavity-SPDC, and the thin etalon modes are degenerate with the Tsunami pump laser), which will actively suppress the emission from the unwanted modes (i.e. those non-degenerate with the Tsunami pump). In addition, having such an additional cavity might increase the brightness of the source, thus further theoretical investigations on the subject matter would be useful.

Alternatively, the cavity-SPDC source could be pumped with a longer Tsunami laser pulse to increase the photon counts for performing HOM measurements. Increasing the pulse length to 150 ps (within the detector timing jitter) would reduce the pulse spectral bandwidth to 2.1 GHz from the current bandwidth of 6.3 GHz. Reducing the pump bandwidth would cause many non-degenerate cavity modes to fail to satisfy the energy conservation requirement, further suppressing the unwanted non-degenerate modes. However, it is important to note that the pulse length needs to be much smaller than the QDs lifetime, as longer pump time means more uncertainty in the SPDC emission time, which further degrades the HOM interference visibility.

The cavity-SPDC count rates can be increased by using a longer down-conversion crystal, as the emission rate increases linearly with the crystal length. This requires a redesign of the cavity parameters and getting a new crystal from our vendor (Raicol).

Once the mentioned challenges are addressed, there are numerous experiments that one could perform that would be of interest for building a quantum network. One could extend the absorption measurement to demonstrate a heralded-absorption measurement by correlating the emitted photons with the spin state of QD. A similar measurement between two QDs has been recently demonstrated by the ETH group [26], where each data point was integrated for 46 hours. Such long integration time is not possible with our current experimental setup, but with the new cryo-free system that we are getting in the near future, such measurements will be possible. One alternative path one could take is investigating the conversion of the idler photon to the telecom wavelength through the use of frequency mixing module. There exist commercial high-power pulsed fiber lasers at around 2200 nm with which an efficient frequency conversion can be achieved [170]. This would be of interest for efficient transport of the down-conversion photons in a fiber, with signal photons at 940 nm centered around InAs/GaAs QD emission wavelength, and idler photons at telecom wavelength (1560 nm).

Another possible experiment is a demonstration of phase-encoded cryptography using single photons and two phase modulators as proposed and experimentally demonstrated by Mérolla using a weak coherent source [55]. The thesis work on phase modulation is a first ever direct verification of modulation spectrum with single photons. The work should lay a foundation for implementing such cryptographic applications with single photons emitted by QDs.

APPENDICES

APPENDIX A

Derivation of a Cavity Field Using an Input-Output Formalism.

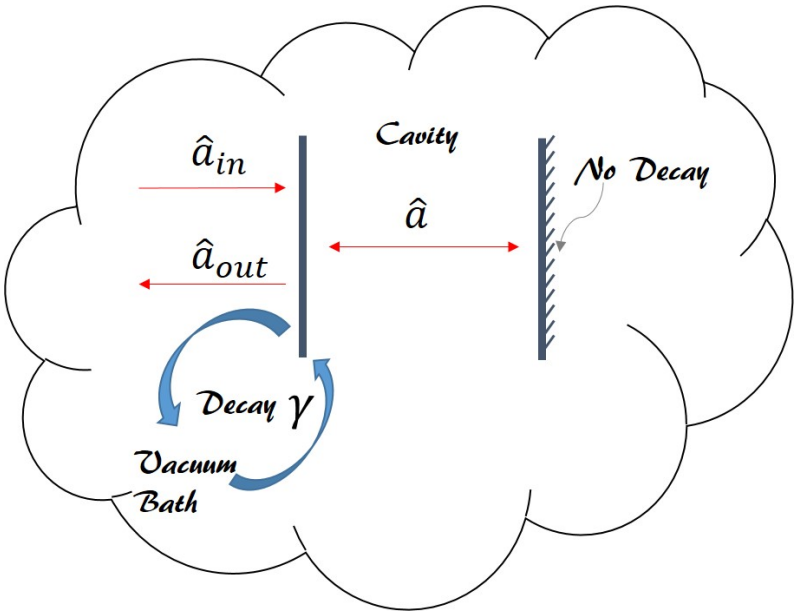

Figure A.1: A cartoon of a single-sided cavity formed with a perfectly reflecting and a leaky mirrors. The leakage is represented as interaction with the vacuum bath with a rate γ

In this Appendix, we will adopt D.F. Walls and G.J. Milburn's derivation of the cavity field calculated using the formalism given by Collett *et al.* to discuss the output

field from a single sided cavity [106, 107]. The formalism is often referred to as cavity input-output formalism. One can construct such a cavity with a highly reflecting mirror and a semi-transparent second mirror. The semi-transparent mirror interacts with the external bath resulting in some finite decay of the cavity. The Hamiltonian for such a system can be written as [106]

$$H = H_{system} + H_{source} + H_{bath} + H_{system-bath} \tag{A.1}$$

where $H_{system} = \hbar\omega_0 a^\dagger a$ is the free single-mode cavity field, H_{source} is a source of the field inside the cavity, the details of which are discussed in Ch. 3, and $H_{bath} = \sum \hbar\omega_j b_j^\dagger b_j$ is an external bath that interacts with the cavity, modeled as evenly spaced nearly degenerate energy levels of vacuum modes. In the limit of interest when the sum over j becomes an integral, the commutation relation for the vacuum modes becomes

$$[a, a^\dagger] = 1, \qquad [b(\omega), b^\dagger(\omega')] = \delta(\omega - \omega') \tag{A.2}$$

The bath is coupled with the modes of the cavity with interaction strength g_j. With the rotating wave approximation (RWA), the interaction between the cavity modes and the bath can be written as,

$$H_{system-bath} = i\hbar \sum g_j (a^\dagger b_j - b_j^\dagger a) \tag{A.3}$$

Taking the bath harmonic oscillators as a continuous spectrum,

$$H_{system-bath} = -i\hbar \int_{-\infty}^{\infty} d\omega k(\omega)(b(\omega)a^\dagger - a b^\dagger(\omega)) \tag{A.4}$$

Solving the Heisenberg equation of motion for the field operators,

$$\frac{db(\omega)}{dt} = -\frac{i}{\hbar}[b(\omega), \hbar b^{\dagger}(\omega)b(\omega)] - \frac{i}{\hbar}[b(\omega), i\hbar \int_{-\infty}^{\infty} d\omega k(\omega) a b^{\dagger}(\omega')] \tag{A.5}$$

where $b(\omega)$ operator is time dependent and $b_0(\omega)$ is for the initial time $t = 0$. Assuming $k(\omega)$ is constant around the frequency of interests,

$$\begin{aligned} \dot{b(\omega)} &= -i\omega b(\omega) + k(\omega)a(t) \\ b(\omega) &= e^{-i\omega(t-t_0)}b_0(\omega) + k(\omega)\int_{t_0}^{t} dt' a(t') e^{-i\omega(t-t'))} \end{aligned} \tag{A.6}$$

similarly for a(t), substituting $b(\omega, t)$,

$$\begin{aligned} \dot{a(t)} &= -\frac{i}{\hbar}[a, H_{system}] - \int_{-\infty}^{\infty} d\omega k(\omega) b(\omega) \\ \dot{a(t)} &= -\frac{i}{\hbar}[a, H_{system}] - \int_{-\infty}^{\infty} d\omega k(\omega) b_0(\omega) e^{-i\omega(t-t_0)} - \int_{-\infty}^{\infty} k^2(\omega) d\omega \int_{t_0}^{t} dt' a(t') e^{-i\omega(t-t')} \end{aligned} \tag{A.7}$$

We take $k^2(\omega)$ to be constant ($= \frac{\gamma}{2\pi}$) over the spectral range of interest which Collett relates to the Markov approximation [106] and redefine the first integrand in Eq. A.7 as $a_{in}(t)$

$$a_{in}(t) = -\frac{1}{\sqrt{2\pi}} \int_{-\infty}^{\infty} d\omega b_0(\omega) e^{-i\omega(t-t_0)} \tag{A.8}$$

where $a_{in}(t)$ satisfies the following commutative rule.

$$[a_{in}(t), a_{in}^{\dagger}(t')] = \delta(t - t') \tag{A.9}$$

With further simplification,

$$\dot{a(t)} = -\frac{i}{\hbar}[a(t), H_{system} + H_{source}] + \sqrt{\gamma}a_{in}(t) - \gamma/2a(t) \tag{A.10}$$

as Collett argued, using time reverse process, we obtain the following relationship

$$\dot{a(t)} = -\frac{i}{\hbar}[a(t), H_{system} + H_{source}] - \sqrt{\gamma}a_{out}(t) + \gamma/2a(t) \tag{A.11}$$

where,

$$a_{out}(t) = \frac{1}{\sqrt{2\pi}} \int_{-\infty}^{\infty} d\omega b_0(\omega) e^{-i\omega(t-t_0)} \tag{A.12}$$

From equations A.10 and A.11 we obtain a boundary condition,

$$a_{out}(t) + a_{in}(t) = \sqrt{\gamma}a(t) \tag{A.13}$$

Once we have obtained the intra-cavity field it is easy to calculate the output field from the above derivation.

APPENDIX B

Mathematica Code to Calculate Cavity Parameters.

ABCD matrix for Gaussian beam

optics to calculate the cavity parameters.

In[51]:=

```
d1 := 5 * 10^-3; (*PPKPT Length*)
d2 := 2 * 10^-3 (* kpt length*)
ne := 1.7418 (*index of refraction extraordinary*)
ne1 = 1; (*index of refraction air*)
no := 1.83482 (*index of refraction ordinary*)
(*f1=19.3*10^-3, 12*10^-3;*)
f1 = 19.3 * 10^-3;
λ = 942 * 10^-9; (*radius of curvature of PPKTP, wavelength of down-conversion*)
(*ABCD matrix propagation through each component. The
 beam starts from the high reflecting end of the PPKTP crystal,
propagates through the free-space of length L and through the KTP crystal. The
  beam reflects from the high reflecting end of the KTP crystal and traves back
  through the same path back to the high reflecting end of the PPKTP crystal.*)
QD[L_, f1_, x1_] := {{1, d1}, {0, 1}}.{{1, 0}, {0, 1/ne}}.{{1, L}, {0, 1}}.{{1, 0}, {0, ne/1}}.{{1, d2}, {0, 1}}.
  {{1, 0}, {2/-f1, 1}}.{{1, d2}, {0, 1}}.{{1, 0}, {0, 1/ne}}.{{1, L}, {0, 1}}.{{1, 0}, {0, ne/1}}.{{1, d1}, {0, 1}}
Rayleigh[λ_, w01_] := π * w01^2 / λ
wQD1[λ_, w01_, z0_] := w01 √(1 + ((z0 λ) / (π w01^2))^2) (*beam waist*)
RQD[λ_, w01_, z0_] := z0 (1 + ((π w01^2) / (λ z0))^2) (*radius of curvature*)
qQD[λ_, w01_, z0_] := ((-i λ) / (π * (wQD1[λ, w01, z0])^2))^-1
qQDn[λ_, w01_, x1_, L_, f1_, z0_] :=
 ((Extract[QD[L, f1, x1], {1, 1}]) * qQD[λ, w01, z0] + Extract[QD[L, f1, x1], {1, 2}]) /
  ((Extract[QD[L, f1, x1], {2, 1}]) * qQD[λ, w01, z0] + Extract[QD[L, f1, x1], {2, 2}])
wQD[λ_, w01_, x1_, L_, f1_, z0_] := (-λ / (π Im[1 / qQDn[λ, w01, x1, L, f1, z0]]))^1/2
(*beam waist*)
inverseQDR[λ_, w01_, x1_, L_, f1_, z0_] := Re[1 / qQDn[λ, w01, x1, L, f1, z0]]
QDR[λ_, w01_, x1_, L_, f1_, z0_] := 1 / inverseQDR[λ, w01, x1, L, f1, z0]
(*Radius of curvature*)
Manipulate[Plot[{({wQD[λ, w * 10^-6, 0, x * 10^-3, f1, 0] - w * 10^-6}) * 10^6,
   inverseQDR[λ, w * 10^-6, 0, x * 10^-3, f1, 0]}, {x, 0, 12},
  AxesLabel → {"cavity length(mm)", "Beam waist(μm), 1/Curvature at ppkpt"},
  PlotRange → {-10, 10}, PlotStyle → {Red, Black}, PlotLegends →
   Placed[{"Beam waist (Initial - final)", "1/Curvature at ppkpt"}, Above],
  ImageSize → Large], {w, 10, 100}]
```

In[67]:=

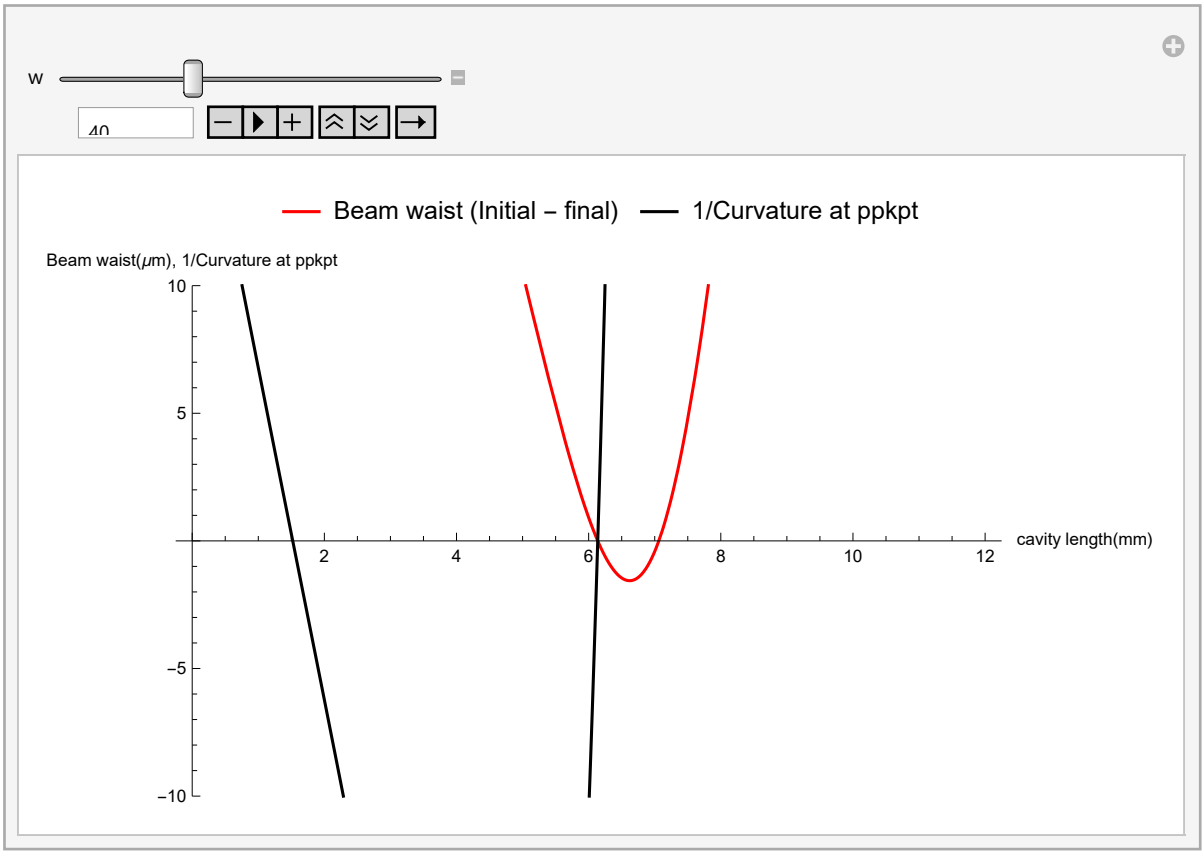

Summary : A stable cavity operation can be achieved when the beam waist of the incident beam matches with the waist of the round – trip beam reflected through the KTP, in other words when the ray diagram is time – reversable. The zero crossing of the red curves are the operation points where the ray – diagram is time – reversable.Theblack curve is 1/(PPKTP curvature), for beam waist 40 μm, there are two time reversable operation points, out of which only one matches the radius of curvature with the KTP crystal.

APPENDIX C

Theoretical Calculations of the Second-Order Intensity Correlation.

In this appendix we will calculate the second-order intensity correlation of photons emitted by a single two-level atom using quantum regression theorem. The calculation is adopted from Paul Berman's lecture notes. A fully quantized Hamiltonian of a two-level system with dipole approximation and rotating wave approximation (RWA) driven with a coherent source can be written as [65],

$$H = \frac{\hbar\omega_0}{2}\sigma_z + \sum_j \hbar\omega_j a_j^\dagger a_j + \sum_j \hbar(g_j\sigma_+ a_j + g_j^* a_j^\dagger \sigma_-) + \hbar\chi(\sigma_+ e^{-i\omega t} + \sigma_- e^{i\omega t}) \quad \text{(C.1)}$$

where,

$$\begin{aligned} \mathrm{g}_k &= -i\mu_{21} Sin\theta_k (\frac{\omega_k}{2\hbar\epsilon_0\nu})^{1/2} \\ \chi &= -\mu_{12}E_0/2\hbar \end{aligned} \quad \text{(C.2)}$$

are the field coupling constants for a two-level system with the excited and ground stated denoted by states $|2\rangle|1\langle$ respectively. The atomic and field operators are defined

as $\sigma_+ = |2\rangle\langle 1|, \sigma_- = |1\rangle\langle 2|, \sigma_2 = |2\rangle\langle 2|, \sigma_1 = |1\rangle\langle 1|, \sigma_z = \sigma_2 - \sigma_1$

With the Hamiltonian, the equation of motion of the atomic and field operators can be calculated in the Heisenberg picture with the following commutation relationship,

$$\dot{O} = \tfrac{1}{i\hbar}[O, H]$$

Solving for operators of our interest,

$$\begin{aligned}
\dot{\sigma_2} &= -i\sum_j g_j\sigma_+ a_j + i\sum_j g_j^* a_j^\dagger \sigma_- - i\chi\sigma_+ e^{-i\omega t} + i\chi\sigma_- e^{i\omega t} \\
\dot{\sigma_1} &= i\sum_j g_j\sigma_+ a_j - i\sum_j g_j^* a_j^\dagger \sigma_- + i\chi\sigma_+ e^{-i\omega t} - i\chi\sigma_- e^{i\omega t} \\
\dot{\sigma_-} &= -i\omega_0\sigma_- + i\sum_j g_j\sigma_z a_j + i\chi\sigma_z e^{-i\omega t} \\
\dot{\sigma_+} &= i\omega_0\sigma_- - i\sum_j g_j^* a_j^\dagger \sigma_z - i\chi\sigma_z e^{i\omega t} \\
\dot{\sigma_z} &= -2i\sum_j g_j\sigma_+ a_j + 2i\sum_j g_j^* a_j^\dagger \sigma_- - 2i\chi\sigma_+ e^{-i\omega t} + 2i\chi\sigma_- e^{i\omega t} \\
\dot{a_j} &= -i\omega_j a_j - i g_j^* \sigma_-
\end{aligned} \tag{C.3}$$

The field operator a_j can be solved to get,

$$a_j(t) = a_j(0)e^{-i\omega_j t} - i g_j^* \int_0^t e^{-i\omega_j(t-t')}\sigma_-(t')dt' \tag{C.4}$$

Substituting $a_j(t)$ to the equation for σ_2,

$$\dot{\sigma_2}(t) = -i\sum_j g_j\sigma_+(t)a_j(0)e^{-i\omega_j t} - \sum_j |g_j|^2\sigma_+(t)\int_0^t e^{-i\omega_j(t-t')}\sigma_-(t')dt'$$
$$+ i\sum_j g_j^* a_j^\dagger(0)\sigma_-(t)e^{i\omega_j t} + \sum_j |g_j|^2\int_0^t e^{i\omega_j(t-t')}\sigma_+(t')dt'\sigma_-(t) - i\chi\sigma_+e^{-i\omega t} + i\chi\sigma_-e^{i\omega t} \tag{C.5}$$

Using Weisskoff-Wigner approximation we can simplify the summation [65]

$$\sum_j |g_j|^2 e^{-i\omega_j(t-t')} = \gamma_2\delta(t-t'), \tag{C.6}$$

where γ_2 is the spontaneous decay rate. With $\int_0^t \delta(t-t')dt' = 1/2$ the above equations can be further simplified as following [65],

$$\dot{\sigma_2} = -i\sum_j g_j\sigma_+(t)a_j(0)e^{-i\omega_j t} + i\sum_j g_j^* a_j^\dagger(0)\sigma_-(t)e^{i\omega_j t} - \gamma_2\sigma_2(t) - i\chi\sigma_+e^{-i\omega t} + i\chi\sigma_-e^{i\omega t}$$
$$\dot{\sigma_1} = i\sum_j g_j\sigma_+(t)a_j(0)e^{-i\omega_j t} - i\sum_j g_j^* a_j^\dagger(0)\sigma_-(t)e^{i\omega_j t} + \gamma_2\sigma_2(t) + i\chi\sigma_+e^{-i\omega t} - i\chi\sigma_-e^{i\omega t}$$
$$\dot{\sigma_-} = -i\omega_0\sigma_-(t) + i\sum_j g_j\sigma_z(t)a_j(0) - \gamma\sigma_-(t) + i\chi\sigma_z e^{-i\omega t}$$
$$\dot{\sigma_+} = i\omega_0\sigma_+(t) - i\sum_j g_j^* a_j^\dagger(0)\sigma_z(t) - \gamma\sigma_+(t) - i\chi\sigma_z e^{i\omega t} \tag{C.7}$$

When taken trace of the above equations by summing over the initial state of the field, which is $|0\rangle$ for the Hamiltonian given in Eq. C.1, the terms with summations go to zero, $\langle a^\dagger(0)\sigma_-(t)\rangle = 0$, $\langle\sigma_+(t)a(0)\rangle = 0$. After the simplification, the expectancy values of the time derivative of the above Heisenberg operators become,

$$
\begin{aligned}
\langle\dot{\sigma_2}(t)\rangle &= -\gamma_2\langle\sigma_2(t)\rangle - i\chi\langle\sigma_+(t)\rangle e^{-i\omega t} + i\chi\langle\sigma_-(t)\rangle e^{i\omega t} \\
\langle\dot{\sigma_1}(t)\rangle &= \gamma_2\langle\sigma_2(t)\rangle + i\chi\langle\sigma_+(t)\rangle e^{-i\omega t} - i\chi\langle\sigma_-(t)\rangle e^{i\omega t} \\
\langle\dot{\sigma_-}(t)\rangle &= -\gamma\langle\sigma_-(t)\rangle - i\omega_0\langle\sigma_-(t)\rangle + i\chi\langle\sigma_z(t)\rangle e^{-i\omega t} \\
\langle\dot{\sigma_+}(t)\rangle &= -\gamma\langle\sigma_+(t)\rangle + i\omega_0\langle\sigma_+(t)\rangle - i\chi\langle\sigma_z(t)\rangle e^{i\omega t}
\end{aligned}
\tag{C.8}
$$

The above equations could be re-written in the field interaction representation where $\tilde{\rho} = e^{-i\omega t\sigma_z/2}\rho e^{i\omega t\sigma_z/2}$, $\tilde{\rho_{mn}} = \rho_{mn}$, $\tilde{\rho_{12}} = e^{-i\omega t}\rho_{12}$. Substituting $\sigma_\pm(t) = \tilde{\sigma_\pm}(t)e^{\pm i\omega t}$, $\Delta_j = \omega_j - \omega$, $\delta = \omega_0 - \omega$, $\tilde{\rho_{ii}} = \rho_{ii}$

$$
\begin{aligned}
\langle\dot{\tilde{\sigma}}_2(t)\rangle &= -\gamma_2\langle\tilde{\sigma_2}(t)\rangle - i\chi\langle\tilde{\sigma_+}(t)\rangle + i\chi\langle\tilde{\sigma_-}(t)\rangle \\
\langle\dot{\tilde{\sigma}}_1(t)\rangle &= \gamma_2\langle\tilde{\sigma_2}(t)\rangle + i\chi\langle\tilde{\sigma_+}(t)\rangle - i\chi\langle\tilde{\sigma_-}(t)\rangle \\
\langle\dot{\tilde{\sigma_-}}(t)\rangle &= -(\gamma + i\delta)\langle\tilde{\sigma_-}(t)\rangle + i\chi(\langle\tilde{\sigma_2}(t)\rangle - \langle\tilde{\sigma_1}(t)\rangle) \\
\langle\dot{\tilde{\sigma_+}}(t)\rangle &= -(\gamma - i\delta)\langle\tilde{\sigma_+}(t)\rangle - i\chi(\langle\tilde{\sigma_2}(t)\rangle + \langle\tilde{\sigma_1}(t)\rangle)
\end{aligned}
\tag{C.9}
$$

The set of differential equations derived above is essentially the optical Bloch equation for a two-level system derived in Chap. 5. The above equations can be expressed as a single differential equation by rewriting it in a matrix form,

$$
\begin{aligned}
\langle\frac{d\sigma}{d\tau}\rangle &= M.\langle\sigma\rangle \\
\langle\sigma(t+\tau)\rangle &= e^{M\tau}\langle\sigma(t)\rangle
\end{aligned}
\tag{C.10}
$$

where, M $= \begin{bmatrix} -\gamma_2 & 0 & i\chi & -i\chi \\ \gamma_2 & 0 & -i\chi & i\chi \\ i\chi & -i\chi & -(\gamma + i\delta) & 0 \\ -i\chi & i\chi & 0 & -(\gamma - i\delta) \end{bmatrix}$ and $\sigma(\tau) = \begin{bmatrix} \tilde{\sigma_2}(\tau) \\ \tilde{\sigma_1}(\tau) \\ \tilde{\sigma_-}(\tau) \\ \tilde{\sigma_+}(\tau) \end{bmatrix}$

From the above differential equation, we can obtain the expectation value of $\sigma_2(t+\tau)$

which will be of interest later to calculate the second-order intensity correlation.

$$\langle\tilde{\sigma_2}(t+\tau)\rangle = e^{M\tau}|_{11}\langle\tilde{\sigma_2}(t)\rangle + e^{M\tau}|_{12}\langle\tilde{\sigma_1}(t)\rangle + e^{M\tau}|_{13}\langle\tilde{\sigma_-}(t)\rangle + e^{M\tau}|_{14}\langle\tilde{\sigma_+}(t)\rangle \quad \text{(C.11)}$$

Now we would like to calculate the second-order intensity correlation using the above equations. Second-order intensity correlation, also referred as $g^2(\tau)$, is given by,

$$g^2(\tau) = t \overset{lim}{\to} \infty \frac{\langle E_s^-(t)E_s^-(t+\tau)E_s^+(t+\tau)E_s^+(t)\rangle}{\langle E_s^-(t)E_s^+(t)\rangle\langle E_s^-(t+\tau)E_s^+(t+\tau)\rangle} \quad \text{(C.12)}$$

The radiation field of an oscillating dipole can be expressed in terms of the atomic operators [65],

$$E_s^+(t,R) = -\frac{\omega_0^2}{4\pi\epsilon_0 c^2 R} 1\mu_z 2Sin\theta\sigma_-(t-R/c)\hat{\theta} \quad \text{(C.13)}$$

Substituting Eq. C.13 to Eq. C.12,

$$g^2(\tau) = t \overset{lim}{\to} \infty \frac{\langle\tilde{\sigma_+}(t)\tilde{\sigma_+}(t+\tau)\tilde{\sigma_-}(t+\tau)\tilde{\sigma_-}(t)\rangle}{\langle\tilde{\sigma_+}(t)\tilde{\sigma_-}(t)\rangle\langle\tilde{\sigma_+}(t+\tau)\tilde{\sigma_-}(t+\tau)\rangle} = t \overset{lim}{\to} \infty \frac{\langle\tilde{\sigma_+}(t)\tilde{\sigma_2}(t+\tau)\tilde{\sigma_-}(t)\rangle}{\langle\tilde{\sigma_2}(t)\rangle\langle\tilde{\sigma_2}(t+\tau)\rangle} \quad \text{(C.14)}$$

When $t \to \infty$, the terms in the denominator become steady state solution to ρ_{22}^{SS} which is independent of time.

$$g^2(\tau) = t \overset{lim}{\to} \infty \frac{\langle\tilde{\sigma_+}(t)\tilde{\sigma_2}(t+\tau)\tilde{\sigma_-}(t)\rangle}{(\rho_{22}^{SS})^2} \quad \text{(C.15)}$$

In order to calculate two-time expectation value of the atomic operators, we can employ regression theorem derived by Melvin Lax [171] which assumes that a given system has a Markovian dynamics. Following calculation is adopted from Girish S. Agarwal's Quantum Optics book [108]. According to the regression theorem extended to quantum dynamics, the mean value of an operator at a given time $t+\tau$ can be

expressed in terms of the expectation values of operators in an earlier time t [171],

$$\langle G(t+\tau)\rangle = \sum_{\alpha} C_{\alpha}(\tau)\langle G_{\alpha}(t)\rangle \tag{C.16}$$

where the coefficients C_{α} can be solved using the optical Bloch equations. The relationship can be extended to the mean value of two-time operator,

$$\langle O_1(t)G(t+\tau)O_2(t)\rangle = \sum_{\alpha} C_{\alpha}(\tau)\langle O_1(t)G_{\alpha}(t)O_2(t)\rangle \tag{C.17}$$

Using the relationship given in Eq. C.16, we can calculate the numerator of the $g^2(\tau)$ function,

$$\langle \sigma_2(t+\tau)\rangle = A(\tau)\langle \sigma_2(t)\rangle + B(\tau)\langle \sigma_1(t)\rangle + C(\tau)\langle \sigma_-(t)\rangle + D(\tau)\langle \sigma_+(t)\rangle \tag{C.18}$$

The respective coefficients are calculated in equation C.11 using the optical Bloch equation. Extending the equation to two-time correlation operators,

$$\begin{aligned}\langle \sigma_+(t)\sigma_2(t+\tau)\sigma_-(t)\rangle &= A(\tau)\langle \sigma_+(t)\sigma_2(t)\sigma_-(t)\rangle + B(\tau)\langle \sigma_+(t)\sigma_1(t)\sigma_-(t)\rangle \\ &\quad + C(\tau)\langle \sigma_+(t)\sigma_-(t)\sigma_-(t)\rangle + D(\tau)\langle \sigma_+(t)\sigma_+(t)\sigma_-(t)\rangle \\ &= B(\tau)\langle \sigma_2(t)\rangle \qquad \text{(C.19)} \\ &= e^{M\tau}|_{12}\langle \sigma_2(t)\rangle \qquad \text{(C.20)}\end{aligned}$$

We can further simplify the equation for g^2 by using all the information we have derived so far,

$$g^2(\tau) = t \overset{lim}{\rightarrow} \infty \frac{e^{M\tau}|_{12}\langle \sigma_2(t)\rangle}{\langle \tilde{\sigma_2}(t)\rangle\langle \tilde{\sigma_2}(t+\tau)\rangle} = t \overset{lim}{\rightarrow} \infty \frac{e^{M\tau}|_{12}}{\langle \tilde{\sigma_2}(t+\tau)\rangle} = \frac{e^{M\tau}|_{12}}{\rho_{22}^{SS}} \tag{C.21}$$

The above relationship gives the equivalent result as derived in Eq. 5.20. To summarize the calculation we have done before, second-order intensity correlation is proportional to the excited level population ρ_{22}. For a two-level system driven by a cw laser, at time zero the correlation is zero, this is inherently quantum mechanical property of the operators ($\langle\sigma_+(t)\sigma_2(t)\sigma_-(t)\rangle = 0$). Immediately after zero time ($\tau > 0$), ρ_{22} has a transient behavior which depends on the excitation power and detuning, this transient behavior is a result of the Rabi oscillations of the atomic operators. For a longer time ρ_{22} goes to a steady state. Experimentally we measure an unnormalized intensity correlation. The correlation could be normalized to the long time when all the transient behavior of the atom has died-off, such properly normalized intensity correlation is referred to as $g^2(\tau)$. The above methods can be easily extended to calculate $g^{(2)}$ for 3-level systems.

BIBLIOGRAPHY

BIBLIOGRAPHY

[1] A. Aspect, P. Grangier, and G. Roger. Experimental test of realistic local theories via Bell's theorem. *Phys. Rev. Lett.*, 47:460–463, 1981.

[2] Mark M. Wilde. From classical to quantum shannon theory.

[3] Johannes Handsteiner, Andrew S. Friedman, Dominik Rauch, Jason Gallicchio, Bo Liu, Hannes Hosp, Johannes Kofler, David Bricher, Matthias Fink, Calvin Leung, Anthony Mark, Hien T. Nguyen, Isabella Sanders, Fabian Steinlechner, Rupert Ursin, Sren Wengerowsky, Alan H. Guth, David I. Kaiser, Thomas Scheidl, and Anton Zeilinger. Cosmic bell test: Measurement settings from milky way stars. *Physical Review Letters*, 118(6), feb 2017.

[4] Michael A. Nielsen and Isaac L. Chuang. *Quantum Computation and Quantum Information (Cambridge Series on Information and the Natural Sciences)*. Cambridge University Press, 2000.

[5] Richard P. Feynman. Simulating physics with computers. *International Journal of Theoretical Physics*, 21(6-7):467488, 1982.

[6] D. Deutsch. Quantum theory, the church-turing principle and the universal quantum computer. *Proceedings of the Royal Society A: Mathematical, Physical and Engineering Sciences*, 400(1818):97117, Aug 1985.

[7] T. D. Ladd, F. Jelezko, R. Laflamme, Y. Nakamura, C. Monroe, and J. L. OBrien. Quantum computers. *Nature*, 464(7285):4553, Apr 2010.

[8] Peter W. Shor. Polynomial-time algorithms for prime factorization and discrete logarithms on a quantum computer. *SIAM Journal on Computing*, 26(5):14841509, 1997.

[9] Charles H. Bennett and Gilles Brassard. Quantum cryptography: Public key distribution and coin tossing. *Theoretical Computer Science*, 560:7–11, dec 2014.

[10] Artur K. Ekert. Quantum cryptography based on bells theorem. *Physical Review Letters*, 67(6):661663, May 1991.

[11] Charles H. Bennett. Quantum information and computation. *Physics Today*, 48(10):24–30, oct 1995.

[12] H. J. Kimble. The quantum internet. *Nature*, 453(7198):1023–1030, jun 2008.

[13] W. K. Wootters and W. H. Zurek. A single quantum cannot be cloned. *Nature*, 299(5886):802803, 1982.

[14] Charles H. Bennett, Gilles Brassard, Claude Crpeau, Richard Jozsa, Asher Peres, and William K. Wootters. Teleporting an unknown quantum state via dual classical and einstein-podolsky-rosen channels. *Physical Review Letters*, 70(13):18951899, 1993.

[15] L.-M. Duan, M. J. Madsen, D. L. Moehring, P. Maunz, R. N. Kohn, and C. Monroe. Probabilistic quantum gates between remote atoms through interference of optical frequency qubits. *Physical Review A*, 73(6), jun 2006.

[16] Cody Jones, Danny Kim, Matthew T Rakher, Paul G Kwiat, and Thaddeus D Ladd. Design and analysis of communication protocols for quantum repeater networks. *New Journal of Physics*, 18(8):083015, aug 2016.

[17] Rodney Meter and Joe Touch. Designing quantum repeater networks. *IEEE Communications Magazine*, 51(8):6471, 2013.

[18] D. Leibfried, E. Knill, S. Seidelin, J. Britton, R. B. Blakestad, J. Chiaverini, D. B. Hume, W. M. Itano, J. D. Jost, C. Langer, R. Ozeri, R. Reichle, and D. J. Wineland. Creation of a six-atom 'schrdinger cat' state. *Nature*, 438(7068):639–642, dec 2005.

[19] Danny Kim, Samuel G. Carter, Alex Greilich, Allan S. Bracker, and Daniel Gammon. Ultrafast optical control of entanglement between two quantum-dot spins. *Nature Physics*, 7(3):223–229, dec 2010.

[20] D. L. Moehring, P. Maunz, S. Olmschenk, K. C. Younge, D. N. Matsukevich, L.-M. Duan, and C. Monroe. Entanglement of single-atom quantum bits at a distance. *Nature*, 449(7158):68–71, sep 2007.

[21] W. B. Gao, P. Fallahi, E. Togan, J. Miguel-Sanchez, and A. Imamoglu. Observation of entanglement between a quantum dot spin and a single photon. *Nature*, 491(7424):426–430, nov 2012.

[22] N. Piro, F. Rohde, C. Schuck, M. Almendros, J. Huwer, J. Ghosh, A. Haase, M. Hennrich, F. Dubin, and J. Eschner. Heralded single-photon absorption by a single atom. *Nature Physics*, 7(1):17–20, oct 2010.

[23] Stephan Ritter, Christian Nlleke, Carolin Hahn, Andreas Reiserer, Andreas Neuzner, Manuel Uphoff, Martin Mcke, Eden Figueroa, Joerg Bochmann, and Gerhard Rempe. An elementary quantum network of single atoms in optical cavities. *Nature*, 484(7393):195–200, apr 2012.

[24] Y. L. A. Rezus, S. G. Walt, R. Lettow, A. Renn, G. Zumofen, S. Gtzinger, and V. Sandoghdar. Single-photon spectroscopy of a single molecule. *Physical Review Letters*, 108(9), feb 2012.

[25] H. M. Meyer, R. Stockill, M. Steiner, C. Le Gall, C. Matthiesen, E. Clarke, A. Ludwig, J. Reichel, M. Atatre, and M. Khl. Direct photonic coupling of a semiconductor quantum dot and a trapped ion. *Physical Review Letters*, 114(12), mar 2015.

[26] Aymeric Delteil, Zhe Sun, Stefan Flt, and Atac Imamoğlu. Realization of a cascaded quantum system: Heralded absorption of a single photon qubit by a single-electron charged quantum dot. *Physical Review Letters*, 118(17), apr 2017.

[27] J. I. Cirac, P. Zoller, H. J. Kimble, and H. Mabuchi. Quantum state transfer and entanglement distribution among distant nodes in a quantum network. *Physical Review Letters*, 78(16):3221–3224, apr 1997.

[28] D. Kielpinski, C. Monroe, and D. J. Wineland. Architecture for a large-scale ion-trap quantum computer. *Nature*, 417(6890):709711, 2002.

[29] Philipp Schindler, Daniel Nigg, Thomas Monz, Julio T Barreiro, Esteban Martinez, Shannon X Wang, Stephan Quint, Matthias F Brandl, Volckmar Nebendahl, Christian F Roos, and et al. A quantum information processor with trapped ions. *New Journal of Physics*, 15(12):123012, Jun 2013.

[30] J. R. Weber, W. F. Koehl, J. B. Varley, A. Janotti, B. B. Buckley, C. G. Van De Walle, and D. D. Awschalom. Quantum computing with defects. *Proceedings of the National Academy of Sciences*, 107(19):85138518, 2010.

[31] Pieter Kok, W. J. Munro, Kae Nemoto, T. C. Ralph, Jonathan P. Dowling, and G. J. Milburn. Linear optical quantum computing with photonic qubits. *Reviews of Modern Physics*, 79(1):135174, 2007.

[32] T. H. Stievater, Xiaoqin Li, D. G. Steel, D. Gammon, D. S. Katzer, D. Park, C. Piermarocchi, and L. J. Sham. Rabi oscillations of excitons in single quantum dots. *Physical Review Letters*, 87(13), sep 2001.

[33] Gang Chen, T.H. Stievater, J.R. Guest, D.G. Steel, D. Gammon, Pochung Chen, C. Piermarocchi, and L Sham. Coherent optical spectroscopy and manipulation of single quantum dots. In T. Takagahara, editor, *Quantum Coherence Correlation and Decoherence in Semiconductor Nanostructures*, chapter 7, pages 281–365. Elsevier Inc., 2003.

[34] Mete Atature, Jan Dreiser, Antonio Badolato, Alexander Hgele, Khaled Karrai, and Atac Imamoglu. Quantum-dot spin-state preparation with near-unity fidelity. *Science*, 312(5773):551–553, apr 2006.

[35] Xiaodong Xu, Bo Sun, Paul R. Berman, Duncan G. Steel, Allan S. Bracker, Dan Gammon, and L. J. Sham. Coherent population trapping of an electron spin in a single negatively charged quantum dot. *Nature Physics*, 4(9):692–695, aug 2008.

[36] David Press, Kristiaan De Greve, Peter L. McMahon, Thaddeus D. Ladd, Benedikt Friess, Christian Schneider, Martin Kamp, Sven Hfling, Alfred Forchel, and Yoshihisa Yamamoto. Ultrafast optical spin echo in a single quantum dot. *Nature Photonics*, 4(6):367–370, apr 2010.

[37] Xiaodong Xu, Wang Yao, Bo Sun, Duncan G. Steel, Allan S. Bracker, Daniel Gammon, and L. J. Sham. Optically controlled locking of the nuclear field via coherent dark-state spectroscopy. *Nature*, 459(7250):1105–1109, jun 2009.

[38] David P. DiVincenzo. The physical implementation of quantum computation. *Fortschritte der Physik*, 48(9-11):771–783, sep 2000.

[39] Daniel Loss and David P. DiVincenzo. Quantum computation with quantum dots. *Physical Review A*, 57(1):120–126, jan 1998.

[40] Xiaoqin Li, Duncan Steel, Daniel Gammon, and Lu J. Sham. Quantum information processing based on optically driven semiconductor quantum dots. *Optics and Photonics News*, 15(9):38, sep 2004.

[41] A. Imamoglu, D. D. Awschalom, G. Burkard, D. P. DiVincenzo, D. Loss, M. Sherwin, and A. Small. Quantum information processing using quantum dot spins and cavity QED. *Physical Review Letters*, 83(20):4204–4207, nov 1999.

[42] Yanwen Wu, Xiaoqin Li, Duncan Steel, Daniel Gammon, and L.J. Sham. Coherent optical control of semiconductor quantum dots for quantum information processing. *Physica E: Low-dimensional Systems and Nanostructures*, 25(2-3):242–248, nov 2004.

[43] J. R. Schaibley, A. P. Burgers, G. A. McCracken, L.-M. Duan, P. R. Berman, D. G. Steel, A. S. Bracker, D. Gammon, and L. J. Sham. Demonstration of quantum entanglement between a single electron spin confined to an InAs quantum dot and a photon. *Physical Review Letters*, 110(16), apr 2013.

[44] Kristiaan De Greve, Leo Yu, Peter L. McMahon, Jason S. Pelc, Chandra M. Natarajan, Na Young Kim, Eisuke Abe, Sebastian Maier, Christian Schneider, Martin Kamp, Sven Hfling, Robert H. Hadfield, Alfred Forchel, M. M. Fejer, and Yoshihisa Yamamoto. Quantum-dot spin–photon entanglement via frequency downconversion to telecom wavelength. *Nature*, 491(7424):421–425, nov 2012.

[45] W.B. Gao, P. Fallahi, E. Togan, A. Delteil, Y.S. Chin, J. Miguel-Sanchez, and A. Imamoğlu. Quantum teleportation from a propagating photon to a solid-state spin qubit. *Nature Communications*, 4, nov 2013.

[46] Aymeric Delteil, Zhe Sun, Wei-Bo Gao, Emre Togan, Stefan Faelt, and Imamoglu Ata. Generation of heralded entanglement between distant hole spins. *Nature Physics*, 12(3):218223, 2015.

[47] Sergey V. Polyakov, Andreas Muller, Edward B. Flagg, Alex Ling, Natalia Borjemscaia, Edward Van Keuren, Alan Migdall, and Glenn S. Solomon. Coalescence of single photons emitted by disparate single-photon sources: The example of InAs quantum dots and parametric down-conversion sources. *Physical Review Letters*, 107(15), oct 2011.

[48] P. G. Kwiat, K. Mattle, H. Weinfurter, A. Zeilinger, A. V. Sergienko, and Y. Shih. New high-intensity source of polarization-entangled photon pair. *Phys. Rev. Lett.*, 75:4337–4341, 1995.

[49] Fumihiro Kaneda, Karina Garay-Palmett, Alfred B. U'Ren, and Paul G. Kwiat. Heralded single-photon source utilizing highly nondegenerate, spectrally factorable spontaneous parametric downconversion. *Optics Express*, 24(10):10733, may 2016.

[50] Z. Y. Ou and Y. J. Lu. Cavity enhanced spontaneous parametric downconversion for the prolongation of correlation time between conjugate photons. *Physical Review Letters*, 83(13):2556–2559, sep 1999.

[51] Long Zhu and Jian Wang. Arbitrary manipulation of spatial amplitude and phase using phase-only spatial light modulators. *Scientific Reports*, 4(1), Nov 2014.

[52] Akira Tomita and Raymond Y. Chiao. Observation of berrys topological phase by use of an optical fiber. *Physical Review Letters*, 57(8):937–940, aug 1986.

[53] J. N. Ross. The rotation of the polarization in low birefringence monomode optical fibres due to geometric effects. *Optical and Quantum Electronics*, 16(5):455–461, sep 1984.

[54] J. Breguet, A. Muller, and N. Gisin. Quantum cryptography with polarized photons in optical fibres. *Journal of Modern Optics*, 41(12):2405–2412, dec 1994.

[55] Jean-Marc Mérolla, Yuri Mazurenko, Jean-Pierre Goedgebuer, and William T. Rhodes. Single-photon interference in sidebands of phase-modulated light for quantum cryptography. *Physical Review Letters*, 82(8):1656–1659, feb 1999.

[56] Joseph M. Lukens and Pavel Lougovski. Frequency-encoded photonic qubits for scalable quantum information processing. *Optica*, 4(1):8, dec 2016.

[57] Stéphane Clemmen, Alessandro Farsi, Sven Ramelow, and Alexander L. Gaeta. Ramsey interference with single photons. *Physical Review Letters*, 117(22), nov 2016.

[58] L. Olislager, J. Cussey, A. T. Nguyen, P. Emplit, S. Massar, J.-M. Merolla, and K. Phan Huy. Frequency-bin entangled photons. *Physical Review A*, 82(1), jul 2010.

[59] J Mora, A Ruiz-Alba, W Amaya, and J Capmany. Dispersion supported BB84 quantum key distribution using phase modulated light. *IEEE Photonics Journal*, 3(3):433–440, jun 2011.

[60] W. E. Lamb. Anti-photon. *Applied Physics B Laser and Optics*, 60(2-3):77–84, 1995.

[61] Ashok Muthukrishnan, Marlan O. Scully, , and M. Suhail Zubairy. The concept of the photonrevisited. In Chandrasekhar Roychoudhuri and Rajarshi Roy, editors, *The nature of light: what is a photon?*, chapter 4, pages S 18–27. CRC Press, 2008.

[62] L. Mandelstam and Ig. Tamm. The uncertainty relation between energy and time in non-relativistic quantum mechanics. *Selected Papers*, page 115123, 1991.

[63] Rodney Loudon. *The Quantum Theory of Light*. Oxford University Press, 2000.

[64] Daniel Steck. *Quantum and Atom Optics*. 2016.

[65] Paul R. Berman and Vladimir S. Malinovsky. *Principles of Laser Spectroscopy and Quantum Optics*. PRINCETON UNIV PR, 2011.

[66] H. J. Kimble, M. Dagenais, and L. Mandel. Photon antibunching in resonance fluorescence. *Physical Review Letters*, 39(11):691–695, sep 1977.

[67] Paul G. Kwiat, Edo Waks, Andrew G. White, Ian Appelbaum, and Philippe H. Eberhard. Ultrabright source of polarization-entangled photons. *Physical Review A*, 60(2):R773–R776, aug 1999.

[68] N. Akopian, N. H. Lindner, E. Poem, Y. Berlatzky, J. Avron, D. Gershoni, B. D. Gerardot, and P. M. Petroff. Entangled photon pairs from semiconductor quantum dots. *Physical Review Letters*, 96(13), Jun 2006.

[69] Gediminas Juska, Valeria Dimastrodonato, Lorenzo O. Mereni, Agnieszka Gocalinska, and Emanuele Pelucchi. Towards quantum-dot arrays of entangled photon emitters. *Nature Photonics*, 7(7):527531, 2013.

[70] Mark Bashkansky, Igor Vurgaftman, Andrew C. R. Pipino, and J. Reintjes. Significance of heralding in spontaneous parametric down-conversion. *Physical Review A*, 90(5), Dec 2014.

[71] N. H. Bonadeo. *Nano-Optics: Coherent Optical Spectroscopy of Single Semiconductor Quantum Dots*. Ph.D. thesis, University of Michigan, Ann Arbor, 1999.

[72] A. S. Lenihan. *Transient Nonlinear Spectroscopy of InAs Quantum Dots: Coherent and Incoherent Dynamics of Confined Excitons*. Ph.D. thesis, University of Michigan, Ann Arbor, 2002.

[73] P. A. Franken, A. E. Hill, C.W. Peters, and G. Weinreich. Generation of Optical Harmonics. *Phys. Rev. Lett.*, 7:118–119, 1961.

[74] D. A. Kleinman. Nonlinear Dielectric Polarization in Optical Media. *Phys. Rev.*, 126:1977–1979, 1977.

[75] R. W. Boyd. *Nonlinear Optics*. Academic Press, Inc., 2008.

[76] G. D. Boyd and D. A. Kleinman. Parametric Interaction of Focused Gaussian Light Beams. *Journal of Applied Physics*, 39:3597–3639, 1968.

[77] Huw E. Major, Corin B.e. Gawith, and Peter G.r. Smith. Gouy phase compensation in quasi-phase matching. *Optics Communications*, 281(19):50365040, 2008.

[78] J. A. Armstrong, N. Bloembergen, J. Ducuing, and P. S. Pershan. Interactions between light waves in a nonlinear dielectric. *Phys. Rev.*, 127:1918–1936, 1962.

[79] J. Yao and Y. Wang. *Nonlinear Optics and Solid-State Lasers*. Springer Series, 2012.

[80] Z. Zeng, H. Shen, H. Xu, Y. Zhou, C. Huang, and D. Shen. Measurements of the refractive index and its thermal coefficients for KTP crystals. *J. Synth. Cryst.*, 16:274–277, 1987.

[81] H. Y. Shen, Y. P. Zhou, W. X. Lin, Z. D. Zeng, R. R. Zeng, G. F. Yu, C. H. Huang, A. D. Jiang, S. Q. Jia, and D. Z. Shen. Second-harmonic generation and sum frequency mixing of dual wavelength Nd:YALO3 laser in flux grown KTiOPO4 crystal. *IEEE J. Quantum Electron.*, 28:48–51, 1992.

[82] K. Kato and E. Takaoka. Sellmeier and thermo-optic dispersion formulas for KTP. *Applied Optics*, 41:5040–5044, 2002.

[83] S. Emanueli and A. Arie. Temperature-dependent dispersion equations for $KTiOPO_4$ and $KTiOAsO_4$. *Applied Optics*, 42:6661–6665, 2003.

[84] A. Einstein, B. Podolsky, and N. Rosen. Can quantum-mechanical description of physical Reality be considered complete? *Physical Review*, 47:777–780, 1935.

[85] David Bohm. A suggested interpretation of the quantum theory in terms of "hidden" variables. i. *Physical Review*, 85(2):166–179, jan 1952.

[86] Reinhard F. Werner. Quantum states with einstein-podolsky-rosen correlations admitting a hidden-variable model. *Physical Review A*, 40(8):4277–4281, oct 1989.

[87] J. Bell. On the Einstein Podolsky Rosen paradox. *Physics*, 3:195–200, 1964.

[88] S. J. Freedman and J. F. Clauser. Experimental test of local hidden-variable theories. *Phys. Rev. Lett.*, 28:938–941, 1972.

[89] D. C. Burnham and D. L. Weinberg. Observation of simultaneity in parametric production of optical photon pairs. *Phys. Rev. Lett.*, 25:84–87, 1970.

[90] R. Ghosh and L. Mandel. Observation of nonclassical effects in the interference of two photons. *Phys. Lett. Rev.*, 59:1903–1905, 1987.

[91] Gregor Weihs, Thomas Jennewein, Christoph Simon, Harald Weinfurter, and Anton Zeilinger. Violation of bells inequality under strict einstein locality conditions. *Physical Review Letters*, 81(23):5039–5043, dec 1998.

[92] Thomas Jennewein, Christoph Simon, Gregor Weihs, Harald Weinfurter, and Anton Zeilinger. Quantum cryptography with entangled photons. *Physical Review Letters*, 84(20):4729–4732, may 2000.

[93] Dik Bouwmeester, Jian-Wei Pan, Klaus Mattle, Manfred Eibl, Harald Weinfurter, and Anton Zeilinger. *Nature*, 390(6660):575–579, dec 1997.

[94] Yoritoshi Adachi, Takashi Yamamoto, Masato Koashi, and Nobuyuki Imoto. Simple and efficient quantum key distribution with parametric down-conversion. *Physical Review Letters*, 99(18), nov 2007.

[95] Norbert Ltkenhaus. Security against individual attacks for realistic quantum key distribution. *Physical Review A*, 61(5), apr 2000.

[96] P. Walther, K. J. Resch, T. Rudolph, E. Schenck, H. Weinfurter, V. Vedral, M. Aspelmeyer, and A. Zeilinger. Experimental one-way quantum computing. *Nature*, 434(7030):169–176, mar 2005.

[97] M. H. Rubin, D. N. Klyshko, Y. H. Shih, and A. V. Sergienko. Theory of two-photon entanglement in type-II optical parametric down-conversion. *Phys. Rev. A*, 50:5122–5133, 1994.

[98] Zhe-Yu Jeff Ou. *Multi-Photon Quantum Interference*. Springer US, 2007.

[99] A. Ling, A. Lamas-Linares, and C. Kurtsiefer. Absolute emission rates of spontaneous parametric down-conversion into single transverse Gaussian modes. *Phys. Rev. A*, 77:043834–1–7, 2008.

[100] M. Hillery and L. D. Mlodinow. Quantization of electrodynamics in nonlinear dielectric media. *Phys. Rev. A*, 30:1861–1865, 1984.

[101] M.M. Fejer, G.A. Magel, D.H. Jundt, and R.L. Byer. Quasi-phase-matched second harmonic generation: tuning and tolerances. *IEEE Journal of Quantum Electronics*, 28(11):2631–2654, 1992.

[102] R. Loudon. *The Quantum Theory of Light*. Oxford science publication, 2000.

[103] H. E. Guilbert. *Efficient Entangled Biphoton Production and Manipulation for Quantum Applications*. (ph.d.) thesis, Duke University, 2015.

[104] Hannah E. Guilbert and Daniel J. Gauthier. Enhancing heralding efficiency and biphoton rate in type-i spontaneous parametric down-conversion. *IEEE Journal of Selected Topics in Quantum Electronics*, 21(3):215–224, may 2015.

[105] Y. J. Lu and Z. Y. Ou. Optical parametric oscillator far below threshold: Experiment versus theory. *Physical Review A*, 62(3), aug 2000.

[106] M. J. Collett and C. W. Gardiner. Squeezing of intracavity and traveling-wave light fields produced in parametric amplification. *Physical Review A*, 30(3):1386–1391, sep 1984.

[107] D. F. Walls and Gerard J. Milburn. *Quantum Optics*. Springer Berlin Heidelberg, 2007.

[108] G. S. Agarwal. *Quantum Optics*. Cambridge University Press, 2012.

[109] Ulrike Herzog, Matthias Scholz, and Oliver Benson. Theory of biphoton generation in a single-resonant optical parametric oscillator far below threshold. *Physical Review A*, 77(2), feb 2008.

[110] R. W. P. Drever, J. L. Hall, F. V. Kowalski, J. Hough, G. M. Ford, A. J. Munley, and H. Ward. Laser phase and frequency stabilization using an optical resonator. *Applied Physics B Photophysics and Laser Chemistry*, 31(2):97–105, jun 1983.

[111] Eric D. Black. An introduction to pound–drever–hall laser frequency stabilization. *American Journal of Physics*, 69(1):79–87, jan 2001.

[112] M. E. Reimer, G. Bulgarini, A. Fognini, R. W. Heeres, B. J. Witek, M. A. M. Versteegh, A. Rubino, T. Braun, M. Kamp, S. Hfling, D. Dalacu, J. Lapointe, P. J. Poole, and V. Zwiller. Overcoming power broadening of the quantum dot emission in a pure wurtzite nanowire. *Physical Review B*, 93(19), may 2016.

[113] J Schaibley. *Spin-Photon Entanglement and Quantum Optics with Single Quantum Dots*. Ph.D. thesis, University of Michigan, Ann Arbor, 2013.

[114] F. Marsili, V. B. Verma, J. A. Stern, S. Harrington, A. E. Lita, T. Gerrits, I. Vayshenker, B. Baek, M. D. Shaw, R. P. Mirin, and S. W. Nam. Detecting single infrared photons with 93% system efficiency. *Nature Photonics*, 7(3):210–214, feb 2013.

[115] G. D. Boyd and H. Kogelnik. Generalized confocal resonator theory. *Bell System Technical Journal*, 41(4):1347–1369, jul 1962.

[116] John P. Goldsborough. Beat frequencies between modes of a concave-mirror optical resonator. *Applied Optics*, 3(2):267, Jan 1964.

[117] Matthias Scholz, Lars Koch, and Oliver Benson. Statistics of narrow-band single photons for quantum memories generated by ultrabright cavity-enhanced parametric down-conversion. *Physical Review Letters*, 102(6), feb 2009.

[118] A. P. Burgers. *Towards Quantum Teleportation from a Spontaneous Parametric Down-Conversion Source to a Quantum Dot Spin by Hong-Ou-Mandel Interference*. Ph.D. thesis, University of Michigan, Ann Arbor, 2015.

[119] Kentaro Wakui, Yujiro Eto, Hugo Benichi, Shuro Izumi, Tetsufumi Yanagida, Kazuhiro Ema, Takayuki Numata, Daiji Fukuda, Masahiro Takeoka, and Masahide Sasaki. Ultrabroadband direct detection of nonclassical photon statistics at telecom wavelength. *Scientific Reports*, 4(1), apr 2014.

[120] B. Yurke and M. Potasek. Obtainment of thermal noise from a pure quantum state. *Physical Review A*, 36(7):3464–3466, oct 1987.

[121] P Grangier, G Roger, and A Aspect. Experimental evidence for a photon anticorrelation effect on a beam splitter: A new light on single-photon interferences. *Europhysics Letters (EPL)*, 1(4):173–179, feb 1986.

[122] Jasprit Singh. *Electronic and Optoelectronic Properties of Semiconductor Structures*. CAMBRIDGE UNIV PR, 2007.

[123] Sadao Adachi. GaAs, AlAs, and AlxGa1-xAs: Material parameters for use in research and device applications. *Journal of Applied Physics*, 58(3):R1–R29, aug 1985.

[124] H. Benisty, H. De Neve, and C. Weisbuch. Impact of planar microcavity effects on light extraction-part i: basic concepts and analytical trends. *IEEE Journal of Quantum Electronics*, 34(9):1612–1631, 1998.

[125] Olivier Gazzano and Glenn S. Solomon. Toward optical quantum information processing with quantum dots coupled to microstructures [invited]. *Journal of the Optical Society of America B*, 33(7):C160, jun 2016.

[126] B. T. Miller, W. Hansen, S. Manus, R. J. Luyken, A. Lorke, J. P. Kotthaus, S. Huant, G. Medeiros-Ribeiro, and P. M. Petroff. Few-electron ground states of charge-tunable self-assembled quantum dots. *Physical Review B*, 56(11):6764–6769, sep 1997.

[127] R. J. Warburton, C. S. Drr, K. Karrai, J. P. Kotthaus, G. Medeiros-Ribeiro, and P. M. Petroff. Charged excitons in self-assembled semiconductor quantum dots. *Physical Review Letters*, 79(26):5282–5285, dec 1997.

[128] Benito Alén, Florian Bickel, Khaled Karrai, Richard J. Warburton, and Pierre M. Petroff. Stark-shift modulation absorption spectroscopy of single quantum dots. *Applied Physics Letters*, 83(11):2235–2237, sep 2003.

[129] M. Bayer, G. Ortner, O. Stern, A. Kuther, A. A. Gorbunov, A. Forchel, P. Hawrylak, S. Fafard, K. Hinzer, T. L. Reinecke, S. N. Walck, J. P. Reithmaier, F. Klopf, and F. Schfer. Fine structure of neutral and charged excitons in self-assembled in(ga)as/(al)GaAs quantum dots. *Physical Review B*, 65(19), may 2002.

[130] C. R. Nelson. *COHERENT NONLINEAR OPTICAL SPECTROSCOPY OF In- GaN DISKS IN GaN NANOWIRES*. Ph.D. thesis, University of Michigan, Ann Arbor, 2017.

[131] Michael Shribak. Polarization aberrations caused by differential transmission and phase shift in high-numerical-aperture lenses: theory, measurement, and rectification. *Optical Engineering*, 41(5):943, may 2002.

[132] Philippe Boucaud, Sébastien Sauvage, and Julien Houel. Intersublevel transitions in self-assembled quantum dots. *Comptes Rendus Physique*, 9(8):840–849, oct 2008.

[133] Oliver Gywat, Hubert J. Krenner, and Jesse Berezovsky. *Spins in Optically Active Quantum Dots*. Wiley VCH Verlag GmbH, 2009.

[134] Khaled Karrai and Richard J. Warburton. Optical transmission and reflection spectroscopy of single quantum dots. *Superlattices and Microstructures*, 33(5-6):311–337, may 2003.

[135] J. R. Schaibley, A. P. Burgers, G. A. McCracken, D. G. Steel, A. S. Bracker, D. Gammon, and L. J. Sham. Direct detection of time-resolved rabi oscillations in a single quantum dot via resonance fluorescence. *Physical Review B*, 87(11), mar 2013.

[136] Xing Ding, Yu He, Z.-C. Duan, Niels Gregersen, M.-C. Chen, S. Unsleber, S. Maier, Christian Schneider, Martin Kamp, Sven Hfling, Chao-Yang Lu, and Jian-Wei Pan. On-demand single photons with high extraction efficiency and near-unity indistinguishability from a resonantly driven quantum dot in a micropillar. *Physical Review Letters*, 116(2), jan 2016.

[137] Marlan O. Scully and M. Suhail Zubairy. *Quantum Optics*. Cambridge University Press, 1997.

[138] David DEnterria and Gustavo G. Da Silveira. Observing light-by-light scattering at the large hadron collider. *Physical Review Letters*, 111(8), 2013.

[139] Mattias Marklund. Fundamental optical physics: Probing the quantum vacuum. *Nature Photonics*, 4(2):7274, 2010.

[140] Roy J. Glauber. The quantum theory of optical coherence. *Physical Review*, 130(6):2529–2539, jun 1963.

[141] C. K. Hong, Z. Y. Ou, and L. Mandel. Measurement of subpicosecond time intervals between two photons by interference. *Physical Review Letters*, 59(18):2044–2046, nov 1987.

[142] Z. Y. Ou. Quantum theory of fourth-order interference. *Physical Review A*, 37(5):1607–1619, mar 1988.

[143] R. Ghosh, C. K. Hong, Z. Y. Ou, and L. Mandel. Interference of two photons in parametric down conversion. *Physical Review A*, 34(5):3962–3968, nov 1986.

[144] H. J. Kimble. The quantum internet. *Nature*, 453(7198):1023–1030, jun 2008.

[145] T. Legero, T. Wilk, A. Kuhn, and G. Rempe. Characterization of single photons using two-photon interference. In *Advances In Atomic, Molecular, and Optical Physics*, pages 253–289. Elsevier, 2006.

[146] Thomas Legero, Tatjana Wilk, Markus Hennrich, Gerhard Rempe, and Axel Kuhn. Quantum beat of two single photons. *Physical Review Letters*, 93(7), aug 2004.

[147] P. Maunz, D. L. Moehring, S. Olmschenk, K. C. Younge, D. N. Matsukevich, and C. Monroe. Quantum interference of photon pairs from two remote trapped atomic ions. *Nature Physics*, 3(8):538–541, jun 2007.

[148] Charles Santori, David Fattal, Jelena Vučković, Glenn S. Solomon, and Yoshihisa Yamamoto. Indistinguishable photons from a single-photon device. *Nature*, 419(6907):594–597, oct 2002.

[149] Edward Flagg, Andreas Muller, Sergey Polyakov, Alex Ling, Alan Migdall, and Glenn Solomon. Interference of single photons from two separate semiconductor quantum dots. *Physical Review Letters*, 104(13), apr 2010.

[150] Franois Hnault. Quantum physics and the beam splitter mystery. *The Nature of Light: What are Photons? VI*, Oct 2015.

[151] Paul R. Berman and George W. Ford. Spontaneous decay, unitarity, and the weisskopfwigner approximation. *Advances In Atomic, Molecular, and Optical Physics Advances in Atomic, Molecular, and Optical Physics*, page 175221, 2010.

[152] A. M. Dyckovsky and S. Olmschenk. Analysis of photon-mediated entanglement between distinguishable matter qubits. *Physical Review A*, 85(5), 2012.

[153] Pavel Kolchin, Chinmay Belthangady, Shengwang Du, G. Y. Yin, and S. E. Harris. Electro-optic modulation of single photons. *Physical Review Letters*, 101(10), Mar 2008.

[154] Matthew T. Rakher and Kartik Srinivasan. Subnanosecond electro-optic modulation of triggered single photons from a quantum dot. *Applied Physics Letters*, 98(21), 2011.

[155] Huafang Dong, Haifeng Pan, Yao Li, E Wu, and Heping Zeng. Efficient single-photon frequency upconversion at 1.06m with ultralow background counts. *Applied Physics Letters*, 93(7), 2008.

[156] Matthieu Bloch, Steven W. McLaughlin, Jean-Marc Merolla, and Frédéric Patois. Frequency-coded quantum key distribution. *Optics Letters*, 32(3):301, jan 2007.

[157] J. Capmany and C. R. Fernandez-Pousa. Realization of single-photon frequency-domain qubit channels using phase modulators. *IEEE Photonics Journal*, 4(6):2074–2084, dec 2012.

[158] T. A. Maldonado. *Handbook of Optics*. McGRAW-HILL, INC, 2 edition, 2001.

[159] G. P. Miroshnichenko, A. D. Kiselev, A. I. Trifanov, and A. V. Gleim. Algebraic approach to electro-optic modulation of light: Exactly solvable multimode quantum model. *arXiv*, 1605.0577, 2016.

[160] P. Kumar and A. Prabhakar. Evolution of Quantum States in an Electro-Optic Phase Modulator. *IEEE JOURNAL OF QUANTUM ELECTRONICS*, 45:149–156, 2009.

[161] W. H. Louisell, A. Yariv, and A. E. Siegman. Quantum Fluctuations and Noise in Parametric Processes. I. *Physical Review*, 124:1646–1654, 1961.

[162] G. A. Barbosa. Wave function for spontaneous parametric down-conversion with orbital angular momentum. *Physical Review A*, 80:063833–1–12, 2009.

[163] Y. Ding and Z. Y. Ou. Frequency down-conversion for a quantum network. *Optics Letters*, 35:2591–2593, 2010.

[164] W.l. She and W.k. Lee. Wave coupling theory of linear electrooptic effect. *Optics Communications*, 195(1-4):303311, Aug 2001.

[165] Milton Abramowitz and Irene A. Stegun. *Handbook of mathematical functions with formulas, graphs, and mathematical tables*. Dover Publ., 2013.

[166] C. Ren and H. F. Hofmann. Simultaneous suppression of time and energy uncertainties in a single-photon frequency-comb state. *Physical Review A*, 89:053823–1–7, 2014.

[167] B. R. Mollow. Power spectrum of light scattered by two-level systems. *Physical Review*, 188(5):19691975, 1969.

[168] R. B. Patel, A. J. Bennett, K. Cooper, P. Atkinson, C. A. Nicoll, D. A. Ritchie, and A. J. Shields. Postselective two-photon interference from a continuous nonclassical stream of photons emitted by a quantum dot. *Physical Review Letters*, 100(20), may 2008.

[169] Raphal Proux, Maria Maragkou, Emmanuel Baudin, Christophe Voisin, Philippe Roussignol, and Carole Diederichs. Measuring the photon coalescence time window in the continuous-wave regime for resonantly driven semiconductor quantum dots. *Physical Review Letters*, 114(6), feb 2015.

[170] Jason S. Pelc, Leo Yu, Kristiaan De Greve, Peter L. Mcmahon, Chandra M. Natarajan, Vahid Esfandyarpour, Sebastian Maier, Christian Schneider, Martin Kamp, Sven Hfling, and et al. Downconversion quantum interface for a single quantum dot spin and 1550-nm single-photon channel. *Optics Express*, 20(25):27510, 2012.

[171] Melvin Lax. Quantum noise. XI. multitime correspondence between quantum and classical stochastic processes. *Physical Review*, 172(2):350–361, aug 1968.